

ADVERTIMENT. La consulta d'aquesta tesi queda condicionada a l'acceptació de les següents condicions d'ús: La difusió d'aquesta tesi per mitjà del servei TDX (www.tesisenxarxa.net) ha estat autoritzada pels titulars dels drets de propietat intel·lectual únicament per a usos privats emmarcats en activitats d'investigació i docència. No s'autoritza la seva reproducció amb finalitats de lucre ni la seva difusió i posada a disposició des d'un lloc aliè al servei TDX. No s'autoritza la presentació del seu contingut en una finestra o marc aliè a TDX (framing). Aquesta reserva de drets afecta tant al resum de presentació de la tesi com als seus continguts. En la utilització o cita de parts de la tesi és obligat indicar el nom de la persona autora.

ADVERTENCIA. La consulta de esta tesis queda condicionada a la aceptación de las siguientes condiciones de uso: La difusión de esta tesis por medio del servicio TDR (www.tesisenred.net) ha sido autorizada por los titulares de los derechos de propiedad intelectual únicamente para usos privados enmarcados en actividades de investigación y docencia. No se autoriza su reproducción con finalidades de lucro ni su difusión y puesta a disposición desde un sitio ajeno al servicio TDR. No se autoriza la presentación de su contenido en una ventana o marco ajeno a TDR (framing). Esta reserva de derechos afecta tanto al resumen de presentación de la tesis como a sus contenidos. En la utilización o cita de partes de la tesis es obligado indicar el nombre de la persona autora.

WARNING. On having consulted this thesis you're accepting the following use conditions: Spreading this thesis by the TDX (www.tesisenxarxa.net) service has been authorized by the titular of the intellectual property rights only for private uses placed in investigation and teaching activities. Reproduction with lucrative aims is not authorized neither its spreading and availability from a site foreign to the TDX service. Introducing its content in a window or frame foreign to the TDX service is not authorized (framing). This rights affect to the presentation summary of the thesis as well as to its contents. In the using or citation of parts of the thesis it's obliged to indicate the name of the author



Ph.D. Thesis

GROUND MOVING TARGET
INDICATION WITH SYNTHETIC
APERTURE RADARS
FOR MARITIME SURVEILLANCE

Author

EDUARDO MAKHOUL VARONA

Thesis advisor

Prof. Antoni Broquetas Ibars



UNIVERSITAT POLITÈCNICA DE CATALUNYA
BARCELONATECH

Departament de Teoria del Senyal
i Comunicacions



UNIVERSITAT POLITÈCNICA
DE CATALUNYA
BARCELONATECH

Ground Moving Target Indication with Synthetic Aperture Radars for Maritime Surveillance

Author

Eduardo Makhoul Varona

Thesis Advisor

Prof. Antoni Broquetas Ibars

A thesis submitted to the Universitat Politècnica de Catalunya (UPC) in
partial fulfillment of the requirements for the degree of
DOCTOR OF PHILOSOPHY

**Department of Signal
Theory and Communications**



Ph.D. program on Signal Theory and Communications
Remote Sensing Laboratory (RsLab) Group
Barcelona, March 2015

Eduardo Makhoul Varona

Ground Moving Target Indication with Synthetic Aperture Radars for Maritime Surveillance

Ph.D. program on Signal Theory and Communications

This work has been supported by FPU Research Fellowship Program, Ministerio de Educación, contract AP2009-4590; by FI-AGAUR Research Fellowship Program, Generalitat de Catalunya, contract 2010FI EM051757; by the Spanish Ministry of Science and Innovation (MICINN) under projects TEC2011-28201-C02-01, TEC2008-06764-C02-01 and CONSOLIDER CSD2008-00068; and by European Commission under FP7-SPACE Projects NEWA Ref. 241630 and SIMTISYS Ref. 263268.

Copyright ©2015 by Eduardo Makhoul Varona, TSC, UPC, Barcelona, Spain. All rights reserved. Reproduction by any means or translation of any part of this work is forbidden without permission of the copyright holder.



Acta de qualificació de tesi doctoral

Curs acadèmic: 2014/2015

Nom i cognoms

Eduardo Makhoul Varona

Programa de doctorat

Teoria del Senyal i Comunicacions

Unitat estructural responsable del programa

Teoria del Senyal i Comunicacions

Resolució del Tribunal

Reunit el Tribunal designat a l'efecte, el doctorand / la doctoranda exposa el tema de la seva tesi doctoral titulada
GROUND MOVING TARGET INDICATION WITH SYNTHETIC APERTURE RADARS
FOR MARITIME SURVEILLANCE.

Acabada la lectura i després de donar resposta a les qüestions formulades pels membres titulars del tribunal, aquest atorga la qualificació:

☐ NO APTE

☐ APROVAT

☐ NOTABLE

☐ EXCEL·LENT

(Nom, cognoms i signatura)		(Nom, cognoms i signatura)	
President/a		Secretari/ària	
(Nom, cognoms i signatura)	(Nom, cognoms i signatura)	(Nom, cognoms i signatura)	(Nom, cognoms i signatura)
Vocal	Vocal	Vocal	Vocal

_____, ____ d'/de _____ de _____

El resultat de l'escrutini dels vots emesos pels membres titulars del tribunal, efectuat per l'Escola de Doctorat, a instància de la Comissió de Doctorat de la UPC, atorga la MENCIÓ CUM LAUDE:

☐ SÍ

☐ NO

(Nom, cognoms i signatura)	(Nom, cognoms i signatura)
President de la Comissió Permanent de l'Escola de Doctorat	Secretari de la Comissió Permanent de l'Escola de Doctorat

Barcelona, ____ d'/de _____ de _____

*To my father Issa, my mother Montserrat
and my sisters Jeannette and Ingrid.
To my beloved Aglaia.*

*The sea, once it casts its spell,
holds one in its net of wonder forever.*
Jacques Yves Cousteau

Preface

Em costa creure que estigui escrivint aquests línies, que son les últimes d'una llarga historia que ja fa més de cinc anys que va començar. Com de segur totes i tots els que han passat per aquesta experiència, estaran d'acord amb mi que aquesta etapa que es tanca la podríem definir com una autèntica muntanya russa; amb molts d'alts i baixos, però una vivència única que m'ha permès créixer com a persona i gaudir de molts bons moments acompanyat sempre d'aquelles persones amb qui he confiat i que han cregut en mi. Es per això que aquestes línies intenten ser un agraïment sincer a totes aquelles persones que sense el seu suport no hauria pogut arribar fins aquest precís moment.

En primer lloc vull agrair al meu director de tesi, el professor Antoni Broquetas, per haver-me donat l'oportunitat de poder realitzar aquesta tesi doctoral i pel seu recolzament. Els seus consells i els seus coneixements tècnics m'han ajudat a desenvolupar el meu propi camí en aquesta tesi. També li vull agrair l'oportunitat de poder participar en diferents projectes que m'ha permès estar en contacte directe amb la indústria aeroespacial europea i altres grups d'investigació.

També vull aprofitar aquest espai per agrair als diferents professors del departament el seu recolzament durant la realització de la tesi doctoral; en especial al professor Carlos López pel seu interès, recolzament i les discussions tècniques que en la ultima etapa de la tesi m'han permès ampliar els meus coneixements cap a una vesant del SAR, la polarimetria, abans desconeguda per mi; i també voldria agrair als professors Albert Aguasca, Jordi Mallorqui i Xavier Fàbregas que sempre han estat disponibles per qualsevol consulta o discussió.

From my stay in Germany I keep many and very pleasing memories, thanks to all the people I met for the second time in the Microwaves and Radar Institute. First of all I thank Dr. Gerhard and Dr. Marwan Younis for giving me that opportunity. I would like to specially thank my colleague Dr. Stefan Baumgartner, who has helped me during my stay and for his dedication in all our discussions on SAR-GMTI. I would like to take the opportunity to thank also Dr. Josef Mittermayer and Marc Rodriguez. I have to mention also my friends Nikola and Mariano, with them I have shared very good moments, making my stay there much more comfortable and funny. No em puc oblidar dels meus companys ("ex-UPCeros"), Sergi, Ricardo i Marivi, que tan be em van acollir a Munich i amb els quals em vaig divertir tant (iala, iala !!!), i amb els quals vam implantar l'esperit TSCero dels cafes postlunch al DLR.

El que ha fet única aquesta experiència ha sigut el gran grup d'amics i companys que m'he trobat durant aquests anys i amb els quals he compartit tants bons moments i

experiències, a més de despatx. Hem esdevingut una gran família que de tant en tant es torna a ajuntar per nadal o al estiu i fem alguna trobada masienca, per gaudir i expandir la nostra cultura gastronòmica. Tot i ser un “intrús”, els “anteneros” m’han acollit molt i molt be en el seu cercle, i es per això que els hi estic molt i molt agraïts pels bons moments gaudits, moltes gràcies nois i noies: Marc, Santi, Enrique, Marta, Maria, Gemma, Dani i Edgar. En aquesta família “TSCera” no hi poden faltar els meus companys “SARistas”, Dani, Giuseppe, Rubén, Pep i Alberto que m’han ajudat quan ho necessitava i amb els que tantes rutes de la tapa he compartit. No em vull oblidar ni de l’Alba ni del Guillem, uns intrusos Camineros, que s’han afegit al cercle viciós del cafè matiner/postlunch al últim tram de la tesi.

Voldria dedicar unes paraules especials d’agraïment per en Santi, que amb molta paciència sempre estava disposat a donar un cop de mà i ajudar-me a resoldre problemes de qualsevol tipus; tots estem en deute amb tu, Santi.

Gràcies al Rol i a la Veva, per haver-me acollit com un més de la família Gómez-D’Alessandro i per tots els dinars i sopars a casa vostra on he après a tenir un visió més crítica de les coses.

Ser quien soy y llegar a donde he llegado se lo debo a mi familia que siempre me ha demostrado su apoyo y cariño sin condiciones, y han creído en mí. No hay suficientes palabras para expresar la inmensa gratitud a mis padres, Issa y Montserrat, que me han transmitido ese espíritu de trabajo y lucha por lo que uno más anhela y desea: *tu como siempre lo sacarás adelante ten paciencia*. Estaré siempre en deuda con vosotros. A mis hermanas, Jeannette e Ingrid, por su amor incondicional y soporte moral, a ellas que han estado a mi lado siempre que lo he necesitado y han cuidado de su hermano pequeño, muchas gracias hermanitas. A mis cuñados Mario y Eduard porque han sabido lidiar con un personaje tan especial como yo, les doy mis más sinceras gracias.

Finalment voldria dedicar aquestes últimes línies a l’Aglaià, que m’ha suportat, pacient, dia a dia durant tota aquesta etapa, sense esperar res a canvi i que m’ha ajudat a relativitzar els meus problemes i buscar les estratègies més adequades per avançar en aquest camí sinuós. Gràcies pel teu suport incondicional, per ser la persona que ets i compartir la teva vida juntament amb mi.

Acknowledgments

The author wants to acknowledge the support of the following institutions:

- **MECD** (Ministerio de Educación, Cultura y Deporte) for providing the pre-doctoral FPU fellowship (Ref. AP2009-4590) during the development of this thesis.
- **AGAUR** (Agència de Gestió d'Ajuts Universitaris i de Recerca) for providing the pre-doctoral FI-AGAUR fellowship (Ref. 2010FI EM051757) during the first months of this doctoral activity.
- **MICINN** (Ministerio de Ciencia e Innovación) for providing financial support to part of the research performed in the frame of this thesis, under projects MUSEO (Ref. TEC2011-28201-C02-01), ACAPMRS (Ref. TEC2008-06764-C02-01) and CONSOLIDER (Ref. CSD2008-00068).
- **EC** (European Commission) for providing financial support to part of the research carried out within the pre-doctoral period, under FP7-SPACE projects NEWA (Ref. 241630) and SIMTISYS (Ref. 263268); and for providing some of the TerraSAR-X dual-polarized data for sea clutter characterization under project FP7-SPACE NEREIDS (Ref. 263468).
- **DLR-HR** (Deutsches Zentrum für Luft und Raumfahrt e.V., Insitut für Hochfrequenztechnik und Radarsysteme) for accepting the author as a guest scientist during his four-month stay in 2013, and also for their support in providing multichannel SAR-GMTI data from F-SAR and TerraSAR-X, under projects OceanSAR2009 and “Study of Novel Spaceborne GMTI Algorithms Using DRA Data” (Ref. MTH1971).
- **EADS-CASA Espacio**, currently integrated in **Airbus Military**, for providing financial support to part of the research carried out in the frame of this thesis, under project entitled “UPC Support to the PAZ Program” (Ref. ECE-C0-B-08-510).

Abstract

The explosive growth of shipping traffic all over the World, with around three quarters of the total trade goods and crude oil transported by sea, has raised newly emerging concerns (economical, ecological, social and geopolitical). In this sense, new regulations to control and minimize the impact of human activities in the marine environment have been promoted; which in turn require proper maritime surveillance mechanisms to gather critical information to act accordingly. Geo-information (location and speed) of ocean-going vessels is crucial in the maritime framework, playing a key role in the related environmental monitoring, fisheries management and maritime/coastal security. The increasing maritime traffic has led to a higher likelihood of accidents, hence increasing co-lateral ecosystem damages, and consequently a growing demand for polluting tankers detection. Likewise, a rise in the number of piracy acts, smuggling and illegal activities (overfishing, illegal immigration, weapon movement...) has stressed the need for ship detection and identification.

In this scenario space-based synthetic aperture radar (SAR) remote sensing is a potential tool for globally monitoring the oceans and seas, providing two-dimensional high-resolution imaging capabilities in all-day and all-weather conditions. Spaceborne SAR has entered the golden age during the last decade, as testified by the increased number of recent and forthcoming missions, e.g., RADARSAT-2 (RS2), TerraSAR-X (TSX), COSMO-SkyMed (CSK), TanDEM-X (TDX), Sentinel-1 and PAZ. The combination of ground moving target indication (GMTI) modes with multichannel spaceborne SAR systems represents a powerful apparatus for surveillance of maritime activities. The level of readiness of such a technology for road traffic monitoring is still low, and for the marine scenario is even less mature. Some of the current space-based SAR missions include an experimental GMTI mode with reduced detection capabilities, especially for small and slow moving targets.

In this framework, this doctoral dissertation focuses on the study and analysis of the GMTI limitations of current state-of-the-art SAR missions when operating over maritime scenarios and the proposal of novel and optimal multichannel SAR-GMTI architectures, able to properly exploit the additional spatial diversity with promising adaptive GMTI algorithms, providing subclutter visibility of small (reduced reflectivity) slow moving vessels. This doctoral activity carries out a transversal analysis embracing system-architecture proposal and optimization, processing strategies assessment, performance evaluation, sea/ocean clutter characterization and adequate calibration methodologies suggestion.

Firstly, the scarce availability of multichannel SAR-GMTI raw data and the related restrictions to access it have raised the need to implement flexible simulation tools for SAR-GMTI performance evaluation and mission prototyping in order to demonstrate the potential capabilities of the proposed alternative multichannel SAR-GMTI missions.

These simulation tools allow the comparative study and evaluation of the SAR-GMTI mode operated with current SAR missions, such as TSX and/or TDX, showing the reduced ability of these missions to detect small and slow boats in subclutter visibility. Improved performance is achieved with the new multichannel architecture based on non-uniformly distributed receivers (with external deployable antennas), setting the ground for future SAR-GMTI mission development.

Some experimental multichannel SAR-GMTI data sets over the sea and acquired with two instruments, airborne F-SAR and spaceborne TerraSAR-X platforms, have been processed to evaluate their detection capabilities as well as the adequate processing strategies (including channel balancing), which integrate classical (for dual-receive channels) and optimum adaptive (for more than two channels) SAR-GMTI techniques. Despite the fact that most of the vessels present in the scenarios have high reflectivity with smooth sea conditions, a proof of concept of the different algorithms and processing methodologies has been validated, in a way that the adaptive GMTI techniques provide in general improved performance when compared to classical approaches.

High fidelity in modeling the maritime scenario is required to provide accurate and realistic radar performance evaluation. This has been a complex and hot topic of research during several decades. This doctoral activity presents a preliminary characterization of the sea clutter returns imaged by the spaceborne TSX instrument in a three-level basis, i.e., radiometric, statistical and polarimetric descriptions using experimental polarimetric data. This study has shown that the system-dependent limitations, such as thermal noise and temporal decorrelation, play a key role in the appropriate interpretation of the data and so should be properly included in the physical models that try to characterize the average backscattering mechanism of sea clutter.

Thanks to the great progress in active phased array antennas (APAAs), current and most of the upcoming SAR missions are based on such technology for the operation of multiple modes of acquisitions. The related calibration is a complex procedure due to the high number of different beams to be operated. Alternative internal calibration methodologies have been proposed and analyzed in the frame of this doctoral thesis to round-off the transversal analysis carried out within this research activity. These approaches improved the radiometric calibration performance compared to the conventional ones. The presented formulation of the system errors, internally monitored by dedicated calibration loops, as well as the proposed alternative strategies set the path to extrapolate the analysis for multichannel SAR systems.

Contents

1	Introduction	1
1.1	Motivation of the thesis	2
1.2	Objectives of the thesis	5
1.3	Structure of the thesis	6
2	GMTI with multichannel SAR (MSAR) systems	9
2.1	GMTI historical evolution	10
2.2	Moving targets in SAR imagery	15
2.2.1	Across-track velocity	17
2.2.2	Along-track velocity	18
2.2.3	Along-track acceleration	19
2.3	MSAR data model	19
2.3.1	Signal	20
2.3.2	Interference	21
2.4	GMTI processing techniques	25
2.4.1	Dual receive channel GMTI techniques	25
2.4.2	Multichannel adaptive GMTI techniques	28
2.5	Concluding remarks	33
3	Multichannel SAR (MSAR) simulation tools	35
3.1	Introduction	36
3.2	Multichannel SAR raw data simulator (MSARRDS)	37
3.2.1	Simulator structure definition and design	38
3.3	MSAR-GMTI mission theoretical performance tool	47
3.4	Monte Carlo (MC) MSAR-GMTI simulator tool	48
3.5	Concluding remarks	49
4	Performance evaluation of SAR-GMTI missions	51
4.1	Introduction	52
4.2	Mission analysis	54
4.2.1	Multichannel configurations	54
4.2.2	SAR-GMTI expected performance	55
4.3	Simulation results: performance evaluation	66
4.3.1	Monte Carlo (MC) approach	67
4.3.2	Synthetic SAR data approach	71

4.4	Concluding remarks	79
5	Experimental MSAR-GMTI over maritime scenarios	81
5.1	Sensor configurations	82
5.1.1	F-SAR airborne system	82
5.1.2	TerraSAR-X spaceborne system	84
5.2	SAR-GMTI processing schemes	87
5.2.1	Adaptive SAR processor	87
5.2.2	GMTI at SAR image level	97
5.2.3	GMTI at range-compressed image level	100
5.2.4	Channel balancing techniques	102
5.3	F-SAR data	104
5.3.1	Data analysis	104
5.3.2	Processing results	108
5.4	TerraSAR-X data	124
5.4.1	Processing results	124
5.5	Concluding remarks	135
6	SAR sea clutter characterization	137
6.1	Introduction	138
6.2	Radar sea clutter theory	139
6.2.1	Radar backscattering coefficient models	139
6.2.2	Statistical models	141
6.2.3	Polarimetric description	144
6.3	Extended X-Bragg (X2-Bragg) model	148
6.3.1	Modeling	148
6.3.2	Evaluation	151
6.4	Sea Clutter Characterization Methodology	153
6.5	Data Set Description	157
6.6	Results	158
6.6.1	Radar backscattering coefficient	158
6.6.2	Statistical characterization	161
6.6.3	Polarimetric characterization	166
6.7	Concluding remarks	170
7	SAR internal calibration strategies	173
7.1	Introduction	174
7.2	SAR calibration	175
7.3	Theoretical formulation	177
7.3.1	Preliminary concepts	177
7.3.2	Accumulated errors of components in parallel	178
7.3.3	Error formulation	179
7.3.4	Residual post-calibration errors	179
7.4	Calibration strategies	183
7.4.1	Calibration with operational excitations	183
7.4.2	Elevation dependent calibration	184
7.5	Numerical results	184
7.6	Concluding remarks	189

8	Conclusions	193
8.1	Main contributions	194
8.2	Main conclusions	196
8.3	Future research lines	197
A	GMTI literature review	201
B	Multichannel SAR (MSAR) signal formulation	215
B.1	Target signal model	216
B.1.1	1D (azimuth) signal modeling	216
B.1.2	2D signal modeling	223
B.2	Discussion on theoretical clutter signal modeling	232
B.3	SAR processing	235
B.3.1	Chirp scaling	235
B.3.2	Range Compression, RCMC and SRC	240
B.3.3	Azimuth focusing and phase correction	241
B.4	Mathematical derivations and approximations	243
B.4.1	Quadratic range phase in range-frequency Doppler domain	243
B.4.2	Range dependent phase after chirp scaling in Doppler domain	245
	Acronyms	247
	Nomenclature	251
	Bibliography	257
	List of Figures	287
	List of Tables	293
	List of Publications	295
	Journal Articles	295
	Conference Articles	295
	Master Thesis Supervised	297
	Participation in R&D Projects	297

1

Chapter 1

Introduction

This chapter is devoted to the describe the motivations that have led to the study carried out within this doctoral activity and the related main objectives to be fulfilled. The structure of this doctoral dissertation is also presented to point out specifically which are the main contributions of each chapter and how they are linked to the fundamental goals.

1.1 Motivation of the thesis

More than 70 per cent of the Earth's surface lies beneath the sea; phenomenas ongoing in, on and above the oceans have a direct consequence on our lives. Water is the principal component of Earth's hydrosphere, is integral to all known life, makes part of the carbon cycle and influences climate and weather patterns. Therefore, monitoring the human related activities in the ocean is of key importance to prevent and mitigate their impact on this global ecosystem.

The ocean is the habitat of 230.000 known species, and so an important source of food with 13 million tonnes of fish and seafood consumption in 2011 according to Food and Agriculture Organization (FAO) [1]. The Ocean has historically been one of the most important means of transport. Unlike in the past, ships currently carry goods rather than people. In the last decades, the globalization of the economy and the related increase of consumerism has lead to a tremendous expansion of the shipping market and flow [2]. According to latest available statistics from the European Commission (EC) [3], in 2012 a total of 1401 billion tonne-kilometer (tkm) of goods were transported by sea, only in 28-member European Union (EU); being the second most important mode after road transport (1692.6 billion tkm). It must be noted that maritime transport represents the most efficient mean with 13.9 percent of total CO₂ emissions from fuel consumption compared to the 71.9 percent of road transportation, the 12.8 % of civil aviation (with 3 billion tkm transported) and 0.6 % of railways (with 407 billion tkm) according to the EC statistics in 2012.

Such figures demonstrate and justify the increasing importance of the sea in the global economy. This situation leads to newly emerging concerns, from the ecological, economical, social and geopolitical points of view; which define specific requirements for globally surveilling seas and oceans. Two main global human activities are jeopardizing the ocean ecosystems and consequently resources and our quality of life. Overfishing and the related overexploitation constitute one of the mainstream of ocean endangering problems. Many conservation organizations, such as World Wide Fund (WWF) and Save Our Seas Foundation (SOSF), have led studies to analyze the fishing patterns concluding that illegal, unregulated and unreported fishing accounts for an estimated 20 percent of the world's catch and as much as 50 percent in some fisheries [4, 5]. Moreover, a related problem is that an important part of the fishing catch is made of unwanted fish and other marine life, in a way that between 8 and 25 percent of the total global catch is discarded [6]. Another important thread for the ocean ecosystem are the marine spills of oil, chemicals and other hazardous substances, which have a dramatic ecological impact but also economic and political costs. The demand of the industrial nations and newly-industrializing emerging economies of energy and mineral resources have led to increasing quantities of oil (and related substances) being transported through oceans and seas. Oil tanker spills amounted 22 thousand tonnes during the last four years (2010-2013) according to not-for-profit organization International Tanker Owners Pollution Federation (ITOPF) [7].

Taking into account that more than 90 percent of the World's trade goods and more than 70 percent of global crude oil are transported by sea, the maritime security becomes an issue of utmost importance. Due to the excessively increasing shipping traffic there is more likelihood of accidents and associated environmental damage and economic loss, but there is also spread of piracy attacks, smuggling and organized crime. In the same

way illicit activities, such as illegal fishing/overexploitation, weapon movement and illegal immigration are phenomenas of growing concern in the new millennium.

In this framework, the governmental authorities all over the world have pointed out the necessity of setting up specific regulations on human activities in and over the seas and oceans to protect the marine environment and to ensure the related economical outcomes. However, such regulations require from entities that ensure their accomplishment by means of *monitoring* the vessels and ships' activities. The first strategies for vessel monitoring were and still are mostly based on specific radio-frequency transponders located in the vessel that provide real-time information of the position, course and speed of ships. Among these, automatic identification system (AIS) [8], vessel traffic services (VTS) [9] and vessel monitoring system (VMS) [10] are widely used for ship monitoring (especially in coastal areas). Nonetheless, this sort of technology is not fully reliable since the vessels do not always transmit radio-frequency signals, precisely those intent on avoiding notice.

In this sense, *remote sensing* has become a valuable procedure to gather and to analyze information about the Earth's properties and dynamics. In a broad and simpler sense, remote sensing is understood as the distant acquisition of information about an object without being in physical contact. It refers to the science of collecting, processing and interpreting data resulting from the interaction between electromagnetic signal and matter. Satellite or spaceborne Earth observation (EO) has become crucial for remote sensing since it can grant the monitoring of the environment at a global scale, preventing and managing natural or industrial catastrophes, anticipating conflicts and administering crises. Protection and preservation (related to humanitarian, natural or technological risks) are mainstream fields of application for EO-based geoinformation services.

The exploitation of radar technology for spaceborne remote sensing of the ocean has indisputable benefits since it provides an all-weather, all-day (independent of the solar light) wide-swath monitoring of the sea. The continuous advances in synthetic aperture radar (SAR) coherent systems, which provide high-resolution two-dimensional reflectivity images of tens of kilometers, has demonstrated the suitability of this technology for EO and particularly for maritime monitoring and surveillance. The launch in 1978 of SEASAT [11] represented an inflexion point for the oceanographic spaceborne remote sensing and for SAR-based missions. Since then, more than 15 spaceborne SAR missions have been operated with 10 more planned to be launched in the next few years.

ground moving target indication (GMTI) is devoted to the detection of moving objects on the Earth's surface (cars, trucks, ships and alike). The integration of GMTI modes in SAR allows additionally high-resolution imagery of the detected vessels when proper processing strategies are considered. Mainly, three different SAR-based approaches can be used for vessel surveillance: reflectivity-based SAR methods using single channel configurations, polarimetry and multichannel GMTI.

Single channel SAR systems exploit the fact that vessels in general have greater reflectivity than the sea itself. Such systems are limited to the detection of vessels with high signal-to-clutter-and-noise ratio (SCNR) and they fail to identify moving vessels hidden by the sea returns, also referred to sea *clutter* as the ocean backscattering represents the unwanted signal.

Migration towards *multidimensional* or *multichannel* SAR systems represents a more powerful approach. In this context, polarimetric SAR (PolSAR) exploits polarimetric

diversity based on the different backscattering response of sea and vessels for detection of the latter. Nevertheless, there is no effective sea clutter cancellation, meaning that subclutter visibility for small boats cannot be accomplished. Moreover, it is not feasible to estimate velocity and direction of motion of the vessels with high accuracy.

Multichannel SAR-GMTI take profit from the spatial diversity to suppress the interfering clutter signals before target detection can be performed; based on the associated inter-channel phase differences, which are distinct for clutter and moving targets. Target parameters of the detected vessels (e.g. along- and across-track velocities) can be also estimated. Extensive research in the multichannel GMTI field, driven mainly by military requirements, has resulted in the development of fully operational airborne GMTI systems for detecting land targets. Nonetheless, these manned aircraft-based sensors will not provide economically viable data sources for civilian applications, where the wide-area coverage is also a driven requirement.

Spaceborne SAR-GMTI radars can overcome the spatial coverage of airborne platforms. To date, both the required technology and the related processing techniques, which could enable operative space-based SAR-GMTI missions, are not fully available. However, the rapid development in efficient, compact satellite design and in active phased array antenna (APAA) have changed the paradigm for SAR-GMTI, reducing capital costs and attracting investment in commercial satellites. Currently, there is no civilian spaceborne radar system with an operational GMTI mode; but state-of-the-art SAR missions, such as RS2 (C-band) and TSX (X-band), make use of the APAA technology to experimentally demonstrate the GMTI capabilities from spaceborne SAR instruments. These instruments are based on dual-receive antenna configurations, and with appropriate antenna switching and/or toggling strategies up to four virtual channels can be configured. Such missions have limited detection capabilities, especially when imaging small and slow moving targets with subclutter visibility. The operation of spaceborne SAR-GMTI has been widely evaluated for detecting land targets, with special interest on road traffic management; and a lot of effort has been devoted to the analysis and definition of the related processing strategies and algorithms. Nevertheless, multichannel SAR-GMTI is not yet being extensively employed in the maritime surveillance field for vessel detection.

As a consequence, this thesis is mainly devoted to the study of the limitations of current SAR-GMTI missions when operated in maritime scenarios and the proposal of optimal multichannel SAR-GMTI architectures that allow subclutter detection of slow moving small (reduced reflectivity) vessels. Performance evaluation of such missions is key to the doctoral activity here considered, where both classical GMTI techniques as well as promising optimum algorithms have been tested. The limited access and availability of real spaceborne multichannel SAR-GMTI data, and the necessity of cost-effectively mission prototyping resulted in the development of flexible simulation tools to demonstrate the validity of the proposed mission architectures. Processing experimental multichannel SAR-GMTI data sets from airborne (F-SAR) and spaceborne platforms (TSX) over maritime scenarios has been also carried. The main goal is to foresee the peculiarities of processing real data with special emphasis on the inter-channel calibration, evaluating the most adequate processing strategies based on existing classical and promising GMTI algorithms.

When evaluating SAR-GMTI capabilities over maritime scenarios, the lack of an accurate modeling of the complex sea clutter background results on one of the main limita-

tions to properly understand the real GMTI performance from spaceborne SAR missions. The interfering sea clutter has specific differential characteristics when compared to inland regions, where the internal clutter motion could be a limiting factor, producing additional decorrelation. In this sense, the availability of spaceborne polarimetric data over maritime scenarios from TSX has been exploited along the thesis, for a preliminary transversal characterization of the sea clutter returns when imaged by an X-band SAR sensor. A radiometric, statistical and polarimetric study has been carried out, emphasizing the system-driven limitations when modeling the ocean returns. It has been also demonstrated how to properly accommodate such system influences (thermal noise and temporal decorrelations) in the widely assumed Bragg surface model for the sea backscattering, exploiting the polarimetric dimension.

The great advance in APAA, central for the further development of the SAR missions, and in particular of the SAR-GMTI sensors, allows a great degree of flexibility in the acquisition mode's operation; but to fully exploit this kind of systems proper calibration strategies are mandatory. This doctoral activity has devoted special effort to the analysis of the current internal calibration methodologies on-board the SAR sensors based on APAA, proposing alternative methodologies to reduce the impact of internally-monitored errors on the final radiometry of the image.

1.2 Objectives of the thesis

The encompassing objective of this doctoral work is the study and analysis of GMTI capabilities with spaceborne SAR sensors for maritime surveillance purposes; based on a transversal study going from the system proposal, passing by processing strategies evaluation, performance assessment and sea clutter characterization, to calibration methodologies recommendation. A detailed enumeration of the main objectives of the thesis follows:

- Study and review of state-of-the-art in the GMTI field with special emphasis in the frame of spaceborne radar systems, which allows the derivation of a map of the current GMTI framework providing insights in the readiness and maturity of the actual SAR-GMTI systems and the applied techniques.
- Development of flexible simulation tools for accurate SAR-GMTI performance evaluation and mission prototyping. The driven requirements are flexibility, modularity and integrability in the design of such software-based tools. Limited access to real multichannel spaceborne SAR-GMTI data requires a realistic simulation environment that can provide SAR-GMTI raw data for a user-defined system configuration/acquisition, supplying the means to evaluate the current GMTI techniques.
- Analysis and evaluation of the GMTI capabilities of current state-of-the-art spaceborne SAR missions when operating over maritime scenarios, showing their limited efficacy for vessel subclutter visibility detection. Proposal of alternative multichannel SAR-GMTI missions exploiting the optimal GMTI processing strategies to enhance the detection of small and slow moving vessels masked by the sea clutter response, validating their potential improvement using proper realistic simulation environments. Assessment of the impact of imaging high-speed boats with SAR systems and how adequate processing strategies can be used to recover the induced

degradation in terms of SAR-GMTI performance.

- Evaluation of classical and optimum adaptive processing GMTI techniques applied to real data over marine environments acquired with airborne and spaceborne SAR-GMTI systems, in order to foresee the peculiarities of working with experimental data sets. Proposal of adequate processing strategies that provide the best performance possible. Validation of the refocusing capabilities of the adaptive SAR focusing algorithm integrated in the GMTI processing chain.
- A characterization of the sea background in terms of mean power reflectivity, statistics and polarimetric behavior due to the lack of exhaustive studies to provide realistic modeling on the complex sea clutter scenarios.
- Study and proposal of (internal) calibration strategies to minimize the impact of system-dependent errors in the final products' radiometry of current spaceborne SAR missions, based on APAA.

1.3 Structure of the thesis

This doctoral dissertation is organized in eight chapters. Additional information is also distributed in two appendices at the end of the thesis.

This **first chapter** introduces the motivation and states the main goals of this work. **Chapters 2 to 7** contain the main contributions of this doctoral research. Each chapter focuses on one of the six main objectives previously detailed:

- **Chapter 2** gives a general overview of the GMTI framework recently exploited by spaceborne SAR missions. A brief review of the general concepts and the techniques is provided. Moreover, a theoretical-based model of the multichannel SAR-GMTI signals is developed at image level, fundamental for a proper theoretical performance evaluation. The exhaustive literature study introduced in **appendix A** represents the basis of the structured historical review presented in this second chapter. A detailed derivation of the moving target multichannel SAR raw data signal is reported in **appendix B**.
- **Chapter 3** describes and presents three simulation tools developed in the frame of this doctoral activity, which have been used to evaluate the GMTI capabilities of current SAR-GMTI missions as well as to propose alternative optimal GMTI spaceborne architectures for maritime surveillance.
- **Chapter 4** carries out an exhaustive SAR-GMTI performance evaluation using the implemented simulation tools, comparing current state-of-the-art SAR missions, such as TSX and TDX, with a new multichannel configuration using non-uniformly distributed receive phase centers and intended for GMTI applications over maritime scenarios, with the aim of detecting small and slow boats in subclutter visibility.
- **Chapter 5** is devoted to the GMTI processing of real multichannel SAR data using acquisitions over marine environments from airborne (F-SAR) and spaceborne (TSX) instruments, considering different state-of-the-art GMTI techniques. The refocusing capabilities of the integrated adaptive SAR processor when imaging moving vessels has been also demonstrated. Special emphasis is being placed on the appropriate inter-channel calibration or balancing and how this could impair the GMTI

performance.

- **Chapter 6** presents a detailed characterization of the sea/ocean clutter returns at X-band imaged by TSX mission, using polarimetric data sets, and in a three-level basis: radiometric, statistical and polarimetric descriptors. The validity of different theoretical models has also been assessed; particularly, the impact of system-related limitations (as thermal noise and temporal decorrelation induced by the acquisition mode) in the physical backscattering model (X-Bragg) has been analyzed, proposing an extension known as X2-Bragg.
- **Chapter 7** introduces a novel approach in the instrumental error analysis of SAR systems based on active phased array antenna (APAA), defining a new term referred as post-calibration residual errors. Alternative (to the more widely used) internal global calibration strategies are proposed to reduce the impact of such errors.

The document is concluded in **chapter 8**, summarizing the main results and contributions presented along the document as well as providing some insights on the eventual continuations of the present research.

2

Chapter 2

GMTI with multichannel SAR (MSAR) systems

This chapter is intended to give a general overview of the ground moving target indication (GMTI) framework recently exploited by spaceborne synthetic aperture radars (SARs). A brief review of the general concepts involved in this field are presented in order to produce a self-contained manuscript. In the first part a detailed and up-to-date review of the GMTI historical evolution is provided, covering from the most classical approaches to the most recent developments. The second section addresses briefly the specificity of imaging moving targets with SAR sensors. The third section focuses on the development of a multichannel SAR data model at image level, fundamental for a proper theoretical characterization of the performance of any SAR-GMTI mission. The last section is devoted to a brief and self-contained recapitulation of the most extendedly used GMTI techniques, starting with the classical dual receive channel algorithms and ending up with the most promising adaptive approaches. This structured compilation of the state-of-the-art GMTI systems and techniques and the related model formulation establishes the context of the work completed in this thesis and sets the foundations of the contributions that will be presented in subsequent chapters.

2.1 GMTI historical evolution

In 1905, Christian Hülsmeyer patented the “Telemobiloscope” which used, for the first time, the electromagnetic waves for detecting the presence of distant objects such as vessels, [12]. This represented the birth of the radar principle applied to object detection. From those early days to date there has been a constant and fast progress on the radar techniques, especially during the second World War.

Moving target indication (MTI), originated in the military field, has been extensively studied and successfully developed in ground-based surveillance radars with the aim of detecting approaching sea and air targets with no image formation process. Fixed radar stations with a rotating antenna installed on the top of a building have been used for this purpose: the two-way travel time of the transmitted and reflected pulse and the angular information of the antenna determine the position of the detected targets. In this case, the angular resolution is limited by the antenna beamwidth (longer antennas provide higher resolution) and the range (distance) resolution is fixed by the transmitted pulse bandwidth.

The evolution towards pulsed Doppler radars allow the MTI operation by exploiting the induced Doppler shift (phase modulation) on the reflected radar signals. In this way, moving targets (with a given Doppler offset) can be distinguished from unwanted stationary or slowly moving background (sea, buildings, mountains, trees and alike), from now on referred as clutter [13]. This Doppler shift is both function on the target’s radial velocity component and the direction of arrival (DOA).

In classical MTI notation, a distinction is made between air moving target indication (AMTI) and GMTI systems. While the first ones are of major concern in the military applications to detect air targets; GMTI focuses on targets moving on the earth’s surface (land and ocean) in the context of flying radar platforms.

The implementation of this capability in airborne or spaceborne radars is more complex, since the platform carrying the radar is also in motion. This movement induces different radial velocities in all static targets in the scene, creating an extended Doppler spectrum, the so called *clutter spectrum*. Hence, slowly moving targets are masked by clutter returns, resulting in a challenging detection problem.

GMTI has been exhaustively studied in the frame of airborne radar systems [14–19], with special interest in military applications, such as the US Joint-STARS program [20, 21]. Classical airborne GMTI, with a single channel, assume that the Doppler shift is high enough to be observed out of the clutter bandwidth. In any case, the capability of detecting moving targets depends on their velocities, the pulse repetition frequency (PRF) and the antenna azimuth beamwidth, which determines the clutter spectral bandwidth. The simplest approach is to synthesize a filter (in Doppler domain) with a notch centered around the Doppler centroid of the fixed scene, such that endo-clutter returns are canceled out. This technique limits the detection of exo-clutter targets with sufficient velocity and/or with high reflectivity or radar cross section (RCS), resulting in high SCNR in a way that even a velocity independent detection can be performed.

Contrary to classical GMTI systems air- and spaceborne SAR missions were primarily designed to provide (high) resolution images of stationary scenes. In 1954, Wiley originally developed the SAR principle in a patent application [22]. He proposed the use of a

coherent pulsed radar system in combination with the Doppler beam sharpening concept such that an improvement of the azimuth resolution was achieved being independent of the range/distance, contrary to real aperture radar (RAR). SAR is a side-looking coherent pulsed radar, where the adequate processing of the received echoes at subsequent positions of the flying platform allows to virtually synthesize a longer antenna (“synthetic aperture”), i.e., narrower beamwidth and so finer resolution [23]. To achieve high resolution SAR images a longer illumination (integration) time is needed and so a smaller azimuth antenna length is required. A thorough review of SAR principles of operation, processing and applications can be found in [24].

The requirement of high resolution SAR (reduced antenna length) stands in contradiction to the classical GMTI operation: the shorter the antenna the larger the beamwidth and hence the spectral contribution of the unwanted clutter signal, reducing the detection capabilities of endo-clutter targets. In conventional SAR processing, assuming a stationary world, moving targets are typically defocused, blurred and imaged at displaced positions (from meters up to several kilometers for spaceborne platforms). The basic effects on SAR imagery caused by moving targets were first investigated in 1971 by Raney in [25]. A brief review of these effects and the related impact on SAR-GMTI are described in section 2.2.

Classical single channel airborne GMTI systems base the detection capabilities in the use of high PRF and narrow antenna beamwidths. However, several shortcomings derive from this operation especially in the case of spaceborne SAR platforms: PRF is quite restrictive in order to achieve the desired trade-off between azimuth resolution and unambiguous swath width, see [23]. Differences between air- and spaceborne platforms include the very high satellite velocities, much steeper incidence angles, and possibly high variation of the clutter statistics. In airborne radars it is feasible to transmit larger power, which combined with the relatively smaller (several kilometers) ranges, allow operating with large signal-to-noise ratio (SNR); whereas spacebased radars operate with limited SNR due to constraints on the transmitted power and the larger radar ranges (hundreds or even thousands of kilometers). For spaceborne platforms the limited PRF operation, which barely samples the 6-dB Doppler (azimuth) bandwidth, leads to a higher ambiguity level compared to airborne systems. On one hand, appropriate coherent integration of the moving target signal during the whole synthetic aperture time is crucial when operating with spaceborne SAR systems to maximize the SCNR for efficient detection and accurate estimation. On the other hand, the increased contribution of the ambiguities for current spaceborne missions should be also properly accounted for when designing the system, as discussed in detail in Chapter 4, such that both unambiguous and ambiguous clutter contributions are minimized and so the effective SCNR is increased.

Radar systems mounted on a moving platform such as an airplane or a satellite can monitor large areas at once, independently of weather conditions during day and night. This makes SAR-GMTI a very attractive tool for many civilian applications: the continuously and disproportionate increase of vehicular traffic all over the world requires efficient traffic management, which in turn demands intelligent monitoring systems. Currently, the data is collected from stationary sensors mounted along the major roads with limited spatial coverage. In this sense, SAR-GMTI proves to fill this information gap as testified by the increasing interest in this research topic [17, 26–29].

Another recent hot topic of research is the application of SAR-GMTI systems for wide

area maritime surveillance serving to a vast variety of interests: environmental monitoring, coastal and maritime security as well as fisheries management. The requirement of ship detection and identification has grown in importance because of the increase of piracy attacks, smuggling and polluting activities, as demonstrated by the ongoing research activities in the European framework [30, 31]. The AIS has been widely used for ship monitoring, but it is not a fully reliable system since vessels do not always transmit this signal, particularly the ones involved in illegal activities. In this sense, SAR-GMTI could represent a powerful tool for maritime traffic monitoring [32, 33], with special emphasis on the detection of small and slowly moving boats in the open sea.

A first approach to discriminate moving targets from the fixed scene in single channel SAR systems is based on their different Doppler spectrum behavior. This method uses a Doppler-like filter such that the signal spectrum is filtered into different sub-bands along azimuth, which corresponds to different portions of the antenna azimuth pattern. The interested reader is referred to [34] for any further details. The main drawback of this single channel approach is the high PRF operation required to locate more energy out of the clutter band, i.e., to make available a region in the Doppler domain free of clutter contribution. Another simple (non-coherent) technique for single receiver SAR is based on splitting the whole integration time in several sub-apertures, focusing each one independently (at reduced azimuth resolution), such that the moving objects appear as changes from one look to the next [35, 36].

Other techniques that consider classical single channel SAR systems to detect moving targets rely on the refocusing and sharpening of moving target SAR response: several approaches based on auto-focusing techniques (compensating for the relative radar-target motion) have been proposed [37–39], which, however, require from a pre-detection step to identify the target of interest. In the same way, algorithms based on a matched filter bank (MFB), [40, 41], have been used to recover the induced degradation of moving objects in SAR imagery, which work well when assuming uniformly accelerated movements for short integration times (spaceborne case). Recently, a new approach for velocity and acceleration measurement using the bi-directional (BiDi) SAR mode has been proposed in [42]. BiDi allows simultaneous acquisition of two images (fore and aft) using a single satellite with a single receiver [43], such that a non-coherent cross-correlation between the two images provides an estimation of the azimuthal velocity.

The previously described single channel SAR-GMTI approaches are effective for targets with relatively high SCNR, but fail to detect those in sub-clutter visibility condition. Moreover, in single channel SAR there is an inherent ambiguity in the Doppler signature (coupling between the azimuth shift and the Doppler shift) since the Doppler shift can be due to either position of the target within the antenna azimuth beam or due to the radial velocity of the moving target. These considerations suggested the development of array techniques using multiple channels or antennas arranged in flight direction, connected to independent receivers, as a single channel antenna with time multiplexing or distributed in a multistatic configuration [27, 44, 45]. This allows improving GMTI detection capabilities and solving the intrinsic ambiguity between radial velocity and azimuth location in a single channel SAR.

Current spaceborne SAR sensors, such as TSX [46], TDX [47] and RS2 [28] allow GMTI experimental assessment based on a two-channel approach. For this dual receive antenna (DRA) configurations, conventional SAR-GMTI processing techniques operating

at image level or raw data (depending on the SNR conditions) can be applied; based either on phase change detection, along-track interferometry (ATI) [48–50] or on clutter cancellation, displaced phase center antenna (DPCA) [49, 50]. These two degrees of freedom (DoF) are not enough to simultaneously suppress the clutter and to accurately estimate the targets' parameters, such as velocity and position [45]. A larger number of parallel receivers or channels improve the detection performance by exploiting space-time adaptive processing (STAP) techniques with SAR, [21, 28, 29, 45]. Theory on such adaptive processing, originally proposed by Brennan and Reed in [51], has been widely developed for airborne surveillance systems and has received lately great interest by the SAR-GMTI community for their potential improvement [28, 29, 41]. The most promising among them are imaging STAP (ISTAP) [28] and extended DPCA (EDPCA) [29].

Spacebased systems have stringent requirements of weight, power consumption and data rate, and so a large number of channels is prohibitive in most cases. SAR systems equipped with APAA have great flexibility in the acquisition, making it possible to vary the amplitude and phase of the different transmit receive modules (TRMs) from pulse to pulse. The combination of transmit toggling (activating some specific parts of the antenna) and alternate switching in reception allows the generation of additional virtual phase centers without compromising hardware complexity, [15, 45, 52]. RADARSAT-2 incorporates the Moving Object Detection EXperiment (MODEX), [52], based on the generation of additional virtual phase centers (up to four channels) by means of either transmitter/receiver toggling between pulses and/or via intelligent receiver excitations, demonstrating the efficiency of adaptive STAP techniques (ISTAP and EDPCA) when combined with such configurations [28, 29]. These kinds of approaches imply an antenna effective area reduction, resulting in a degradation of the SNR and increased effective¹ PRF requirements to reduce azimuth ambiguities.

A similar approach to increase the spatial diversity without adding new hardware is presented in [53], where a third virtual channel is generated by means of processing the signals from the available two physical channels. This is achieved via the summation of the fore and aft recorded data, such that a third phase center is generated halfway between the phase centers of the two-channel system, introducing a different antenna weighting, which should be taken into consideration in the calibration procedure to ensure no balancing errors between the channels.

Alternative multichannel approaches are based on the deployment of coherently operating SAR constellations [27], where a conventional SAR is used as source of illumination with a cluster of small cost-effective passive receiving satellites. These configurations allow more flexible remote sensing architectures. A better angular and Doppler resolution will be possible thanks to the extended apertures (longer baseline separation between the receivers). A first analysis of a general multistatic constellation for GMTI purposes is carried out in [27], demonstrating improved capabilities when combined with sub-optimal STAP algorithms.

Bistatic configurations such as TanDEM-X (TDX) mission will allow some tests and evaluations of GMTI modes with four physical channels and different baseline configurations [54]. Although the main objective of TDX is topographic mapping, [55], it will

¹Effective PRF refers to the sampling rate at each of the final channels and not the operational one, which depending on the configuration can be twice the effective.

provide some experimental data for GMTI performance assessment. In [54] a preliminary performance analysis for TDX configuration in terms of detection capability and relocation accuracy is presented. Different acquisition strategies are considered, taking advantage from the DRA mode at each satellite and aperture antenna switching concepts. It must be noted that the accurate performance is obtained assuming a perfect synchronization of the satellites both temporally and spatially. In [47] a non-coherent method for GMTI is evaluated with experimental data from a TDX and TSX flying formation in an along-track configuration with a large baseline. The method allows accurate repositioning of the moving targets in the SAR images to their true broadside position as well as an estimation of their velocity and/or accelerations.

The technological complexity and cost of maintaining a constellation of satellites is rather high. Moreover, they suffer from a higher number of ambiguous velocities. It must be also noted that when using this sort of architectures for maritime surveillance, an important factor to be considered is the related sea temporal decorrelation, which depending on the meteorological conditions and baseline configurations can be a limiting factor for proper GMTI operation. From these considerations, part of the work presented in this thesis proposes and studies alternative configurations, defining a complete SAR-GMTI mission, with the aim of keeping a reduced technological complexity and at the same time providing improved detection capabilities for targets with sub-clutter visibility in maritime scenarios, as described and analyzed in Chapter 4.

A promising spaceborne SAR operational mode with great interest to GMTI for maritime applications is the high-resolution wide-swath (HRWS), combining a high-resolution wide area surveillance system in a single satellite. This mode is based on SAR systems employing multiple transmit/receive channels in combination with digital beam-forming (DBF) techniques to overcome the classical SAR constrain of simultaneous high resolution imaging and wide coverage [56, 57]. The HRWS SAR system is based on a DBF processing in elevation (Scan-on-receive) such that the beam follows the echo on ground, [58, 59], allowing a wider range coverage limiting the impact of the range-ambiguities. Additionally, a DBF in azimuth (multiple receiving channels in along-track) is used to reduce the azimuth ambiguities keeping a high-resolution imaging capability.

A first mission performance evaluation considering HRWS SAR and GMTI is presented in [60]. As noted in [61], HRWS and GMTI have contradicting PRF requirements: GMTI exploits redundancy in the data acquisition, whereas HRWS tries to minimize this redundancy (enough measurements to sample the whole bandwidth). The processing algorithm proposed by Sikaneta *et al.* in [62] allows to provide simultaneous HRWS and GMTI acquisitions, being robust to the optimal GMTI PRF selection as shown by processing RS2 real data. In a similar fashion, Baumgartner has proposed in [63] a novel method for simultaneous GMTI and SAR-HRWS operation using a low PRF system, such that moving targets are properly imaged and their kinematic parameters accordingly estimated, allowing simultaneously wide-swath and high-resolution GMTI operations.

The application of multiple-input multiple-output (MIMO) concept to the radar field represents an emerging research activity for future active sensors [64]: the use of multiple transmit antennas together with a multichannel receiver allows increasing the spatial coverage of the system with improved resolution, minimizing both range and azimuth ambiguities. Moreover, additional baseline diversity is obtained, which can be efficiently exploited by a GMTI operation mode to provide a wide area surveillance system with high-

resolution imaging capabilities. MIMO operation provides more virtual phase centers and with larger baselines compared to the real array. Therefore, MIMO-SAR systems have higher sensitivity to slowly moving targets and at the same time provide improved clutter cancellation capabilities, [65], since this suppression is performed both in transmission as well as in reception [66]. Waveform design with adequate cross-correlation properties is a key point in the study of MIMO radars, since channel decorrelation is quite dependent on the quality of the waveforms [65]. From the GMTI point of view, channel decorrelation is critical for a proper operation as stated in [50] and observed from the studies carried out in Chapter 4. Reliable separation of the radar echoes from the simultaneous use of multiple transmit signals is mandatory for proper operation of future SAR-MIMO systems. The interested reader is referred to [64] for discussions on this topic.

A step forward in the field of GMTI radars is the so called cognitive radar approach, intuitively described by Guerri in [67]. This type of system is a fully adaptive (transmit/receive) MIMO radar with knowledge-aided processing, where a dynamic (“learning”) database integrated in the real-processor chain uses both endogenous and exogenous information. In this way, the radar achieves some cognitive characteristics as “perceiving/sensing”, “remembering/database” and “thinking/adaptive algorithms”. This means that, e.g., in the case of maritime surveillance a low-complexity real-time GMTI processor on-board the platform could provide a preliminary detection. Then, for a region where an event is present the system redirects the resources towards that specific area of interest improving the detection with (possibly) higher resolution imaging capabilities.

This historical review of the GMTI has been based on an exhaustive bibliographic research and study carried out during the initial phase of the thesis and it has been accordingly updated. In appendix A Table A.1 compiles more than 200 bibliographic references from early 80s, till 2014 specifying different classification concepts, giving a snapshot of the GMTI context and the related state-of-the-art.

2.2 Moving targets in SAR imagery

SAR systems achieve high resolutions in the range direction through pulse compression of the wave-encoded chirp signal and the fine resolution in azimuth by means of cross-correlating the theoretical stationary target’s phase response with the received data [23]. Hence, the SAR image formation requires to accurately model the imaging system, the transmitted signal, the acquisition geometry and its evolution through time. In case of moving targets the assumption of stationary world matched filter (SWMF) is not valid any more (filter mismatch), leading to non-correctly focused moving targets in the SAR image, which can become completely masked by clutter and noise.

The study of the different impacts of imaging a moving object with a SAR sensor was originally developed by Raney in [25] and since then a lot of work has followed. For the interested reader comprehensive and intuitive descriptions as well as the mathematical foundations are thoroughly presented in the work of Sharma [68,69] and Baumgartner [70]. In the following lines a general review of the main impairments on moving target SAR imaging is reported. The aim is to stress the need to identify those effects and their origins, in order to develop proper processing SAR-GMTI strategies. In Chapter 4, where an optimized SAR-GMTI mission proposal is evaluated, the integration of target kinematics in the SAR processing step proves to be fundamental for the detection of

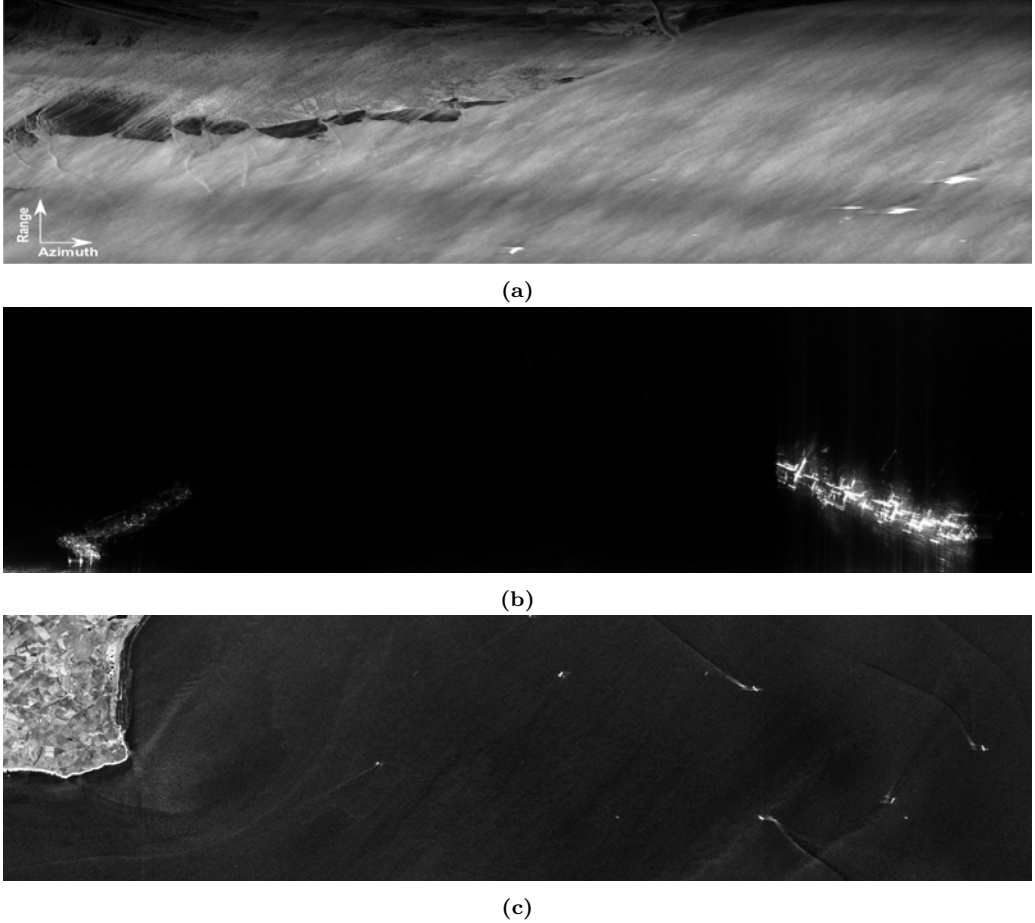


Figure 2.1: Moving vessels in SAR imagery: (a) F-SAR (X-band) image over the Elbe Mouth (19.11.2009), (b) ONERA BUSARD (Ka-band) image over Fos-sur-Mer close to Marseille (18.10.2012) and (c) TerraSAR-X acquisition over the Strait of Dover (01.05.2010).

slowly moving targets; but even more important for high-speed boats, where the induced dynamics could ruin the performance due to SCNR degradation. In Chapter 5, where real experimental data has been processed, section 5.2.1 is devoted to the description of an adaptive SAR processor based on a MFB using the range-Doppler (RD) algorithm. High-resolution images of moving vessels have been recovered for F-SAR airborne data, where the longer integration time degrades their response when imaged with a SWMF.

When performing conventional SAR processing under the assumption of SWMF, moving targets appear in general defocused/blurred and displaced from their actual position. In Figure 2.1, these effects can be observed when imaging moving vessels with different sensors. Fig. 2.1a corresponds to a high-resolution image (65 cm by 6 cm, range-azimuth) close the Elbe Mouth obtained with the airborne sensor F-SAR [71], where the vessels are sailing along the river. Azimuth defocusing on the vessels can be recognized probably induced by the along-track velocities and/or across-track accelerations over the long

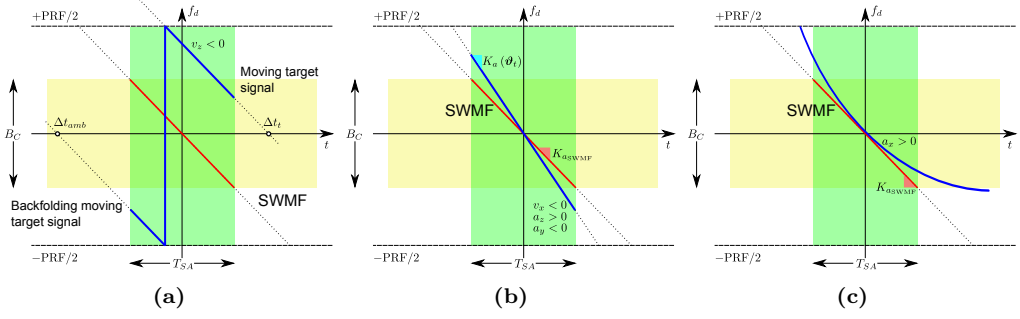


Figure 2.2: Doppler histories (in time-frequency) of a moving target with different motion parameters (in blue) and of the SWMF (in red): (a) across-track velocity v_z ; (b) along-track velocity v_x , across-track acceleration a_x and vertical (elevation) acceleration a_y ; (c) along-track acceleration a_x ; T_{SA} and B_C refer to synthetic aperture time and clutter bandwidth, respectively (figures adapted from [70]).

integration time (around 6 seconds). A high-resolution image of two tankers close to Marseille imaged by the Ka-Band SAR DRIVE [72] is shown in Fig. 2.1b. In this case, defocusing effects are not so evident probably because the vessels are anchored at the port of Fos-sur-Mer. In Fig. 2.1c, a TSX image over the Strait of Dover, the so called “ship-of-the-wake” effect can be clearly recognized, such that the across-track velocity (its projection to the line-of-sight) produces an azimuth displacement w.r.t the corresponding wake due to the induced Doppler shift, taking into account that SAR processors image the scene at its zero Doppler position. Compared to the airborne F-SAR case, azimuth defocusing is negligible for typical spaceborne synthetic aperture times T_{SA} around 1 second.

A schematic representation of the Doppler histories of a moving target in the time-frequency domain are depicted in Fig. 2.2. These graphs help understanding the impact of different motion parameters in the final SAR images. The vertical axis corresponds to the Doppler frequency and the horizontal to the slow-time (azimuth time). The signal of the moving target is represented as solid blue lines and the corresponding time-frequency representation of the SWMF is also included as solid red lines.

Fig. 2.3 shows the impact of different motion parameters on the azimuth point spread function (PSF) of a simulated point-like target for the X-band system considered in Table 4.1. The target is located at an incidence angle of 33.17 degrees. Each motion parameter has been independently analyzed considering 150 MHz and 2.8 KHz of processing bandwidths in range and azimuth, respectively, with a Kaiser spectral weighting of 2.5. In the following subsections the major impacts of the different motion parameters are briefly described.

2.2.1 Across-track velocity

The projection of the across-track velocity into the line-of-sight, known as radial velocity, produces a wrong positioning (azimuthal shift) of the target in the final image. This misplacement is denoted by Δt_t in Fig. 2.2a, which corresponds to the azimuth time

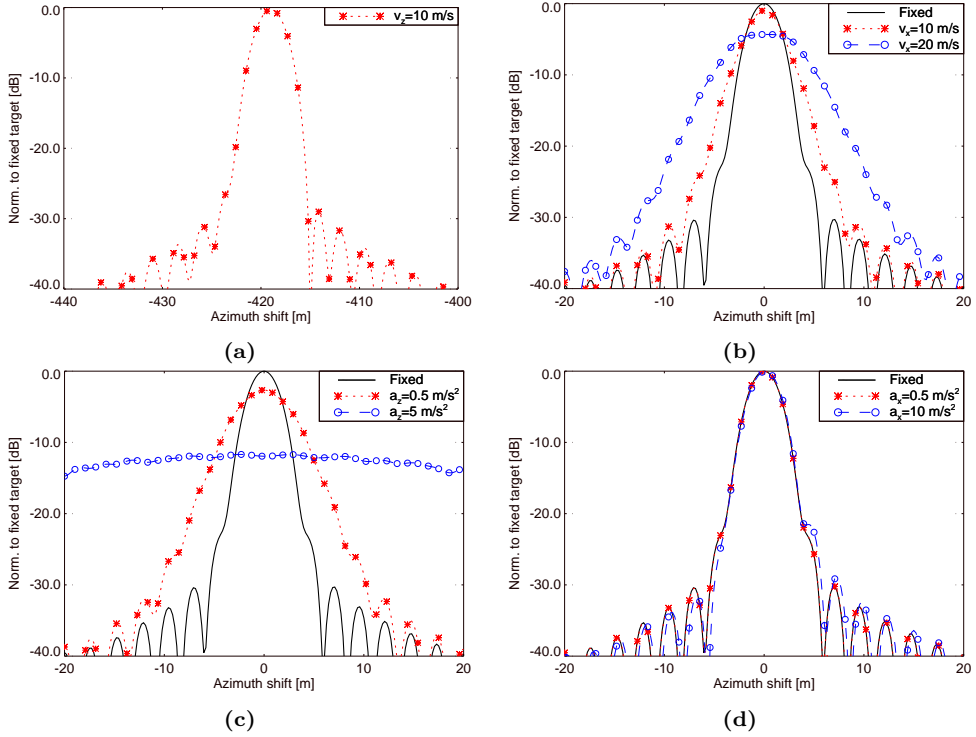


Figure 2.3: Impact of different motion parameters on the azimuth PSF of a simulated point-like target for the X-band system defined in Table 4.1 at an incidence angle γ_0 of 33.17 degrees: (a) across-track ground velocity v_z , (b) along-track velocity v_x , (c) across-track ground acceleration and (d) along-track acceleration a_x ; the PSF of a fixed target in solid black line is also included for comparison purposes except in (a) (150 MHz and 2.8 KHz azimuth and range processing bandwidths using a Kaiser window with spectral weighting of 2.5).

where the target is imaged. Ill-positioning in azimuth can be also caused when the target’s radial velocity is higher than half the PRF, due to Doppler aliasing: in this case the target is imaged at different positions (“real” target and its related ambiguities, known as “ghosts”). In Fig. 2.2a, Δt_{amb} corresponds to the time at which the ambiguous (backfolded) portion of the target is imaged.

As the across-track velocity increases the spectral overlap between the target’s Doppler history and the SWMF decreases producing a widening of the PSF as well as degradation on its peak response. Therefore, the full Doppler bandwidth determined by the PRF should be considered in the processing to avoid filtering out fast moving targets.

2.2.2 Along-track velocity

Along-track velocity produces defocusing of the azimuth impulse response since this motion parameter changes the quadratic part of the target’s range history (evolution of the distance during the acquisition time), which translates into a variation of the Doppler rate

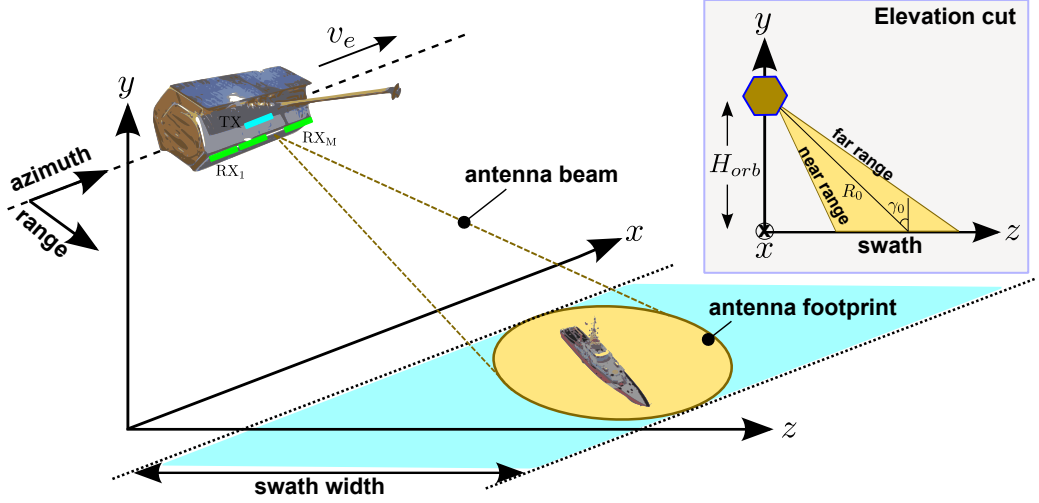


Figure 2.4: Multichannel SAR (MSAR) acquisition geometry.

(slope) compared to SWMF. This effect is sketched in Fig. 2.2b, where negative along-track velocities v_x and vertical accelerations a_y as well as positive across-track ground accelerations a_z produce an increase of the Doppler rate compared to the SWMF.

The change on the range history curvature produces also a residual range cell migration (RCM) not properly compensated in the common SAR processors, such that the energy is spread among several range cells producing additional azimuth defocusing and range smearing.

Fig. 2.3b presents comparatively the azimuth PSF when using a SWMF, assuming a fixed target as well as the same target with different along-track velocities v_x . Similar effects are also obtained when changing the across-track acceleration as shown in Fig. 2.3c. Along-track velocity and across-track accelerations produce non-distinguishable effects and cannot be separated using only the Doppler slope information. In the same line and as analyzed in Chapter 4, vertical accelerations contribute to the radial acceleration, analogous to the across-track ones and hence these two components cannot be decoupled.

2.2.3 Along-track acceleration

Along-track accelerations produce third-order phase errors in the range history or equivalently a deflection in the Doppler history as schematically represented in Fig. 2.2c, which become important for longer integration times like in the case of airborne systems. The major impact is a non-symmetric behavior on the sidelobes of the azimuth PSF as shown in Fig. 2.3d for an extreme and improbable acceleration of $a_x = 10 \text{ m/s}^2$.

2.3 MSAR data model

In the following section a general data model at SAR image pixel level is described, required to understand the related operation of the different GMTI techniques working

directly on SAR images, such as DPCA, ATI and EDPCA. This mathematical modeling is used in the theoretical performance evaluation presented in Chapter 4 for different SAR-GMTI missions and it is of key importance to properly interpret and analyze the obtained results. For GMTI techniques, such as ISTAP, working with range-compressed data in the Doppler domain and prior to image formation, this theoretical model can be extended to the range-Doppler domain as briefly described in section 2.4.2.2.

Consider a general multichannel SAR configuration, consisting of M parallel receivers (RXs) collocated in the along-track direction x , which are displaced $\{d_{x_i}\}_{i=1}^M$ from the transmit (TX) reference phase center as depicted in Fig. 2.4. A flat Earth geometry is assumed, such that the satellite, orbiting at H_{orb} , moves with an effective velocity v_e , [73].

The detection of the moving target, whose multichannel signal is denoted by $\mathbf{s}(\boldsymbol{\vartheta}_t)$, can be understood as a hypothesis testing problem

$$\begin{aligned} H_1 &: \mathbf{x} = \mathbf{s}(\boldsymbol{\vartheta}_t) + \mathbf{c}(\boldsymbol{\vartheta}_c) + \mathbf{n} \\ H_0 &: \mathbf{x} = \mathbf{c}(\boldsymbol{\vartheta}_c) + \mathbf{n} \end{aligned} \quad (2.1)$$

driven by the presence of interference \mathbf{q} , which consists of background clutter $\mathbf{c}(\boldsymbol{\vartheta}_c)$ and thermal noise \mathbf{n} . $\boldsymbol{\vartheta}_t = \{v_x, v_z, R_0, \sigma_t^2\}$ and $\boldsymbol{\vartheta}_c = \{v_{x_c}, v_{z_c}, R_0, \sigma_c^2\}$ are parameter vectors of the moving target and clutter, respectively; where the first two elements of the vectors correspond to the along- and across-track velocities, with R_0 the slant range of closest approach (for the stationary scene) and the related power levels indicated by the sigma terms.

2.3.1 Signal

The target, modeled as a single-like point scatter moves on the ground plane ($y = 0$) with a uniformly accelerated movement in both along-track (x) and across-track ground (z) directions, as generally assumed in the literature [16, 69]:

$$\begin{aligned} x(t) &= x_0 + v_x t + \frac{a_x}{2} t^2 \\ z(t) &= z_0 + v_z t + \frac{a_z}{2} t^2 \end{aligned} \quad (2.2)$$

where t stands for slow time (or azimuth time). At $t = 0$ the target is located at x_0 and z_0 , which corresponds to the along- and across-track coordinates, respectively. The along- and across-track velocities of the target are represented by v_x and v_z , whereas their associated accelerations are a_x and a_z .

The multichannel signal of the moving target, at resolution cell level, can be formulated using vectorial notation as:

$$\mathbf{s}(\boldsymbol{\vartheta}_t) = \alpha_t \boldsymbol{\Delta}_{\text{ATI}}(\boldsymbol{\vartheta}_t) \quad (2.3)$$

where it is assumed that the different SAR images have been properly co-registered and balanced, [74]. It is well-known that the target RCS varies with the aspect angle for road traffic [26] as well as for maritime targets [75, 76]. In case of a deterministic target model the RCS it is assumed to be constant during the synthetic aperture formation, such that for calibrated images, α_t is directly related to the RCS square root. In (2.3), the term $\boldsymbol{\Delta}_{\text{ATI}}(\boldsymbol{\vartheta}_t)$ collects the ATI phase for the different channels at the displaced image position

of the moving target:

$$\Delta_{\text{ATI}}(\boldsymbol{\vartheta}_t) = \begin{bmatrix} \exp\{j\psi_{t_1}(\boldsymbol{\vartheta}_t)\} \\ \vdots \\ \exp\{j\psi_{t_1}(\boldsymbol{\vartheta}_t)\} \end{bmatrix} \quad (2.4)$$

when considering a focusing function matched to the quadratic part of the moving target's range equation.

In (2.2), as it is widely considered in literature [53,69], $x_0 = 0$ is assumed for simplicity in the mathematical notation without losing generality. Then, the interferometric phase component of the i th channel can be expressed as [69]

$$\psi_i(\boldsymbol{\vartheta}_t) = \frac{\pi d_{x_i} v_r}{\lambda} \cdot \left[\frac{1}{v_e} - \frac{v_x - v_e}{v_{rel}^2}(\boldsymbol{\vartheta}_t) \right] \quad (2.5)$$

where λ is the carrier wavelength; v_r refers to the radial velocity, i.e., line-of-sight projection of the ground range velocity $v_r = v_z \sin \gamma_0$, where γ_0 is the incidence angle; and the relative velocity term v_{rel} is expressed as:

$$v_{rel}(\boldsymbol{\vartheta}_t) = \sqrt{(v_x - v_e)^2 + v_z^2 \left(1 - \frac{z_0^2}{R_0^2} \right) + z_0 a_z} \quad (2.6)$$

A more realistic modeling, which accounts for the target's random variability on the radar response, is a zero-mean complex Gaussian scattering center, [77], i.e. $\alpha_t \in \mathbb{C} \sim \mathcal{N}(0, \sigma_t^2 = RCS)$. Then, the multichannel target signal $\mathbf{s}(\boldsymbol{\vartheta}_t)$ is characterized by its covariance matrix

$$\mathbf{R}_t = E \left\{ \mathbf{s}(\boldsymbol{\vartheta}_t) \mathbf{s}(\boldsymbol{\vartheta}_t)^H \right\} = \begin{bmatrix} \sigma_{t_1}^2 & \dots \rho_{t_1,M} \sqrt{\sigma_{t_1}^2 \sigma_{t_M}^2} e^{j\Delta\psi_{t_1,M}} \\ \vdots & \ddots & \vdots \\ \rho_{t_1,M} \sqrt{\sigma_{t_1}^2 \sigma_{t_M}^2} e^{-j\Delta\psi_{t_1,M}} & \dots & \sigma_{t_M}^2 \end{bmatrix} \quad (2.7)$$

where $(\cdot)^H$ is the Hermitian and complex conjugate operator; and $E\{\cdot\}$ the statistical expectation. Decorrelation effects induced either by the own movement of the target or by the internal clutter motion (ICM), [78,79], can be modeled through the correlation coefficient between each pair of channels $\rho_{t_{i,j}}$. $\Delta\psi_{t_{i,j}}$ refers to the ATI phase between the i th and j th channels.

2.3.2 Interference

GMTI processing intends to detect moving targets masked by the presence of interference, consisting of the background clutter $\mathbf{c}(\boldsymbol{\vartheta}_c)$ and the unavoidable thermal noise \mathbf{n} of the receiver². The latter is generally modeled as a zero-mean complex Gaussian process, $\mathbf{n} \in \mathbb{C} \sim \mathcal{N}(\mathbf{0}, \mathbf{R}_n)$. The noise has neither a temporal nor a spatial structure, $\mathbf{R}_n = \sigma_n^2 \mathbf{I}$,

²In the Military field Jammers are sources of additional interference, but are not considered through the thesis.

where \mathbf{I} stands for identity matrix (unitary diagonal matrix). For calibrated SAR images the noise mean power is related to the noise-equivalent sigma zero (NESZ) and the ground resolution cell area.

The clutter has specific temporal and spatial correlations, which account for both temporal and spatial variability of its radar returns. As it is extendedly considered in the literature [29, 44, 45, 80], the clutter is assumed to have a stationary zero-mean complex Gaussian distribution $\mathbf{c}(\boldsymbol{\vartheta}_c) \in \mathbb{C}^{M \times 1} \sim \mathcal{N}(\mathbf{0}, \mathbf{R}_c)$. This hypothesis breaks down when considering realistic scenarios that may contain highly heterogeneous terrains, such as urban or industrial areas [50]. In the maritime case, it has been widely assumed that a K-distribution (compound model) fits well the sea clutter returns [81, 82]. In Chapter 6, the statistical characterization of an X-band sea clutter using TSX polarimetric data shows a good fitting of the K-distribution to the magnitude. In this regard and to complement the mission performance evaluation carried out in Chapter 4 a K-distributed sea clutter has been also considered in order to understand the impact of non-Gaussian statistics.

A way to provide a more realistic maritime scenario is two-folded: account for specific clutter decorrelation between the different channels induced by the ICM and the inclusion of an ATI phase, which can be related to a mean surface velocity on the sea structure. In this sense, the covariance matrix of the clutter \mathbf{R}_c collects those parameters as

$$\mathbf{R}_c(\boldsymbol{\vartheta}_c) = E \left\{ \mathbf{c}(\boldsymbol{\vartheta}_c) \mathbf{c}(\boldsymbol{\vartheta}_c)^H \right\} = \begin{bmatrix} \sigma_{c_1}^2 & \dots & \rho_{c_1, M} \sqrt{\sigma_{c_1}^2 \sigma_{c_M}^2} e^{j\Delta\psi_{c_1, M}} \\ \vdots & \ddots & \vdots \\ \rho_{c_1, M} \sqrt{\sigma_{c_1}^2 \sigma_{c_M}^2} e^{-j\Delta\psi_{c_1, M}} & \dots & \sigma_{c_M}^2 \end{bmatrix} \quad (2.8)$$

where $\sigma_{c_i}^2$ refers to the clutter power for the i th channel, which is related to the normalized radar backscattering coefficient σ^0 and the ground resolution cell area. For maritime scenarios, this coefficient can be obtained from several semi-empirical models given specific system parameters (frequency, polarization, incidence angle) and scenario conditions (sea state or wind velocity). For further details the reader is referred to section 6.2.1, where a brief review of the most extendedly used σ^0 models is presented.

The phase term $\Delta\psi_{c_i, j}$ in (2.8) represents the ATI phase between channels i and j due to a mean Doppler velocity induced by the clutter scattering points within a resolution cell [83]. This mean Doppler velocity includes the current surface (line-of-sight or radial) velocity of the sea, as well as two other components [83]: the phase velocity of radially traveling Bragg-resonant surface waves (major backscattering mechanism) and the orbital velocity of the gravity waves.

In (2.8), the correlation coefficient $\rho_{c_i, j}$ between channels i and j takes into account the temporal decorrelation induced by the ICM and is related to the (baseline) time-delay $\tau_{i, j}$ between those two channels (equivalent two-way phase center). From [79] and under the assumption of Gaussian distributed clutter, the $\rho_{c_i, j}$ has a Gaussian-like shape:

$$\rho_{c_i, j} = \exp \left\{ - \left(\frac{\tau_{i, j}}{\tau_c} \right)^2 \right\} = \exp \left\{ - \left(\frac{\left(\frac{d_{x_i} - d_{x_j}}{2 \cdot v_{rel}(\boldsymbol{\vartheta}_c)} \right) \cdot v_e}{\tau_c} \right)^2 \right\} \quad (2.9)$$

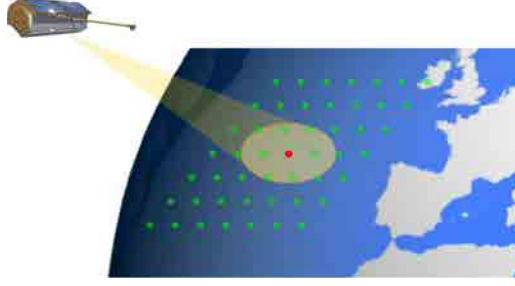


Figure 2.5: Grid of clutter patches: main clutter patch (in red) and the related ambiguous clutter patches (in green) due to the combined range-azimuth ambiguities.

where τ_c is the clutter correlation time, which for an X-band system can vary between 10 to 60 ms, depending on the sea conditions and system resolution, [83, 84].

As the radar measures range and (Doppler) velocity ambiguously, the moving target competes also with ambiguous clutter patches. Therefore, for the main non-ambiguous clutter patch (Fig. 2.5 in red), a grid of ambiguous clutter responses (Fig. 2.5 in green) should be also considered when modeling the clutter [26, 27, 29, 44, 45]:

$$\mathbf{c}(\boldsymbol{\vartheta}_c) = \alpha_c \boldsymbol{\Delta}_{\text{ATI}}(\boldsymbol{\vartheta}_c) + \sum_{k,l}^{N_{amb}} \alpha_{c_{k,l}} \boldsymbol{\Delta}_{\text{ATI}_{k,l}}(\boldsymbol{\vartheta}_c), \quad (k, l) \in \mathbb{Z}^2 \setminus \{0, 0\} \quad (2.10)$$

where α_c and $\alpha_{c_{k,l}}$ refer, respectively, to the reflectivity of the main clutter and the ambiguous k, l th clutter patch (associated to the k th range and l th azimuth ambiguity). In (2.10), $(k, l) \in \mathbb{Z}^2 \setminus \{0, 0\}$ denotes the set of those whole-numbered index pairs of admissible range-azimuth ambiguities except for $k = l = 0$, which refers to the non-ambiguous clutter patch of interest. The vectors $\boldsymbol{\Delta}_{\text{ATI}}(\boldsymbol{\vartheta}_c)$ and $\boldsymbol{\Delta}_{\text{ATI}_{k,l}}(\boldsymbol{\vartheta}_c)$ collect the ATI-phases induced by the clutter's mean Doppler velocity, accordingly.

Considering a homogeneous (stationary) complex Gaussian sea clutter surface and uncorrelated ambiguities, the interference covariance matrix can be expressed as

$$\mathbf{R}_q(\boldsymbol{\vartheta}_c) = \mathbf{R}_{c_0}(\boldsymbol{\vartheta}_c) + \sum_{k,l}^{N_{amb}} \mathbf{R}_{c_{k,l}}(\boldsymbol{\vartheta}_c) + \mathbf{R}_n, \quad (k, l) \in \mathbb{Z}^2 \setminus \{0, 0\} \quad (2.11)$$

where $\mathbf{R}_{c_0}(\boldsymbol{\vartheta}_c)$ is the covariance matrix for the main³ clutter patch [as expressed in (2.8)]. Assuming the same sea correlation properties as for the main patch, the covariance matrix for the k, l th ambiguous patch is analogously defined by

$$\mathbf{R}_{c_{k,l}}(\boldsymbol{\vartheta}_c) = E \left\{ \mathbf{c}_{k,l}(\boldsymbol{\vartheta}_c) \mathbf{c}_{k,l}(\boldsymbol{\vartheta}_c)^H \right\} = \begin{bmatrix} \sigma_{c_1}^2 & \dots & \rho_{c_1,M} \sqrt{\sigma_{c_1}^2 \sigma_M^2} e^{j\Delta\beta_{1,M}^l} \\ \vdots & \ddots & \vdots \\ \rho_{c_1,M} \sqrt{\sigma_{c_1}^2 \sigma_M^2} e^{-j\Delta\beta_{1,M}^l} & \dots & \sigma_M^2 \end{bmatrix} \quad (2.12)$$

³From now on the subindex 0 refers always to the main clutter patch.

The off-diagonal phase terms of $\mathbf{R}_{c_{k,l}}(\boldsymbol{\vartheta}_c)$ are modeled as

$$\Delta\beta_{i,j}^{k,l} = \Delta\psi_{c_{i,j}} - 2\pi \cdot l \cdot \text{PRF} \cdot \frac{(d_{x_i} - d_{x_j}) \cdot v_e}{2 \cdot v_{rel}^2(\boldsymbol{\vartheta}_c)} \quad (2.13)$$

The first term in (2.13) accounts for the interferometric phase $\Delta\psi_{c_{i,j}}$ induced by the clutter's mean Doppler velocity. The second term models the residual phase due to wrong channel coregistration on the ambiguities as pointed out in [29]. This spatial alignment (coregistration) is accomplished by time-shifting the signals of the different channels via interpolation, efficiently performed applying a phase ramp in the Doppler domain. Due to partial backfolding of the different Doppler ambiguities, this phase ramp produces a residual constant phase error [52], modeled by the second phase term in (2.13). This residual error vanishes when the DPCA condition holds, i.e., the satellite's displacement between pulses is a multiple of the baseline separation between the involved channels.

For simplicity the main clutter and the related ambiguous patches are assumed to have equal radar backscattering coefficient σ^0 (homogeneous open sea conditions). In this case, the power of the k, l th ambiguous patch for the i th channel can be expressed as

$$\sigma_{c_i}^2 = \sigma_{c_i}^2 \cdot \text{CRAASR}_{k,l} \quad (2.14)$$

where $\text{CRAASR}_{k,l}$ refers to the combined-range-azimuth-ambiguity-to-signal ratio for the k, l th ambiguity. This new defined metric provides a single SAR ambiguity performance metric that combines the definition of both the azimuth-ambiguity-to-signal ratio (AASR) as well as the range-ambiguity-to-signal ratio (RASR) [23] for the grid of N_{amb} ambiguities⁴:

$$\begin{aligned} \text{CRAASR} &= \sum_{k,l}^{N_{amb}} \text{CRAASR}_{k,l}, \quad (k,l) \in \mathbb{Z}^2 \setminus \{0,0\} \\ &= \sum_{k,l}^{N_{amb}} \frac{R_0^3 \cdot \sin(\gamma_0) \cdot |D_{2-w}(\theta_{k,l}, \phi_{k,l})|^2}{R_{k,l}^3 \cdot \sin(\gamma_{k,l}) \cdot |D_{2-w}(\theta_0, \phi_0)|^2} \cdot \frac{\int_{-B_a/2}^{B_a/2} |P_{2-w}(f_d + l \cdot \text{PRF})|^2 df}{\int_{-B_a/2}^{B_a/2} |P_{2-w}(f_d)|^2 df} \end{aligned} \quad (2.15)$$

where R_0 and $R_{k,l}$ correspond to the slant range for the main and the k, l th ambiguous clutter patches, respectively; $\gamma_{k,l}$ refers to the incidence angle for the k, l th ambiguous clutter patch. The impact of the two-way antenna patterns is accounted for in the $D_{2-w}(\theta_{k,l}, \phi_{k,l})$ term, where $\theta_{k,l}$ and $\phi_{k,l}$ are the spherical angles in the antenna coordinate system for the specific ambiguous clutter patch. The term $P_{2-w}(f_d)$ models the Doppler spectrum, including the antenna pattern and the azimuth window used in SAR focusing for a specific (azimuth/Doppler) processing bandwidth B_a .

⁴In case of AASR only the impact of the (azimuth) ambiguities with the same iso-range as the patch of interest is included in the definition (varying $l \neq 0$ for fixed $k = 0$ in CRAASR definition). Analogously for RASR, solely the ambiguities from broadside (zero-Doppler) and at different ranges w.r.t the patch of interest are considered (varying $k \neq 0$ for a fixed $l = 0$ in CRAASR definition). In this sense, and taking into account that a grid of N_{amb} ambiguities around the main clutter patch exist, the different combinations of range-azimuth ambiguity pairs are accounted for in the CRAASR definition, which are accordingly weighted by the two-dimensional antenna pattern. Therefore, in the CRAASR not only the two main axial ambiguities (as considered by AASR and RASR) are included in the ambiguity performance but also any other possible combination in the two-dimensional plane around the main non-ambiguous clutter patch.

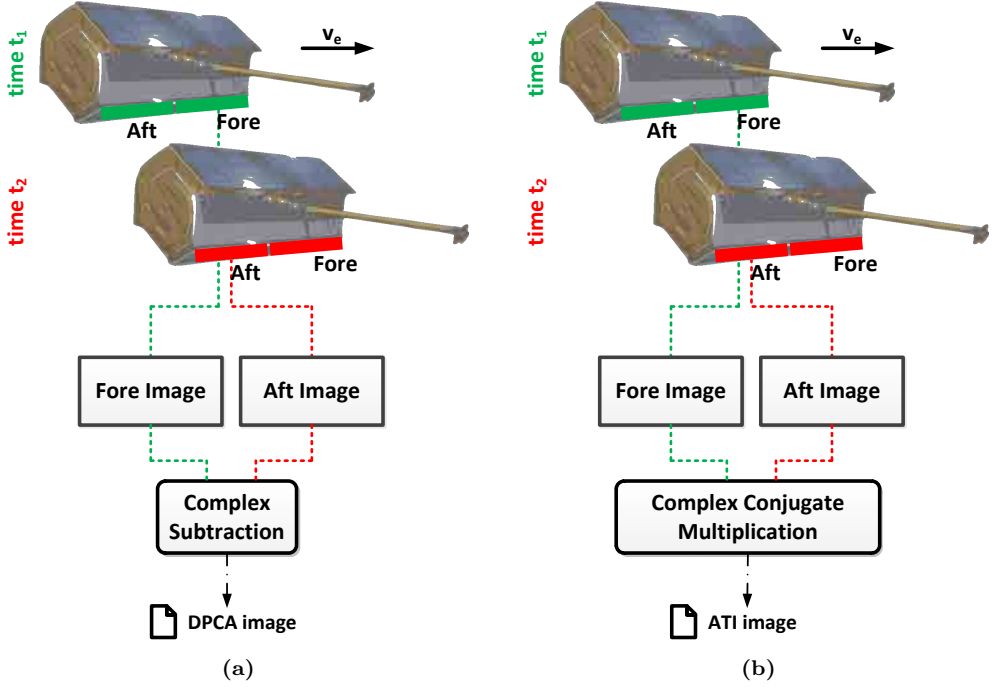


Figure 2.6: Dual receive antenna configuration: (a) DPCA and (b) ATI principles.

2.4 GMTI processing techniques

This section describes a general framework for GMTI processing, introducing the different algorithms, starting from the classical dual receive antenna techniques to the most promising novel adaptive ones.

2.4.1 Dual receive channel GMTI techniques

2.4.1.1 Displaced phase center antenna (DPCA) technique

The DPCA technique has been extensively used in the frame of airborne MTI to enhance performance detectability by means of clutter cancellation [20, 85, 86]. During the last decade, this classical technique has been widely adopted in the SAR-GMTI field [16, 17, 49, 50, 52, 87]. In Fig. 2.6a the operational principle of the DPCA is presented, where the receiving antenna is split into two sub-apertures (channels). The DPCA is a motion compensation technique, such that the two sub-apertures observe the same scene at different times. The whole antenna transmits different pulses, whose echoes are sampled simultaneously at different spatial locations (or equivalently at different times). Then, the PRF is adjusted according to the satellite velocity and the separation (baseline) between the RX antennas in a way that the (effective two-way⁵) phase center of the

⁵The effective two-way phase center corresponds to an equivalent monostatic phase center located at the mid-point between the transmit and receive phase centers.

aft antenna at the second pulse spatially matches the (two-way phase center) position of the fore channel for the first pulse, see Fig. 2.6a. Hence, the clutter is observed from the same spatial location but at different instants. Then, the clutter contribution can be canceled out subtracting the images from the two channels, whereas the moving targets will remain.

The DPCA processing chain is depicted in Fig. 2.6a where the two co-registered SAR images are subtracted to form the DPCA image. Ideally, DPCA could completely remove the clutter up to noise floor, but in real operation, clutter suppression is limited by possible clutter decorrelation (ICM), coregistration errors and channel imbalances.

The main drawback of the DPCA technique, apart from the accurate modeling and calibration of the channel imbalances, is the tight restriction on the PRF in order to satisfy the so called DPCA condition (the effective two-way phase center coincide for sub-subsequent sampling times). This restriction is more severe in the case of spaceborne platform, [23]. As stated in [68] such restrictions on the PRF can be relaxed since spatial alignment of the fore and aft channels can be obtained interpolating the aft samples at non-sampled times (channel coregistration) as long as the PRF is above the Nyquist criterion [52]. Nevertheless, if the “hardware” DPCA condition is not fulfilled a residual phase error exists in the (Doppler) ambiguous clutter patches as described by the second term in (2.13). Thus, they are not completely removed by the DPCA processor and could be misinterpreted as false moving targets.

Assuming clutter and noise to be zero-mean complex Gaussian processes, the residual interference after DPCA (on channels i and j) has the same distribution with variance:

$$\begin{aligned} \sigma_{\text{DPCA}_{qi,j}}^2 &= 2\sigma_n^2 + \sigma_{c_i}^2 + \sigma_{c_j}^2 - 2\rho_{c_{i,j}} \sqrt{\sigma_{c_i}^2 \sigma_{c_j}^2} \cos(\Delta\psi_{c_{i,j}}) \\ &+ \sum_{k,l}^{N_{amb}} \sigma_{c_i^{k,l}}^2 + \sigma_{c_j^{k,l}}^2 - 2\rho_{c_{i,j}} \sqrt{\sigma_{c_i^{k,l}}^2 \sigma_{c_j^{k,l}}^2} \cos(\Delta\beta_{i,j}^{l,k}), \quad (k,l) \in \mathbb{Z}^2 \setminus \{0,0\} \end{aligned} \quad (2.16)$$

Based on a parametric constant false alarm rate (CFAR) detector, the DPCA magnitude is compared against a threshold ξ , which can be determined from the desired probability of false alarm P_{fa} as

$$P_{fa} = \int_{\xi}^{\infty} p_{Y_{qi,j}}(Y_{qi,j}) dY_{qi,j} \quad (2.17)$$

where $Y_{qi,j}$ is the magnitude of the residual interference at the DPCA processor’s output, and $p_{Y_{qi,j}}(Y_{qi,j})$ the probability density function (PDF) of $Y_{qi,j}$.

2.4.1.2 Along-track interferometry (ATI)

ATI has been traditionally used to measure sea surface currents [88–92]. The high sensitivity of the interferometric phase to slight variations in the scene allows exploiting the ATI to perform detection of slowly moving targets [16, 26, 46, 49, 50, 77, 93, 94]. ATI, as DPCA, is a dual-channel antenna technique, where the formation of the interferogram allows both detection of the moving target and estimation of its radial velocity. Different from DPCA, in the ATI processing there is no clutter cancellation. Therefore, the presence of both clutter and noise produces a phase noise that can impair the detection and

estimation of the target's radial velocity [95]. The ATI signal (at range-compressed or image level) is formed as the complex conjugate multiplication of the two coregistrated channels as depicted in Fig. 2.6b

$$\text{ATI}_{i,j} = \frac{1}{L} \sum_l^L [\mathbf{x}]_{i,l} [\mathbf{x}]_{j,l}^* \quad (2.18)$$

where L corresponds to the number looks.

The estimation of the interferometric phase can be affected by systematic errors as: (i) differential phase between the channels, i.e., the two channels having different responses or being unbalanced, which is translated into additional bias in the ATI phase; (ii) different phase delays between the two receiver's chains; (iii) variations in the antenna phase centers; (iv) different antenna patterns and (v) multi-path effects (echoes scattered from the wings and fuselages in the case of airborne data).

An additional consideration that directly impacts the potentiality of the ATI for GMTI is related to the ambiguous phase. The measured interferometric phase is restricted to the interval $[0, 2\pi)$, if this interval is exceeded a phase unwrapping operation is required, which presents ambiguous solutions. In [68] three different types of ambiguities are considered: (i) directional ambiguities, i.e., the phase history difference of the two channels is greater than π , which is translated in an ambiguous directional velocity; (ii) blind-velocities occur when the ATI phase is a multiple of 2π ; (iii) additional ambiguous returns appear when the target velocity induces a Doppler shift resulting in a target spectrum exceeding the $\pm\text{PRF}/2$ limits, as sketched in Fig. 2.2a.

In the literature different ATI CFAR detectors have been proposed and analyzed [48, 49, 96]. Traditionally, the ATI phase was used as CFAR test statistic. However, the phase-only metric cannot detect and correctly estimate low-reflectivity, slowly moving targets. The two-step CFAR detector uses both ATI phase (ψ) and magnitude⁶ (η), as proposed in [48]. In this case, independent magnitude and phase thresholding is assumed, using the marginal PDFs of ATI phase and magnitude. As pointed out in [96], the performance of this two-step detector can be improved if the marginal PDF of magnitude is replaced by the one conditioned to a fixed phase. For both two-step detectors, there exist an infinite number of threshold pairs that achieve the desired P_{fa} . Therefore, the user must carefully choose an operating point that maximizes the probability of detection P_d ; which becomes a crucial step in the design of the detector, affecting the resulting performance.

The two-step CFAR detectors assume that there is no coupling between the ATI phase and magnitude, which can lead to either too many false alarms or few detected targets [96, 97]. In the evaluation of the ATI performance here considered, a CFAR detector exploiting the joint PDF of ATI magnitude and phase has been selected as it could provide improved performance compared to the two-step detectors [97]. As in the two-step detector, the operating-point, in this case a curve or function $\gamma(\psi)$ on the magnitude-phase PDF plane, should be carefully selected. If the thresholding function $\gamma(\psi)$ is selected considering a constant-density contour line of the joint PDF $f_{\eta,\psi}(\eta, \psi) = C$, the P_d is maximized [96]. For a given P_{fa} the related contour line (and the thresholding

⁶ η refers to the normalized ATI magnitude, using the channels' geometric mean power as normalization factor.

function) is obtained through numerical integration of:

$$P_{fa} = \int_{-\pi}^{\pi} \int_{\gamma(\psi)}^{\infty} f_{\eta,\psi}(\eta, \psi) d\eta d\psi \quad (2.19)$$

where the interference joint PDF of the ATI magnitude and phase, for a complex Gaussian distributed interference, can be expressed as [48]

$$f_{\eta,\psi}(\eta, \psi) = \frac{2L^{L+1}\eta^L}{\pi\Gamma(L)(1-|\rho_{i,j}|^2)} \exp\left(\frac{2L\eta|\rho_{i,j}|\cos\psi}{1-|\rho_{i,j}|^2}\right) \cdot K_{L-1}\left(\frac{2L\eta}{1-|\rho_{i,j}|^2}\right) \quad (2.20)$$

where K_L is the modified Bessel function of order L [48, 97]. The interference coherence coefficient between the i th and j th channels $|\rho_{i,j}|$ is obtained as

$$|\rho_{i,j}| = \left| \frac{\rho_{c_{i,j}} \left(\sqrt{\sigma_{c_i^0}^2 \sigma_{c_j^0}^2} e^{j\Delta\psi_{c_{i,j}}} + \sum_{k,l}^{N_{amb}} \sqrt{\sigma_{c_i^{k,l}}^2 \sigma_{c_j^{k,l}}^2} e^{j\Delta\beta_{i,j}^l} \right)}{\sqrt{\left(\sigma_{c_i^0}^2 + \sum_{k,l}^{N_{amb}} \sigma_{c_i^{k,l}}^2 + \sigma_n^2 \right) \left(\sigma_{c_j^0}^2 + \sum_{k,l}^{N_{amb}} \sigma_{c_j^{k,l}}^2 + \sigma_n^2 \right)}} \right|, \quad (k, l) \in \mathbb{Z}^2 \setminus \{0, 0\} \quad (2.21)$$

under the assumption of (spatially) stationary homogeneous clutter, such that the main clutter and the ambiguous patches have the same correlation properties as well as mean Doppler velocity.

2.4.2 Multichannel adaptive GMTI techniques

2.4.2.1 Space-time adaptive processing (STAP)

STAP can be viewed as a generalization of the non-adaptive DPCA technique when working with multichannel architectures, exploiting optimally the additional DoF offered both in time and space to enhance the detection capability. STAP has been extensively studied for GMTI operation in airborne radar [21, 67, 98, 99], and in recent years is receiving an increasing interest for GMTI operation with spaceborne SAR systems [21, 28, 29, 41, 44, 100]. An exhaustive analysis of the principles and applications of STAP can be found in the work of *Klemm* [13, 21]. A recapitulation of STAP concepts and taxonomies is thoroughly introduced by Ward in [98] and Melvin in [101].

STAP is understood as a two-dimensional filter (in the temporal/Doppler and in the spatial/azimuth-angle domain) that allows canceling out the clutter and at the same time enhancing the target detection to an optimal level, which translates into the ability to detect slowly moving targets. The adaptive processing can take into account that clutter characteristics may change while being illuminated by the radar.

To understand the optimality of STAP filtering the PSD of the background clutter in the normalized angle-Doppler plane is represented in Fig. 2.7. The radar platform motion induces a clutter spectrum, whose Doppler shift varies over the (azimuth) angle, with a coupling in angle and Doppler (frequency) as it is represented by the PSD diagonal ridge in Fig. 2.7.

Conventional temporal filters suppress clutter, but low moving targets will be closely located to the stop-band of those inverse filters as can be seen in Fig. 2.7. For spatial

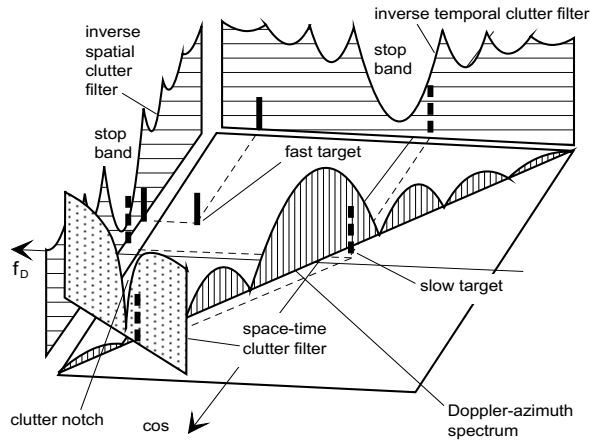


Figure 2.7: Clutter power spectral density (PSD) and STAP principle (adapted from [102]).

(angle) filters the slow targets fall within the main beam clutter or conversely into the stop-band of the spatial filter. Hence, STAP is a two-dimensional space-time filter that forms a very narrow notch along the trajectory of the clutter so that even slow targets that fall within the pass band of such a filter can be detected.

As a first step, STAP requires the estimation of the interference (clutter-plus-noise) covariance matrix and the related inversion in order to perform the adaptation of the filter to the actual received clutter. Then, the received echoes are accordingly filtered to cancel the clutter component. The remaining signal, which is made up of a mixture compound of moving targets and white noise, is processed via a space-time matched filter. Finally the output of such filter is fed to a test block, where the signal is compared with a detection threshold.

STAP adaptively adjusts a two-dimensional (angle-Doppler) filter in order to maximize the output SCNR. This processing allows obtaining the optimal performance (detection of the lowest moving targets with the lowest reflectivity) at expenses of high complexity, since the estimation of the covariance matrix requires a wide set of data and the associated inversion results also in a high computational cost [44, 101]. Different sub-optimum STAP approaches have been analyzed in order to reduce the computational burden and complexity of the fully adaptive STAP approach, see [13, 103, 104], with the objective to break a complex problem (fully adaptation) into a number of smaller and more manageable adaptive problems achieving near-optimum performance.

2.4.2.2 Post-Doppler STAP

An efficient and practically implementable partially adaptive STAP is the so called post-Doppler STAP, [44], also known as factored STAP. This reduced-dimension STAP technique operates in the Doppler domain considering only the spatial DoF. It has been widely used in classical GMTI for airborne data [13, 67, 99] and lately considered in the field of SAR-GMTI [28, 41, 44, 45].

Analogous to the formulation presented in section 2.3, the received (range-compressed) signal from a point target, at a single range cell after azimuth Fourier transform, can be expressed (in the Doppler domain) using vectorial notation⁷

$$\mathbf{x} = \alpha_t \mathbf{d}(\mathbf{u}_t, f_d, \boldsymbol{\vartheta}_t) + \mathbf{q}(f_d, \boldsymbol{\vartheta}_c) = \alpha_t \mathbf{d}(\mathbf{u}_t, f_d, \boldsymbol{\vartheta}_t) + \mathbf{c}(f_d, \boldsymbol{\vartheta}_c) + \mathbf{n}(f_d) \in \mathbb{C}^{M \times 1} \quad (2.22)$$

where α_t refers to the target reflectivity and f_d is the Doppler frequency. The spatial channel information is collected in the beamformer vector $\mathbf{d}(\mathbf{u}_t, f_d, \boldsymbol{\vartheta}_t)$, where the characteristics of the transmit and receive antenna patterns for the specific target direction \mathbf{u}_t are included⁸. As already described in section 2.3, the interference, made up of clutter $\mathbf{c}(f_d, \boldsymbol{\vartheta}_c)$ and thermal noise $\mathbf{n}(f_d)$, is modeled by the $\mathbf{q}(f_d, \boldsymbol{\vartheta}_c)$ vector.

A moving target with azimuth direction u_t (projection of \mathbf{u}_t onto \vec{x} axis) and radial velocity v_r will produce the same Doppler f_d as a (main) clutter patch at $u_c = u_t - v_r/v_e$ (flat earth assumption) for a satellite moving with an effective velocity of v_e . However, the target competes also with ambiguous clutter patches (Fig. 2.5). Under the hypothesis of spatially stationary homogeneous (Gaussian) clutter, perfectly correlated between the different channels (with balanced response), the interference covariance matrix \mathbf{R}_q can be expressed as

$$\begin{aligned} \mathbf{R}_q(f_d, \boldsymbol{\vartheta}_c) &= \mathbf{R}_{c_0}(f_d, \boldsymbol{\vartheta}_c) + \sum_{k,l}^{N_{amb}} \mathbf{R}_{c_{k,l}}(f_d, \boldsymbol{\vartheta}_c) + \mathbf{R}_n(f_d), \quad (k,l) \in \mathbb{Z}^2 \setminus \{0,0\} \\ &= \sigma_c^2 \mathbf{d}(\mathbf{u}_{c_0}, f_d, \boldsymbol{\vartheta}_t) \mathbf{d}^H(\mathbf{u}_{c_0}, f_d, \boldsymbol{\vartheta}_t) \\ &\quad + \sum_{k,l}^{N_{amb}} \sigma_{c_{k,l}}^2 \mathbf{d}(\mathbf{u}_{c_{k,l}}, f_d, \boldsymbol{\vartheta}_t) \mathbf{d}^H(\mathbf{u}_{c_{k,l}}, f_d, \boldsymbol{\vartheta}_t) + \sigma_n^2 \mathbf{I} \end{aligned} \quad (2.23)$$

where σ_c^2 and $\sigma_{c_{k,l}}^2$ correspond to the clutter power for the main patch and the k, l th ambiguous one (k th range and l th azimuth ambiguities); \mathbf{u}_{c_0} and $\mathbf{u}_{c_{k,l}}$ refer, accordingly, to the main patch and the k, l th ambiguity directions. The noise, modeled as a Gaussian complex process, is completely uncorrelated with power σ_n^2 .

The capability of a radar system to detect moving targets in an interference scenario depends on the SCNR that can be achieved after data processing. The upper bound of the SCNR at the output of the post-Doppler STAP, before azimuth focusing, can be expressed as [44]:

$$\text{SCNR}(v_z, f_d) = \alpha_t^2 \mathbf{d}^H(\mathbf{u}_t, f_d, \boldsymbol{\vartheta}_t) \mathbf{R}_q^{-1}(f_d, \boldsymbol{\vartheta}_c) \mathbf{d}(\mathbf{u}_t, f_d, \boldsymbol{\vartheta}_t) \quad (2.24)$$

which is an excellent tool for the performance evaluation of GMTI systems as the probability of detection P_d is proportional to the SCNR for a given P_{fa} .

⁷For the interested reader a detailed mathematical derivation of the multichannel SAR signal for a moving target is presented in Appendix B at raw data, range-compressed and range/azimuth-compressed levels in the time and Doppler domains.

⁸Any direction is denoted in the antenna coordinate system by the unit vector $\mathbf{u} = [u, v, \eta]$ originating from the center of the antenna coordinate system, such that u and v refer to the azimuth and elevation directional cosines, respectively.

2.4.2.3 Extended DPCA (EDPCA)

EDPCA is an adaptive optimum processing technique proposed by Cerutti *et. al* in [29]. EDPCA is an extension of the classical DPCA and ATI algorithms for architectures with more than two receiving channels, exploiting a sub-optimal STAP algorithm, which uses only the spatial DoF. The different steps of the EDPCA algorithm can be traced from the flow chart of the implemented SAR-GMTI processor at image level, in Fig. 5.13, integrating EDPCA, DPCA and ATI techniques, and used for real data evaluation.

After range compression, the different channels are spatially coregistered and (if necessary) balanced/calibrated. In order to maximize the target SCNR (before clutter cancellation), an adaptive SAR processing (for every channel) is performed via a MFB, where the different kinematic parameters are properly considered in both range cell migration correction (RCMC) and azimuth focusing steps⁹ as described in section 5.2.1. The required number of filters to be integrated in the MFB depends on the accepted loss in SCNR when compared to the ideal case. Some insights are given in section 4.3.2, when considering the case of imaging high-speed boats with vertical and horizontal accelerations.

According to [13, 67, 101], the weights of the clutter cancellation filter that maximize the SCNR at EDPCA processor's output, $y = \mathbf{w}^H(\boldsymbol{\vartheta}_t) \mathbf{x}$, are :

$$\mathbf{w}(\boldsymbol{\vartheta}_t) = \beta \mathbf{R}_q^{-1}(\boldsymbol{\vartheta}_c) \mathbf{d}(\boldsymbol{\vartheta}_t) \in \mathbb{C}^{M \times 1} \quad (2.25)$$

where $\mathbf{d}(\boldsymbol{\vartheta}_t)$ refers to the spatial beamformer adapted to the target parameters, such that phase differences between the channels are compensated

$$\mathbf{d}(\boldsymbol{\vartheta}_t) = \boldsymbol{\Delta}_{\text{ATI}}(\boldsymbol{\vartheta}_t) \in \mathbb{C}^{M \times 1} \quad (2.26)$$

The theoretical interference covariance matrix \mathbf{R}_q can be pre-computed if system, instrument and clutter parameters are perfectly characterized *a priori*. Otherwise, \mathbf{R}_q is replaced by its maximum likelihood (ML) estimation (sample covariance matrix)

$$\hat{\mathbf{R}}_q(\boldsymbol{\vartheta}_c, \boldsymbol{\vartheta}_t) = \frac{1}{P} \sum_{p=1}^P \mathbf{x}_p(\boldsymbol{\vartheta}_c, \boldsymbol{\vartheta}_t) \mathbf{x}_p^H(\boldsymbol{\vartheta}_c, \boldsymbol{\vartheta}_t) \in \mathbb{C}^{M \times M} \quad (2.27)$$

where $\{\mathbf{x}_p(\boldsymbol{\vartheta}_c, \boldsymbol{\vartheta}_t)\}_{p=1}^P$ correspond ideally to P independent and identically distributed (i.i.d.) pixels of training data over an homogeneous region, where no target is present, avoiding the so called moving target *self-whitening*. As pointed out in [105] “a rule of thumb” to achieve a minimum degradation of 3 dB in the SCNR performance, requires the number of i.i.d. P samples to be greater than $2M$. The dependency of $\hat{\mathbf{R}}_q$ with $\boldsymbol{\vartheta}_t$ has been included to point out that the estimation is performed over the M SAR images adapted to specific target kinematic parameters, i.e., for a given iteration of the MFB.

In order to have CFAR test statistics at the EDPCA processor's output, the scalar

⁹No compensation of the Doppler shift (azimuth shift) is carried out, since, otherwise, the target will appear at different azimuth positions for different v_z of the filter bank, posing difficulties to efficiently compare the outputs of the bank of filters.

term β in (2.25) is properly chosen as:

$$\beta = \frac{1}{\sqrt{\mathbf{d}^H(\boldsymbol{\vartheta}_t) \hat{\mathbf{R}}_q^{-1}(\boldsymbol{\vartheta}_c, \boldsymbol{\vartheta}_t) \mathbf{d}(\boldsymbol{\vartheta}_t)}} \quad (2.28)$$

ensuring a unitary power residual interference. Similar to DPCA, the output's magnitude is compared against a threshold for a given P_{fa} .

2.4.2.4 Imaging STAP (ISTAP)

In classical GMTI operation STAP is operated as filter with no image formation process. In this sense, Cerutti has proposed in [28] the ISTAP algorithm, efficiently integrating a post-Doppler STAP in the SAR processing chain, such that well-focused SAR images of moving targets are obtained. The clutter cancellation is performed in the Doppler domain and per Doppler bin only using the spatial DoF. This approach works well under the assumption of interference decoupling between the different Doppler bins, which for moderate synthetic aperture times is fulfilled [44,45]. Contrary to classical factored STAP techniques, ISTAP does not perform any segmentation of the acquisition time into short coherent processing intervals (CPIs), but instead processes the whole integration time (through SAR focusing) maximizing the output SCNR.

A full processing chain integrating ISTAP with a SAR processor based on a MFB has been implemented for real data operation, see flow chart in Fig. 5.14. Contrary to EDPCA, in ISTAP the interference covariance matrix is estimated once and not for every filter of the MFB. This means also that clutter cancellation (by means of $\hat{\mathbf{R}}_q^{-1}$) is performed only once. Moreover, SAR processing (per each adaptive filter) is applied over a single range-compressed and clutter canceled image, while in EDPCA M independent SAR images should be processed per MFB iteration. From these considerations, it is clear that ISTAP is computationally more efficient.

In this case the Doppler-dependent interference covariance matrix is estimated for each Doppler bin averaging over a set of P range cells, as done in post-Doppler STAP:

$$\hat{\mathbf{R}}_q(f_d, \boldsymbol{\vartheta}_c) = \frac{1}{P} \sum_{p=1}^P \mathbf{x}_p(f_d, \boldsymbol{\vartheta}_c) \mathbf{x}_p(f_d, \boldsymbol{\vartheta}_c)^H \in \mathbb{C}^{M \times M} \quad (2.29)$$

The ISTAP Doppler-dependent weights before SAR focusing can be written as

$$\mathbf{w}(f_d, \boldsymbol{\vartheta}_t) = \frac{\hat{\mathbf{R}}_q^{-1}(f_d, \boldsymbol{\vartheta}_c) \mathbf{d}(\mathbf{u}_t, f_d, \boldsymbol{\vartheta}_t)}{\sqrt{\mathbf{d}^H(\mathbf{u}_t, f_d, \boldsymbol{\vartheta}_t) \hat{\mathbf{R}}_q^{-1}(f_d, \boldsymbol{\vartheta}_c) \mathbf{d}(\mathbf{u}_t, f_d, \boldsymbol{\vartheta}_t)}} \in \mathbb{C}^{M \times 1} \quad (2.30)$$

where $\mathbf{d}(\mathbf{u}_t, f_d, \boldsymbol{\vartheta}_t)$ corresponds to the steering vector, which compensates for the phase differences between the different channels for that moving target, incorporating the two-way receive antenna pattern information. This beamformer corresponds to the product of diagonal matrices $\mathbf{D}(f_d, \Delta f_d, \boldsymbol{\vartheta}_t)$ (antenna pattern) and $\boldsymbol{\psi}(f_d, \Delta f_d, \boldsymbol{\vartheta}_t)$ (beamformer phase) as defined in (B.32) and (B.33). Such a formulation can be traced from the detailed mathematical derivation of the multichannel SAR raw data signal of a point-like moving target presented in Appendix B. After SAR processing (RCMC and azimuth-compression) for each filter in the MFB the magnitude at ISTAP output is compared against a threshold for a given P_{fa} .

2.5 Concluding remarks

A general picture of the GMTI framework has been described in this chapter, based on a comprehensively review of the GMTI state-of-the-art. In this way, it is easier to understand the limitations of current SAR missions to detect slow and small moving objects with especial emphasis on the maritime scenario and the need to define optimized SAR-GMTI configurations to this purpose. The level of maturity and readiness of the SAR-GMTI for spaceborne operation is low; there is still a lot of work to be done, especially in the case of maritime surveillance from space platforms.

The impact of moving targets on SAR imagery has been briefly reviewed. The knowledge about these effects is essential for the proposal of adequate processing strategies: the induced image and radiometric degradations of moving targets when imaged by a SWMF could ruin GMTI performance if the related kinematics are not properly considered.

A multichannel SAR data model at image level has been also derived. This mathematical formulation constitutes the basis of the theoretical performance evaluation of any SAR-GMTI mission when considering GMTI techniques that operate at image level, such as DPCA, ATI and EDPCA. In this derivation it has been stressed the need to properly account for the ambiguities' impact, which could play an important role in the expected SAR-GMTI performance. In this sense, the CRAASR has been defined to unify the impact of the combined range-azimuth ambiguities in a single ambiguity metric.

Classical dual channel GMTI techniques, such as DPCA and ATI, have been described, since they are of special interest for current SAR-GMTI missions, equipped at most with two parallel receivers. Such configurations provide limited detection capabilities and additional spatial diversity (additional phase centers) is required to exploit the optimum adaptive techniques based on STAP, resulting in enhanced GMTI performance. A brief description of STAP concepts has been also carried out, with special emphasis on the sub-optimum post-Doppler technique that has received lately special attention by the SAR community. Based on the data model at image level, a simplistic formulation in the range-compressed Doppler domain has been derived, which demonstrates to be useful for preliminary validation of some mission when using a post-Doppler approach. The promising SAR-GMTI techniques as EDPCA and ISTAP, which exploit optimally the spatial DoF, have been also reviewed.

Lately, the efforts in the GMTI research are directed to rethink the operation of GMTI in combination with promising modes as HRWS SAR and MIMO SAR. This would allow a wide area surveillance system with high-resolution imaging capabilities. Therefore, new processing algorithms should be proposed, where system complexity and computational load reductions are the driven requirements.

3

Chapter 3

Multichannel SAR (MSAR) simulation tools

To understand the limitations of current state-of-the-art SAR-GMTI missions as well as to evaluate the applicability and performance of different GMTI processing techniques on new mission concept designs, the implementation of flexible simulation tools plays a pivotal role in the research carried out through this thesis. The restricted access to experimental raw data and the limited number of spaceborne SAR sensors with GMTI capabilities has suggested the necessity to define and develop different simulation systems (with different levels of complexity). These tools facilitate the transversal assessment and validation of SAR-GMTI missions from the architectural configuration to the processing techniques, passing by the appropriate modeling of the calibration requirements. This chapter describes the three main simulation tools developed within this doctoral activity. The first part is devoted to introduce the multichannel SAR raw data simulator (MSARRDS). In the second part of the chapter, a SAR-GMTI mission performance tool is presented, based on theoretical characterization of both SAR and GMTI operation. Finally, a Monte Carlo (MC) like performance simulator is described.

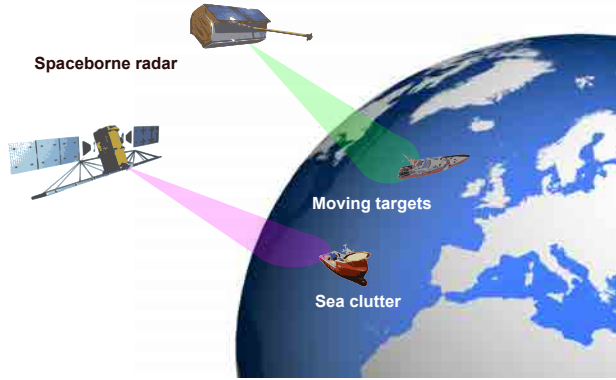


Figure 3.1: Schematic representation of the spaceborne GMTI paradigm.

3.1 Introduction

The prohibitive cost of constructing and testing spaceborne radar prototypes for future missions has motivated the necessity to further develop simulation technologies that can help in the development process. The rapid evolution of the electronic technology, allowing powerful computing resources in general-purpose machines, jointly with the availability of precise mathematical models for the spaceborne radar paradigm, Fig. 3.1, enables the implementation and validation of radar missions in reasonable times.

A lot of effort has been devoted to the proper simulation of radar operation from the research/academic point of view [31, 106–110] to the commercial one [111–114], where fidelity and speed are the main driven parameters. The conceptual definition, design and implementation of radar simulation environments is a complex process, which requires the merging of multidisciplinary knowledge (system engineering, mission performance, signal processing and algorithms' coding). In this sense, proper design strategies are required to deal with sophisticated simulation environments; some guidelines to emulate radar systems can be found in reference textbooks as [115–117].

With proper conditioned simulation tools, spaceborne SAR-GMTI radar missions (or general purpose radar) can be accurately modeled, such that a complete and exhaustive performance evaluation can be carried out under different design parameters, operating system and scenario conditions, considering the related trade-offs. In this way, they can be used to design optimized radar system configurations, and at the same time to test potential processing algorithms.

The schematic representation of the spaceborne GMTI paradigm, shown in Fig. 3.1, allows understanding the general problem of emulating and modeling the operation of an imaging radar that should be able to detect moving targets on the Earth surface. Fig. 3.1 helps breaking down this complex conglomerate into different macro conceptual modules that can be separately modeled and designed, which in turn can be used either as an integral part of a hierarchical-like simulator or as an isolated simulation entity.

The flying platform that carries the sensor should be properly modeled and parametrized, taking into account the basic operational parameters (frequency, bandwidth, PRF, re-

ceiver noise and alike), the number of receiving channels and the antenna pattern integration. This latter plays an important role when considering the accurate impact of radar ambiguities and possible system-dependent errors in the SAR-GMTI performance evaluation. The acquisition geometry and so the coordinate system should be properly characterized upon a given level of complexity, especially when a realistic orbital simulation is expected.

Accuracy and fidelity on modeling realistic environments (scenarios) to validate the GMTI capabilities of any radar mission, is one of the most demanding and complex topics to be faced when implementing such simulation tools. The environment model includes both moving target and background clutter; and for the particular case of SAR-GMTI over maritime scenarios, additional considerations to account for the internal motion of the sea clutter should be made. Different approaches have been proposed to properly emulate the radar response of sea clutter, following a physical (electromagnetic) description [118–121], or as in [49, 122–124] trying to extrapolate the electromagnetic interaction between the radar signal and the sea to a stochastic process. A statistical-like approach has been considered in the different implemented simulation tools to model the impact of background clutter (for given spatial and temporal correlations), since one of the main objectives of the thesis is the validation of SAR-GMTI missions using different processing algorithms. Further research and discussions on sea clutter statistics and characterization at SAR image level are carried out in Chapter 6, with experimental data from the spaceborne TSX mission.

The design of any radar simulation tool should be flexible enough to accommodate different design options in terms of system configurations and processing algorithms so that different system/techniques can be optimized. At the same time it should be able to simulate selectable scenario conditions (using a data base of target models and clutter parameters), such that the performance of any SAR-GMTI mission/processing technique can be fully characterized and compared in a wide variety of realistic acquisition scenarios.

3.2 Multichannel SAR raw data simulator (MSARRDS)

One of the objectives of this thesis is to evaluate the applicability and performance of GMTI techniques using spaceborne SAR platforms in order to understand their limitations, allowing the proposal of optimized system configurations as well as adequate processing strategies. In the framework of this doctoral activity, a raw data simulation tool is defined and developed, providing SAR-GMTI data sets for user-defined scenarios and system configurations.

With this tool the different GMTI processing/detection techniques can be assessed and validated, for any given configuration and system parameter specifications, at any time and with a reduced cost. The requirements defined for this SAR-GMTI simulator tool are:

- Flexibility in the system configuration, acquisition and scenarios definition
- Emulation of realistic potential scenarios

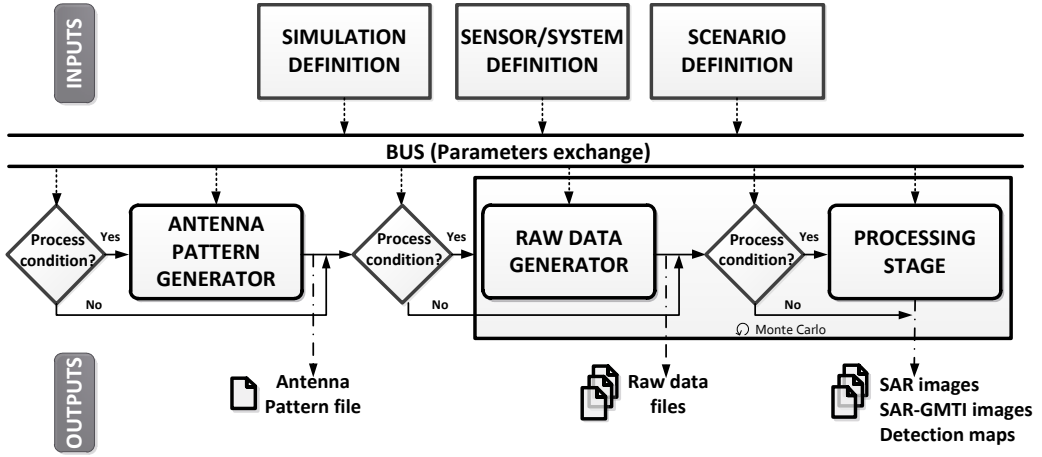


Figure 3.2: Block diagram of the multichannel SAR raw data simulator (MSARRDS).

- Mono- and multistatic acquisition configurations
- Integration of GMTI as well as SAR processing techniques
- Evaluation and performance analysis of the different GMTI techniques

The software implemented in this thesis sets the basis for the development of part of the SIMulator for Moving Target Indicator SYStem (SIMTISYS) [31], an FP7 Copernicus research project to support EU's maritime surveillance with the aim of improving citizen security and environmental monitoring. The SIMTISYS simulator will be a useful and powerful tool, which will assist users (coast guard authorities) with the detection and tracking of vessels in the context of pre-defined scenarios. The SIMTISYS consortium is formed by seven partners from three European countries with extensive experience in the field of Maritime radar surveillance and spacebased simulation tools.

3.2.1 Simulator structure definition and design

During this thesis special effort has been devoted to develop a system-level simulator, whose basis is flexibility, modularity and interoperability at both system configuration and processing stages. In this way, different levels of complexity can be easily incorporated when modeling/defining both raw data generation as well as processing. Single and multichannel acquisitions can be configured, such that additional operational modes can be efficiently integrated. Emulating realistic clutter is a key point for proper evaluation of the SAR-GMTI missions along with the involved processing algorithms. In this sense, maritime environments represent challenging scenarios to be simulated. Therefore, an adequate clutter modeling is required, enabling a versatile operation, while keeping efficiency as a driven characteristic of the generation process.

Fig. 3.2 shows a simplified high-level description of the simulator flow chart. Four main components can be differentiated: (i) the input interface, where the system configuration, scenario and simulation options are defined; (ii) the interconnecting bus, where the different information is accordingly exchanged between the different entities of the

simulator and it is also in charge of managing the workflow, i.e., the sequence of tasks to carry out a simulation activity; (iii) the core of the simulator, which consists of three main modules (antenna pattern generator, raw data generator and the processing stage); and (iv) the output interface, where the different results (intermediate and final products) are provided to the user in terms of figures or text files.

3.2.1.1 Inputs definition

As an input to the simulator three main definition blocks are specified (sensor, scenario and simulation), encapsulated as independent structures of parameters.

Sensor definition

The configuration of the flying platform is characterized in terms of:

- Radar and operation mode parameters: frequency of operation, pulse duration, bandwidth, PRF, incidence angle, platform, spot and effective velocities¹.
- Instrument hardware configuration: number of transmit and receive channels, antenna configuration and type, tilt and squint angle acquisition².
- Antenna tapering configuration, indicating the type of tapering both in the vertical and horizontal dimensions of the antenna, being subswath and pulse sequence (toggling/switching modes) dependent.
- Polarization configuration, either HH or VV.
- Front end: transmitted peak power, noise figure and receiver/transmitter losses.

Scenario definition

The scene/environment to be simulated is described by means of:

- Ground extension (in range and azimuth), beam of operation, and incidence angles at center, near and far range.
- Clutter type (land or sea), azimuth and range separation of the scattering points, radar backscattering coefficient model, and temporal/spatial correlation properties.
- Moving target parameters: ground (along-, across-track and vertical) velocities and accelerations, positions w.r.t the center of the scene and RCS.

At this point it must be noted that one of the main difficulties in modeling sea clutter, aside from its simulation (section 3.2.1.3) and statistical description (analyzed in chapter 6), has been to find an appropriate model of sea radar backscattering coefficient σ^0 . The fundamental requirement was to find a mathematical model properly parametrized in order to allow a certain degree of flexibility when simulating different operating and scenario conditions. Moreover, the model should be able to provide realistic values of σ^0 for spaceborne SAR imaging acquisitions. Due to the high variability and randomness of the

¹The different parameters in the mode of operation structure can be defined as subswath dependent, when operating with different beams to cover different incidence angles.

²The antenna configuration (length, height, number of elements in TX/RX for an active array, separations, physical positions of receiver channels) can be specified for each TX/RX channel for each subswath, and for each pulse sequence when using toggling/switching modes of operation, [45].

ocean conditions, a theoretical (analytical) description of its reflectivity using microwave frequencies is not yet available. A lot of effort has been devoted to develop semi-empirical models that could relate the σ^0 to radar parameters, acquisition geometry and sea conditions. The most representatives are: the Georgia Institute of Technology (GIT) [125], the Hybrid (HYB) [126], the Technology Service Corporation (TSC) [127] and the Naval Research Laboratory (NRL) [128]. The TSC and NRL models have been integrated in MSARRDS, since they provide the widest range of incidence angles, covering most radar bands of interest. Further discussions on the available σ^0 models can be found in section 6.2.1.

Simulation definition

In the simulation parameters definition block specific operation conditions and flags are activated and/or inputed giving control over the simulation process and its different stages. In this manner, the raw data generation block can be activated/deactivated, with the possibility to pass specific external (raw) data files to the processing stage. It also incorporates flags to consider the inclusion, one by one, of moving targets, clutter and/or thermal noise.

As it is discussed in section 3.2.1.3, there are different selectable ways to generate raw data for the clutter. Like for the raw data generation, the antenna pattern computation stage can be turned on/off, feeding the current simulation with a new antenna pattern or using one already generated. The simulator includes also the option of running different trials as part of a Monte Carlo performance evaluation approach, such that different sets of raw data are generated and accordingly processed.

The type of processing to be carried out can also be chosen, specifying the SAR processing parameters (processing bandwidths and windowing type), GMTI technique (DPCA, ATI, EDPKA and ISTAP) and multilooking. As a pre-processing operation, channel balancing/calibration and coregistration are optional operations. The CFAR detection approach can be also selected, using a sliding window approach or selecting a portion of the image for interference statistical parameters' estimation. Once the detection map has been generated the detected pixels can be clustered for further post-processing purposes.

If desired, the user, through the simulation definition block, can indicate whether intermediate figures and/or data products, mostly related to the processing stage, should be saved for their further inspection and analysis.

3.2.1.2 Antenna pattern generation

A dedicated module, Fig. 3.3, has been implemented to accurately model the antenna patterns of any multichannel configuration, based on the specified input antenna structure. The output of the module is also a data structure containing for each channel: (i) the two-dimensional gain pattern in transmission and reception, as a function of the antenna angles θ and ϕ ; (ii) the elevation and azimuth antenna pattern cuts and (iii) the related 3 dB beamwidths for TX and RX. It must be noted that in case of toggling/switching operations [45], the corresponding antenna patterns are also computed, since the antenna configuration can be modified from pulse-to-pulse. The user can indicate the step size

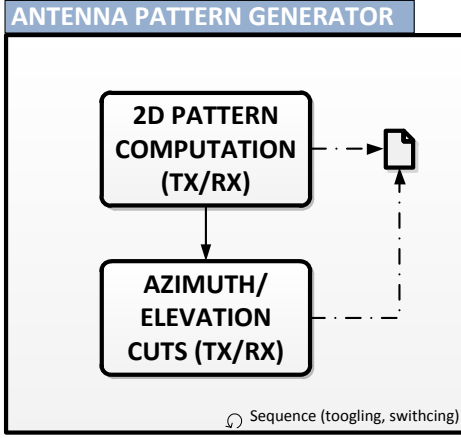


Figure 3.3: Block diagram of the antenna pattern generator.

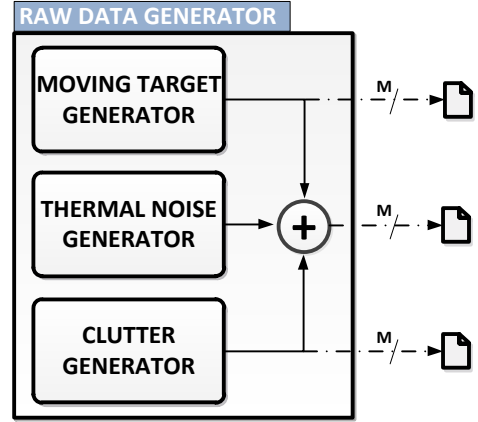


Figure 3.4: Block diagram of the raw data generator stage.

and the range of the antenna angles (θ and ϕ) for which the antenna diagrams have to be computed.

The current version of this module integrates the generation of the antenna pattern for any desired planar active array configuration: the weights on each of the transmit receive module (TRM) can be defined as an external file for the specific beam of operation; otherwise, the user can simply specify the type of weighting in both dimensions of the antenna (uniform, hamming or chebyshev) and the corresponding beam steering (elevation and azimuth). The basic radiating element of the planar array can also be modeled. In the current version, a 16-element subarray (in azimuth axis) and a rectangular patch are integrated in the submodule in charge of generating the corresponding antenna pattern; with future updates the desired antenna pattern of the basic element will be given as an input file.

3.2.1.3 Raw data generation

The proposed simulator is a time-domain type, using a baseband signal approach, i.e., the full expanded transmitted waveform (pulse) is modeled. This kind of approach allows greater fidelity in the modeling since possible hardware errors can be easily incorporated, [21]. As sketched in Fig. 3.4, three main submodules can be recognized: moving target raw data generator, the additive thermal noise source and the clutter raw data generator. In this manner three different raw data files can be saved separately, such that either of the three can be reused/reloaded in any new simulation run with no need to regenerate data, assuming that the same conditions/scenario will be considered. The three sub-modules can be independently activated/deactivated allowing a great flexibility in the simulation process. Under these considerations, and once the corresponding independent raw data signals are generated, they are combined coherently, producing a data cube (or stack) for multichannel acquisitions.

Moving target generation

For each scattering center of the moving target, the transmitted pulse and the received echo are emulated for each pulse repetition interval (PRI), updating the positions accordingly of each point-like scatterer and the related platform/channel location (assuming a rectilinear trajectory)³. Currently, a uniformly accelerated movement in the three-dimensions (along-track, across-track and vertical) has been assumed for each point-like scatterer. Further ameliorations contemplate the integration of a given random target movement using an external file, which describes the three-dimensional positions of the different scattering centers per transmitted pulse.

At this point it must be noted that the actual version of the simulator considers the different targets (or vessels) as a collection of dominant point-like scattering centers whose RCS keeps constant during the acquisition time. Nevertheless, it is well-known that the reflectivity of complex targets, such as vessels, can dramatically vary with the aspect angle during the synthetic aperture formation [76]. Target motion itself jointly with the sea interaction can produce large variations on this angle. Typical RCS values and their variability have been reported in [75] for different types of vessels. The RCS of targets, such as ships or airplanes, is obtained either experimentally or through numerical simulations, based on high frequency approximations [107]. Geometric and physical optics are widely used, where the impact of multiple reflections can be modeled through ray-tracing algorithms [107, 108]. In the current version of MSARRDS, the user describes each of the vessels to be included in the scenario as a collection of scatterers, providing their relative positions (in the three axis) w.r.t a given reference and the RCS for each one. Two different type of ships (ramshackle and civil cargo), whose electromagnetic modeling and RCS extraction have been performed by Telespazio VEGA UK in the frame of SIMTISYS FP7 project [76], are available in the target's catalog of the simulator.

Noise generation

The (thermal) noise contribution is simply obtained as two-dimensional (raw data image) zero-mean complex Gaussian random process, characterized by the transmitted bandwidth of the chirp pulse and the receiver noise figure, which is specified for each channel.

Clutter generation

Simulation of realistic sea clutter scenarios is one of the most complex topics and has received a lot of attention in the radar simulation field. Mainly, two different strategies to model the radar response of maritime scenarios are followed: a physical emulation of the electromagnetic interaction between the radar and the sea waves as suggested in [118–120] and references herein; and a statistical description of such a process [122–124, 127]. This second approach has special interest in the radar community for system design and performance prediction.

For the first type of radar sea clutter modeling, a general approach considers the description of the sea surface's elevation as a sum of regular sinusoidal waves of different amplitudes, frequencies and directions, such that the amplitude of these sinusoids is driven

³Future updates of the simulator foresee the integration of an orbital simulator to account for a more precise description of spaceborne platforms as studied in [129].

by a given specific sea spectrum, [130–132]. The UPC GRECOSAR simulator [107, 108, 131] provides SAR images of the ocean based on a dynamic and multi-harmonic elevation model exploiting high-frequency methods, as physical optics, physical theory of diffraction and ray-tracing algorithms, to compute the backscattering coefficient. To obtain accurate modeling of the radar sea clutter response, high density of facets should be considered, which prevents the simulation of big scenes due to the high computational cost.

From these considerations, and taking into account that the main objective of the simulator is the performance evaluation of SAR-GMTI missions, a statistical based modeling of the sea clutter has been considered for the corresponding raw data generation. It is well-known that the echo returns of a distributed scene, in a pulse-by-pulse basis, corresponds to the coherent integration of the backscattered signals from the multiple scattering centers. In this regard, and to simulate the acquired raw data, the clutter has been modeled as a collection of point-like scatterers uniformly distributed over the scene to be imaged, with many scattering centers per resolution cell. Then, a reflectivity map is generated for this collection of points according to a statistical model. This map is, in fact, a data cube accounting for the spatial distribution of the reflectivity (azimuth and ground-range) and its temporal evolution during the acquisition. It is generally assumed that for low resolution radars, the sea clutter can be described by a complex Gaussian process (Rayleigh distributed in amplitude). However, as the resolution increases, a non-Gaussian behavior is expected, and its amplitude is commonly described by a K-distribution [82, 133, 134], modeling the spikier returns. Chapter 6 is devoted to study the applicability of such statistical descriptors using spaceborne TSX data.

The physical foundation of the K-distribution is the so called compound model theory [82, 134]. Two main components with differentiated temporal/spatial correlation properties are incorporated: the underlying mean value of the (amplitude) reflectivity, characterized by a Chi distribution (or Gamma distribution in intensity), models the spatial variability associated to the gross wave structure; this component modulates the fast varying component of the clutter (speckle), due to the coherent combination of several mechanisms in a resolution cell (interference between capillary waves), and it is characterized by a complex Gaussian process. Fig. 3.5 depicts a procedure to obtain a K-distributed (in amplitude) data cube, showing how to properly incorporate the related spatial (Gamma) and temporal (speckle) correlations [124, 127].

The current version of the clutter sub-module raw data generator allows selecting between Gaussian and K-distributed modeling options. Moreover, two different approaches for raw data generation have been included. The so called “brute force method” models the exact echo return at each PRI and for each scattering center of the clutter’s grid. However, this option requires demanding computational times when considering medium to big scenes (above 1 km by 1 km) and a high density of scattering centers per resolution cell. In order to speed up this process, the simulator integrates the option to create several threads running in parallel, where each one is in charge of generating the clutter’s raw data for a given temporal portion of the synthetic aperture. This is a trade-off solution since the different threads are sharing/accessing the same clutter’s reflectivity data cube and so the effective improvement in simulation time is obtained at expense of a higher memory load.

An alternative efficient method has been implemented based on a spatial 2-dimensional convolution of the raw data PSF of a point-target in the center of the scene with the spatial

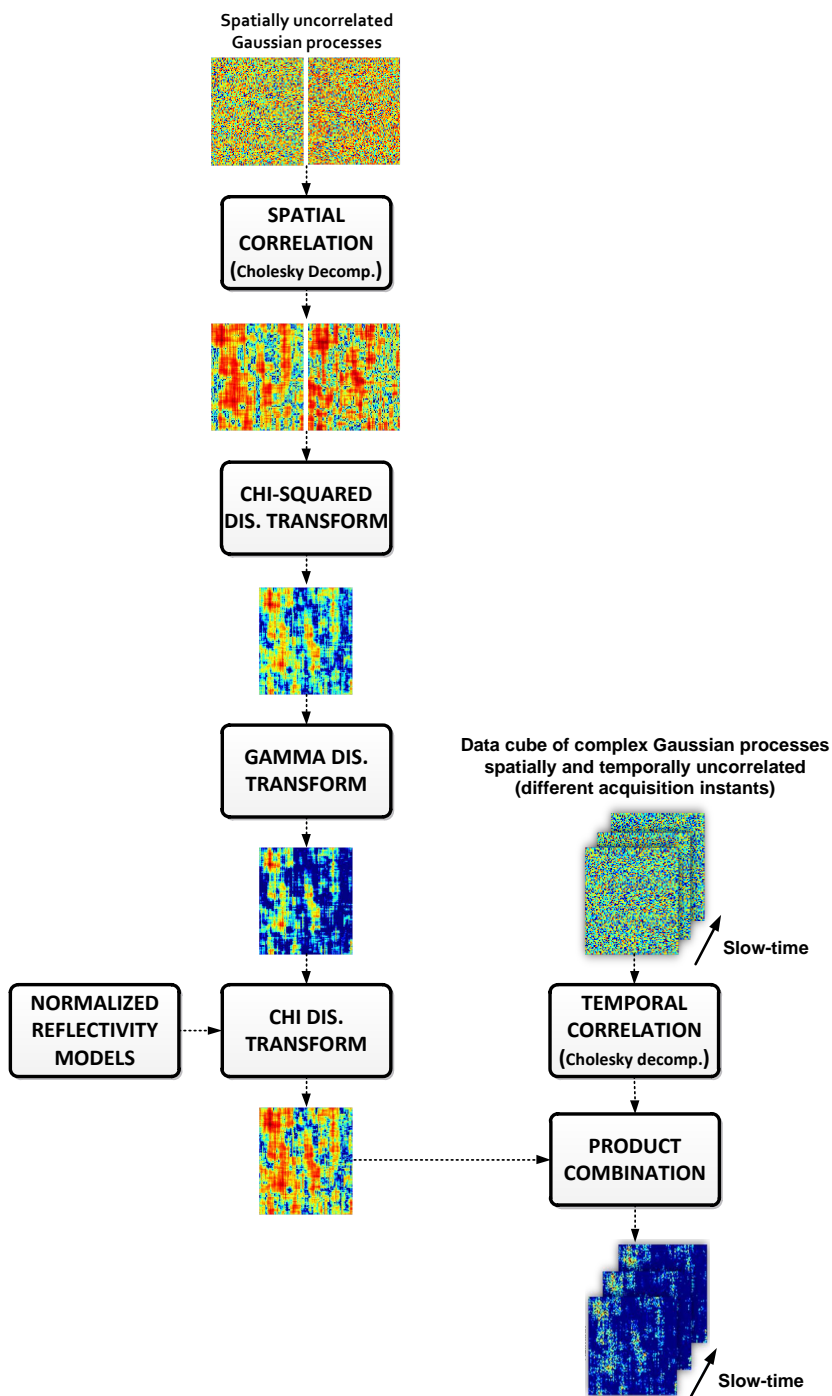


Figure 3.5: Flow chart for a K-distributed reflectivity data cube generation.

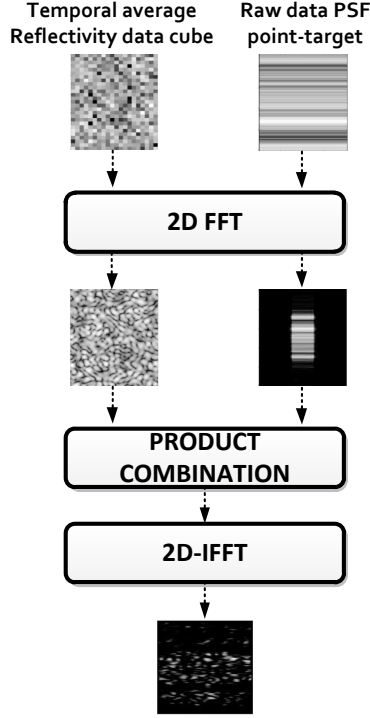


Figure 3.6: Flow chart of the efficient convolutional approach to generate clutter's raw data.

clutter reflectivity map (obtained as a temporal averaging of the clutter's reflectivity data cube). This convolution can be efficiently performed in the spectral domain, accelerating considerably the generation of the clutter's raw data, as represented in Fig. 3.6. The temporal variability has been included on the point-target response as a spatial averaging of the reflectivity data cube. This simplistic approach assumes that the spatially distributed scatterers in the scene have the same temporal evolution, which to small/medium image scene extensions can be regarded as true.

As evaluated in Chapter 4, range/azimuth ambiguities should be properly considered since they impact directly on the SAR-GMTI performance. In Fig. 2.5 the grid of ambiguous clutter patches (range/azimuth) are schematically represented. These ambiguities can be several kilometers away from the AOI to be imaged. Therefore, and in order to include the impact of these ambiguities, ideally, a patch bigger than the AOI (tens of kilometers) should be simulated, but it would require higher computational times. A simplified approach has been integrated in the simulator, where for each scattering point of the clutter the associated ambiguities are assumed to have the same reflectivity behavior, and their contribution is coherently added, with the corresponding antenna pattern weighting, to the echo return of the point-like target of interest. In this way it is possible to select the number of combined range-azimuth ambiguities to be included in the raw data generation (the higher this number, the higher the simulation time). In the convolutional efficient generation approach the ambiguities' contribution is computed for the reference point-like

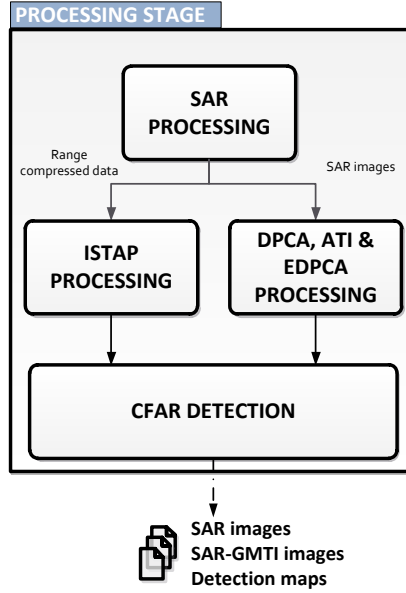


Figure 3.7: Block diagram of the processing stage.

target, such that its impact is included in the raw data PSF, and so the different parts of the scene have the same ambiguity influence.

An alternative approach to simulate the clutter’s contribution is to generate this component directly at SAR image level, speeding up the computational time. The reflectivity data cube (for a given stochastic descriptor) is generated according to the final image size and two-dimensional sampling. The third dimension of this data stack refers to the different channels, where the correlation between them is introduced based on the temporal decorrelation of the clutter and the corresponding baseline time-delays. Then, this data cube is filtered by the SAR two-dimensional PSF to include the impact of SAR imaging formation process⁴. This alternative way to generate the clutter component is very attractive, especially for the evaluation of GMTI techniques operating directly on the SAR images, such as DPCA, ATI and EDPKA.

The different modules have been designed in a way that Monte Carlo trials can be carried out. In this manner, a frequency of detection over a set of trials can be obtained, analogous to the probability of detection metric. For this type of simulation run, moving targets’ raw data is generated once, while the noise and clutter contributions are produced sequentially per trial. The pseudo-random number generator updates accordingly its seed so the different random processes are uncorrelated from trial to trial.

⁴In case of adaptive SAR processing (to a given set of target kinematic parameters), the two-dimensional PSF is updated accordingly and so the clutter’s contribution.

3.2.1.4 Processing stage

The raw data cube is passed to the processing stage, see Fig. 3.7, providing different final products: (i) a stack of SAR images, per channel and per iteration, in case of MFB processing; (ii) the SAR-GMTI images, for each selected processing technique; and (iii) the corresponding detection maps. Both SAR and SAR-GMTI images can be expressed in terms of SCNR metrics to facilitate the performance comparison of the different GMTI techniques.

The simulator integrates an adaptive range-Doppler processor, based on a MFB, to compensate for the induced imaging degradations, maximizing the moving target response. A detailed description of such a processor is presented in section 5.2.1. Processing bandwidths, spectral windowing and MFB's specifications are input parameters that can be selected.

Three main GMTI processing techniques can be selected to obtain the aforementioned products: DPCA, ATI, EDPCA and ISTAP. For the classical dual-channel techniques (DPCA and ATI), the user indicates which channel combinations to be used (for more than 2-receiver configurations). Processing chains similar to the ones depicted in Fig. 5.13 and Fig. 5.14 have been incorporated to the processing stage, for further details the reader is referred to sections 5.2.2 and 5.2.3.

3.3 MSAR-GMTI mission theoretical performance tool

To complement the raw data SAR simulator a modular performance analysis tool has been developed. The aim of this flexible software is to evaluate the potentiality of general purpose multichannel SAR missions, with emphasis on the GMTI capabilities, such that the expected performance can be anticipated with reduced computational cost, based on a theoretical modeling and description of the SAR-GMTI operation. In this regard, an efficient optimization of the SAR-GMTI mission can be accomplished for a given set of mission requirements.

Fig. 3.8 depicts a high-level description of this performance tool, where the input parameters and specifications are based on data structures (loaded to a bus for their exchange), profiting from the same definitions considered in the raw data simulator. A similar conceptual architecture to the MSARRDS has been defined. Three main input blocks can be distinguished:

- Sensor definition: configuration parameters (frequency, number of channels, baselines, antenna type, noise factor and alike) and access range (number of beams and the related incidence angles to be operated).
- GMTI processing: technique to be selected (DPCA and EDPCA in current version), channel combination and processing bandwidths (and windowing type).
- Scenario definition:
 - Target: type (deterministic or complex Gaussian), velocity, RCS and coherence time for Gaussian target modeling.
 - Clutter: radar backscattering coefficient σ^0 , coherence time and mean surface velocity.

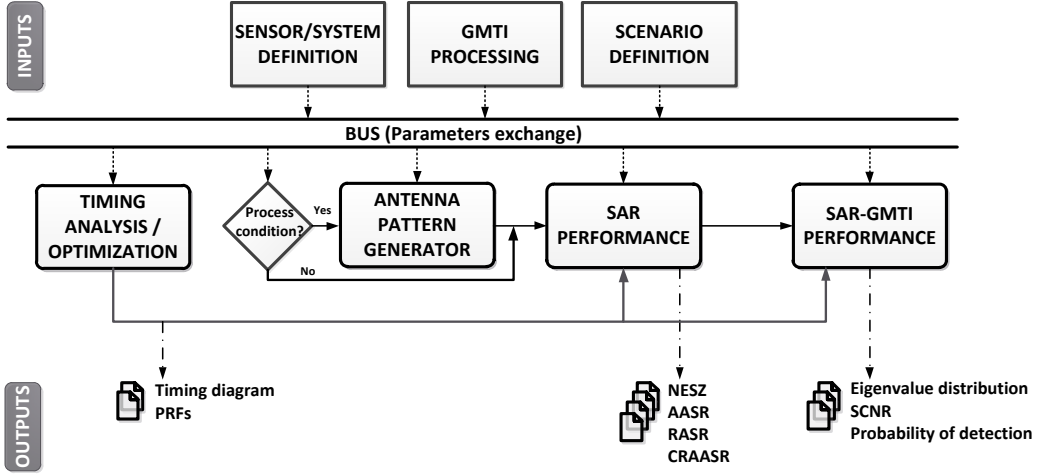


Figure 3.8: Block diagram of the MSAR-GMTI mission theoretical performance tool.

The core of the simulator is composed by three performance modules: timing analysis/optimization, SAR and SAR-GMTI performance. For a given orbit height a timing analysis (based on the diamond diagram computation) is performed to determine the selectable PRFs for the different subswaths (beams) to be operated covering the specific access range. PRF definition has a direct impact on the ambiguity performance and consequently on the SAR-GMTI performance. This information is inputted to the SAR performance module, which is in charge of computing different SAR metrics. Characterization of such metrics requires an accurate modeling of the antenna patterns for the different beams to be operated. The antenna diagrams can be obtained from the antenna pattern generator, already implemented in the raw data simulator, or loaded from external files. The SAR performance module computes NESZ, AASR, RASR and combined-range-azimuth-ambiguity-to-signal ratio (CRAASR) for the different subswaths, where the corresponding number of combined range-azimuth ambiguities to be included is a selectable parameter.

The SAR-GMTI performance module exploits the outcome of the SAR performance stage, and based on a theoretical description, provides detection metrics in terms of SCNR at the processor's output as well as probabilities of detection P_d for the different set of velocities, RCS and operational beams. It can also provide the eigenvalue distribution as a function of the incidence angle. This metric is a useful indicator of the predominant (interference) mechanism, against which the moving targets should compete.

3.4 Monte Carlo (MC) MSAR-GMTI simulator tool

The detection capabilities of any GMTI system can be statistically quantified through the probability of detection P_d . In this sense, MC simulations provide a very useful tool to asymptotically characterize this probability for specific system and scenario conditions. A flexible SAR-GMTI performance simulator tool, based on MC simulations at image level, has been implemented to provide the statistical metrics P_d and P_{fa} . This tool avoids

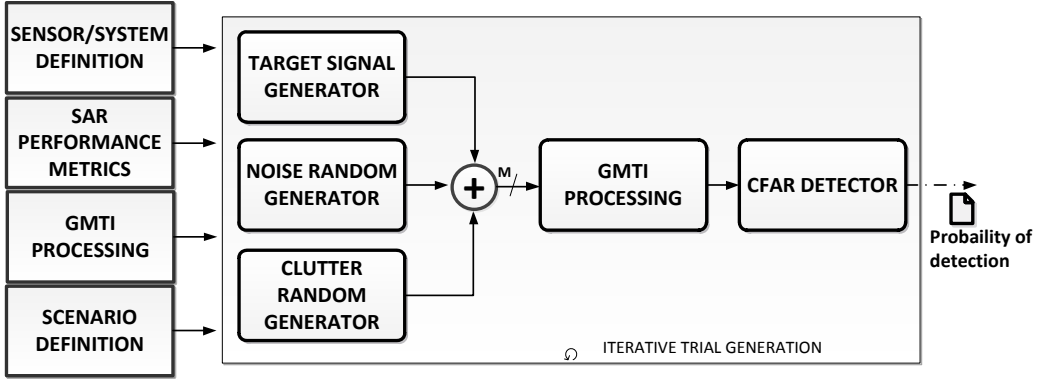


Figure 3.9: Block diagram of the Monte Carlo (MC) MSAR-GMTI performance tool.

generating and processing iteratively synthetic raw data for a given system/scenario to characterize the P_d , which otherwise could be time-consuming.

A flow chart of the MC simulator is depicted in Fig. 3.9. This flexible tool enables the analysis of any type of configuration/GMTI technique, for any given scenario definition. Range values can be specified simultaneously for up to nine different scenario parameters: RCS, ground radial velocity, target type (deterministic or Gaussian), target correlation, clutter reflectivity, clutter correlation and clutter mean velocity.

The system is defined through antenna configuration/baselines, NESZ, CRAASR, PRF and resolutions. Three different SAR-GMTI techniques are integrated in the performance tool: ATI, based on a 2D (phase-magnitude) parametric (Gaussian clutter case) CFAR detector; DPCA and EDPCA using both a magnitude-based parametric CFAR detector. It is also possible to specify a multilook processing, indicating both the number of looks to be used as well as in which looks the target is present. Then, an exhaustive data base of probability of detections can be properly parametrized for a given SAR-GMTI mission and easily extrapolated to any configuration with proper parameter scaling to avoid re-computation.

3.5 Concluding remarks

Special effort and dedication has been devoted to the definition, design and implementation of different software simulators through this doctoral activity. The development of these tools is crucial for the evaluation, analysis and proposal of an optimized SAR-GMTI mission as discussed in the next chapter. The MSARRDS is the most complete simulator among the developed ones. The potentiality of this simulator is its capability to generate multichannel SAR raw data with a realistic emulation of the acquisition process. Its modular design enables easily the integration of further updates that can provide a much more accurate and complex modeling of the SAR operation, e.g., orbital model of the platform or system dependent errors. Different from the other simulators, MSARRDS provides final SAR image products, at expense of more demanding computational cost and memory allocation.

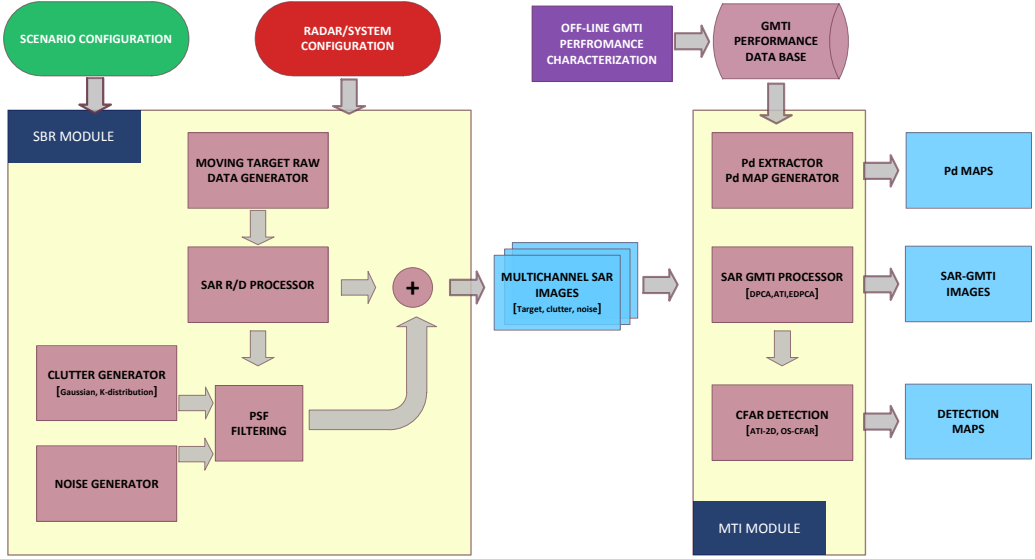


Figure 3.10: Flow chart of the simulator tool developed by the UPC team in the frame of SIMTISYS project.

The mission theoretical performance simulator and the MC based one are a perfect complement to the MSARRDS since they can be used as a forecasting tools to anticipate the capabilities of a given configuration when processed with a specific technique. The reduced computational load of the theoretical performance simulator is its most appealing characteristic. Nevertheless, its range of application is limited to the ability to theoretically define (in a closed form) the operation of a given SAR-GMTI technique under given scenario conditions. The SAR-GMTI metrics computed by the theoretical performance simulator are exploited by the MC like simulator to properly assess the operation of a given mission. The MC tool provides a complete data base of probabilities of detection sampling a wide range of different scenario parameters, avoiding the high computational cost and memory allocation of doing so with the MSARRDS. Such data base can be used to complement the information on the final SAR-GMTI products provided by the MSARRDS, i.e., indicate the expected P_d for the different detected targets on the output images.

The experience gained in the development of the different software simulation radar tools, has been exploited in the design, as a part of a team, of the SIMTISYS simulator [31]. The block diagram corresponding to the part implemented by the UPC team is shown in Fig. 3.10, where two main modules can be differentiated: first, the SBR (spaceborne radar) stage, is responsible for the generation of the synthetic multichannel SAR images, taking advantage of the basis of the MSARRDS. The second stage carries out the GMTI processing, providing SAR-GMTI synthetic images as well as detection maps, where the probability of detection is obtained from the developed off-line Monte Carlo MSAR-GMTI simulator.

4

Chapter 4

Performance evaluation of SAR-GMTI missions

THIS chapter compares current state-of-the-art SAR missions, such as TerraSAR-X (TSX) or TanDEM-X (TDX), with a new multichannel configuration based on non-uniformly displaced phase centers, intended for GMTI applications over maritime scenarios. The GMTI capabilities of the different configurations are analyzed in a three-level performance approach. The expected theoretical performance of the optimized SAR-GMTI mission is first evaluated. In a second step, an intensive numerical simulation evaluation, based on MC trials, is carried out in order to characterize the probabilities of detection under different system parameters as well as scenario conditions. Different GMTI techniques, DPCA, ATI and EDPCA, are assessed. Finally, synthetic simulated SAR data, obtained in a study case scenario, is used to demonstrate the potential improvement of the proposed multichannel configuration compared to the current SAR missions, providing subclutter visibility for maritime surveillance of small and slow moving boats¹.

¹This chapter includes figures and text fragments, sometimes verbatim, of the author's publication [JA1].

4.1 Introduction

SAR systems for remote sensing applications have been gaining special interest during the last decade, as testified by the increased number of recent and forthcoming missions: TSX, TDX, CSK, RS2, Sentinel-1 and PAZ. Some of them include an experimental mode that adds GMTI capabilities from spaceborne platforms, which allows covering the requirements on the so called *Situation Awareness*. The objective of the SAR-GMTI is to detect moving targets on the Earth surface (cars, trucks, ships,...) and focus them into high resolution synthetic aperture images. This kind of missions will provide a powerful tool to globally monitor road and maritime traffic (fisheries management, coastal and maritime security).

Single channel GMTI systems operate high PRF and narrow antenna beamwidths, limiting the detection to fast targets with strong reflectivity [68]. However, several shortcomings derive from this method especially when they are applied in spaceborne platforms, where PRF is quite restrictive in order to achieve the desired trade-off between azimuth resolution and unambiguous swath width, [23]. In single channel SAR systems there is an intrinsic ambiguity between radial velocities and azimuth location in SAR images [44]. This ambiguity problem can be solved by means of multiple receive channels, which provide improved detection capabilities thanks to the increased spatial diversity. Current SAR missions, as TSX, TDX and RS2, equipped with two parallel receivers, have limited capabilities to detect weak and slow moving targets, as could be the case of small boats in the sea. For these dual receive antenna (DRA) mode configurations, conventional SAR/GMTI processing techniques operating on the SAR processed images can be applied, based on either phase subtraction, ATI, or simultaneous phase and amplitude subtraction, DPCA.

In order to obtain adequate performance, by means of STAP, more than two receive antennas are required [44]. One way to obtain additional spatial diversity, without increasing the system complexity, is based on the use of suitable antenna switching and toggling modes [45]. These kinds of approaches imply an antenna effective area reduction, resulting in a degradation of the SNR and increased PRF requirements to reduce azimuth ambiguities [15, 45].

The evolution to multichannel approaches based on the deployment of SAR constellations could provide better performances (angular and Doppler resolutions) thanks to extended apertures. Two different GMTI strategies can be followed: (i) a coherent GMTI processing, where moderate baselines (a few hundreds of meters) with highly overlapping antenna footprints are required, [27, 54]; (ii) an incoherent GMTI processing, where the train of satellites' temporal gap can vary from seconds up to minutes, [47]. In the latter case, sub-clutter detection is not possible as the critical baseline separations, [27], have been overcome and hence neither of the coherent processing techniques exploiting multichannel configurations can be used. Therefore, coherently operating constellations permit large but sparse antenna apertures and so potential GMTI improvement. However, such configurations suffer from a high number of grating lobes, creating numerous blind velocities. Moreover, the technological complexity and cost of maintaining a constellation of satellites is rather high. From these considerations, the current chapter comparatively evaluates an architecture based on a multichannel monostatic satellite with non-uniformly spaced phase centers, briefly discussed in [135]. The goal of this mission

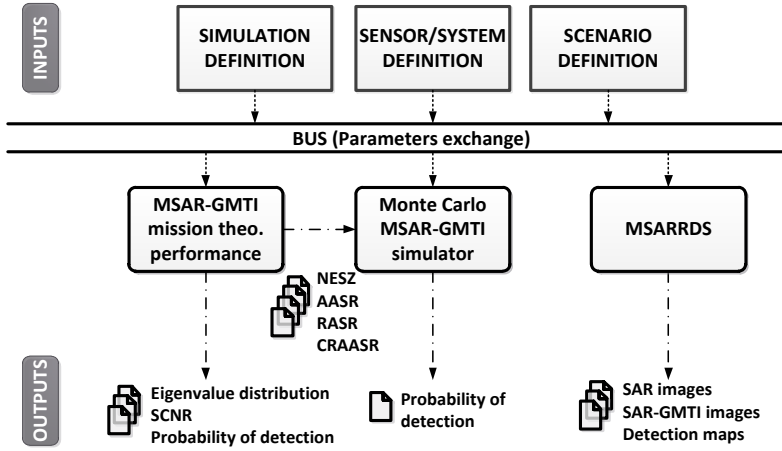


Figure 4.1: Block diagram of the simulation environment used in the SAR-GMTI mission performance evaluation.

is to provide sub-clutter visibility for maritime surveillance of small slow moving boats. This optimized multichannel configuration in combination with the new optimum GMTI processing techniques, such as ISTAP and EDPKA, is expected to provide improved SAR-GMTI performance [28, 29].

The objective of this chapter is the GMTI performance evaluation of the current state-of-the-art SAR missions in comparison to the proposed multichannel configuration. GMTI capabilities are analyzed and characterized in terms of probability of detection, based mainly on intensive numerical simulations (MC) at image level, which are complemented with processed (simulated) synthetic raw data. Fig. 4.1 shows a high-level description of the simulation environment used in the performance evaluation of the different configuration-techniques: the three simulation tools presented in Chapter 3 have been considered.

The theoretical SAR-GMTI capabilities are mainly based on the derived data model presented in section 2.3. Through the chapter a Gaussian-like model for the sea clutter is assumed. Nevertheless, and as it has been verified with experimental TSX data over maritime scenarios (see chapter 6), this hypothesis breaks down depending on system, acquisition geometry and sea conditions. It has been observed that in some cases K-distribution provides a good fitting on the sea clutter magnitude at SAR image level. In this sense, and for analysis completeness, additional processed simulated raw data results are included when considering a non-Gaussian sea clutter based on K-distribution.

It is clear that the scope of the new optimized SAR-GMTI mission is to detect small and slow moving targets. However, from an operational point of view in maritime surveillance applications great interest is reserved to the detection of small boats with high-speed and complex motion. In this very case, and as briefly discussed in section 2.2, high induced target dynamics could produce severe degradation in the imaging quality (defocusing and smearing); but more importantly a reduction on the effective SCNR, which, could ruin

the detection performance, if target dynamics are not properly accounted for in the processor. A preliminary study on the impact of SAR imaging high-speed boats (with large vertical and horizontal accelerations) has been also carried out using simulated raw data. To this end a complete SAR-GMTI processing chain has been implemented, integrating a matched filter bank (MFB) based on an adaptive RD processor, as proposed in section 5.2.1 for real data. The aim is to demonstrate that the proposed SAR-GMTI mission in combination with an appropriate processing strategy will be able to detect also this high-speed moving targets. Therefore, high-resolution images of the moving vessels can be obtained, as validated with airborne real data in section 5.2.1, of key importance for post-processing recognition/classification purposes.

Three SAR-GMTI processing techniques operating directly on SAR images have been considered in the performance evaluation: the classical DPCA and ATI for dual-channel systems and the new promising adaptive EDPCA technique. Clutter homogeneity plays an important role in the estimation of the interference covariance matrix performed by ISTAP and EDPCA, and so directly affects the GMTI performance. In this sense, the EDPCA processing is preferred on maritime scenarios since it operates at image level, allowing selection and processing of homogeneous patches. Moreover, the performance characterization of the ISTAP via MC simulations would require its evaluation in the range-Doppler domain, leading to a computationally much more costly approach compared to the efficient one presented in section 3.4, which operates at image level. Both ISTAP and EDPCA provide the same GMTI performance when the DPCA condition is fulfilled; otherwise, ISTAP gives improved results as pointed out in [28].

4.2 Mission analysis

4.2.1 Multichannel configurations

State-of-the-art SAR missions, as TSX, RS2 and TDX, equipped with two receivers, have limited GMTI capabilities to detect slow moving targets, due both to a reduced number of channels and to the short baselines (2.4 m one way) that determine the minimum detectable velocity (MDV). The deployment of coherently operating SAR constellations, as TDX, provides improved performance in terms of Doppler (velocity) and angular resolution, but at the expense of a reduced range of unambiguous velocities (1.4 m/s), caused by the longer baselines (around 200 m). In maritime scenarios, where sea coherence time could reach tens of milliseconds [83, 84], depending on the sea conditions, the channel coherence (for the longer baseline) could drop off dramatically, and so would the capability of clutter rejection. Therefore, a trade-off solution, is to consider a monostatic multichannel configuration with non-uniformly spaced receivers, taking advantage from baseline diversity to ensure high sensitivity to slow moving targets (with the largest baseline), and simultaneously alleviating the Doppler ambiguities (with the shorter ones); in a way that channel coherence could be kept high enough to ensure proper detection capabilities.

From these considerations, a three-channel configuration is proposed, where the two external antennas are deployed using a telescopic boom, as originally suggested in [135], and an unfolding system, respectively. The number of channels has been selected to limit the system complexity and at the same time to fulfill the required degrees of freedom

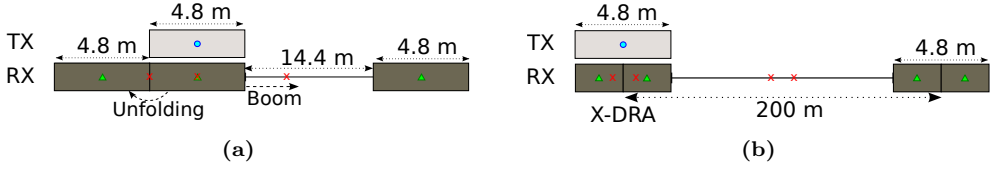


Figure 4.2: Schematic representation of the different configurations to be analyzed: (a) proposed Boom configuration and (b) Tandem (two flying X-DRA satellites); transmit (TX) phase center denoted by the solid circle, receive (RX) by the triangle symbol and effective two-way (2-W) by the cross symbol.

driven by the eigenvalue distribution of the interference covariance matrix, as discussed in section 4.2.2. The length of the boom has been selected to deliver a probability of detection (P_d) close to one for a 1 m^2 RCS target, whose ground range velocity is greater than 5.5 m/s when processing the three-channel data cube with EDPKA. The boom length is a multiple of the antenna length assuming a telescopic structure will be used for deployment. The system operates in X-band, equipped with a configurable 4.8 m -length phased-array antenna, with 32×12 transmit receive modules (TRMs). The main radar mission parameters, similar to TSX, are summarized in Table 4.1. From now on the proposed configuration will be referred as Boom system, and its SAR-GMTI performance will be compared against two different systems that emulate current state-of-the-art SAR missions: a 4.8 m -length single satellite operating in DRA mode (2.4 m per receiver), named as X-DRA; and a Tandem configuration, where two X-DRA fly in formation (only one TX)² with a baseline of 200 m , as schematically represented in Fig. 4.2b. At this point it must be noted that perfect time and frequency (coherence) synchronization between the two satellites is assumed. It is well known that TSX and TDX do not fly in a train-like configuration but rather in a HELIX formation [55] and hence there is an across-track baseline coupled with the along-track of interest. In this sense, it is assumed that the across-track baseline could be perfectly compensated (or coregistered), [48].

4.2.2 SAR-GMTI expected performance

An orbital height of 514 Km has been selected to ensure an incidence range coverage from 14 - 60 degrees (swath ground extension of 640 Km), intended to be covered with 27 subswaths, whose extension is in the order of 30 Km . PRF is a key parameter in the operation of any SAR-GMTI mission: from the GMTI operation point of view, the highest PRF possible is required to ensure that the fastest ground velocity to be detected is not ambiguous. However, the higher the PRF, the smaller the unambiguous (range) swath extension.

Fig. 4.3 shows the timing (diamond) diagram as a function of PRF and incidence angle for a fixed pulse duration of $45 \mu\text{s}$, and indicates whether the echo delay is such that the signal doesn't superimpose either on the transmit instances (gray strips) or on the nadir

²In [54] Gierull refers to this configuration as *classic* coherent tandem concept, where one satellite transmits and both receive the backscattered signal simultaneously.

Table 4.1: Radar system parameters.

Parameter	Value	Units
Satellite velocity	7604.8	m/s
Spot (ground) velocity	7311.6	m/s
TX (transmit) antenna length	4.8	m
RX (receive) antenna length Boom/Tandem	4.8/2.4	m
TX/RX antenna height	0.7	m
Number of TRMs	32x12	
Carrier frequency	9.65	GHz
Peak transmitted power	2.2	KW
Polarization	HH	
Noise factor	4.3	dB
Transmitter losses	2	dB
Receiver losses	2	dB

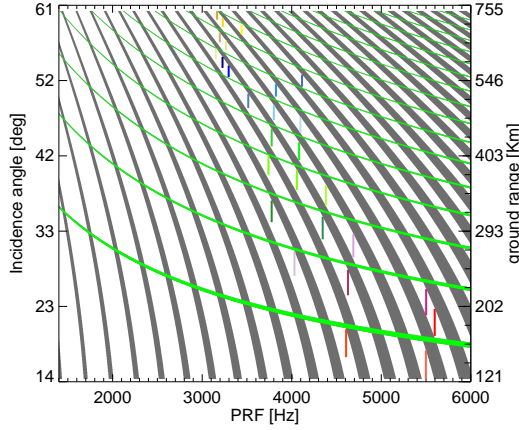


Figure 4.3: Timing (diamond) diagram for an orbit height of 514 Km and a fixed pulse duration of 45 μ s: the restrictions on the receive echo window due to transmit instances (grey strips) and nadir echoes (green strips) are shown. The extension of the 27 different subswaths for the selected PRFs is shown on top of the image as colored polygons.

returns (green strips). From beam 1-19 the highest possible PRF has been selected, while for beams 20-27 (with higher incidence angle) a trade-off between azimuth and range ambiguities level has been considered to choose the PRF. Fig. 4.4a represents the NESZ metric of the Boom system, i.e., a measure of the system's sensitivity to areas of low radar backscatter. This metric indicates the normalized radar backscattering coefficient σ^0 that provides a unitary SNR, [23]. NESZ as a function of slant range R_0 (or equivalently w.r.t incidence angle γ_0) has been computed according to the formulation in [136] like

$$\text{NESZ} = \frac{2(4\pi)^3 P_n \text{PRF}}{c_0 \lambda^2 P_{av} G_{TX} G_{RX}} \cdot \frac{N_{az} \sin \gamma_0}{\delta_{az}} \cdot \frac{1}{\left| \sum_{i=1}^{N_{az}} D_{2-w}(\theta_{0_i}, \phi_{0_i}) / R_0^2(\theta_{0_i}, \phi_{0_i}) \right|^2} \quad (4.1)$$

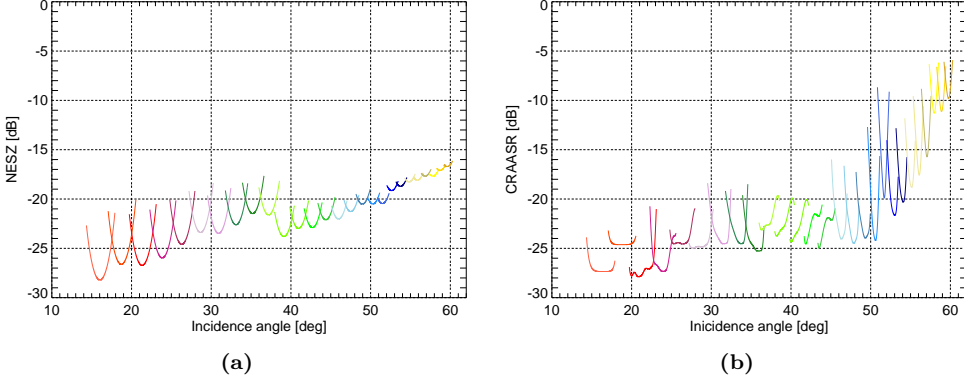


Figure 4.4: SAR performance of the proposed Boom system versus incidence angle: (a) NESZ and (b) CRAASR (the different subswaths are identified with different colors).

where P_n refers to the equivalent receiver noise power; P_{av} is the average transmitted power; G_{TX} and G_{RX} are the antenna gains in transmission and reception, respectively; c_0 represents the speed of light; λ is the carrier wavelength; δ_{az} corresponds to the azimuth resolution; and $N_{az} = \lambda R_0 \text{PRF} / 2\delta_{az}$ refers to the number of pulses coherently processed during azimuth focusing.

For the proposed system, and assuming uniform tapering on the TRMs, NESZ keeps below -20 dB for the typical SAR incidence angles of interest 20-40 degrees. However, for low-grazing angles the noise contribution increases up to -17 dB. It must be noted that the system operates with a pulse bandwidth of 150 MHz for beams 1-10 and half of it for the rest of the subswaths to reduce the NESZ.

As described in section 2.3.2, and noted in [26] and [45], the contribution of the ambiguous clutter returns should be taken into consideration as they play an important role in the SAR-GMTI performance: the residual coregistration error on the ambiguities, as denoted by the second term in (2.13), when the DPCA condition does not hold, produces additional eigenvalues different from the noise floor, and therefore more RX channels are required to cancel out both unambiguous and ambiguous clutter patches, [29]. Moreover, temporal decorrelation of the sea clutter returns, present also in the ambiguous patches, could produce additional eigenvalues different from the noise level. These impacts depend in turn on the level of ambiguous returns w.r.t. the main clutter, as modeled by the new CRAASR metric, defined in (2.15).

Fig. 4.4b shows the CRAASR for the boom system as a function of the incidence angle, considering a processing kaiser window (coefficient 2.5) with processing bandwidths of 2.8 KHz in azimuth and the (subswath dependent) pulse bandwidth in range. The first 440 combined ambiguities have been included in the computation of CRAASR, which keeps below -20 dB for the range of interest (20-40 degrees incidence angle). The ambiguities' impact increases substantially for beams with high incidence angle (above 50 degrees), mainly due to range ambiguities. Assuming the ambiguous clutter returns have the same σ^0 as the main patch (close to the noise level for those incidence angles)³, the impact of

³Sea clutter backscattering decreases as a function of the incidence angle as verified by real data analysis of the estimated σ^0 , refer to section 6.6.1.

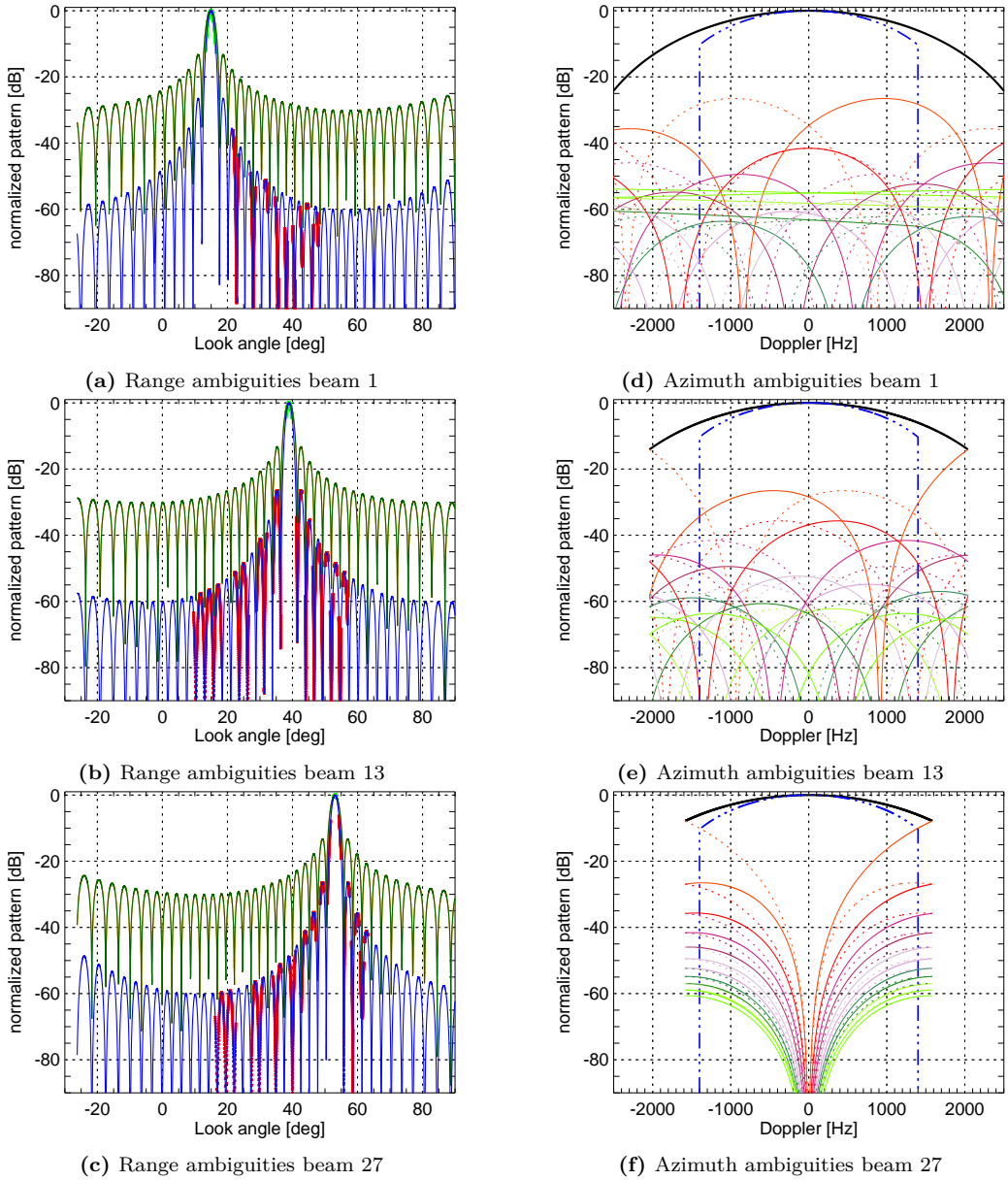


Figure 4.5: Elevation pattern and Doppler spectrum weighting on range (left) and azimuth ambiguities (right): (a)-(c) antenna elevation impact on the range ambiguities for beams 1, 13 and 27 (TX and RX elevation pattern in green, 2-W in blue, signal of interest as light green strips and range ambiguities as red strips); (d)-(f) Doppler spectrum impact on the azimuth ambiguities for beams 1, 13 and 27 (main Doppler spectrum as solid black line, processing window as dash-dot-dot blue line and different ambiguities' spectral contribution in a color dependent variation from red to yellow - solid lines correspond to positive order ambiguities and the dotted ones to negative orders).

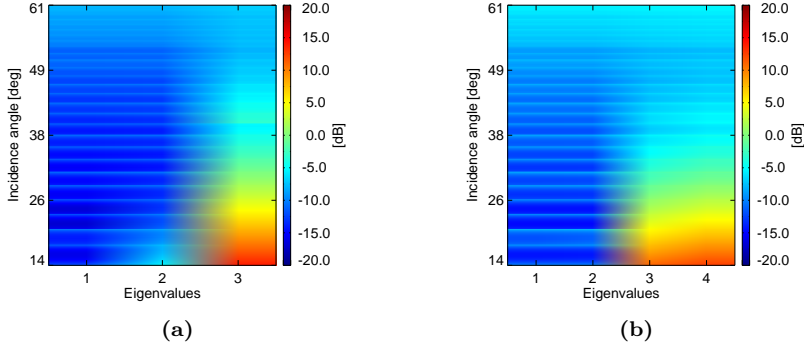


Figure 4.6: Eigenvalue distribution for a Gaussian sea clutter with 10-ms coherence time, assuming a sea state 4 under the σ^0 NRL model: (a) Boom and (b) Tandem configurations.

the ambiguities gets masked by the noise floor.

Fig. 4.5 depicts the weighting of both the elevation pattern and the Doppler spectrum on the range and azimuth ambiguities, respectively, for near (beam-1), middle (beam-13) and far (beam-27) incidence angle regions. From Figs. 4.5a-c it can be clearly appreciated how the range ambiguities are getting closer to the main lobe of the antenna as the range (incidence angle) increases. Analogously, the impact of azimuth ambiguities in the Doppler domain is represented in Figs. 4.5d-f, where the main clutter patch spectrum is represented by a solid black line and the processing window by a dash-dot-dot solid blue line. The different Doppler ambiguities' spectral contribution are depicted in a color dependent variation from red to yellow, where solid lines correspond to positive order ambiguities and the dotted ones to negative orders.

Fig. 4.6a and Fig. 4.6b show the eigenvalue distribution of interference covariance matrix \mathbf{R}_q , modeled in (2.11), as a function of the incidence angle for the Boom and Tandem configurations, respectively. This kind of chart is a useful tool to understand how both system design and environmental scenario conditions impact on interference distribution and characterization as a function of the incidence angle, providing a picture on the predominant type of mechanism, against which moving targets should compete. The eigenvalue distribution has been used as performance evaluation tool for STAP-like techniques as described in [13, 29].

If the only source of decorrelation is the noise (no ICM is present), the DPCA condition is closely fulfilled and sufficient CNR is available, a single dominant eigenvalue different from the noise floor is present. This means that clutter occupies only the space spanned by the eigenvector associated to the largest eigenvalue. Then, only two channels are required to cancel out both the main clutter and its related ambiguities. In case the dominant mechanism is noise (flat eigenvalue distribution), the additional gain (in terms of SCNR) is provided by the coherent combination of the channels, i.e., an improvement factor (IF) equal to the number of channels. Two different situations can produce leakage of the clutter into eigenvectors different from the one related to the predominant eigenvalue: coregistration mismatch on the ambiguities produces a residual phase error (when DPCA condition is not fulfilled) that translates into additional eigenvalues; clutter decorrelation, which depends on the scenario itself due to ICM and on the baseline

configuration, produces the same effect, such that in the limit a complete decorrelation between the different channels will lead to a noise-like dominant mechanism. In this sense, the eigenvalue distribution can help complementing the SAR-GMTI mission performance, since it can be used as a forecast mechanism to understand the limitations of the proposed system for given scenario conditions.

In Fig. 4.6 a Gaussian-like sea clutter with a 10-ms coherence time and a normalized radar reflectivity σ^0 obtained from the NRL model for a sea state 4 (Beaufort scale) has been considered⁴. For Boom configuration, Fig. 4.6a, and incidence angles between 14 and 40 degrees, there is a predominant eigenvalue, such that two receiving channels are sufficient to cancel out the clutter and its ambiguities. For higher incidence angles, noise contribution masks clutter response (the three eigenvalues are similar). Comparatively, for Tandem, Fig. 4.6b, two predominant eigenvalues are present due to the major impact of clutter decorrelation, [13], induced by the longer baseline configuration. SAR-GMTI techniques at image level require channel coregistration, by means of a time-shift related to the baseline time-delay $\tau_{i,j}$, such that they observe the scene from the same position but at different instants of time. During this time frame sea has evolved, and so clutter returns have decorrelated from a statistical standpoint. For the longest baseline separation and 10-ms coherence time, sea clutter coherence drops off to values around 0.15, according to (2.9). This translates directly into a GMTI performance degradation, as pointed out by the theoretical and simulation results.

SCNR is a good indicator of the system detection capabilities: maximizing SCNR results in a maximized probability of detection P_d . Fig. 4.7 and Fig. 4.8 show SCNR at EDPCA processor's output for Boom and Tandem configurations, respectively. These maps⁵ represent the distribution of SCNR as a function of incidence angle and ground range velocity v_z for different scenario conditions (no clutter decorrelation and 10-ms coherence time).

In Fig. 4.7a, where a deterministic target and no clutter decorrelation have been assumed, the EDPCA SCNR for the Boom system is plotted. In the computation of this theoretical SCNR it has been assumed that the SAR processing has been perfectly adapted to the moving target. For incidence angles below 38 degrees, a notch around the zero-radial velocity can be recognized, not present for higher incidence angles since the thermal noise starts to be the dominant interference contributor, in accordance to the eigenvalue distribution in Fig. 4.6a. When compared to Fig. 4.7b, assuming a 10-ms sea clutter coherence time, there is a SCNR degradation, especially visible in the small incidence angle region, where clutter's contribution is higher. In this region it can also be noticed that the notch around zero velocity is wider⁶ compared to Fig. 4.7a, and so the system is less sensitive in the range of slow velocities.

Analogously, Fig. 4.8 illustrates the EDPCA SCNR for Tandem configuration. As expected, there is a sharper notch along the zero ground range velocity due to the longer composite aperture, which in turn creates an undesired grid of detection holes (blind

⁴From now on this scenario corresponds to the reference one used through the chapter for comparative purposes.

⁵The edge-like effects along the incidence angle are related to beam transitions (superposition between beams is not represented).

⁶The widening effect on the main notch as the incidence angle decreases is due to the lower radial velocity component (line-of-sight projection of v_z).

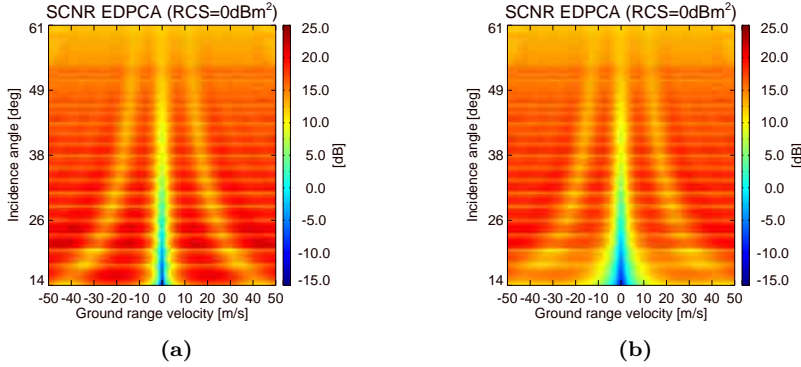


Figure 4.7: Boom-SCNR maps (as a function of incidence angle and ground range velocity) for EDPKA processing assuming a deterministic target and different clutter correlations: (a) no clutter decorrelation and (b) 10-ms clutter coherence time (sea state 4 under σ^0 NRL model and target with 0 dBm² of RCS).

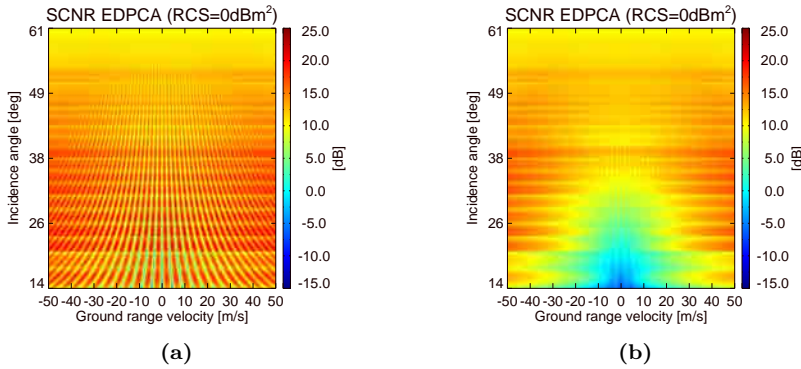


Figure 4.8: Tandem-SCNR maps (as a function of incidence angle and ground range velocity) for EDPKA processing assuming a deterministic target and different clutter correlations: (a) no clutter decorrelation and (b) 10-ms clutter coherence time (sea state 4 under σ^0 NRL model and target with 0 dBm² of RCS).

velocities), as observed from Fig. 4.8a for the case where no clutter decorrelation is present. From Fig. 4.8b a substantial degradation is observed in the case of considering a 10-ms clutter coherence time and so the gain in sensitivity to slow moving targets is lost, as predicted from the eigenvalue distribution chart in Fig. 4.6b.

In Fig. 4.9, SCNR cuts as a function of ground range velocity and at beam center of subswath 8 are represented for different system-technique combinations, assuming the two scenario conditions considered in Fig. 4.7 and Fig. 4.8. The input single channel SCNR for the different missions is also reported whose values are around 6-7 dB.

From now on, the comparative performance analysis is considered for a given set of system-technique combinations: classical (two-channel) GMTI techniques, such as DPCA and ATI, are presented only for X-DRA system, showing the available capabilities for the current state-of-the-art SAR-GMTI missions with two RX channels; the optimum (>two RXs) EDPKA technique is considered for Boom and Tandem configurations to

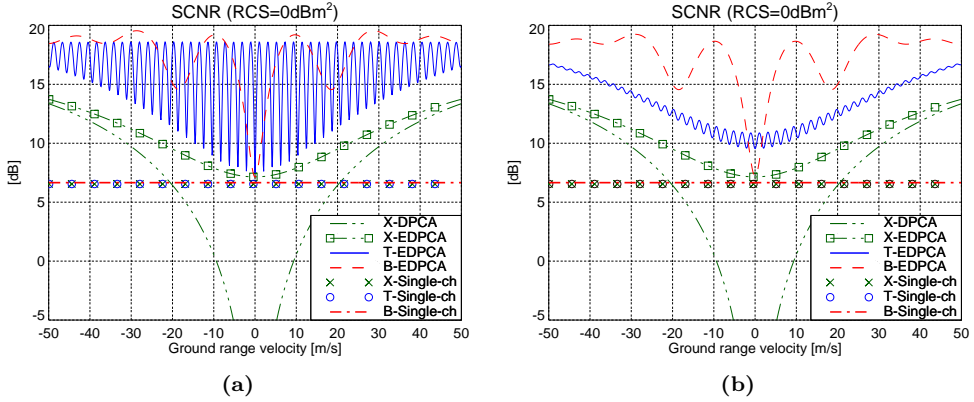


Figure 4.9: SCNR as a function of ground range velocity at beam center of subswath 8 (γ_0 of 33.17 degrees) assuming a deterministic target (RCS of 0 dBm²) and sea state 4 (σ^0 NRL model) Gaussian clutter with different correlations: (a) no clutter decorrelation and (b) 10-ms clutter coherence time (X refers to X-DRA system, T and B to Tandem and Boom configurations, respectively).

demonstrate the potentiality of oncoming SAR-GMTI architectures.

For the ideal non-realistic scenario conditions, Fig. 4.9a, with no sea decorrelation, Tandem system with EDPCA processing provides the highest sensitivity to slow moving targets, but at the expense of a higher number of secondary notches. Nevertheless, when considering realistic operations, see Fig. 4.9b, assuming a 10-ms sea coherence time, Tandem experiences a severe degradation. Processing with EDPCA the data cube of the proposed Boom system (dash red line) provides improved SCNR when compared to DPCA and EDPCA techniques applied to the X-DRA system, dash-dot-dot green lines with and without square markers, respectively. The proposed Boom system proves improved detection capabilities, being more robust to clutter induced decorrelation effects, compared to Tandem system. The corresponding EDPCA SCNR (solid blue line) has a similar trend as X-DRA but with a mean SCNR 3 dB higher thanks to the two additional DoF. At this point it must be also noted that for $v_z = 0$ m/s and Tandem configuration the EDPCA SCNR IF with respect to the single channel case (denoted by the blue circle markers) is around 3 dB, and better than the Boom configuration case. It can be theoretically demonstrated that for $v_z = 0$ m/s, and in the limit of zero clutter coherence between the different channels, IF tends to the number of channels M , since in this case clutter has no spatial structure and behaves like noise. As the worst clutter coherence is 0.15 according to (2.9) for the longest baseline and a 10-ms clutter coherence time, IF is expected to be lower than M .

To complement the theoretical analysis, the EDPCA SCNR for different variations of the proposed Boom configuration is reported in Fig. 4.10 as a function of the across-track ground velocity. Apart from the considered Boom architecture (solid red line), three alternatives are analyzed: the first two (blue asterisk and green diamond solid lines) have the same configuration as the Boom system but with a mast length of 28.8 m and 57.6 m, respectively; the third system (black circles solid line), referred as XDB, is a Boom configuration where the two first channels are X-DRA like (2.4 m separation and no unfolding)

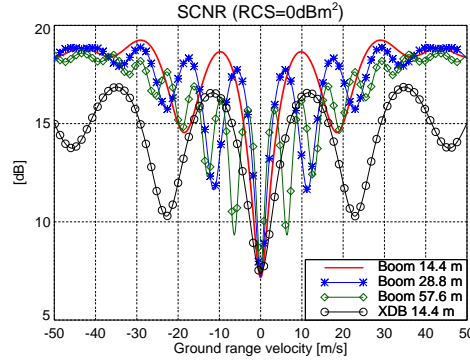


Figure 4.10: SCNR as a function of ground range velocity (at center of subswath 8) for EDP-CA technique considering different variants of the Boom configuration, assuming a deterministic target (RCS of 0 dBm²) and a sea state 4 (σ^0 NRL model) Gaussian clutter with 10-ms coherence time; XDB corresponds to a Boom configuration where the two first channels are X-DRA like (2.4 m separation with no unfolding) and the third one (2.4 m antenna length) is located on a 14.4 m mast.

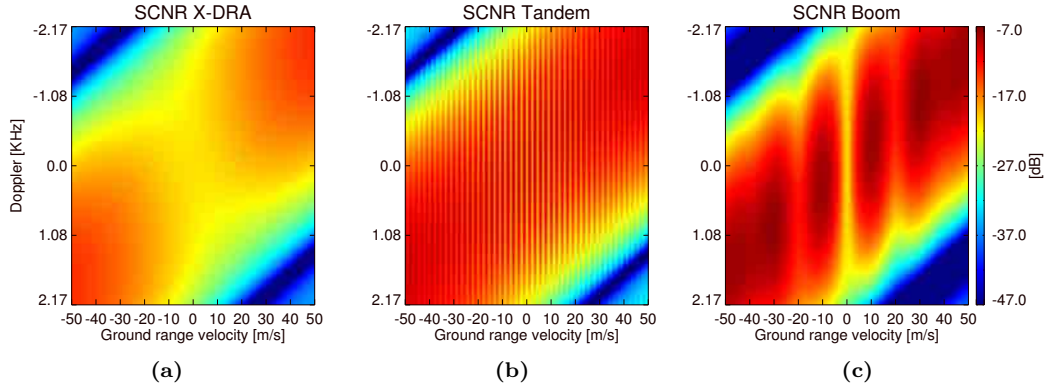


Figure 4.11: Post-Doppler STAP SCNR for system configurations in Fig. 4.2 with radar parameters defined in Table 4.1: (a) X-DRA configuration, (b) Tandem and (c) Boom; deterministic target with RCS of 0 dBm² and a sea state 4 (σ^0 NRL model) Gaussian clutter with no temporal decorrelation are assumed.

and the third antenna is deployed with a mast of 14.4 m. The proposed configuration (red solid line) provides an overall improved SCNR compared to the alternative systems. Increasing the mast separation allows a slightly narrower notch response (around zero velocity), at the expense of additional steeper secondary notches. Moreover, there is a progressive degradation in the SCNR peaks due to clutter decorrelation higher impact. For XDB a generally reduced SCNR is observed since the antenna dimensions are half of the Boom architecture. Secondary notches, much steeper, are located at slightly higher velocities because of effective shorter baselines.

To give some insight in the operation of STAP-like algorithms, the SCNR at the output of a post-Doppler STAP (as in ISTAP) is represented in Fig. 4.11 as a function of the target's ground range velocity (v_z) and the Doppler frequency (at which the target

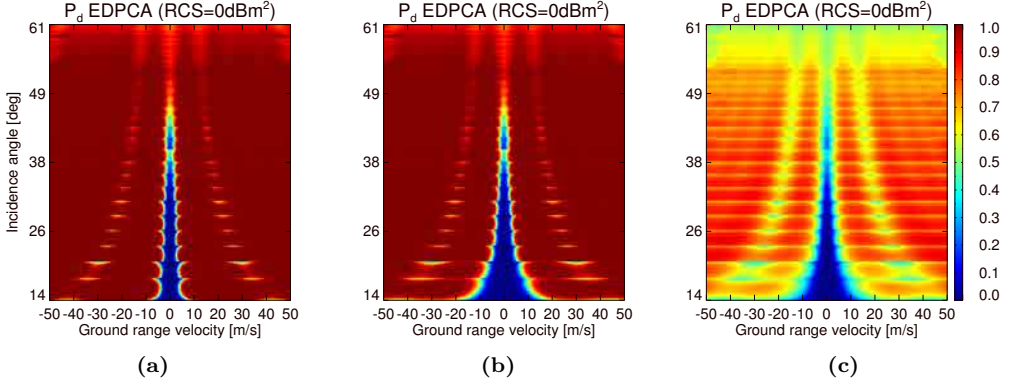


Figure 4.12: Boom P_d map (as a function of incidence angle and ground range velocity) for EDPCA processing under different scenario conditions: (a) deterministic target with no clutter decorrelation; (b) deterministic target with 10-ms clutter coherence time and (c) Gaussian target with 10-ms clutter coherence time (sea state 4 under σ^0 NRL model and target with 0 dBm² of RCS).

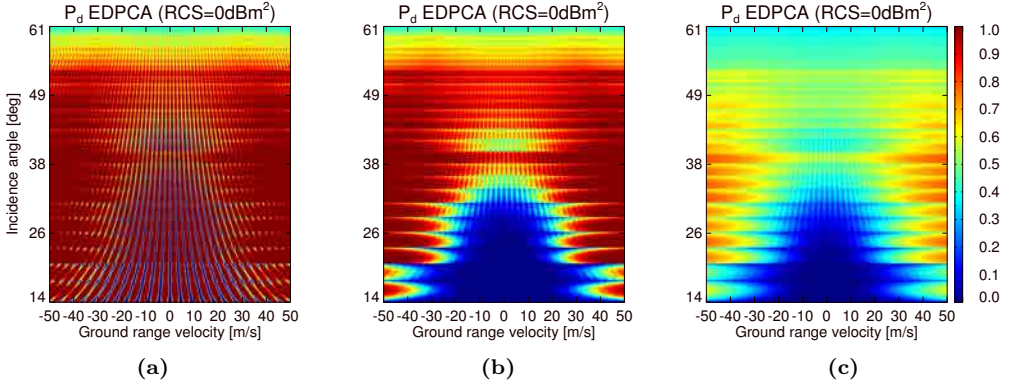


Figure 4.13: Tandem P_d map (as a function of incidence angle and ground range velocity) for EDPCA processing under different scenario conditions: (a) deterministic target with no clutter decorrelation; (b) deterministic target with 10-ms clutter coherence time and (c) Gaussian target with 10-ms clutter coherence time (sea state 4 under σ^0 NRL model and target with 0 dBm² of RCS).

is detected) for the different configurations. This SCNR has been computed according to the model presented in (2.24). No decorrelation of the Gaussian sea clutter has been considered. As expected, the STAP filter forms a notch along the clutter trajectory at $v_z = 0$. Comparatively, the Tandem configuration provides the steeper main notch, i.e., higher sensitivity to slow motion, with increased number of blind velocities. In this sense, the proposed Boom configuration shows a good compromise between ambiguous velocities and sensitivity to slowly moving targets with an improved SCNR (before azimuth focusing) for a much greater extent in the Doppler-velocity plane (ideally a complete dark-red plane would be desirable). As the synthetic aperture is formed the target and clutter pass through the beam and the corresponding directions and slant ranges vary and consequently the directing cosine of the related ambiguous clutter. In this case, the SCNR

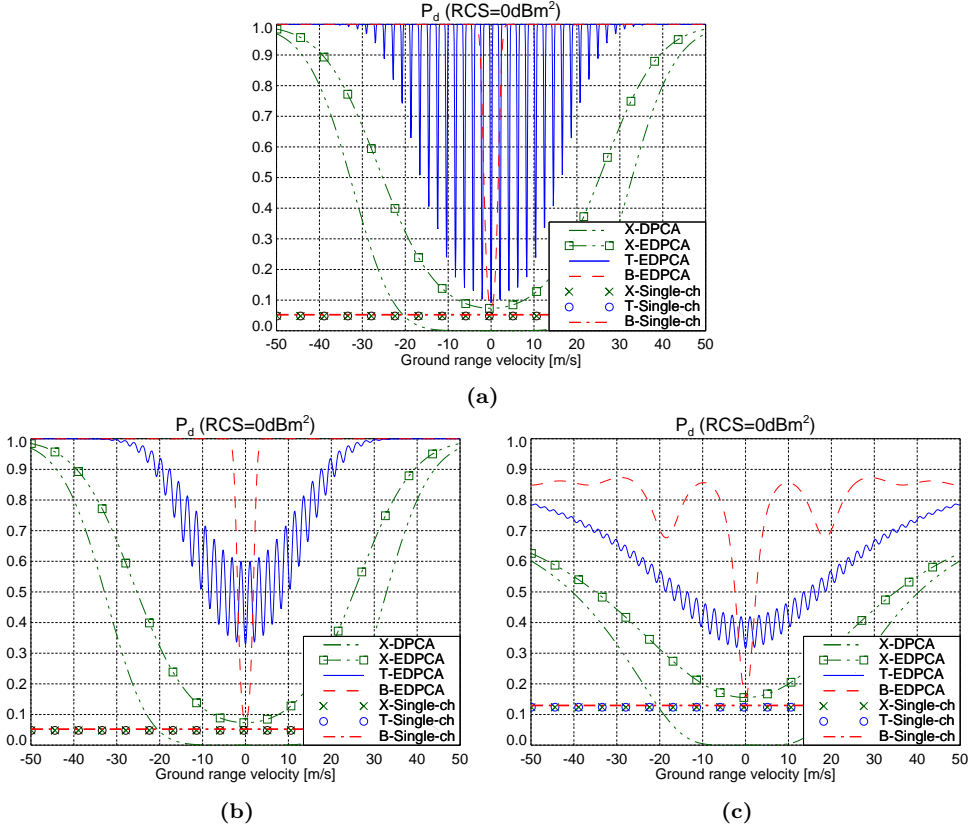


Figure 4.14: P_d as a function of the ground range velocity for different system-technique combinations at beam center of subswath 8 (33.17 degrees) and for different scenario conditions: (a) deterministic target with no clutter decorrelation; (b) deterministic target with 10-ms clutter coherence time and (c) Gaussian target with 10-ms clutter coherence time (sea state 4 under σ^0 NRL model and target with 0 dBm² of RCS).

would correspond to the integration of the one in (2.24) along the Doppler frequency, once an appropriate adaptive SAR processing (to the moving target of interest) is performed, similar to the ISTAP operation [28].

Analogous to the SCNR maps presented in Fig. 4.7 and Fig. 4.8, probability of target detection P_d charts can also be theoretically obtained as shown in Fig. 4.12 and Fig. 4.13 for Boom and Tandem configuration, respectively, when processed with EDPCA. P_d has been theoretically computed considering CFAR detectors ensuring a P_{fa} of $1 \cdot 10^{-5}$ for different scenario conditions: Fig. 4.12a and Fig. 4.13a consider a deterministic target model with no clutter decorrelation; Fig. 4.12b and Fig. 4.13b show the reference scenario results (deterministic target and 10-ms clutter coherence time); and a worse case scenario is assumed in Fig. 4.12c and Fig. 4.13c, where a Gaussian target model (completely correlated) and 10-ms coherence time have been considered. The different trends on the P_d maps can be easily extrapolated from the SCNR results. Generally speaking, Boom mission with EDPCA processing provides better detection capabilities all over the range

of incidence angles (14-60 degrees) and for the different scenario conditions, especially when some sea clutter decorrelation is assumed. For the worse case scenario, where the target is modeled as complex Gaussian process and considering a 10-ms clutter coherence time, the detection capabilities are degraded for both configurations, with Boom EDPCA outperforming Tandem architecture.

For analysis completeness and to show the improved SAR-GMTI performance obtained with the proposed Boom configuration, P_d cuts as a function of v_z at beamcenter of subswath 8 ($\gamma_0 = 33.17$ degrees) for different system-technique combinations and scenario conditions are reported in Fig. 4.14. Boom architecture with EDPCA technique provides in general a better P_d for realistic scenario operation when compared to the rest of system-technique combinations. When considering a Gaussian target modeling, Fig. 4.14c, a lower average P_d is obtained with a flatter response as a function of the ground range velocity. Nevertheless, it must be noted that for $|v_z| < 20$ m/s, where P_d is below 0.3, target randomness provides slightly improved performance compared to the deterministic target, which is easily recognized for DPCA and EDPCA with X-DRA as well as for the single-channel detection performance.

Table 4.2: Monte Carlo (MC) simulation parameters.

Parameter	Value	Units
RCS	-10 to 20	dBm ²
v_z	0 to 50	m/s
Target type	Deterministic/Gaussian	-
Target correlation	-/10	ms
Sea state	4	-
Clutter correlation	-/10	ms
Mean clutter velocity	0.0	m/s
γ_0 (incidence angle)	33.17	deg
MC trials	$5 \cdot 10^6$	-
P_{fa}	$1 \cdot 10^{-5}$	-
Looks	1/4	-
Looks per target	1/4	-

4.3 Simulation results: performance evaluation

In this section the theoretical performance of the proposed boom system is validated through simulation results. As depicted in the simulation environment (see Fig. 4.1), two different methodologies are considered: first, intensive Monte Carlo (MC) simulations are carried out to obtain the probabilities of detection; in a second step, and complementing the MC approach, multichannel synthetic raw data sets, generated using the MSARRDS simulator tool, are processed for the different configurations and techniques.

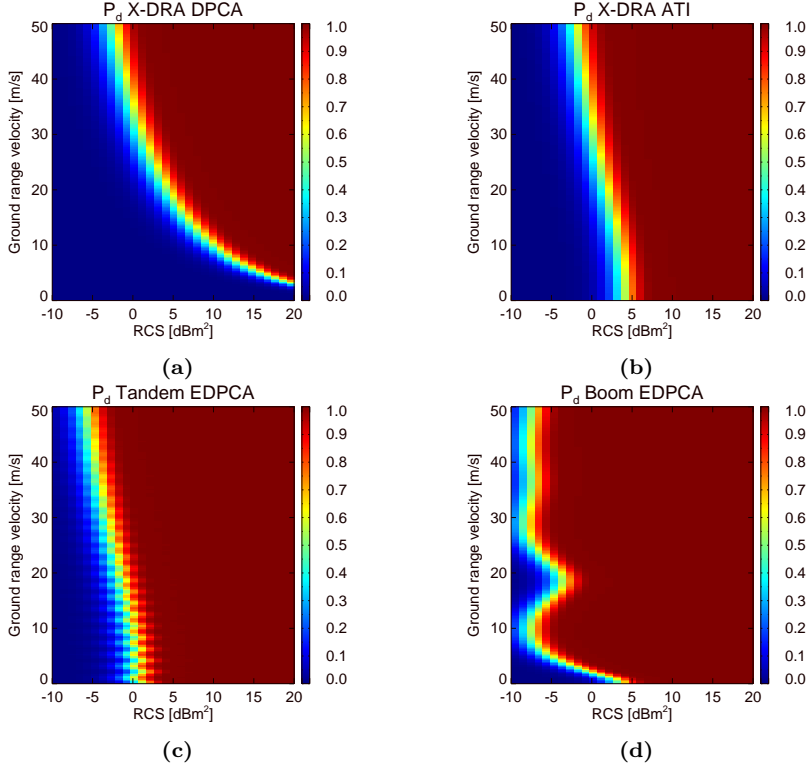


Figure 4.15: P_d maps (as a function of RCS and ground range velocity) obtained from MC simulations assuming a deterministic target model (RCS of 0 dBm²) and a Gaussian-like sea clutter (sea state 4 under σ^0 NRL model) with 10-ms coherence time: (a) X-DRA DPCA, (b) X-DRA ATI, (c) Tandem EDPCA and (d) Boom EDPCA.

4.3.1 Monte Carlo (MC) approach

For the MC simulations presented in this section some hypothesis have been assumed: (i) clutter is a zero-mean complex Gaussian process with given spatial (along different channels) correlation properties; (ii) SAR processing has been adapted to the target kinematic parameters⁷; (iii) the residual phase error (due to coregistration mismatch) defined by the second term of (2.13) has been included for the first 440 combined range-azimuth ambiguities; and (iv) the target (either deterministic or Gaussian) is correlated from look to look, while clutter has been assumed uncorrelated. Table 4.2 summarizes the different parameters of the MC simulations considering the center of subswath 8 with an incidence angle of 33.17 degrees.

Fig. 4.15 shows probability of detection maps as a function of RCS and ground range velocity for different system-techniques combinations, when considering a deterministic target and 10-ms clutter coherence time (with no multilook processing). Boom system in combination with EDPCA, Fig. 4.15d, provides improved performance compared to the rest, especially in the region of slow and low reflectivity moving targets. DPCA technique

⁷Discussion about SAR focusing mismatch on fast moving boats is considered in 4.3.2.

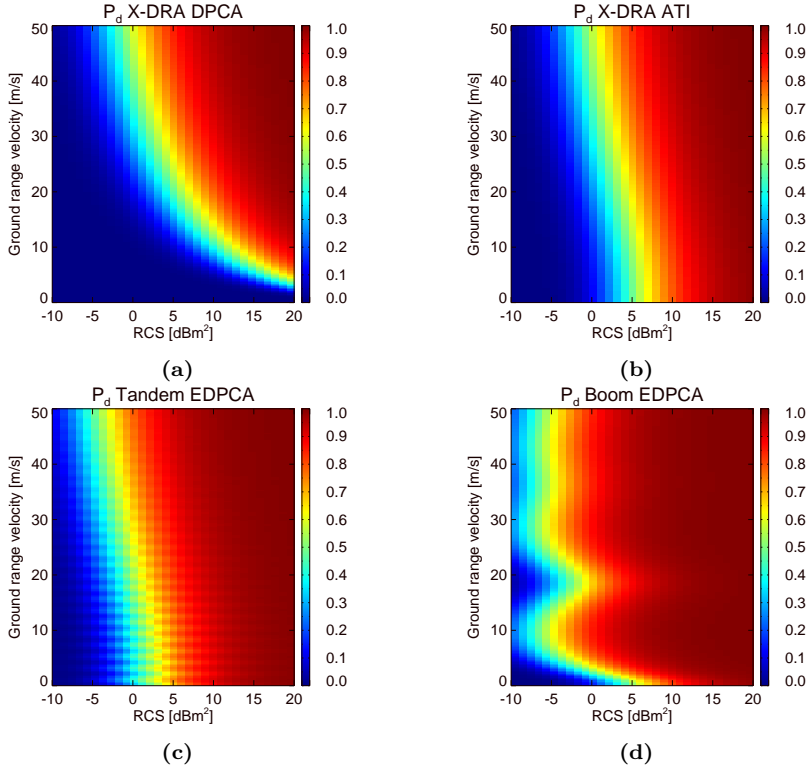


Figure 4.16: P_d maps (as a function of RCS and ground range velocity) obtained from MC simulations assuming a Gaussian target model (RCS of 0 dBm²) and a Gaussian-like sea clutter (sea state 4 under σ^0 NRL model) with 10-ms coherence time: (a) X-DRA DPCA, (b) X-DRA ATI, (c) Tandem EDPKA and (d) Boom EDPKA.

applied to X-DRA data shows the worst P_d in this region, Fig. 4.15a. However, the joint 2D phase-magnitude ATI detector on the X-DRA system, Fig. 4.15b, gives comparatively a better performance, close to the EDPKA applied to Tandem system, Fig. 4.15c, where the induced higher clutter decorrelation is the driven parameter; but still EDPKA on Tandem has a threshold RCS, approximately 5 dB below the ATI case. In Fig. 4.15d, the secondary notch around 20 m/s and for RCS below 0 dBm² is related to the degradation in SCNR, caused by the sensibility loss associated to the longer baseline.

In Fig. 4.16 a worst case scenario has been considered, where the target is modeled as a complex Gaussian process. A general degradation in the P_d is obtained for the different system-technique configurations, with a smoother transition as a function of RCS. Moreover, for a given fixed ground range velocity a higher RCS is required to obtain the same P_d as in Fig. 4.15.

Fig. 4.17a and Fig. 4.17b show cuts of the P_d for the different system-technique combinations as a function of across-track ground velocity (for a RCS of -5 dBm²) and versus RCS (for $v_z = 1$ m/s), respectively. Two sea clutter coherence times (∞ and 10 ms) are reported for each system-technique combination to illustrate the impact of clutter decor-

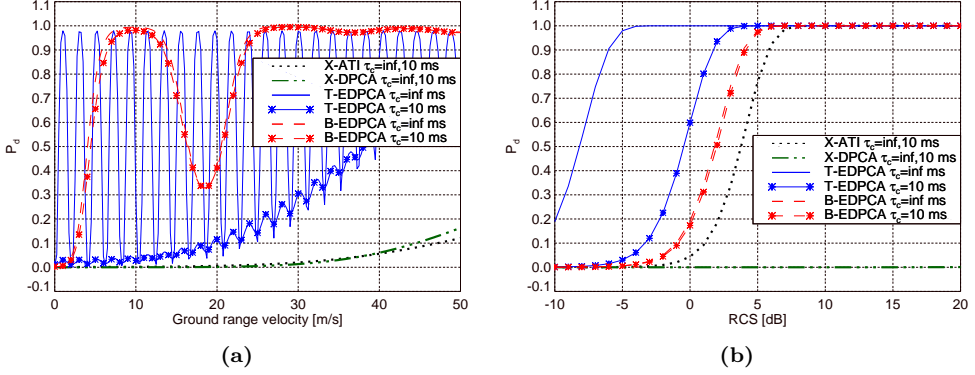


Figure 4.17: System-technique comparison of the P_d obtained from MC simulations assuming a deterministic target and for different clutter correlations ($\tau_c = \text{inf}$ and 10-ms): (a) cut at RCS of -5 dBm^2 as a function of ground velocity and (b) cut at $v_z = 1 \text{ m/s}$ as a function of RCS; no multilook processing is considered (X refers to X-DRA system, T and B to Tandem and Boom configurations, respectively).

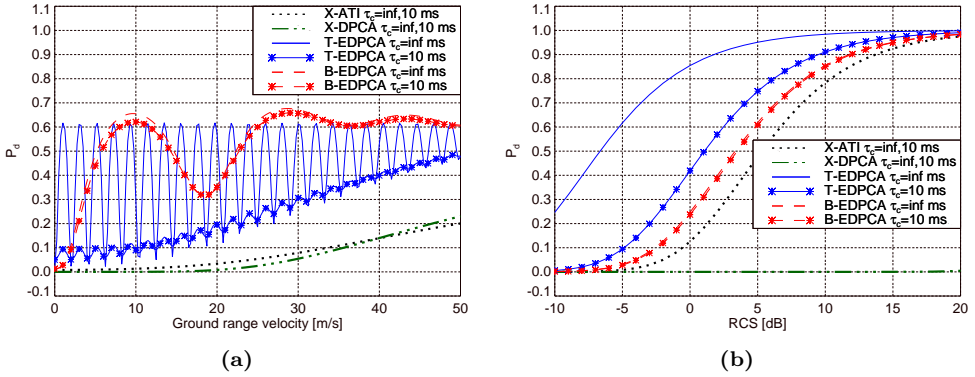


Figure 4.18: System-technique comparison of the P_d obtained from MC simulations assuming a complex Gaussian target and for different clutter correlations ($\tau_c = \text{inf}$ and 10 ms): (a) cut at RCS of -5 dBm^2 as a function of ground velocity and (b) cut at $v_z = 1 \text{ m/s}$ as a function of RCS; no multilook processing is considered (X refers to X-DRA system, T and B to Tandem and Boom configurations, respectively).

relation. For a completely correlated sea clutter the Tandem configuration with EDPCA processing (solid blue line) provides the highest sensitivity to slow moving targets, at the expense of a reduced unambiguous range of velocities. However, for realistic scenario operations clutter decorrelation impairs especially the performance of the Tandem system (solid blue line with asterisk); while Boom configuration shows a robust behavior (comparing red dashed lines with and without asterisk markers), providing the best detection capabilities as a function of the across-track velocity for a small target. ATI (dotted black line) and DPCA (dash-dot-dot green line) for X-DRA prove to have very limited capabilities to detect boats with reduced reflectivity (-5 dBm^2), being almost insensitive to clutter decorrelation since X-DRA has the smallest baseline, 2.4 m. When considering the

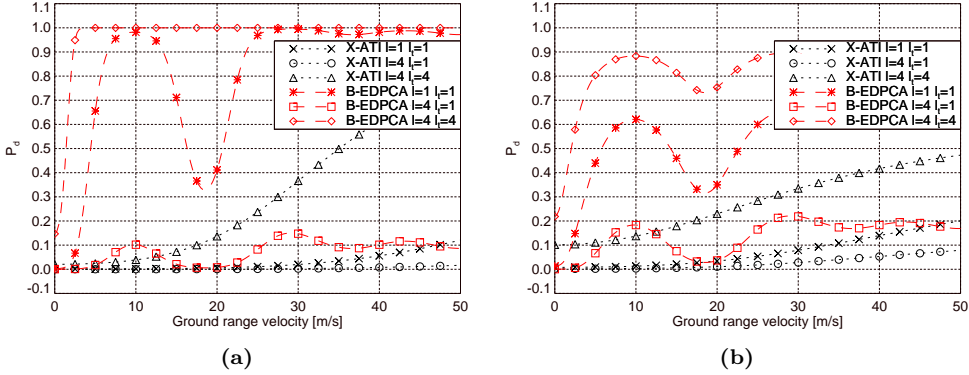


Figure 4.19: P_d as a function of ground velocity for different multilook processing (l looks), no multilook (1 look) and four looks (target present in a single look $l_t=1$ and in all of them $l_t=4$); Gaussian sea clutter with and 10-ms coherence time and target with -5 dBm² of RCS (a) deterministic model and (b) Gaussian model.

performance as a function of RCS for slow moving boats (v_z of 1 m/s), DPCA technique for X-DRA provides the worst results, unable to detect targets even with moderate to high reflectivity. For the same configuration, ATI 2D detector gives much better results, and gets closer to the Boom-EDPCA, which still requires lower RCS to obtain the same P_d . In this regard, and even for a 10-ms coherence time, Tandem configuration provides the lowest threshold RCS value, since the boat velocity is still in the range of $v_z = \pm 1.5$ m/s, where as already observed in Fig. 4.9b the Tandem SCNR is around 3 dB higher.

Analogously, Fig. 4.18 shows the same P_d cuts but for a worse case scenario, where the target has been modeled as a complex Gaussian process (completely correlated from channel to channel). Comparing both situations, Fig. 4.17 and Fig. 4.18, target randomness provides in average a smaller P_d as a function of v_z , smoothing the trend of P_d as a function of the RCS. For the Gaussian target and for P_d below a threshold level of 0.3, improved performance is obtained w.r.t. a deterministic case, whereas for P_d above this value there is a global degradation.

The impact of data averaging (multilook processing) on P_d is presented in Fig. 4.19 for a 10-ms clutter coherence with a deterministic target, Fig. 4.19a, and completely correlated Gaussian target, Fig. 4.19b. It can be observed that the performance improves as the number of looks increases, whenever the target occupies a sufficient number of single-look resolution cells to avoid degradation in the effective SCNR after multilook processing. It has been assumed that each scattering point of the target located at each resolution cell has the same RCS, and assumed to be correlated from look to look, while clutter and noise are decorrelated. Hence, it is expected that if the target size is so that the moving object lies in the different single-look cells to be averaged, a clear improvement is obtained, since the effective SCNR increases. On an opposite situation, if the target is present only in one of the looks this SCNR gets reduced (even compared to the single-look case) and so an important degradation in the performance is expected. Therefore, multilook processing should not be discarded as notable improvement can be obtained, but the boxcar size for multilook processing should be properly selected depending on the size of the expected targets, [50].

Table 4.3: Scene parameters.

Parameter	Value	Units
Scene extension (in ground)	1 x 1	Km x Km
γ_0 (center scene)	33.17	deg
Sea state	4	-
Mean clutter σ^0	-15.1	dB
Clutter temporal correlation	10	ms

4.3.2 Synthetic SAR data approach

To complement the MC simulations, synthetic multichannel data is generated using the flexible MSARRDS simulator tool described in section 3.2, where different systems, modes of operation and scenarios can be easily configured.

In order to provide an analogous metric to the probability of detection, several raw data simulations (20 trials) have been carried out, such that a frequency of detection can be extracted. A complete processing chain has been implemented integrating a MFB (based on a RD processor) with the different GMTI techniques, similar to the ones proposed in [29, 41]. The block diagrams of both adaptive RD algorithm and the complete SAR-GMTI processor (including ATI, DPCA and EDPCA algorithms) are described presented in Fig. 5.13 in section 5.2.2. Each filter of the MFB performs an adaptive SAR processing, at both RCMC and azimuth focusing steps, for a specific set of kinematic parameters (v_z , a_z and v_x), trying to recover a well focused moving object. No compensation of the Doppler shift (azimuth shift) is carried out, since, otherwise, the target will appear at different azimuth positions for different v_z of the filter bank, posing difficulties to efficiently compare the outputs of the bank of filters.

The scenario parameters considered in the raw data simulator are summarized in Table 4.3. In a first approach, a zero-mean complex Gaussian reflectivity for sea clutter has been assumed, in a downwind acquisition. To complement these results, and for the same sea conditions, a K-distributed clutter has also been considered, trying to emulate more realistic maritime scenarios. Six deterministic moving targets are included in the scenario as indicated in Table 4.4, where two different types of vessels (ramshackle T1 and a civil cargo T2) have been modeled as a collection of point-like targets. The electromagnetic modeling and RCS extraction of these vessels have been carried out by the company Telespazio Vega UK, in the cooperation frame of the European Commission FP7 funded Project SIMTISYS, [31]. In a first approximation, targets were simulated as rigid bodies. Targets T3 and T4 are single scattering points modeling low reflectivity slow moving targets in order to prove the potential improvement of the proposed Boom configuration. High-speed boats can reach velocities between 40 and 70 Knots (20.6-36 m/s) experiencing longitudinal and/or vertical accelerations up to several g -forces, depending on sea conditions, [137]. Point-targets T5 and T6 represent high-speed boats moving in along- and across-track directions, respectively, with vertical accelerations a_y of $0.35g$ m/s² and longitudinal ones, $a_x = 0.25g$ m/s² (T5) and $a_z = 0.25g$ m/s² (T6).

Table 4.4: Target parameters (coordinate system defined in Fig. 2.4; a_i and v_i correspond to acceleration and velocity in the i th dimension, respectively).

Target	Type	Scatterers	mean RCS [dBm ²]	max. RCS [dBm ²]	v_x [m/s]	v_z [m/s]	a_x [m/s ²]	a_y [m/s ²]	a_z [m/s ²]
T1	Ramshackle	53	4.5	17	-1.12	6.25	-0.69	0.0	-0.30
T2	Civil cargo	102	28.2	40	-6.73	3.0	-0.22	0.0	-0.29
T3	Point target	1	-5	-5	0	5	-0.69	0.0	-0.4
T4	Point target	1	0	0	0	2.5	-0.69	0.0	-0.4
T5	Point target	1	5	5	20.6	0.0	2.45	3.43	0.0
T6	Point target	1	5	5	0.0	20.6	0.0	3.43	2.45

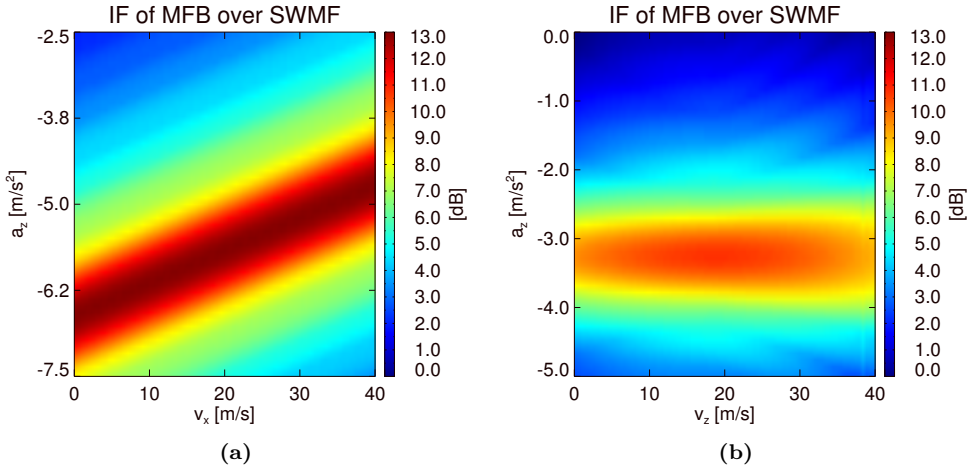


Figure 4.20: Improvement factor (IF) of the MFB with respect to SWMF: (a) target T5, v_x versus a_z map; (b) target T6, v_z versus a_z map.

It is well-known that if target kinematic is not accounted for in the SAR processor, severe degradations are observed in the SAR image and this in turn prevent proper SAR-GMTI detection, especially for small and fast moving objects. Fig. 4.20a and Fig. 4.20b show the IF maps provided by the MFB w.r.t. a SWMF for T5 and T6, respectively. In case of T5, with a purely along-track movement and no a_z accelerations, MFB can provide up to 13 dB of improvement for a set of a_z - v_x pairs, as denoted by the diagonal strip in Fig. 4.20a. Two conclusions are extracted from these results: first, vertical acceleration a_y on T5 produces equivalently similar effects as an a_z acceleration from the SAR processing point of view, since a_y contributes also to a radial acceleration (line-of-sight projection); second, there is a coupling between across-track acceleration a_z and along-track velocity v_x , giving rise to indistinguishable effects. For a fixed v_x , a MFB step size below 0.5 m/s² on a_z , produces losses on peak response below 3 dB. Analogously, for a fixed a_z the step on v_x is below 13 m/s. The impact of a_x , inducing third-order phase errors, produces mainly an asymmetric sidelobe response for the considered acquisition time (under one second).

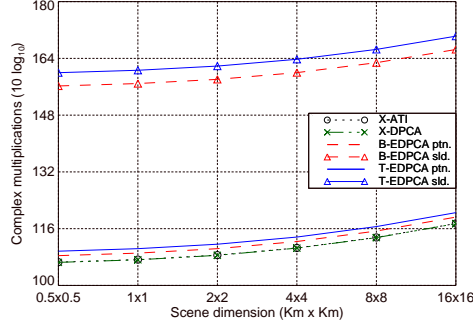


Figure 4.21: Computational load comparison considering a MBF with 33 filters; in legend portion (ptn.) and sliding (sld.) refer to the type of approach followed to estimate/invert the interference covariance matrix in the EDPCA processing, using a single portion of the image (512x512 pixels) and a sliding boxcar (512x512 pixels size), respectively.

For T6, moving in the across-track direction, the combination of a_z and a_y produces an effective across-track acceleration different from the target's original one (2.45 m/s^2), see Fig. 4.20b, with an IF around 11 dB. Similar to T5, a MFB step size below 0.5 m/s^2 on a_z produces losses lower than 3 dB, while the sensitivity w.r.t. v_z is quite flat, with a degradation around 2 dB for a variation of 20 m/s. It must be noted that azimuth processing is performed around the target's Doppler centroid with the given processed bandwidth, and so if there were any backfolding of the target's spectrum (as schematically sketched in Fig. 2.2a), the processing window should be properly adapted to maximize the spectral overlap, reducing the defocusing effects. The adaptive SAR processor has been derived assuming uniformly accelerated movements for the vessels during the synthetic aperture time, considering second order Taylor's series expansion for the slant range history. However, such an assumption might not be true, especially for small and high-speed boats sailing on rough seas [138]. Therefore, in realistic scenarios, the proposed adaptive SAR processor will not be able to fully recover the induced image degradations. Alternative SAR processing strategies should be considered as well as realistic modeling of the complex dynamics of high-speed boats on open seas.

The required computational cost of the implemented processing chain is represented in Fig. 4.21 in terms of complex multiplications as a function of the scene dimension. In this case, 33 filters have been used to sample the range of $a_z = \pm 10.0 \text{ m/s}^2$ with a step of 0.5 m/s^2 , producing a degradation below 3 dB on the peak response. For X-DRA configuration ATI and DPCA techniques (lines with circle and cross markers) have the lowest computational burden compared to EDPCA, where the required number of operations increases with the number of additional channels and especially when considering a sliding boxcar approach for \mathbf{R}_q (interference's covariance matrix) estimation/inversion.

Fig. 4.22 show different SCNR images (for a single data trial) considering an adaptation to target T2, T3 and T6 from left to right. In order to provide the SCNR metric, the mean interference power (before and after GMTI processing) is estimated from an image patch, where no targets are present. This very patch has been also used for the estimation of the covariance matrix required by the EDPCA processing.

In the first row of images, Figs. 4.22a-c, the single channel SCNRs for Boom configu-

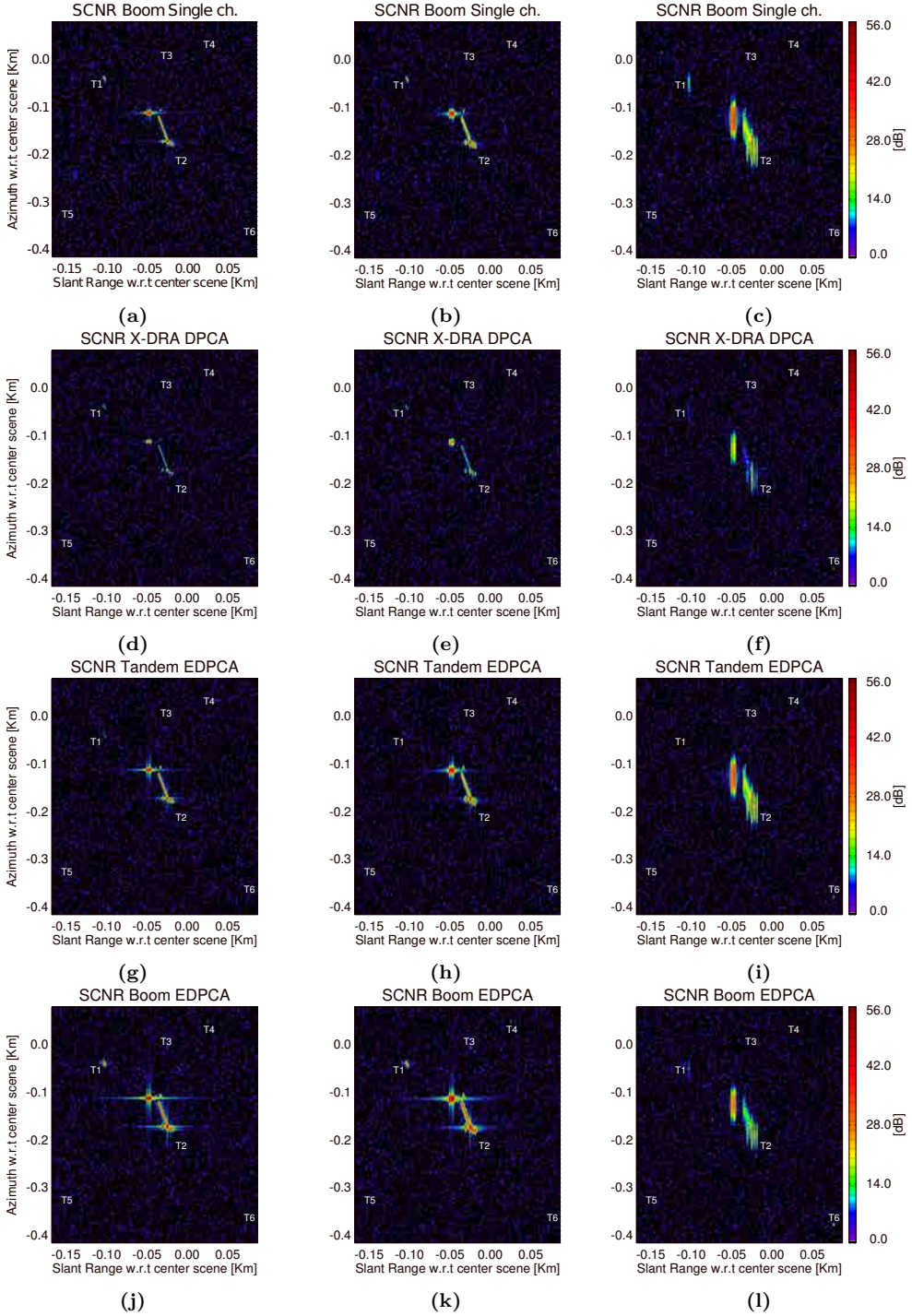


Figure 4.22: SCNR images (for a single data trial) adapted to different targets (T2, T3 and T6 from left to right): (a)-(c) Boom single channel, (d)-(f) DPCA X-DRA, (g)-(i) EDPKA Tandem and (j)-(l) EDPKA Boom.

ration and prior to GMTI processing are shown. In this case, the ramshackle (T1) and civil cargo (T2) can be easily identified, T6 is barely identified, whereas point-like targets T3, T4 and T5 are masked by the interference. The impact of SAR processing filter mismatch can be easily recognized by the produced defocusing on T1 and T2 in Fig. 4.22c when the MFB is adapted to T6. For X-DRA configuration and processing with DPCA technique, Figs. 4.22d-f, T6 is more visible, especially when SAR processing is adapted to this target. The slow moving targets T3 and T4, and the along-track fast boat T5 (no radial velocity) do not appear in the image. From Figs. 4.22d-f, it can be also appreciated that DPCA reduces signal contribution for T2 (especially visible on the sidelobe responses), moving with a ground range velocity of 3.0 m/s. This behavior is expected from the theoretical SCNR analysis in Fig. 4.9, where the SCNR degradation for DPCA processing can be clearly appreciated for ground velocities under 20 m/s. For Tandem configuration, Figs. 4.22g-i, the small and slow moving targets T3 and T4, even for T3 adaptation, Fig. 4.22h, do not show up in the SCNR images due to the higher induced decorrelation on the longer baseline. The single-point fast moving vessel (in across-track direction) T6 can be recognized, when the processing is accordingly adapted to this target as observed from Fig. 4.22i.

EDPCA processing the data of the proposed Boom architecture, Figs. 4.22j-l, provides subclutter visibility for targets T3 and T4, especially appreciable when the full SAR-GMTI processing is adapted to these two targets (only the case of T3 adaptation Fig. 4.22k is reported). In Fig. 4.22l the high-speed boat T6 can be clearly recognized, much more visible when compared to the rest of system-technique combinations. Regarding T5, it must be noted that SAR-GMTI adaptive processing (to T5) using EDPCA technique with Boom configuration shows this high-speed boat in the final SCNR image, not included in Fig. 4.22 to keep readability of the different images.

To better understand the improved capabilities provided by the proposed SAR-GMTI mission compared to other system-technique configurations, the combined detection maps are very useful visual indicators, collapsing the different target adaptive processing in a single image. Fig. 4.23 and Fig. 4.24 show these maps over the 20 trials assuming a complex Gaussian and a K-distributed (shape parameter of $v = 5$) sea clutter, respectively. The combined detection map per trial is obtained as the aggregation of the different detection images (each adapted to each one of the six targets) through the logical operator *OR*. It must be noted that the strips (along azimuth) of detected pixels around T1 and especially T2 are present because of the defocusing induced by the matched filters adapted to T5 and T6, such that those pixels are still above the threshold established by the CFAR detector.

From Fig. 4.23 and Fig. 4.24 it can be generally stated that T1, T2 and T6 targets are well detected by the different system-technique combinations over the various trials. Considering X-DRA configuration, small and slow moving targets T3 and T4 are neither detected by ATI, Fig. 4.23b, nor by DPCA, Fig. 4.23a, for which MC P_d is close to zero. Unlike DPCA, ATI is able to provide around 9 detections for T5 (MC estimates a P_d of 0.76). When considering a K-distributed clutter, Fig. 4.24b, the overall detection performance is maintained at the expense of increased false alarms (see Table 4.5), since the parametric ATI 2D-CFAR detector still assumes a Rayleigh distributed magnitude on the clutter; however, as there is no clutter cancellation this hypothesis breaks down. In this line, a trivial way to lower this effective false alarm rate is to increase the de-

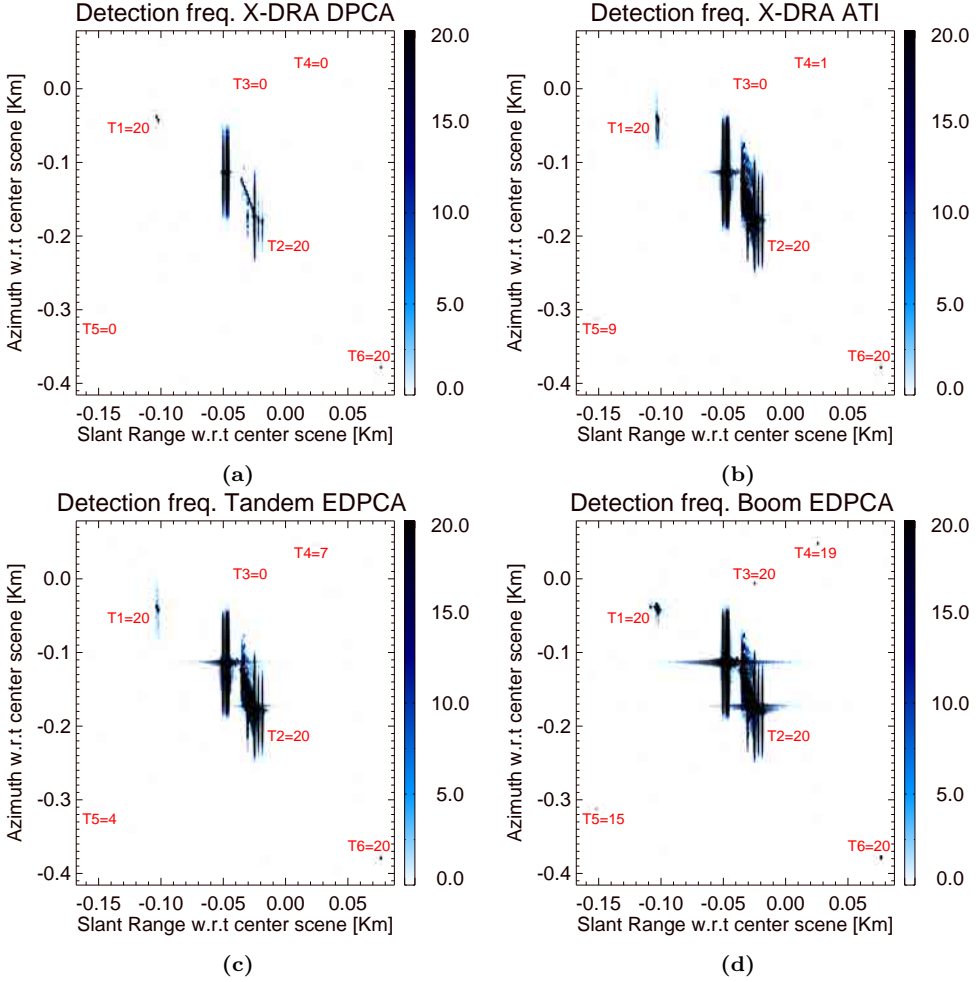


Figure 4.23: Combined detection maps assuming a complex Gaussian distributed sea clutter (number of detections per target detailed): (a) X-DRA DPCA, (b) X-DRA ATI, (c) Tandem EDPCA and (d) Boom EDPCA (CFAR detectors with $P_{fa} = 10^{-5}$ under Gaussian hypothesis).

tection threshold; however, this reduces in turn the detectability of the targets. Further studies are required to theoretically derive a 2D-ATI parametric detector considering a K-distributed clutter in magnitude (or more generally a compound model statistical family). Recently, Gierull *et. al* have proposed in [50] a double test-statistic for heterogeneous terrain (with special interest on urban areas), based on compound clutter models, using a two-step DPCA-ATI detector. Initially a high P_{fa} for DPCA processing is chosen to ensure detection of most true targets, while accepting an excessive number of false alarms. In a second step, an ATI phase only detector is used to lower those false alarms while not compromising the target detection performance. Although ATI phase detector is not optimum, it shows robustness against heterogeneity of the clutter since when the ATI

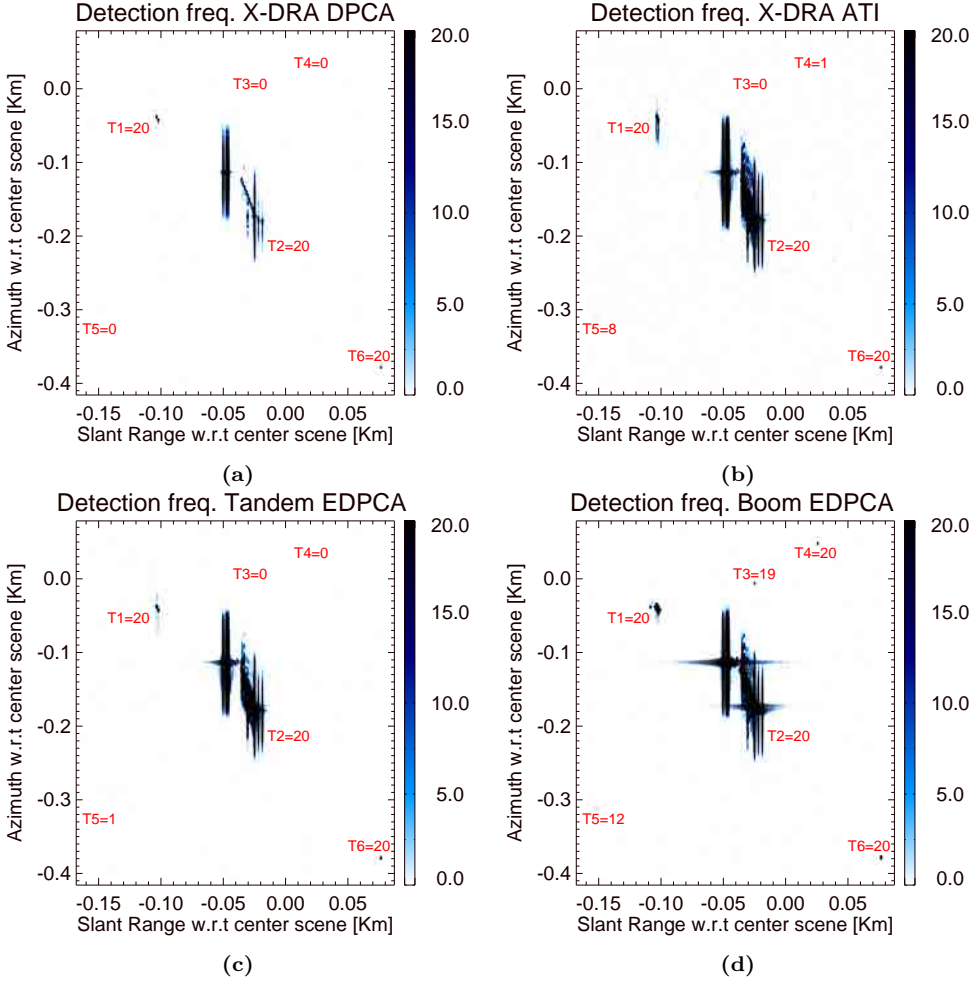


Figure 4.24: Combined detection maps assuming a K-distributed sea clutter (number of detections per target detailed): (a) X-DRA DPCA, (b) X-DRA ATI, (c) Tandem EDPCA and (d) Boom EDPCA (1D-CFAR DPCA/EDPCA magnitude detectors constructed under K-distribution hypothesis, and 2D-CFAR ATI detector under Gaussian hypothesis with $P_{fa} = 10^{-5}$).

phase is computed the texture of the compound model cancels out. In this regard, the proposed two-step detector is an appealing solution for vessel detection and should be further investigated.

In EDPCA-Tandem, Fig. 4.23c, T3 is not at all detected and T4 is gathered in 7 out of 20 trials, under the assumption of a complex Gaussian clutter, as predicted by MC with a P_d of 0.03 (T3) and 0.43 (T4). For a K-distributed sea clutter, Fig. 4.24c, neither T3 nor T4 are detected using EDPCA-Tandem combination with a CFAR detector fitted to a K-distribution. For this case the required threshold (to keep the same P_{fa}) is higher compared to Rayleigh case.

Table 4.5: Estimated P_{fa} for different techniques, clutter and CFAR statistics (averaged over 20 trials and 6 filters).

	Gaussian	K-distributed	
		Rayleigh CFAR	K-distributed CFAR
X-DRA DPCA	1.05e-5	1.05e-5	1.05e-5
X-DRA ATI	1.06e-5	1.70e-4	-
Tandem EDPCA	1.14e-5	2.0e-4	1.40e-5
Boom EDPCA	1.14e-5	4.44e-5	1.88e-5

The low reflectivity slow point-like targets T3 and T4 are well detected (almost in all trials) applying EDPCA with the proposed Boom configuration, Fig. 4.23d, according to the predicted P_d (0.65 and 0.82) from MC simulations. The number of detections over the reduced set of trials for the raw data processing approach provides a general picture of the expected performance, but cannot be directly compared to the intensive MC simulation P_d , which have been computed using 5 millions of iterations. EDPCA with Boom configuration appears to be more robust to the clutter statistical variation, comparing Fig. 4.23d (Gaussian case) and Fig. 4.24d (K-distributed case), since the overall detection performance is kept, specifically for T3 and T4.

MC simulations predict a P_d around 1 for target T5 and Tandem configuration using EDPCA processing. However, from Fig. 4.23c, the number of detections is 4, appearing at a displaced azimuth position compared to the other system-technique combinations. From the inspection of the individual coregistrated SAR images, an azimuth displacement on the T5 peak response can be recognized, around 4 m for the longest baseline configuration. This shift is due mainly to the high vertical acceleration a_y and partially to the along-track velocity v_x . In fact, a_y translates into a radial acceleration, which produces a variation on the effective radial velocity (during the coregistration time or equivalently the baseline time delay) observed by the different channels, producing a different azimuth displacement between channels. Such statement has been confirmed by additional simulations, where the same T5 kinematics with no a_y have been considered, and a slight shift is observed between target peak responses due to v_x . Therefore, the azimuth displacement (mostly caused by a_y) avoids the full coherent integration of EDPCA, since target response appears on different pixels for different channels, reducing the detection capabilities compared to MC simulations, where it has been ideally assumed that target response among receivers lies on the same resolution cell. For the more compact Boom architecture, such a displacement is below 1.0 m, keeping T5 peak responses within the same resolution cell, in a way that EDPCA processing is still effective providing 14 detections out of 20, in line with the predicted P_d of 0.84.

Table 4.5 presents the average (over the 20 trials and 6 filters) estimated P_{fa} for the considered system-technique combinations and for the two types of clutter statistics, complex Gaussian (2nd column) and K-distributed in magnitude (3rd and 4th columns). For the latter case two CFAR parametrization, Rayleigh (3rd column) and K-distribution (4th column), are evaluated only for DPCA and EDPCA. As expected, DPCA processing on X-DRA keeps the same level of false alarms for the different clutter statistics and CFAR settings. However, for ATI processing, P_{fa} is one order of magnitude higher for

the K-distributed clutter when a 2D-CFAR detector under the assumption of Gaussian-like interference is used. Similarly, EDPCA processing on Tandem and Boom present a higher P_{fa} (especially Tandem due to higher impact of clutter decorrelation) when using a Rayleigh CFAR detector for the K-distributed scenario; but it gets reduced for the most appropriate K-distributed CFAR scheme. Sikaneta *et. al* proposed in [139] a solution to the problem of high false alarm rates in heterogeneous terrain. It considers an adaptive CFAR detector that does not depend on terrain heterogeneity, avoiding the definition of a parametric texture distribution. This alternative is based upon a multiplicative noise model rather than a texture (compound) model, assuming high correlation between the noise-free clutter measurements. Such hypothesis should be further investigated in the case of sea clutter, taking into account the impact of sea decorrelation.

4.4 Concluding remarks

The GMTI performance of different multichannel SAR missions using state-of-the-art GMTI techniques (ATI, DPCA and EDPCA) has been evaluated in this chapter over maritime scenarios. A new multichannel SAR configuration, based on non-uniformly displaced receive phase centers, has been compared with TSX and TDX like missions. With such a multichannel configuration it is possible to discern small slow moving vessels, usually undetected with present SAR systems. Under certain hypothesis (homogeneous open sea), the proposed mission tries to maximize the SAR-GMTI performance by minimizing the noise contribution, in terms of NESZ, and ambiguities' level in the region of interest (20-40 degrees of incidence angle), while keeping a low system complexity with an optimized number of channels. Boom system has been designed trying to keep the new ambiguity metric CRAASR as low as possible in the region of operation. In the far range region (40-60 degrees) the impact of range ambiguities increases and so does CRAASR. Therefore, the performance is expected to degrade for the case of non-homogeneous ambiguous returns, especially close to coastal areas. A way to circumvent these impairments is to consider a future SAR-GMTI mission concept exploiting azimuth phase coding (APC) in combination with digital beamforming, such that a high-resolution wide-swath (HRWS) mode can be operated [140].

The proposed architecture has been evaluated comparatively in a two-level simulation performance approach over maritime scenarios. In a first step, the probability of detection has been characterized through intensive MC simulations under different scenario conditions. Several synthetic multichannel SAR raw data sets have been processed iteratively to complement MC simulations for a realistic maritime scenario. The different simulations' results indicate the potential improvement provided by the proposed Boom configuration when using adaptive processing approaches such as EDPCA. The simulations results are in good agreement with the theoretical expected performance. Boom configuration has been designed, such that it is slightly affected by internal clutter motion and at the same time enables high sensitivity to low reflectivity slow moving targets, alleviating Doppler (velocity) ambiguities thanks to its baseline diversity. It must be pointed out that this configuration can be scaled down (in terms of size) for a higher operating frequency, with the appropriate modification of the sea clutter modeling.

The performance evaluation of the proposed mission has been carried out assuming a complex Gaussian model for the sea clutter. Additional raw data simulations assuming a

K-distributed sea clutter have been performed, showing the robustness of Boom configuration when processed with EDPCA. For ATI, where no clutter cancellation is performed, a new formulation of the 2D-CFAR detector should be derived to consider a K-distributed sea clutter.

The impact of SAR imaging high-speed boats has been preliminarily analyzed, showing the need to properly account for target kinematics in the SAR-GMTI processing chain via a MFB since, otherwise, the induced image degradation could impair the GMTI performance, particularly for small and fast boats. From these considerations, it can be stated that experimental campaigns over maritime scenarios are mandatory to understand and validate a sea clutter model (for the usual range of SAR incidence angles), in terms of its statistics and mean power reflectivity, and at the same time try to grasp the impact of realistic target kinematics.

5

Chapter 5

Experimental MSAR-GMTI over maritime scenarios

THIS chapter is devoted to the SAR-GMTI evaluation of real multichannel SAR data over maritime scenarios. Two different type of data sets have been evaluated: (i) airborne X-band data from the F-SAR sensor and (ii) spaceborne X-band data from TerraSAR-X German satellite. The capability of refocusing moving vessels with an adaptive SAR processor is demonstrated. The impact of channel balancing/calibration on the GMTI performance is analyzed with special interest throughout the chapter. The chapter starts with an overview of the sensors' configuration, followed by the description of the GMTI techniques used to process the experimental data sets and integrated in the implemented processing chains. In the second part of the chapter the different results of SAR-GMTI processing experimental data are presented first for the airborne case (F-SAR) and then for the spaceborne TerraSAR-X mission¹.

¹This chapter includes figures and text fragments, sometimes verbatim, of the author's publication [JA2].

5.1 Sensor configurations

5.1.1 F-SAR airborne system

The increasing demand on air-to-ground surveillance and reconnaissance multi-task systems, with high resolution and long range imaging capabilities, poses stringent requirements on the design of new radar sensors. A clear example is the development of an efficient traffic monitoring system, driven by the dramatical increase of road traffic, which allows to monitor large areas at once at any time (day/night) and under any weather conditions. In this sense, radar systems represent an ideal tool for efficient and continuous traffic monitoring, being the airborne sensors the precursor of such GMTI capabilities. From the operational point of view, the airborne platforms are more attractive, thanks to the higher flexibility, shorter revisit times and longer acquisitions, at expenses of a reduced spatial coverage compared to the spaceborne sensors. During the last decade there has been a continuous development of airborne radar system trying to fulfill these requirements. At European level three main research groups are working towards this end:

1. The French aerospace laboratory ONERA has a wide experience in the development of airborne SAR and GMTI systems, with special emphasis on defense applications. From the knowledge gained on the *RAMSES* system a new compact radar concept for SAR-GMTI operation is being developed, the so called *CURACAO* [18,19].
2. The Fraunhofer-Institut für Hochfrequenzphysik und Radartechnik (FHR) has designed a multimodal and multichannel experimental airborne radar system *PAMIR* that delivers high resolution SAR and Inverse SAR (ISAR) images, integrating the GMTI operation on the basis of five parallel receiving channels [15,141,142]. This GMTI mode is designed to rapidly monitor wide areas using a narrow antenna in a scanning operation, such that the revisit time is reduced and the detection capability for a given target can be increased as it can be seen from different angles during the scanning, [14].
3. The Institut für Hochfrequenztechnik und Radarsysteme (HR), at the Deutsches Zentrum für Luft- und Raumfahrt (DLR), is responsible for the development of the airborne SAR system *F-SAR*, contributing to the demonstration/validation of new technologies and applications. The F-SAR system is the successor to the well-known *E-SAR*, providing the capability to acquire different wavelengths and polarizations simultaneously [71,143]. An experimental GMTI mode, with four receiving channels, is being used to assess different GMTI algorithms with respect to their capabilities for traffic monitoring [16,17], in the frame of two main projects, TRAM-RAD [26] and VABENE [144].

The airborne F-SAR sensor is a multichannel and multifrequency polarimetric system. It can operate in X- (8-12 GHz), C- (4-8 GHz), S- (2-4 GHz), L- (1-2 GHz) and P-bands (250-500 MHz) with simultaneous polarimetric capability and single-pass polarimetric interferometric capability only in X- and S-bands. The SAR-GMTI mode is an experimental one, where at most four receiving channels can be used when operating in switched aperture dual-receive X-band mode.

In Fig. 5.1a, the multichannel F-SAR configuration and operation mode are depicted. The receive and transmit antennas have 20 cm length and are co-located in the along-

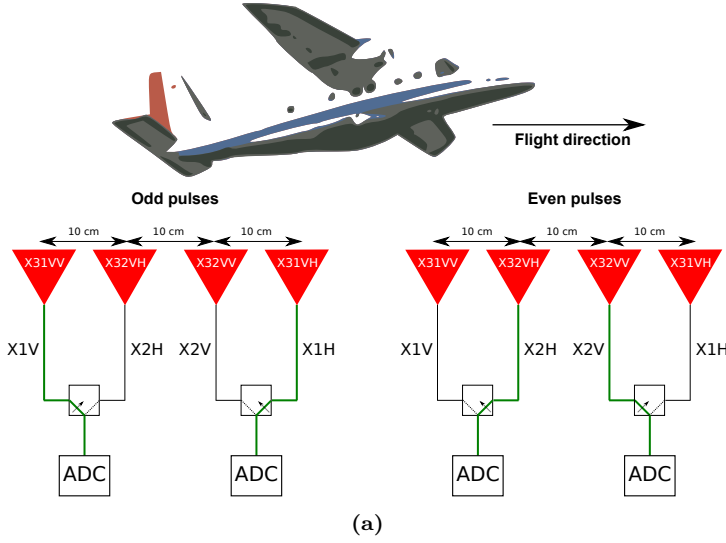


Figure 5.1: F-SAR sensor SAR-GMTI acquisition configuration in the switched dual-receive mode (effective two-way baselines are indicated).

track or flight direction. The front-end of the system integrates only two analog-to-digital converters (ADCs), such that only two antennas can receive simultaneously. In order to obtain a 4-channel configuration, the system is operated in a switched receive mode as sketched in Fig. 5.1a, and hence the per-channel PRF is half of the operational one. The original channel nomenclature has been preserved, such that for odd pulses channels X31VH and X31VV are acquired, while for even pulses X32VV and X32VH. At this point it must be noted that the sensor was configured in VV polarization, i.e., vertical transmit and receive polarizations.

5.1.1.1 Data set description

As a part of the doctoral studies, a short stay as visiting researcher has been carried out at the DLR-HR institute. During this period, multichannel airborne F-SAR data has been processed over maritime scenarios. The different available data sets were collected in 2009 in the frame of the DLR internal project Ocean SAR, and they correspond range-compressed products with and without MOTion COmpensation (MOCO). Due to the lack of precise antenna pattern measurements for the configuration that acquired those data takes, the antenna patterns in elevation and azimuth were not compensated to avoid introducing artifacts on the data. Unfortunately, no ground truth was available for this campaign, and so no information on the scenario (vessels' velocities and sea conditions) can be used to support the SAR-GMTI processing.

An acquisition over the Elbe's Mouth (*09tdxsim0104*), see Fig. 5.2, has been selected for SAR-GMTI processing evaluation. In this data take, a large land portion in the image is available. It can be used as a reference patch for proper channel balancing or calibration, co-registration (if required) and antenna pattern estimation (in case of ISTAP technique). The main acquisition and processing parameters for this data take

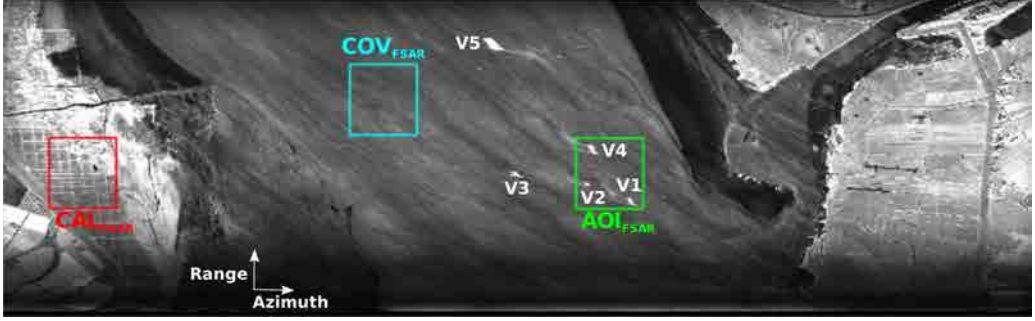


Figure 5.2: SSC image of the F-SAR GMTI acquisition *09tdxsim0104* over the Elbe's mouth in the North Sea: AOI_{FSAR} denotes the sea patch of interest to be processed delimited by a green box; the red solid box delimits the reference land patch CAL_{FSAR} for calibration purposes (channel balancing) and region COV_{FSAR} , confined by the light blue solid rectangle, could be used as a reference patch for interference covariance matrix estimation.

Parameter	Value	Units
v_s (sensor velocity)	85.814	m/s
H_0 (sensor altitude)	2497.476	m
Ψ (squint)	9.039	deg
PRF (per-channel)	2016.129	Hz
B_a (azimuth processed bandwidth)	1832.844	Hz
B_r (range processed bandwidth)	300	MHz
Hanning spectral weighting	0.54	-

Table 5.1: F-SAR acquisition and processing parameters for the *09tdxsim0104* data take over the Elbe's mouth in the North Sea.

are summarized in Table 5.1.

A single look slant range complex (SSC) image of the data take produced by the DLR is shown in Fig. 5.2. The figure also indicates several regions of interest: AOI_{FSAR} represents the region of interest to be processed containing three vessels V1, V2 and V4; a reference sea patch COV_{FSAR} , free of vessels, which could be used for covariance matrix estimation when processing with EDPCA or ISTAP; and a reference calibration land patch CAL_{FSAR} , covering the same slant range variation as AOI_{FSAR} , to extract the channel balancing weights.

5.1.2 TerraSAR-X spaceborne system

The successful TSX satellite, launched in summer 2007, is the first German radar satellite implemented under a public-private partnership between DLR and EADS Astrium GmbH [145]. TSX is equipped with a phased array antenna of 4.8 m length that allows for multimodal operations: conventional SAR stripmap, SCanSAR and Spotlight. Two different multichannel acquisition concepts in along-track configuration have been implemented as schematically depicted in Fig. 5.3. The first one is the so called aperture

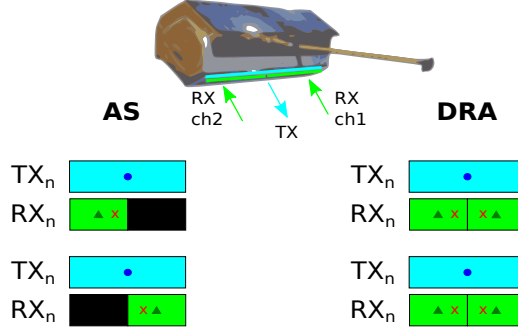


Figure 5.3: TSX-ATI modes: aperture switching (AS) and dual-receive antenna (DRA); transmit (TX) phase center denoted by the solid circle, receive (RX) by the triangle symbol and effective two-way (2-W) by the cross symbol (figure adapted from [46]).

switching (AS), where the whole antenna is used to transmit, while the fore and aft parts of the antenna are alternatively activated to receive in a pulse-basis sequence [146]. In this AS mode, the effective PRF per channel is half of the operational one. For the second concept, known as dual receive antenna (DRA), the whole antenna is also used to transmit but is split into two halves that receive simultaneously [147]. The availability of two receiving channels provides TSX some GMTI capabilities, with special interest on traffic monitoring [46, 47, 148] and current field measurements [91, 92].

In the DRA mode, TSX uses the redundant receiver unit to sample the second channel, such that the fore and aft channels are combined through the hybrid coupler providing the sum and difference data. For SAR-GMTI purposes the fore and aft channels should be reconstructed using proper algorithms, such that hardware impact (gain and phase errors) is compensated minimizing channel imbalances [74, 148].

In collaboration with the DLR and in the frame of the scientific project proposal, *Study of Spaceborne GMTI Algorithms Using DRA Data* (Ref. MTH1971), several TSX data sets are available for SAR-GMTI evaluation purposes. This data corresponds to a dedicated DRA acquisition mode campaign carried out from April to May 2010. Experimental ATI products are acquired in stripmap single polarization mode. These level-1b products are SSC, containing three images: the single receive antenna (SRA) channel, processed as a nominal stripmap product and two DRA images, DRAFore and DRAAft. These latter are processed using the full azimuth bandwidth (limited by the PRF) with neither azimuth nor range windowing. Therefore, the impact of ambiguities is expected to be high, due also to the widening of the receive antenna (half of the TX). These effects can be observed in Fig. 5.4, which corresponds to the color composite image (SRA, DRAFore and DRAAft channels) over the Strait of Dover, and where the ambiguities show up as yellow coded pixels.

5.1.2.1 Data set description

From the different data sets of the TSX-DRA campaign for ATI configuration (April-May 2010), an acquisition over the Strait of Dover has been selected for SAR-GMTI processing evaluation, see Fig. 5.4. The main acquisition and processing parameters for this data



Figure 5.4: SSC color composite image of the TSX-DRA acquisition over the Strait of Dover in the North Sea: AOI_{TSX} denotes the sea patch of interest to be processed indicated as green box; red solid box delimits the reference land patch CAL_{TSX} for calibration purposes (channel balancing); and region COV_{TSX} , confined by the light blue solid rectangle, could be used as reference patch for interference covariance matrix estimation.

Parameter	Value	Units
v_s (sensor velocity)	7682.782	m/s
v_g (spot/ground velocity)	7065.511	m/s
PRF (per-channel)	3807.03	Hz
B_a (azimuth processed bandwidth)	3807.03	Hz
B_r (range processed bandwidth)	150	MHz
Hamming spectral weighting	1.0	-

Table 5.2: TSX-DRA acquisition and processing parameters for a data take over the Strait of Dover in the North Sea.

take are summarized in Table 5.2. A quicklook SSC image of the data take produced by the DLR is shown in Fig. 5.4. The figure also indicates a number of regions relevant to processing and evaluation: AOI_{TSX} represents the region of interest to be processed containing six vessels; a reference sea patch COV_{TSX} , free of vessels, which could be used for covariance matrix estimation when processing with EDPCA or ISTAP; and a reference calibration land patch CAL_{TSX} .

5.2 SAR-GMTI processing schemes

This section describes the algorithms and processing chains used for the SAR-GMTI evaluation of the different experimental data over maritime scenarios. The objective is to provide flexible and fully integrable processing modules such that any type of data, either airborne or spaceborne, can be assessed with different GMTI techniques providing both SAR-GMTI images as well as detection maps.

5.2.1 Adaptive SAR processor

In the near future, SAR-GMTI systems are required to detect slowly moving targets with low radar reflectivity (low RCS) in subclutter conditions and at the same time image them in high-resolution SAR images. Therefore, the intrinsic imaging degradation of the moving targets on SAR images, when focusing with stationary world matched filter (SWMF), should be properly compensated. An adaptive SAR processing, which includes the target kinematic parameters, allows image quality and SCNR degradation recovery, especially important when imaging low reflectivity targets. Several approaches can be followed to properly focus the moving targets in SAR images, e.g., autofocus techniques [37,38] or matched filter bank (MFB) [40,69,149] among others. Assuming no *a priori* information regarding the target motion, a MFB has been used, based on a range-Doppler (RD) algorithm [73], which takes into account adaptive range cell migration correction (RCMC) and azimuth reference function. Following a similar approach as in [28,29,41], this processor has been integrated in the different SAR-GMTI processing chains.

The different effects of moving targets on SAR imagery were first analyzed by Raney in [25]. Further detailed studies can be also found in [68,70]. In chapter 2, the impact of different target kinematics have been evaluated by means of processing raw data simulations. Hereafter, a brief mathematical formulation of the moving target slant range history is reported, pointing out how the target motion impairs the SAR focusing.

Let's assume a flat earth geometry in the SAR acquisition as depicted in Fig. 2.4, where the platform moves at constant height H_{orb} and effective velocity v_e along the azimuth (along-track) direction. As extendedly assumed in the GMTI literature, the motion of the target can be simplified to a linear movement with constant acceleration (in both azimuth and ground range) during the formation of the synthetic aperture, which is fairly true for spaceborne platforms, where the integration time is in the order of one second:

$$\begin{aligned} x(t) &= x_0 + v_x t + \frac{a_x}{2} t^2 \\ z(t) &= z_0 + v_z t + \frac{a_z}{2} t^2 \end{aligned} \quad (5.1)$$

In (5.1), t stands for slow time (or azimuth time). At $t = 0$ (mid-acquisition time) the target is located at x_0 and z_0 , which corresponds to the along- and across-track coordinates, respectively. The along-track and across-track velocities of the target are represented by v_x and v_z , whereas the associated accelerations are a_x and a_z . For simplicity on the mathematical formulation, the target is assumed to be moving in the $y = 0$ plane without any vertical (elevation) movement.

The slant range distance between the target and the SAR sensor can be expressed as

$$R(t, \boldsymbol{\vartheta}_t) = \sqrt{H_{orb}^2 + \left(x_0 + v_x t + \frac{a_x}{2} t^2 - v_e t\right)^2 + \left(z_0 + v_z t + \frac{a_z}{2} t^2\right)^2} \quad (5.2)$$

where $\boldsymbol{\vartheta}_t$ is the vector of target parameters $\boldsymbol{\vartheta}_t = [x_0, z_0, v_x, v_z, a_x, a_z, \alpha_t]$.

A second order Taylor's series expansion of (5.2) around $t = 0$ allows to understand the impact of imaging moving targets with SWMF compared to the stationary case²:

$$\begin{aligned} R(t, \boldsymbol{\vartheta}_t) &\approx R_0 + \frac{z_0 v_z}{R_0} t + \frac{v_{rel}^2(\boldsymbol{\vartheta}_t)}{2R_0} t^2 \\ &= R_0 + \frac{z_0 v_z}{R_0} t + \frac{1}{2R_0} \left\{ (v_x - v_e)^2 + v_z^2 \left(1 - \frac{z_0^2}{R_0^2}\right) + z_0 a_z \right\} t^2 \end{aligned} \quad (5.3)$$

where R_0 is the slant range at $t = 0$ and v_{rel} the relative velocity. In (5.3) it has been assumed $x_0 = 0$ without loss of generality.

The moving target's Doppler frequency, obtained as the time derivative of the azimuth phase $\varphi(t, \boldsymbol{\vartheta}_t) = -\frac{4\pi}{\lambda} R(t, \boldsymbol{\vartheta}_t)$ (for the monostatic case), can be expressed as

$$\begin{aligned} f_d &\approx -\frac{2}{\lambda R_0} \{z_0 v_z\} - \frac{2}{\lambda R_0} \left\{ (v_x - v_e)^2 + v_z^2 \left(1 - \frac{z_0^2}{R_0^2}\right) + z_0 a_z \right\} t \\ &= f_{DC} + K_a(\boldsymbol{\vartheta}_t) t \end{aligned} \quad (5.4)$$

where $K_a(\boldsymbol{\vartheta}_t)$ refers to the target's azimuth (Doppler) chirp rate. In a more general case, the Doppler centroid f_{DC} can eventually include the impact of a squint angle Ψ , between the antenna's broadside and the perpendicular to the platform's path

$$f_{DC} \approx -\frac{2}{\lambda} \left\{ (v_x - v_e) \sin \Psi + \frac{z_0 v_z}{R_0} \right\} \quad (5.5)$$

From (5.4) two main effects on the SAR image due to target motion will be present. The across-track velocity v_z produces a shift of the Doppler centroid f_{DC} , in a way that the target is imaged at a displaced position respect to its original one. This displacement can be computed as [70]:

$$\Delta x_{img} = -\frac{f_{DC}}{K_{a_{SWMF}}} v_e \quad (5.6)$$

with $K_{a_{SWMF}}$ as the Doppler rate for the stationary (SWMF) case.

Across-track accelerations a_z and along-track velocities v_x impair on the Doppler rate, i.e., a variation on the quadratic term of the slant range history (5.3), which translate into smearing or defocusing in the azimuth dimension, when imaging with a SWMF. Hence, this filter mismatch produces a degradation in the azimuth resolution as well as in the moving target's signal intensity after focusing due to the reduced coherent integration.

When considering the RCMC, an across-track velocity increases the range walk (linear component of the RCM), such that a residual RCM is present for a SWMF-RCMC, [70].

²A detailed mathematical derivation of the bidimensional MSAR signals before and after SAR processing can be found in Appendix B.

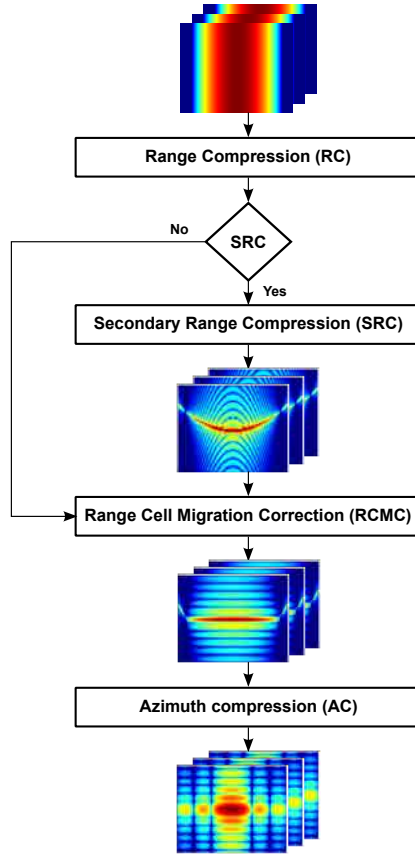


Figure 5.5: Block diagram of the implemented adaptive RD-SAR processor.

This results into range displacements, which are small, specially for spaceborne platforms and slow moving targets. Across-track accelerations and/or along-track velocities affect range curvature, i.e., the quadratic component of the RCM, and so residual RCM is expected after RCMC for the stationary world.

All these considerations suggest the implementation of an adaptive SAR processing, both in the RCMC and azimuth reference focusing function, adapted to the target Doppler parameters f_{DC} and $K_a(\vartheta_t)$. Fig. 5.5 sketches a simplified block diagram of the adaptive RD SAR processor implemented following the algorithm described in [73]. The basis of this processor is flexibility and modularity in a way that single or multichannel airborne and spaceborne data can be treated.

From Fig. 5.5 four main modules can be distinguished: range compression (RC), secondary range compression (SRC), range cell migration correction (RCMC) and azimuth compression (AC). In a first step and as detailed in Fig. 5.6a, the RC is performed as a matched filter operation in the range frequency azimuth time domain through a multiplication with a quadratic phase. Under the principle of stationary phase (PSP) a parabolic phase in time domain transforms also to a parabolic phase in the frequency

domain [150]. The type of windowing to reduce the sidelobes as well as the processing bandwidth can be adjusted.

A second optional module, SRC, corrects for the misfocusing caused by the strong cross coupling between range and azimuth in the case of high squint angles [73]. For airborne platforms this angle Ψ can be in the order of 10 degrees for some acquisitions. In Fig. 5.6b, the block diagram of the implemented SRC module is shown, where two options (accurate and approximate) have been included according to [73]. Both are based on a linear FM matched filter operation, where the FM rate can be expressed as

$$K_{src}(f_d, R_{ref}, \boldsymbol{\vartheta}_t) = \frac{|K_a(\boldsymbol{\vartheta}_t)|c_0^2 D^3(f_d, R_{ref}, \boldsymbol{\vartheta}_t)}{\lambda^2} \text{ for } |f_d| \leq \frac{\text{PRF}}{2} - f_{DC}(\boldsymbol{\vartheta}_t) \quad (5.7)$$

where $D(f_d, R_{ref}, \boldsymbol{\vartheta}_t)$ refers to the migration factor

$$D(f_d, R_{ref}, \boldsymbol{\vartheta}_t) = \sqrt{1 - \frac{f_d^2}{\frac{2}{\lambda} R_{ref} |K_a(\boldsymbol{\vartheta}_t)|}} \quad (5.8)$$

In the accurate approach, the SRC is performed in the range frequency Doppler domain for a reference range gate R_{ref} , which is precise for range invariant regions³. The approximate SRC option is applied in the range frequency azimuth time domain, considering the Doppler frequency as constant, i.e., $f_d = f_{d_{src}}$ in (5.7), and hence the correction is accurate only for this reference frequency.

³To update the range dependence R_{ref} , the whole image could be divided into small range blocks such that the correction amount held constant within the block.

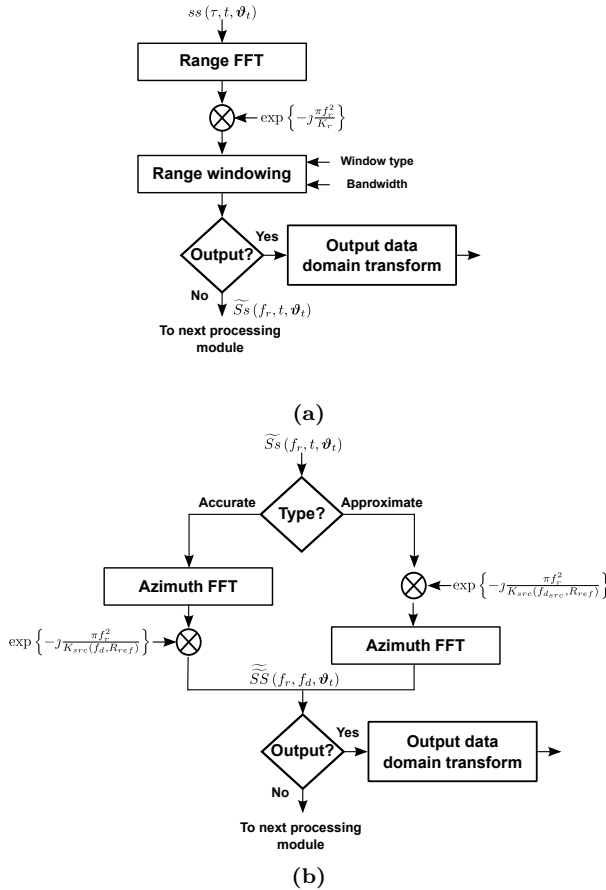


Figure 5.6: Block diagrams of (a) range compression (RC) and (b) secondary range compression (SRC).

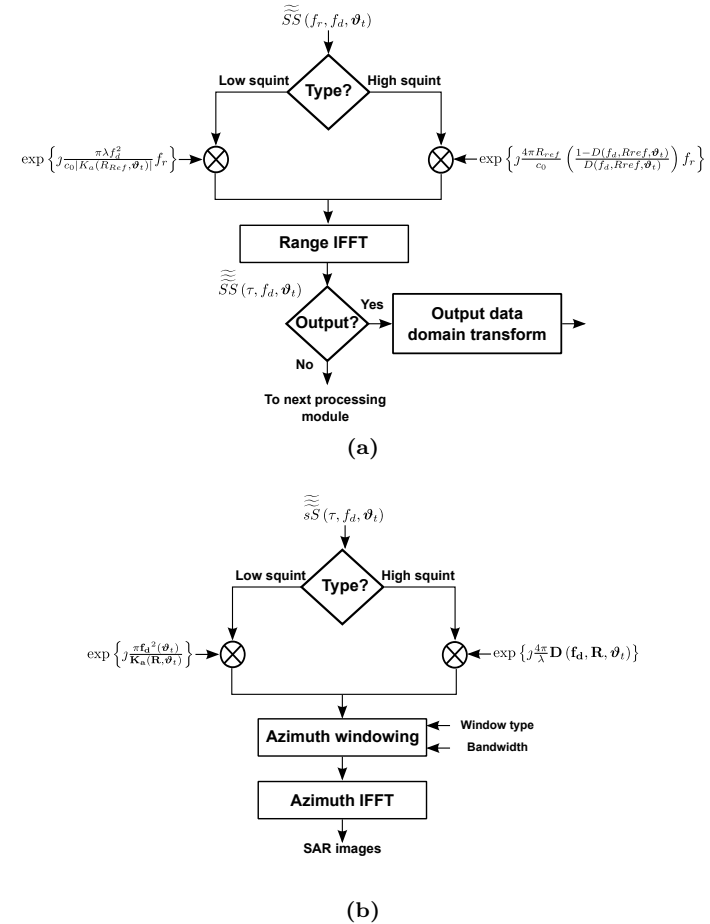


Figure 5.7: Block diagrams of (a) range cell migration correction (RCMC) and (b) azimuth compression (AC).

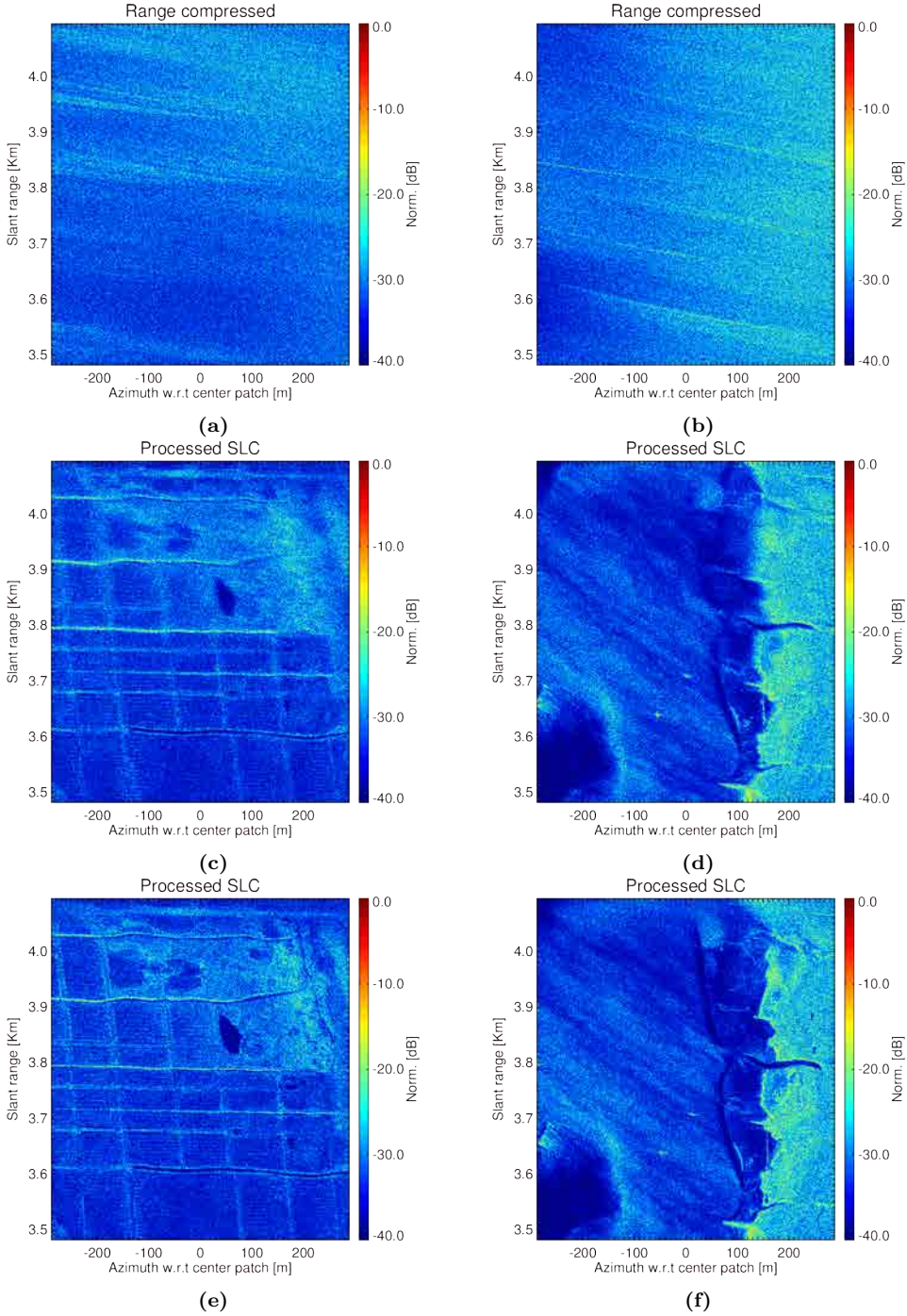


Figure 5.8: Processed F-SAR images (SSC) over the North Sea (Elbe river), land (left column) and sea (right column) patches are shown: (a)-(b) range-compressed data; (c)-(d) SAR images using low squint approach in the processing without SRC and azimuth focusing with a reference range; and (e)-(f) SAR images using high squint approach with SRC and range-dependent azimuth compression.

The third processing block corresponds to the range cell migration correction [see Fig. 5.7a]. Two different options (low and high squint cases) have been integrated. In both cases the RCMC is carried out in the range frequency Doppler domain as a bulk phase correction for a reference range gate R_{ref} .

The last module in the RD processing chain is the azimuth focusing [see Fig. 5.7b], where the low and high squint cases have been considered. The azimuth compression is performed in the range Doppler domain via a phase correction, which could be performed either using a reference gate or as a range dependent compensation.

Fig. 5.8 shows different single channel SAR images obtained using the implemented processor over range-compressed data [Figs. 5.8a-b], acquired by the airborne F-SAR sensor over the Elbe's Mouth in the North Sea (data take *09tdxsim0104*). The acquisition and processing parameters are summarized in Table 5.1. Fig. 5.8c and Fig. 5.8d depict the result of processing, respectively, a land and a sea patch, with a low squint approach and a bulk azimuth compression assuming a reference range (center of the scene). As expected the image quality and focusing sharpness improves substantially when considering a high squint approach with SRC and a range-dependent azimuth focusing, see Fig. 5.8e and Fig. 5.8f.

A SAR-GMTI system is typically required to detect and produce high resolution images of the moving targets. Therefore, the degradation effects caused by the target's motion must be compensated, such that the SCNR can be recovered when compared to the SWMF approach. In this sense, and assuming no *a priori* information regarding target motion is available, a RD focusing algorithm based on a MFB has been implemented. In Fig. 5.9, the output of such a processor is shown for three different sets of motion target parameters. A specific patch of the F-SAR data over the Elbe's mouth has been processed, containing a moving vessel named V4. This complex focusing algorithm implements an adaptive SRC, RCMC and azimuth focusing.

The improvement in the imaging quality can be clearly appreciated when considering an adaptation on the across-track acceleration, $a_z = -0.095 \text{ m/s}^2$ [Fig. 5.9b] or on the along-track velocity, $v_x = 1.8 \text{ m/s}$ [Fig. 5.9c], compared to the conventional SWMF [Fig. 5.9a]. As expected, across-track accelerations and along-track velocities affect the quadratic term $R(t, \boldsymbol{\vartheta}_t)$, and so the Doppler rate $K_a(\boldsymbol{\vartheta}_t)$, producing indistinguishable effects on the image. This is demonstrated by the similar responses of the two matched filters in Figs. 5.9b-5.9c. Therefore, it is not possible to separate both motion parameters without any *a priori* information. Nevertheless, Baumgartner has proposed in [16] an acceleration-independent method to estimate the along-track velocity component. This information can be fed to the MFB, providing an estimation of the across-track acceleration.

For airborne data, where synthetic apertures are longer, the sensitivity of the matched filter to variations on the motion parameters is much higher than for the spaceborne case. Big vessels (such as V4) are complex targets, composed of multiple scattering centers, which could have different induced motion parameters. This adds more complexity to the whole adaptive imaging process. Fig. 5.10 shows the response of the MFB in its two-dimensional representation for different motion parameters' adaptation. The analysis have been done over three extracted range lines along the vessel (from near to far range), as indicated by the dashed-lines in Fig. 5.9c. For the across-track acceleration based MFB

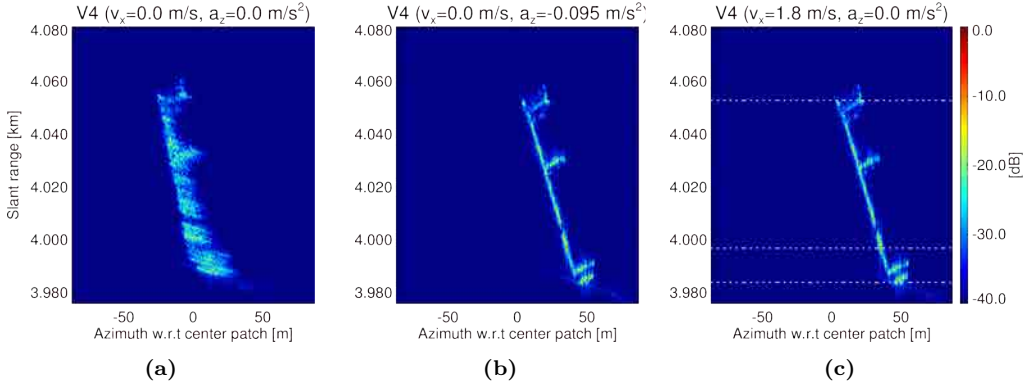


Figure 5.9: F-SAR processed images using the implemented adaptive RD processor on vessel V4 over the Elbe's mouth (*09tdxsim0104*): (a) SWMF, (b) adaptation on the across-track ground acceleration $a_z = -0.095\text{m/s}^2$ and (c) on the along-track ground velocity $v_x = 1.8\text{m/s}$ (three range lines extracted for MFB validation are indicated as dotted white lines).

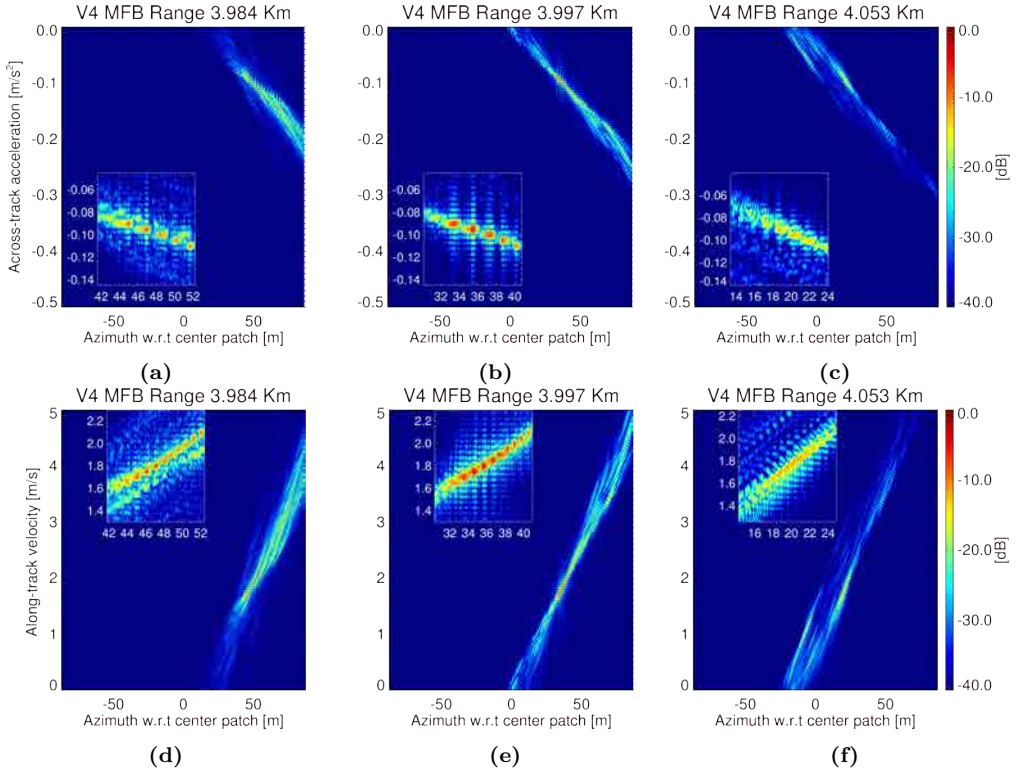


Figure 5.10: MFB maps on three extracted range lines [see 5.9c] for vessel V4 over the Elbe's mouth F-SAR acquisition (*09tdxsim0104*): (a)-(c) across-track ground acceleration variation and (d)-(f) along-track velocity variation (zoomed areas around the maximum are also included).

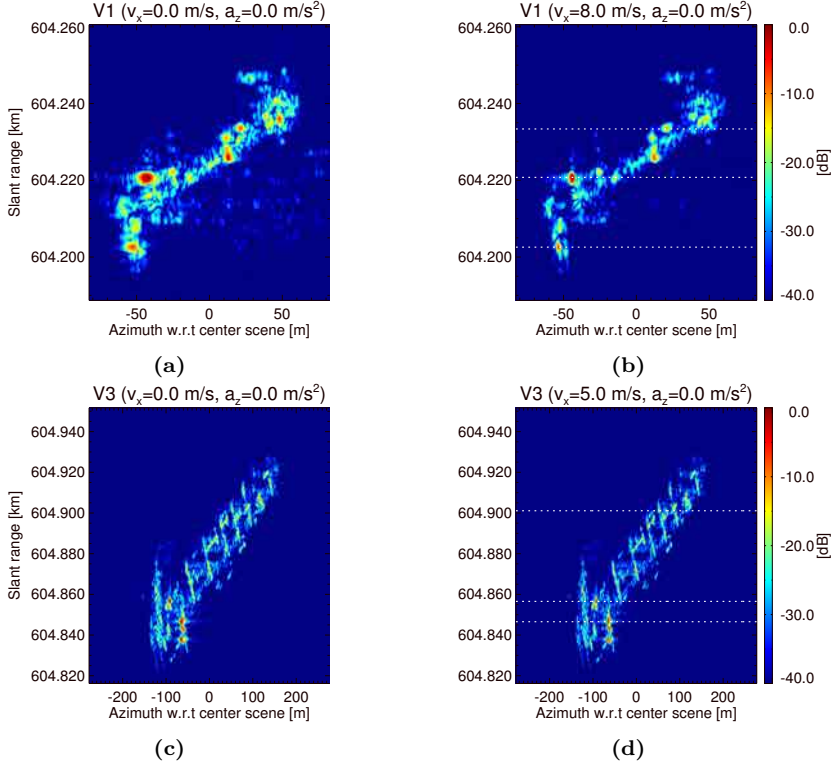


Figure 5.11: TSX-DRA processed images (DRAFore channel) using the implemented adaptive RD processor on vessels V1 and V3 over the Strait of Dover [see Fig. 5.4]: (a) SWMF over V1; (b) adaptation on the along-track velocity $v_x = 8.0$ m/s over V1; (c) SWMF over V3; (d) adaptation on the along-track velocity $v_x = 5.0$ m/s over V3 (three range lines extracted for matched filter bank validation are indicated as dotted white lines).

[Figs. 5.10a-c], the peak response for the different range lines is concentrated around $a_z = -0.095$ m/s², while for the along-track velocity based MFB [Figs. 5.10d-f] it is close to $v_x = 1.8$ m/s. From the similar MBF response of the vessel V4 as a function of range, it can be stated that V4 was not performing any maneuver (e.g. turning) during the formation of the synthetic aperture, which otherwise could have lead to much differentiated defocusing between the bow and stern.

The implemented adaptive processor has been also validated for spaceborne data, using the TSX-DRA acquisition over the Strait of Dover as shown in Fig. 5.11. The processing has been applied over two vessels, V1 and V3, considering a SWMF [Figs. 5.11a and 5.11c] and an adaptation on v_x [Figs. 5.11b and 5.11d]. For clarity in the representation, the images in Fig. 5.11 are the interpolated versions of the RD processor output, with an interpolation factor of 8 in range and azimuth. The improvement in the image quality comparing the MFB and the SWMF is not as important as in the airborne case. This is because for the spaceborne case the coherent processing interval is under 1 second. The azimuth sharpness gets better for an adaptive processing, especially evident in the brightest scatterers of vessels V1 and V3.

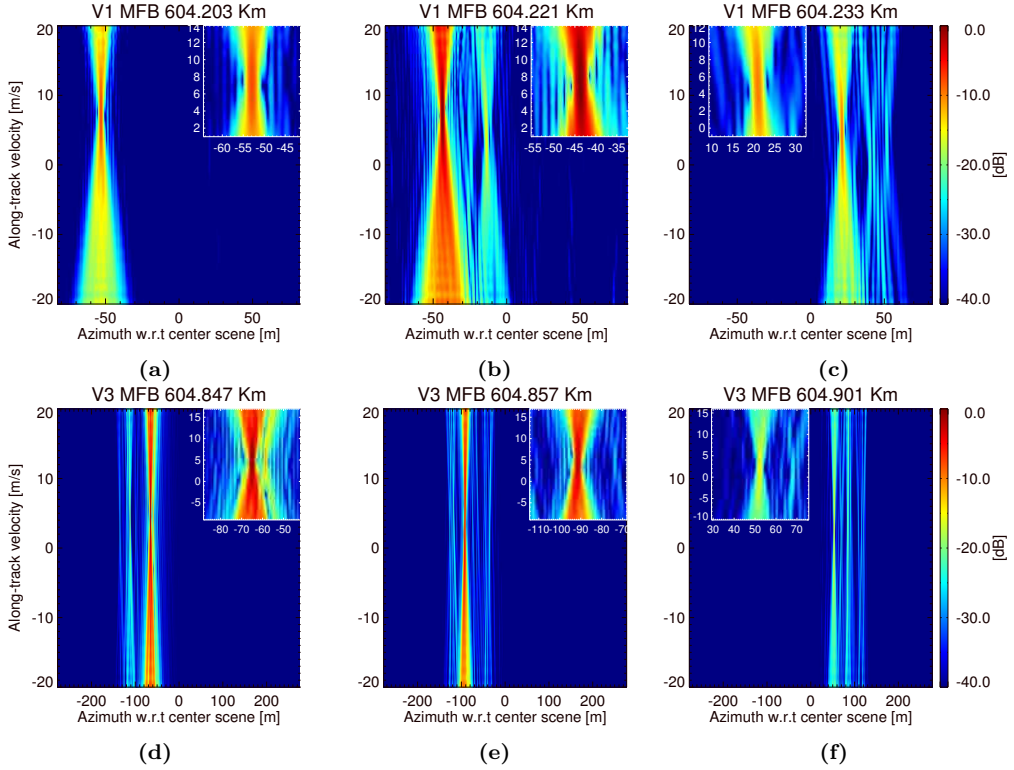


Figure 5.12: MFB maps (along-track velocity variation) on three extracted range lines (see Fig. 5.11) for vessel V1 and V3 over the Strait of Dover TSX-DRA acquisition: (a)-(c) V1 and (d)-(f) V3 (zoomed areas around the maximum are also included).

Analogous to the analysis done with the F-SAR data, the MFB maps for three extracted range lines over both vessels are shown in Fig. 5.12. The vertical axis corresponds to the along-track velocity variation considered in the MFB operation, and the horizontal axis represents the azimuth position (w.r.t. scene center). For representation purposes, the results shown in Fig. 5.12 correspond to the interpolated (factor 8) results of a MFB sweeping v_x from -20 m/s to 20 m/s with a 1 m/s step. The different images in Fig. 5.12 are normalized to the maximum response of the MFB along the corresponding vessels. As a general trend and unlike the airborne case, the sensitivity of the MFB as a function of v_x is comparatively lower. For V1, v_x of 8 m/s provides the highest peak response of the brightest point along the vessel (at a slant range of 604.221 Km), with an improvement of around 5 dB w.r.t the SWMF approach. The variation of the MFB along V1 is kept more or less constant, with a slightly better response at v_x of 5 m/s for the scattering point with a slant range of 604.233 Km [Fig. 5.12c]. As far as V3 is concerned the best response is obtained when v_x is 5 m/s, where the improvement factor (IF) is 2 dB over the SWMF case for the brightest scattering center (at a slant range of 604.847 Km).

Target detection could be performed also using such MFB maps applying a certain amplitude thresholding. MFB is an attractive solution to resolve multi-target scenarios providing simultaneously target separation as well as parameter estimation (Doppler rate).

Nevertheless, the computational cost and subclutter conditions (reduced SCNR scenarios) are two issues that limit its operation.

5.2.2 GMTI at SAR image level

In classical multichannel SAR-GMTI processing, moving target detection is performed in a pixel basis on the processed SAR images by means of either phase subtraction, ATI or both phase and magnitude difference, DPCA. These techniques were originally developed for dual-receive channel configurations. Then, a generalization of the DPCA for any number of receiving channels has been lately proposed by Cerutti *et al.* [29]. These techniques have been already introduced in chapter 2, and a detailed description of these algorithms can be found in [29, 49].

Fig. 5.13 depicts the block diagram of the implemented SAR-GMTI processing chain operating at image level, which integrates EDPCA, DPCA and ATI algorithms. In the conception of this processing chain, the modularity and flexibility have been the main driven requirements in order to fit any possible input data from any possible sensor configuration. Three main modules can be differentiated: *pre-processing*, *MFB adaptive SAR focusing* and *SAR-GMTI processing*.

The first one corresponds to the *pre-processing* stage, where five different sub-processing stages can be optionally activated:

1. *Inverse azimuth SAR processing* is carried out when the original experimental data is a set of focused SSC images, as in TSX-DRA products. Based on the RD processor presented in the previous section, an azimuth inverse SAR compression is performed and the RCMC is re-introduced, using the processing parameters specified in the SSC products.
2. *Range compression* of the raw data products based on the module in Fig. 5.6a.
3. *Coregistration* of the different channels with respect to a reference. The coregistration or spatial alignment of the different channels is performed in both the azimuth and the range dimension. In this sense, two different coregistration options have been included: (i) a 2D approach that performs linear phase ramps compensation in the 2D spectral domain, such that the ATI phase (azimuth baseline) and the range difference (across-track baseline) are estimated from the given input data in the range frequency Doppler domain; (ii) a two-step approach, where the coregistration in the two dimensions is performed sequentially by a phase ramp removal estimated in the corresponding 1D spectral domains, i.e., range Doppler and range frequency azimuth-time domains, or vice versa, depending on the selected option, azimuth-range or range-azimuth.
4. *Aperture switching and baseline delays compensation* is optionally performed, when no accurate data-based coregistration is possible. This is due to non-spatially homogeneous clutter conditions and/or reduced clutter-to-noise ratio (CNR). The accurate knowledge of the baselines and positions of the receiving antennas from on-board inertial system measurements and/or ground characterization is an attractive alternative solution. In any case, accurate (azimuth/along-track) coregistration via interpolation (phase ramp removal in frequency) is achieved whenever the Nyquist sample theorem is fulfilled, i.e., the PRF is high enough to avoid signal

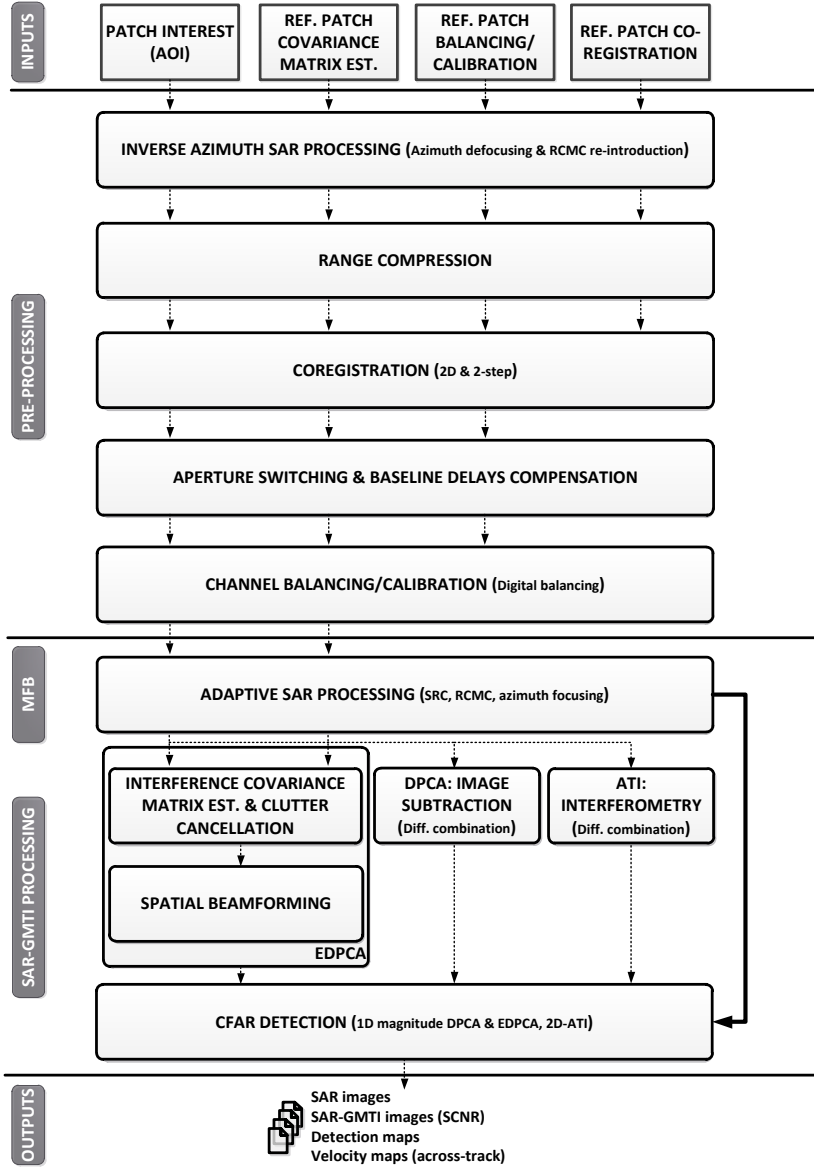


Figure 5.13: Block diagram of the integrated EDPKA, DPCA and ATI processing.

aliasing in the Doppler domain. These ambiguities can cause additional decorrelation between channels due to coregistration errors, as they fold back in the Doppler band ($\pm \text{PRF}/2$) and the phase ramp removal leaves constant phase errors, [29, 151]. Therefore a degradation on the GMTI performance capability is expected as already analyzed in Chapter 4.

5. *Channel calibration/balancing* is performed to equalize the response of the different channels. To obtain precise detection performance, the response of the different

channels should be well calibrated and balanced; otherwise, phase and magnitude channel and/or antenna imbalances could impair the GMTI operation. Section 5.2.4 briefly describes the different channel balancing methodologies that have been considered in the processing chain.

Once the pre-processing operations have been performed, the next stage corresponds to the *adaptive SAR processing*, already presented in section 5.2.1, synthesizing several filters, each one matched to a different set of kinematic parameters (MFB). For each filter an adaptive SRC (for F-SAR data), RCMC and azimuth focusing are performed trying to maximize the SCNR of the targets prior to GMTI processing.

The next stage carries out the *SAR-GMTI processing* of the data per filter iteration:

1. In the EDPCA case, the interference covariance matrix is estimated and inverted for clutter cancellation prior to spatial beamforming, which is adapted to the same target parameters of the bank of filters:
 - The covariance matrix estimation and clutter cancellation can be performed using two different approaches. In the first one, a specific portion of the image or the whole image is used for estimation purposes. The inverse of this matrix is applied over the whole image (for clutter cancellation), reducing the computational cost, but at the expense of possible GMTI degradation in case of non-homogeneous clutter background⁴. The second approach, which requires a higher computational effort, is based on a sliding window with a pixel basis displacement. The clutter cancellation is performed pixel by pixel, using the area that surrounds a given guard zone around the pixel under test.
 - The SAR-GMTI processed image (for each filter) is fed to a parametric CFAR detector based on the magnitude of the data. Similar to the covariance matrix estimation and clutter cancellation, two operative options are integrated for the estimation of the residual interference statistical parameters, either a specific portion of the image is selected or instead a sliding window approach is used.
2. For DPCA and ATI algorithms, complex image subtraction and complex conjugate multiplication are performed, respectively, for the selected pair of channel combinations and for each filter of the MFB. Then, the different SAR-GMTI images are passed through parametric CFAR detectors, 1D (magnitude) and 2D (magnitude and phase) for DPCA and ATI, accordingly.

From the analysis and processing of the multichannel experimental data, it has been observed that channel calibration/balancing, coregistration and covariance matrix estimation steps play a main role in the proper GMTI operation, when using the data of interest for that aim. In this sense and as depicted in Fig. 5.13, the possibility of using patches or regions different from the one to be processed has been integrated in the processing chain. Therefore, dedicated reference patches can be optionally used for interference covariance matrix estimation, channel balancing and coregistration, such that the processing stages over the different patches can be interconnected as shown in Fig. 5.13.

⁴The impact of non-homogeneity can be solved dividing the whole image scene in several homogeneous invariant regions, applying the specific estimated covariance matrix.

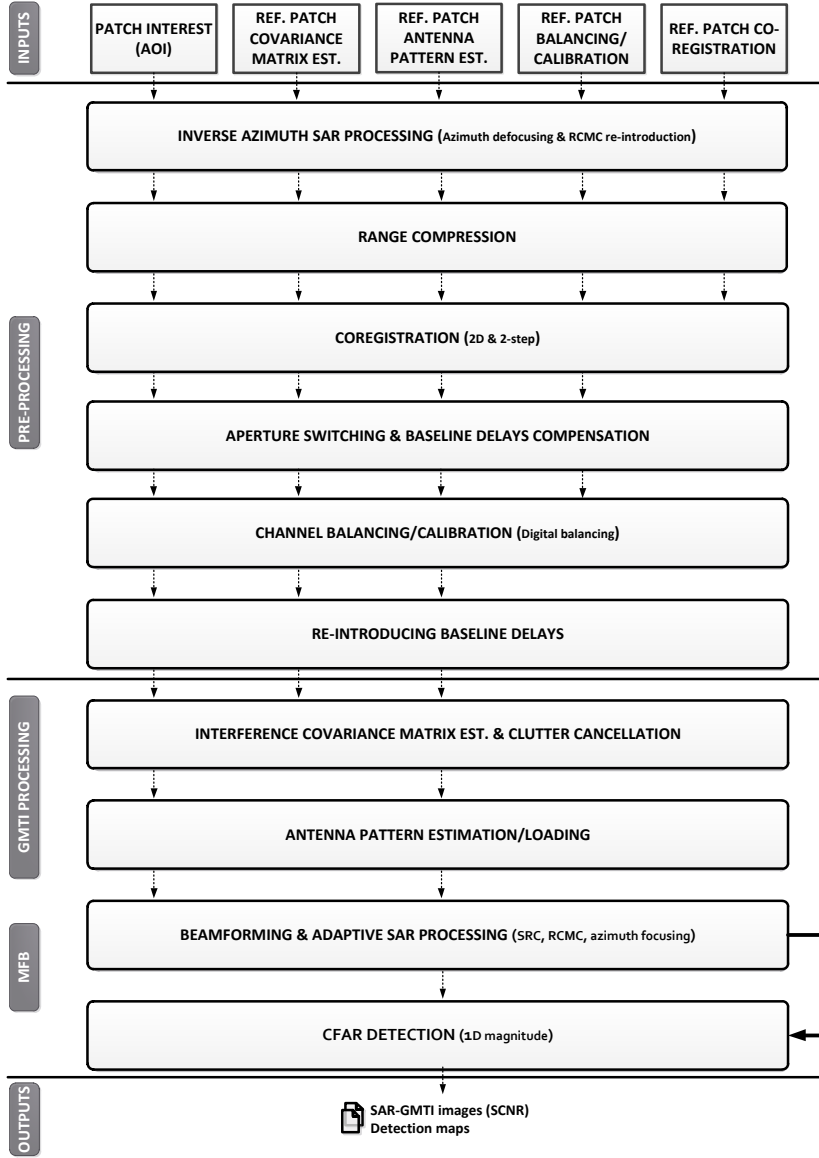


Figure 5.14: Block diagram of the ISTAP processor.

5.2.3 GMTI at range-compressed image level

It is well known that sufficient detection performance is only achieved, when using configurations with more than two receiving antennas in junction with full STAP [21]. DPCA, ATI and EDPKA methods, which exploit the SCNR enhancement after coherent integration (SAR focusing), operate in the SAR image domain; whereas conventional STAP methods, such as the suboptimal post-Doppler STAP are applied in the range-compressed data domain [14, 44].

In [28], Cerutti *et al.* propose the so called imaging STAP (ISTAP), which is a combination of post-Doppler STAP and SAR focusing. A similar approach has been also investigated by Cristallini in [41], where a post-Doppler STAP approach is integrated in a MFB based on a chirp scaling algorithm (CSA), known as multichannel-bank of CSA (MC-BCSA). In both cases, clutter cancellation is performed in the range-compressed Doppler domain using only the spatial DoF. It is assumed that the time base (SAR acquisition time) is sufficiently long to allow asymptotic decoupling of the different Doppler frequency bins [44, 45]. Unlike conventional post-Doppler STAP, there is no segmentation of the time basis into small coherent processing intervals (CPIs) and hence the whole data is coherently integrated. This provides an increase in the SCNR at the final SAR-GMTI image, making ISTAP well suited for spaceborne configurations.

Fig. 5.14 shows the flowchart for the implemented ISTAP processing chain. Three main modules can be differentiated: the first corresponds to the *pre-processing* stage, which includes all the processing steps indicated in Fig. 5.13. A new submodule has been included after channel balancing, which re-introduces baseline delays (coregistration process in the along-track dimension) since the post-Doppler STAP processor requires this inherent systematic phase.

The second module carries out the *interference covariance matrix estimation and clutter cancellation* (via covariance matrix inversion) in the range-compressed Doppler domain. For these combined operations two options have been considered: (i) for each Doppler bin a set of range lines are used to estimate a single covariance matrix applied over the whole set of ranges; (ii) a range sliding window approach (with higher computational burden), where for each range of interest a guard zone is used to exclude the presence of moving targets. From the computational cost point of view ISTAP is more efficient compared to EDPCA as the clutter covariance estimation and clutter cancellation is performed only once and not for every filter of the MFB as EDPCA does.

The last stage in Fig. 5.14 is devoted to perform the *spatial beamforming and azimuth SAR focusing*, both adapted to moving target parameters via a MFB. The spatial beamforming operation, using the beamformer $\mathbf{d}(\mathbf{u}_t, f_d, \vartheta_t)$, coherently combines the clutter canceled range-compressed data to maximize the SCNR for the specific matched filter. This step is performed in the range-Doppler domain and it requires the knowledge of the antenna pattern. This information can be *a priori* known, by means of on ground measurements or from calibration campaigns, as it is the case of TSX. However, for the processed F-SAR data sets, the quality of the available antenna pattern measurements was not good and so it should be estimated from the data itself. A magnitude-based CFAR detector is applied over the final ISTAP image, where it is possible to select an isolated region for statistical parameters estimation or, alternatively, using a sliding window.

Analogous to the processing concept presented in section 5.2.2, dedicated reference patches (different from the one of interest) can be optionally used for interference covariance matrix estimation, channel balancing/calibration, coregistration and also antenna pattern estimation. This flexibility in the processing chain is mandatory for a correct operation of the ISTAP processor over the available real data.

Fig. 5.15 illustrates schematically the input block of data⁵ per channel, feeding the

⁵This input portion is either range-compressed data for F-SAR operation or SSC images in the TSX case.

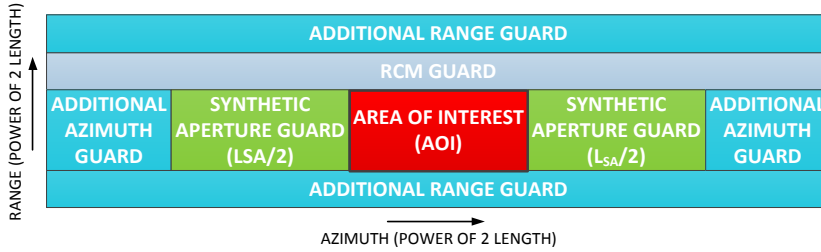


Figure 5.15: Schematic representation of the input data block’s conditioning.

different processing chains. For an area of interest (AOI) to be processed, guards accounting for half of the synthetic aperture L_{SA} (symmetric at both sides in azimuth dimension) should be considered. To ensure a power of two azimuth length of the data block, additional data is included symmetrically at both sides for efficient fast Fourier transform (FFT) based processing. Analogously, additional samples are considered in the range dimension for proper inclusion of the RCM in the far range region and also to ensure the total number of range samples is a power of two.

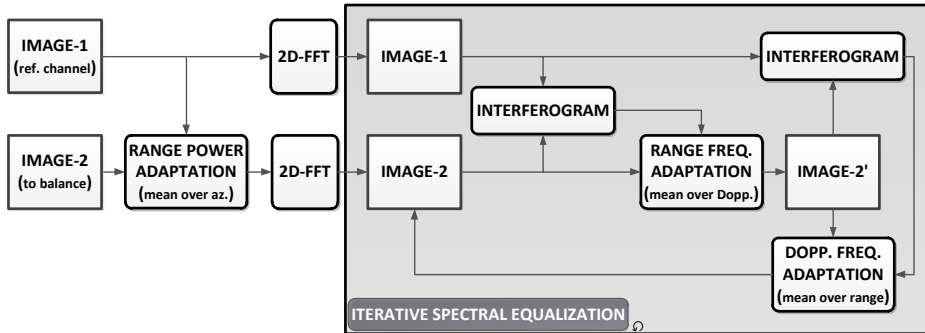


Figure 5.16: Flow chart of the 2D digital balancing (DB) method.

5.2.4 Channel balancing techniques

The 2D adaptive balancing method, from now on referred as digital balancing (DB), represents the core of the different calibration algorithms integrated in the pre-processing step. Originally proposed by Ender [152] and further developed by Gierull [74], it performs a phase and magnitude balancing between the channel transfer functions.

This is an iteratively adaptive method that operates in the 2D frequency domain (range frequency/Doppler), trying to equalize the spectral responses of the different channels even if they are not coregistered, since it removes any phase ramp in the frequency domain [74]. A schematic representation of the 2D digital balancing operation is presented in Fig. 5.16. This sort of method does not modify the reference channel and so it is useful to calibrate the responses of the different channels for configurations with more than two receivers.

Ideally, this 2D adaptive channel balancing algorithm adjusts the second channel spec-

tral response $X_2(f_r, f_d)$ to reference channel one $X_1(f_r, f_d)$ by a least square minimization

$$\min_{H_{1,2}^{(r)}(f_r), H_{1,2}^{(a)}(f_d)} \int \left| X_1(f_r, f_d) - X_2(f_r, f_d) H_{1,2}^{(r)}(f_r) H_{1,2}^{(a)}(f_d) \right|^2 df_r df_d \quad (5.9)$$

where an approximation of the calibration weights $H_{1,2}^{(r)}(f_r)$ and $H_{1,2}^{(a)}(f_d)$ can be iteratively solved via

$$\begin{aligned} X_2^{(n+1)}(f_r, f_d) &= X_2^{(n)}(f_r, f_d) H_{1,2}^{(n,r)}(f_r) = \\ &X_2^{(n)}(f_r, f_d) \frac{\int X_1(f_r, f_d) X_2^{(n)*}(f_r, f_d) df_d}{\int \left| X_2^{(n)}(f_r, f_d) \right|^2 df_d}, \\ X_2^{(n+2)}(f_r, f_d) &= X_2^{(n+1)}(f_r, f_d) H_{1,2}^{(n+1,a)}(f_d) = \\ &X_2^{(n+1)}(f_r, f_d) \frac{\int X_1(f_r, f_d) X_2^{(n+1)*}(f_r, f_d) df_r}{\int \left| X_2^{(n+1)}(f_r, f_d) \right|^2 df_r} \end{aligned} \quad (5.10)$$

In (5.10), $X_2^{(n)}(f_r, f_d)$ for $n=0,1,2,\dots$ refers to the iteratively improved calibration of the second channel spectral data. The iterative range frequency and Doppler dependent calibration weights, $H_{1,2}^{(n,r)}(f_r)$ and $H_{1,2}^{(n+1,a)}(f_d)$ defined in (5.10), can be understood as a measure of complex coherence between the channels to be calibrated. This digital channel equalization can be performed over a specific spectral extension

$$\begin{aligned} f_d &= \left[f_{DC} - \frac{B_{a,c}}{2}, f_{DC} + \frac{B_{a,c}}{2} \right], \\ f_r &= \left[-\frac{B_{r,c}}{2}, \frac{B_{r,c}}{2} \right] \end{aligned} \quad (5.11)$$

to avoid considering spectral regions with reduced CNR conditions and/or high ambiguities' impact. In (5.11), $B_{a,c}$ and $B_{r,c}$ correspond to the azimuth (Doppler) and range calibration bandwidths, respectively.

In practice, and following the implementation proposed by Gierull in [74], the iterative balancing process in (5.10) stops if one of two conditions is met:

1. The number of iterations n is greater than a specified maximum.
2. The difference between the mean values of the range frequency and Doppler dependent calibration weights is smaller than a threshold, i.e.,

$$\left| \int H_{1,2}^{(n,r)}(f_r) df_r - \int H_{1,2}^{(n+1,a)}(f_d) df_d \right| \leq \eta_{thres} \quad (5.12)$$

When applying DB over real data, it has been observed that there is an important degradation of the second channel response in terms of magnitude due to channel decorrelation. Spectral components away from the so called mainlobe response have degraded CNR conditions and/or higher impact of the ambiguities. This would require to drastically reduce the calibration bandwidths, especially for the case of TSX in the DRA

configuration, where the reduced CNR and the azimuth ambiguities are issues of major concern. In this regard, a first alternative has been considered, where only the phase component of the calibration weights $H_{1,2}^{(n,r)}(f_r)$ and $H_{1,2}^{(n+1,a)}(f_d)$ is included.

Based on the iterative channel balancing principle, a different and simplistic approach, referred from now on as modified digital balancing (MDB), has been implemented to avoid magnitude degradation of second channel response for those spectral components away from the mainlobe response. For this methodology the complex iterative calibration weights are computed as

$$\begin{aligned} H_{1,2}^{(n,r)}(f_r) &= \frac{\int |X_1(f_r, f_d)| df_d}{\int |X_2^{(n)}(f_r, f_d)| df_d} \exp \left\{ j \angle \left[\frac{\int X_1(f_r, f_d) X_2^{(n)*}(f_r, f_d) df_d}{\int |X_2^{(n)}(f_r, f_d)|^2 df_d} \right] \right\}, \\ H_{1,2}^{(n+1,a)}(f_d) &= \frac{\int |X_1(f_r, f_d)| df_r}{\int |X_2^{(n+1)}(f_r, f_d)| df_r} \exp \left\{ j \angle \left[\frac{\int X_1(f_r, f_d) X_2^{(n+1)*}(f_r, f_d) df_r}{\int |X_2^{(n+1)}(f_r, f_d)|^2 df_r} \right] \right\} \end{aligned} \quad (5.13)$$

For the different calibration methodologies, a range power (profile) adaptation of the second channel to the first is performed at (range-compressed) image level before the iterative two-dimensional spectral balancing, as suggested in [153]. This correction calibrates only the amplitude of the channel to be equalized using an averaging along azimuth for each range bin of the range-compressed image.

Differences between each channel and the reference one, named *channel imbalances*, can be computed in the two-dimensional spectral domain as [148]

$$I(f_{r,k}, f_{d,l}) = \frac{\sum_{i=-L_r}^{L_r} \sum_{j=-L_a}^{L_a} X_1(f_{r,k+i}, f_{d,l+j}) X_2^*(f_{r,k+i}, f_{d,l+j})}{\sum_{i=-L_r}^{L_r} \sum_{j=-L_a}^{L_a} |X_1(f_{r,k+i}, f_{d,l+j})|^2} \quad (5.14)$$

where a moving average filter (boxcar) is applied, using $2L_r + 1$ range frequency and $2L_a + 1$ Doppler neighboring bins.

5.3 F-SAR data

5.3.1 Data analysis

In this section a preliminary analysis of the multichannel data to be processed has been carried out. This study has been useful to provide some insights in the required channel balancing/calibration strategies to be considered in the SAR-GMTI processing as well as to identify possible anomalies in the available data.

In a first iteration of the data processing, a range (elevation) dependent antenna pattern compensation was performed on the available range-compressed data and analogously an azimuth pattern compensation during the azimuth focusing. The processing of this data showed that the azimuth pattern considered in the correction was not the real one, as it introduced artificially ambiguous vessel responses. Taking into account these considerations, no antenna pattern correction, either in range or in azimuth, has been

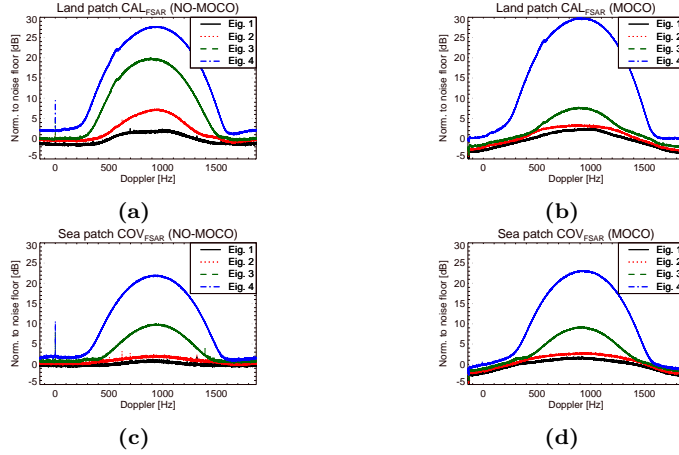


Figure 5.17: Average (along range) eigenvalue spectra (normalized to the average noise floor) versus Doppler of the range-compressed data before (left column) and after (right column) MOTion Compensation (MOCO): (a)-(b) land region CAL_{FSAR} ; and (c)-(d) sea patch COV_{FSAR} .

applied on the data to be processed. Therefore, it is not possible to extract information that requires absolute calibration of the data, e.g., the radar backscattering coefficient σ^0 . In this sense, the goal of the processing is to apply adequate relative calibration (balancing) between the different channels trying to equalize their response, ensuring a better operation of the different SAR-GMTI techniques.

The analysis of the eigenvalue (spectral) distribution is a good indicator of the required number of spatial degrees for clutter cancellation. In Fig. 5.17 the average (along range) eigenvalue distribution as a function of the Doppler frequency is represented, before MOTion Compensation (MOCO) [Figs. 5.17a and 5.17c] and after MOCO [Figs. 5.17b and 5.17d]. Land CAL_{FSAR} [Figs. 5.17a-b] and sea COV_{FSAR} [Figs. 5.17c-d] patches have been considered. The different average spectra are normalized to the noise floor, which has been estimated as the mean value (over range and Doppler) of the smallest eigenvalue.

After MOCO [Figs. 5.17b and 5.17d], it can be clearly observed that a predominant eigenvalue (indicating the level of CNR after coherent combination of the different channels) is present in the land patch (25 dB above the second eigenvalue). For the sea patch the two highest eigenvalues get closer, due to the reduced CNR and the higher sea clutter internal decorrelation. In the land patch case and after MOCO, two channels may be sufficient for clutter cancellation. No MOCO on the data translates into an increase of the second and third eigenvalues, clearly visible in the eigenvalue distribution over the land patch [Fig. 5.17a]. This behavior can be attributed to the higher impact of channel decorrelation induced by the non-proper compensation of motion induced phase errors. For the sea patch [Fig. 5.17c], clutter decorrelation keeps being the prevalent effect as the second eigenvalue has not increased compared to the scenario with MOCO [Fig. 5.17d].

For appropriate GMTI operation any imperfections and/or imbalances between the different channels must be properly compensated. In the case of ATI processing, such residual phase errors could shift the phase component of the PDF used for CFAR de-

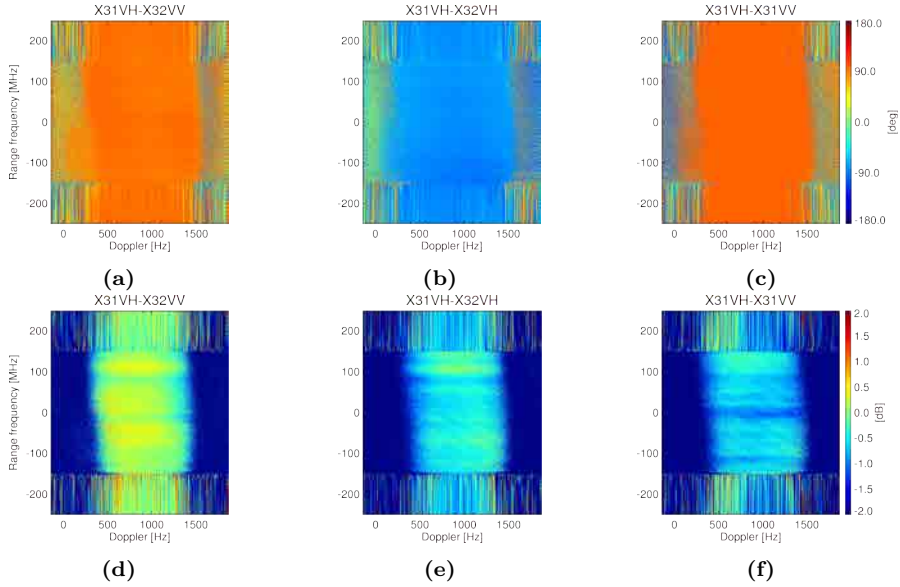


Figure 5.18: F-SAR channel imbalances w.r.t reference X31VH channel for region CAL_{FSAR} before calibration and as a function of range frequency and Doppler (X32VV, X32VH and X31VV from left to right): (a)-(c) phase imbalances in degrees; and (d)-(f) amplitude imbalances in dB.

tection and so impair target detection as well as the across-track velocity estimation. Analogously, clutter subtraction techniques as DPCA and EDPCA, require also balancing of both phase and magnitude. The amplitude and phase imbalances defined in (5.14) over region CAL_{FSAR} and after MOCO are represented in Fig. 5.18 as a function of the range frequency and Doppler for different channels, being X31VH the reference. In this case a boxcar filtering of 3×3 has been used to reduce the noisy-like pattern and enhance the image quality. Phase imbalances can be clearly recognized in Figs. 5.18a-c, which are almost invariant with range frequency and Doppler within the clutter bandwidth and appear basically as a phase offset. Noticeable amplitude imbalances can be observed, which vary as a function of range and Doppler frequencies, between -0.5 dB and 0.5 dB for the different channels.

The different calibration strategies described in section 5.2.4, based on an iterative spectral equalization, have been considered to reduce channel imbalances. The spectral domain of calibration has been limited to 900 Hz in Doppler and 300 MHz in range frequency around the corresponding spectral centroid to avoid an excessive degradation of inter-channel correlation due to reduced CNR conditions. In Fig. 5.19 the phase imbalances corresponding to channel X31VV w.r.t X31VH are represented after calibration with the original DB technique proposed by Gierull in [74]. A significant reduction of the phase imbalances is achieved; analogously, phase errors for channels X32VH and X32VV are also reduced. Similar results are obtained for the other two alternative calibration methodologies, which exploit the phase compensation of the original DB approach.

Fig. 5.20 shows the amplitude imbalances for channel X31VV w.r.t X31VH after

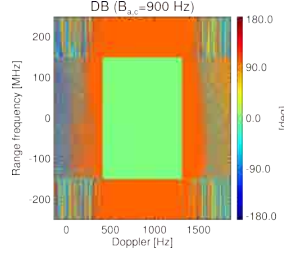


Figure 5.19: F-SAR X31VV phase imbalance w.r.t reference X31VH channel for region CAL_{FSAR} after digital balancing and as a function of range frequency and Doppler (calibration bandwidths in range frequency $B_{r,c}$ and Doppler $B_{a,c}$ of 300 MHz and 900 Hz, respectively).

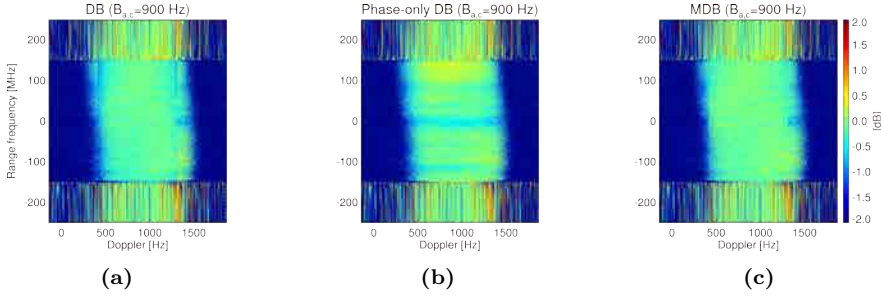


Figure 5.20: F-SAR X31VV amplitude imbalances w.r.t reference X31VH channel for region CAL_{FSAR} after channel balancing and as a function of range frequency and Doppler (calibration bandwidths in range frequency $B_{r,c}$ and Doppler $B_{a,c}$ of 300 MHz and 900 Hz, respectively): (a) digital balancing (DB); (b) phase-only DB; and (c) modified digital balancing (MDB).

channel calibration with three different strategies. Compared to case with no balancing [Fig. 5.18f], it can be generally stated that a reduction in the amplitude imbalances has been achieved. This improvement is more uniform over range frequency and Doppler for the original and modified DB approaches [Figs. 5.20a and 5.20c], compared to the phase-only DB approach [Fig. 5.20b]. When using the original DB technique a slight degradation at the edges of the Doppler clutter bandwidth (losing effective CNR) can be recognized w.r.t. applying the modified DB strategy.

Similarities in the response of the different calibration methodologies can be noted from the comparative representation of the different channels' Doppler spectra in Fig. 5.21. They have been averaged over the whole range-bins in the range Doppler domain. This suggests that not many differences are expected in terms of GMTI operation when considering any of the balancing algorithms. Extending the calibration bandwidth in the Doppler domain to the whole PRF band, produces an important degradation on the balanced channels when using the original DB technique. This effect gets worse for Doppler bins away from the mainlobe clutter response due to reduction on the channel coherence, as shown in Fig. 5.22a. Nevertheless, for the modified digital balancing (MDB) strategy this degradation is not present in the spectra of the balanced channels [see Fig. 5.22b].

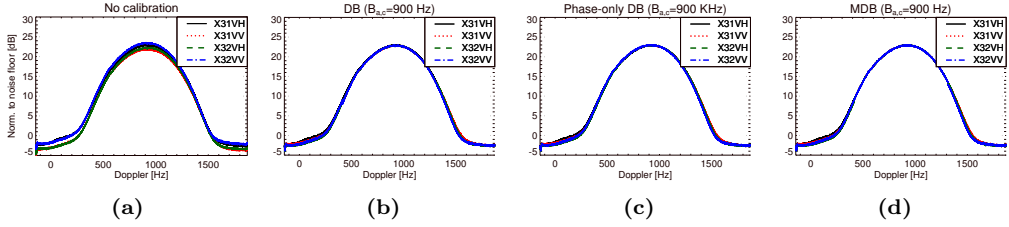


Figure 5.21: F-SAR average Doppler spectra for region CAL_{FSAR} : (a) no channel balancing, (b) DB, (c) phase-only DB and (d) MDB (CAL_{FSAR} patch as reference for channel balancing, calibration bandwidths in range frequency $B_{r,c}$ and Doppler $B_{a,c}$ of 300 MHz and 900 Hz, respectively).

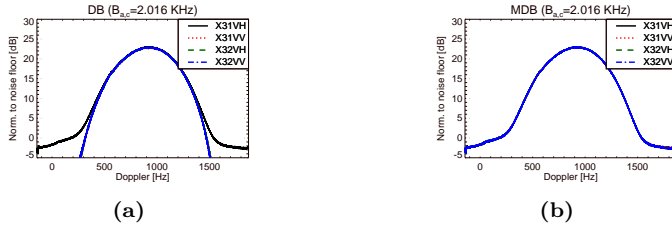


Figure 5.22: F-SAR average Doppler spectra for region CAL_{FSAR} after channel balancing using the whole PRF band for the spectral calibration: (a) DB and (b) MDB.

This is because for MDB the amplitude calibration weights are based on the averaged absolute spectral ratio between the iteratively balanced channel and the reference as defined in (5.13).

When operating over maritime scenarios, it must be taken into account that under specific conditions, the CNR is lower compared to a land patch and hence special care should be taken when applying digital balancing techniques. Moreover, any kind of calibration using the same patch under interest will equalize any interferometric phase between the different channels, compensating even the one related to possible ocean or river currents. This might be of interest for estimation of current velocities. From these considerations, channel balancing of the sea patch of interest AOI_{FSAR} is performed using the calibration weights obtained from reference land patch CAL_{FSAR} .

5.3.2 Processing results

The first part of this section describes the outcomes of the SAR-GMTI processing at image level, considering three main techniques ATI, DPCA and EDPCA. Across-track ground velocity maps for the moving targets as well as for the sea (induced current motion) are generated exploiting the along-track velocity information from the different channel pair combinations. In the second part, an analysis of the SAR-GMTI processing using the ISTAP method is carried out.

5.3.2.1 DPCA processing

DPCA is a classical clutter cancellation technique used in GMTI, based on a simple subtraction of two channels with a given spatial (along-track) separation, once coregistration has been performed. In Fig. 5.23, the output of the DPCA processor applied over the land patch CAL_{FSAR} is shown for two baseline combinations, the longest one X31VH-X31VV (2nd column of figures) and the shortest X31VH-X32VV (3rd column). The different images are represented in terms of the CNR, where the noise floor has been estimated as the average smallest eigenvalue of the covariance matrix eigendecomposition over the whole image patch. For comparison purposes the CNR of the single processed SAR image of channel X31VH is also shown [see Fig. 5.23a]. For a land (fixed) patch, ideally a clutter cancellation down to the noise level should be obtained (CNR around 0 dB). However, no clutter cancellation is observed at DPCA's output for the two baseline combinations, when no channel balancing is applied [Figs. 5.23b-c].

When applying channel equalization using the original DB technique, either on phase and amplitude [Figs. 5.23d and 5.23e], or only on phase [Figs. 5.23f and 5.23g], clutter cancellation is properly performed, with similar results for both approaches. From these results it can be also observed that such clutter subtraction is much better for the shortest baseline (X31VH-X32VV), compared to the longest one (X31VH-X31VV), due to the higher induced decorrelation effects on the latter. The main differences are related to the regions of the image with highest reflectivity, which correspond to the double bounce scattering mechanism induced by the edges of some irrigation canals, properly oriented to the F-SAR sensor. In the upper part of the image, where some irrigated regions with more vegetated areas are present, the degradation in the clutter cancellation capability is more evident for the longer baseline channel combination, due to the higher impact of the channel decorrelation for these areas.

The operation of the DPCA processor over the sea patch of interest AOI_{FSAR} , containing three vessels (V1 lower-right corner, V2 middle-left and V4 upper-left corner), is shown in Fig. 5.24, considering the longest baseline combination (2nd column of figures) and shortest one (3rd column). The different images are represented in terms of SCNR with the same dynamic range, also for the EDPCA and ISTAP results introduced later on. An adaptive SAR imaging to recover the loss in SCNR induced by the motion of the vessels is performed prior to DPCA processing, where the motion parameters $v_z = -5$ m/s and $v_x = 1.8$ m/s have been considered. For comparison purposes the processed SAR images of channel X31VH are also depicted assuming a SWMF and an adaptive focusing ($v_z = -5$ m/s and $v_x = 1.8$ m/s), Figs. 5.24a and 5.24b, respectively. A comparison between the two of them shows the improvement in terms of SCNR and image sharpness over vessels V1 and V4, as already discussed in section 5.2.1. Similar results, as the ones shown in Fig. 5.24, have been obtained for an adaptive SAR processing with motion parameters $v_z = -5$ m/s and $a_z = 0.095$ m/s², since both across-track accelerations and along-track velocities affect the Doppler rate, producing indistinguishable effects on the image.

Proper calibration strategies are necessary to obtain an adequate operation of the DPCA processor as already seen from the analysis performed over the land patch AOI_{FSAR} . Therefore, when no channel balancing is considered, unexpected results can be obtained as shown in Fig. 5.24d, where vessels' response is buried in the clutter due to the non-calibrated residual phase between the involved channels. Using the reference land patch CAL_{FSAR} for calibration, an improvement in the SCNR is obtained as Fig. 5.24f indi-

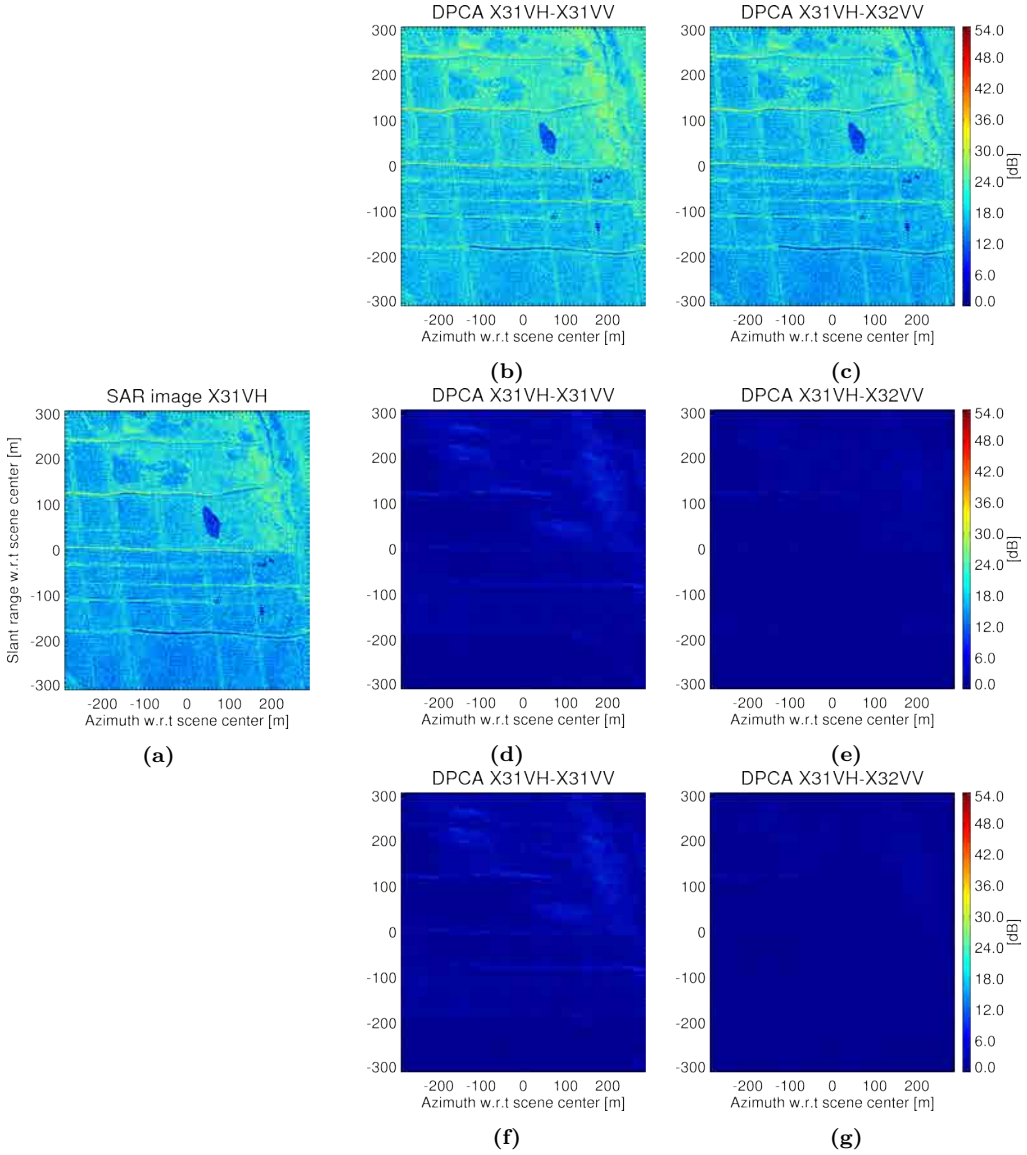


Figure 5.23: CNR images over land patch CAL_{FSAR} ; longest X31VH-X31VV (2nd column) and shortest X31VH-X32VV (3rd column) baseline combinations using a SWMF: (a) SAR image of channel X31VH; (b)-(c) DPCA images with no calibration/balancing; (d)-(e) with DB calibration; and (f)-(g) with phase-only DB.

cates. For the longest baseline X31VH-X31VV a degradation is obtained, mainly induced by the loss in channel coherence, see Fig. 5.24e. If the region AOI_{FSAR} itself is used for calibration purposes [Figs. 5.24g and 5.24h], which means including the targets in the calibration weights extraction, the SCNR is impaired. Similar results have also been obtained for the MDB strategy, as indicated in Table 5.4 (end of F-SAR results section).

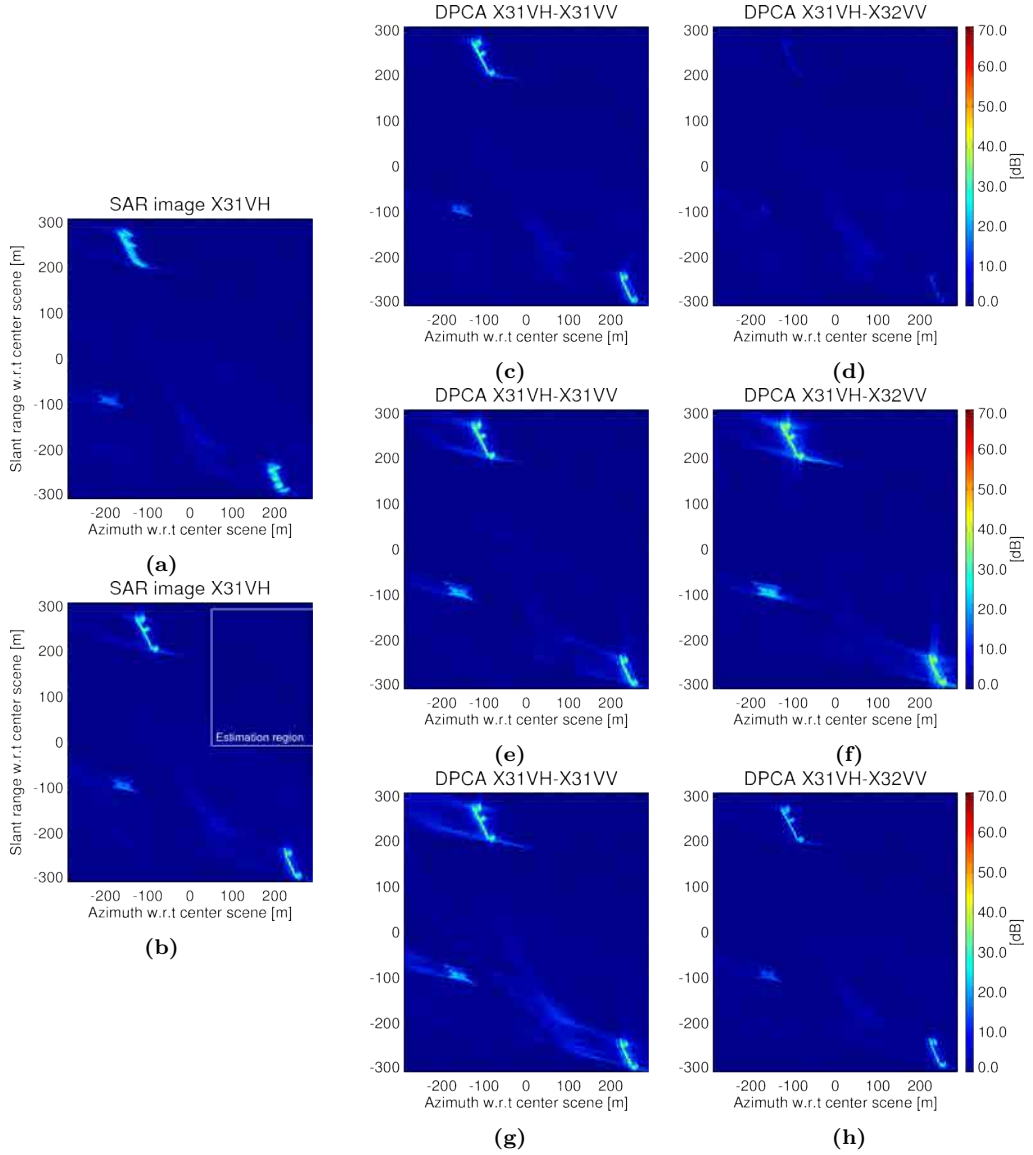


Figure 5.24: SCNR images for DPCA over sea patch AOI_{FSAR} , longest X31VH-X31VV (2nd column) and shortest X31VH-X32VV (3rd column) baseline combinations: (a) SAR image of channel X31VH with a SWMF and (b) with adaptive focusing ($v_z = -5$ m/s and $v_x = 1.8$ m/s); (c)-(d) DPCA images with no channel balancing; (e)-(f) with DB using reference land patch CAL_{FSAR} for calibration; and (g)-(h) with DB using AOI_{FSAR} itself for calibration (adaptive SAR imaging, $v_z = -5$ m/s and $v_x = 1.8$ m/s, used for (c)-(h) images).

DPCA detection maps are displayed in Fig. 5.25 when considering DB (on phase and magnitude) for the longest [Fig. 5.25a] and shortest [Fig. 5.25b] baseline configurations. As expected from the SCNR performance, a much higher number of detected pixels over

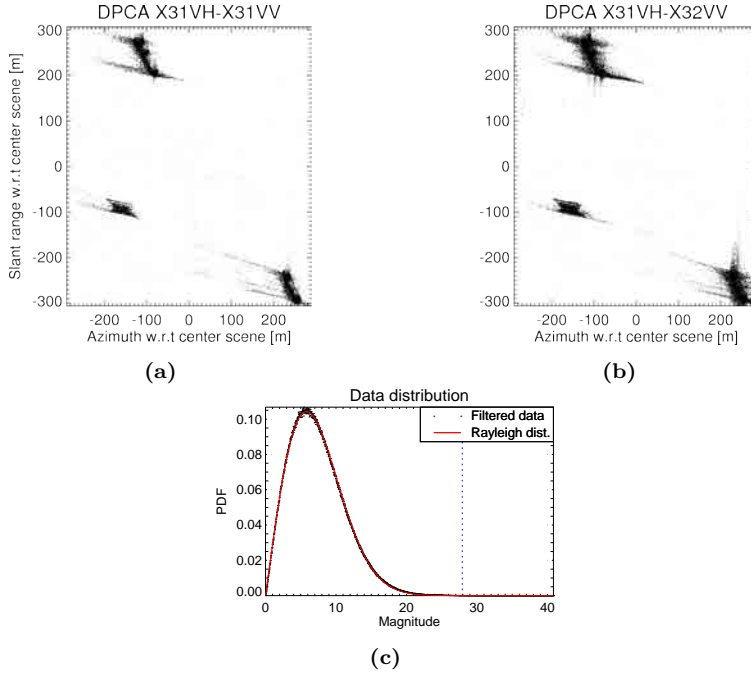


Figure 5.25: Detection maps for DPCA technique over sea patch AOI_{FSAR} acquired with F-SAR platform (DB has been applied using the reference CAL_{FSAR} region): (a) longest baseline; (b) shortest baseline; and (c) residual interference (clutter + noise) data distribution for DPCA X31VH-X32VV using a portion of image as indicated by the white box in Fig. 5.24b (Rayleigh PDF fitting and CFAR threshold level are included).

the different vessels is obtained for the shortest configuration due to the lower impact of clutter decorrelation. In order to set up the threshold of the magnitude CFAR detector, a portion of the image (indicated by the solid white box in Fig. 5.24b), free of moving targets, has been selected to estimate the related statistical parameters under the assumption of a Rayleigh distributed amplitude. Data distribution and the corresponding fitting of a Rayleigh statistics are in good agreement as sketched in Fig. 5.25c, where the estimated CFAR threshold level is also (as vertical dashed blue line).

5.3.2.2 ATI processing

In the implemented processor, the ATI algorithm has been used as a moving target detector and as an across-track ground velocity estimator over the detected pixels, exploiting the interferometric phase information. A 2D-CFAR parametric detector, based on the joint PDF of ATI magnitude and phase, has been used under the assumption of a complex Gaussian distributed sea clutter. Two approaches have been considered to estimate the across-track ground velocity. The first one, *polynomial* method, estimates the across-track ground velocity v_z inverting the complete expansion of the ATI phase in (2.5), which includes the impact of motion parameters such as v_x and a_z . This inversion requires the solution of a third order polynomial, where complex root solutions are excluded as po-

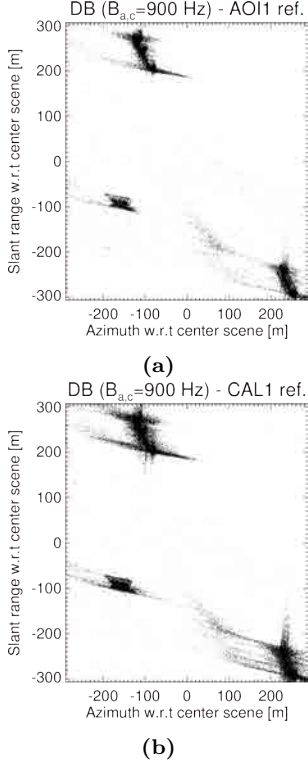


Figure 5.26: ATI detection maps over the sea patch AOI_{FSAR} for the shortest baseline configuration X31VH-X32VV, DB on phase and magnitude has been applied: (a) using the AOI_{FSAR} region itself for calibration and (b) with CAL_{FSAR} as reference.

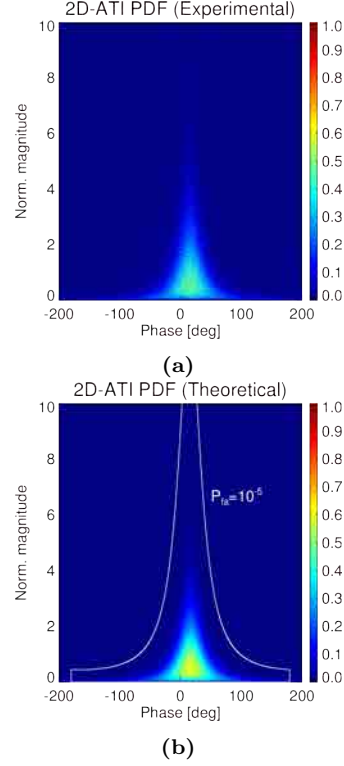


Figure 5.27: (a) Two-dimensional distribution of the ATI (X31VH-X32VV) phase and magnitude of the interference data (clutter+noise) for the rectangular delimited region in Fig. 5.24b (DB using CAL_{FSAR} as reference); (b) fitted theoretical PDF for Gaussian distributed clutter.

tential velocities. To complement this across-track velocity estimator, the *linear* method exploits the widely used approximate relationship $\psi_{ij}(\boldsymbol{\vartheta}_t) = 2\pi(d_{x_i} - d_{x_j})v_z \sin \gamma_0 / v_e \lambda$.

Two detection maps obtained from the 2D-CFAR ATI detector, are presented in Fig. 5.26 for the shortest baseline configuration (X31VH-X32VV), once digital channel balancing has been applied. No multilook processing has been considered in the processor. If the reference region CAL_{FSAR} is used for inter-channel calibration [Fig. 5.26b] better results are obtained compared to the case of considering the region of interest itself [Fig. 5.26a], as demonstrated by the higher density of detected pixels.

For the case analyzed in Fig. 5.26b, the two-dimensional data distribution (histogram) and its fitted theoretical PDF, (2.20), under Gaussian distributed clutter hypothesis, are compared in Fig. 5.27, showing good agreement. Note that the 2D-PDF is not centered at zero phase due to the shift induced by the clutter motion (sea/river current), since the reference (non-moving) land patch CAL_{FSAR} has been used for calibration; otherwise,

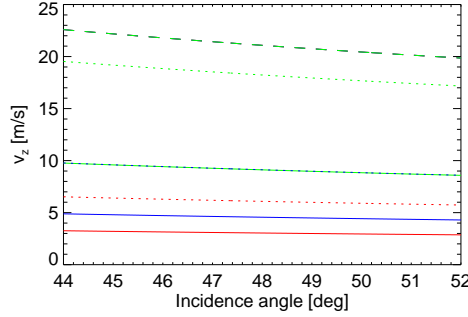


Figure 5.28: ATI related ambiguous velocities (ground) for the different baselines (color coded, X31VH-X31VV in red, X31VH-X32VH in blue and X31VH-X32VV in green): directional ambiguity in solid lines, first blind velocities as dotted lines and first Doppler ambiguous velocities as long dashed lines.

this motion-related phase would have been compensated. The thresholding function used in the 2D-CFAR detector is plotted on top of Fig. 5.27b and it is obtained as a constant-density contour line of the joint PDF, such that the integration of the PDF outside this region gives the desired probability of false alarm.

The ATI phase is subject to several ambiguities that can impair the estimation of v_z , [68, 154]. The *directional ambiguities* occur when the difference in the two-way propagation distance to the target (from the two receive channels) exceeds $\lambda/2$, i.e., the ATI phase is greater than π . *Blind velocities* appear when the target two-way slant range variation over the time between receiver channels⁶ is $n\lambda/2$, such that the ATI phase is a multiple of 2π , appearing as a zero phase. *Doppler ambiguities* occur due to the finite azimuth bandwidth sampling, i.e., when the Doppler frequency of the moving target exceeds $\pm\text{PRF}/2$, these components are wrapped to the opposite side of the spectrum. Fig. 5.28 shows these ambiguous velocities for the different baseline configurations as a function of the incidence angle corresponding to the region CAL_{FSAR} ⁷. The X31VH-X31VV combination, with the largest separation, has a directional ambiguous ground velocity (solid red line) around 3 m/s; the Doppler ambiguous ground velocities (long dashed lines), which depend only on the operated PRF and incidence angle, have the same variation from 23 m/s to 20 m/s for the different baselines.

The information of the detected pixels is used to generate the estimated across-track ground velocity maps of the vessels accordingly, as illustrated in Fig. 5.29 for the shortest baseline formation X31VH-X32VV. Figs. 5.29a and 5.29b correspond, respectively, to the first and third roots of the polynomial used to estimated the v_z , including the impact of a_z and v_x . The first root indicates the negative values of v_z , showing an estimated value between -2.5 m/s and -5 m/s; whereas the third root refers to the positive, mostly related to the sidelobes of the vessels, where the phase behavior could be ambiguous producing velocity wrapping. For the linear relationship between ATI phase and v_z [Fig. 5.29c] good agreement is observed when compared to the polynomial approach [Fig. 5.29a].

The velocity distributions for the different baselines and the two estimation methods

⁶It corresponds to the time it takes the two apertures or receiving antennas to spatially coincide.

⁷Only the positive value has been represented since the negative ones are symmetrical.

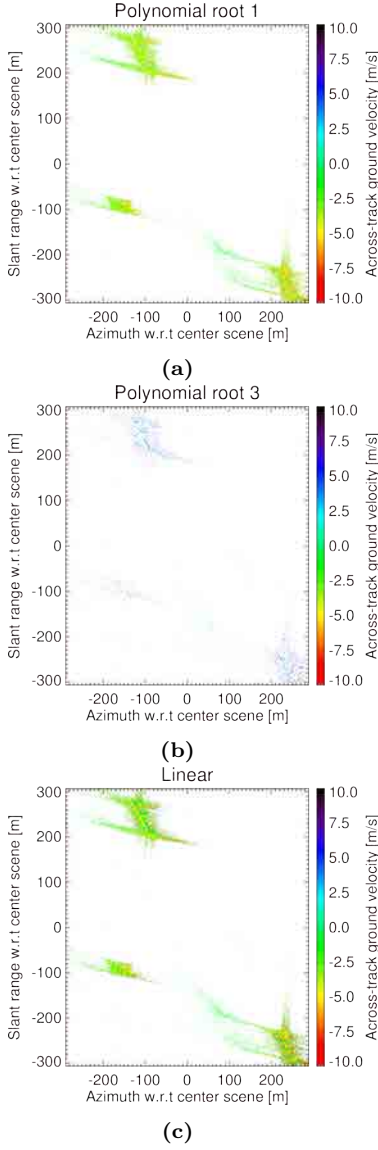


Figure 5.29: Vessels' estimated across-track ground velocity maps from the shortest baseline configuration X31VH-X32VV over sea patch AOI_{FSAR}, DB on phase and magnitude has been applied (using CAL_{FSAR} as reference): (a) first and (b) third roots of the polynomial v_z inversion method; and (c) estimation based on the approximately linear relationship between ATI phase and v_z .

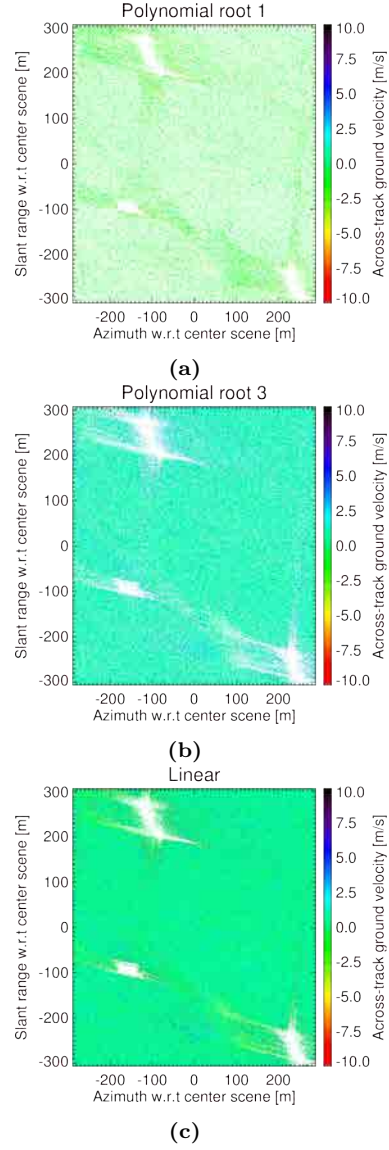


Figure 5.30: Sea clutter's estimated across-track ground velocity maps from the shortest baseline configuration X31VH-X32VV over sea patch AOI_{FSAR}, DB on phase and magnitude has been applied (using CAL_{FSAR} as reference): (a) first and (b) third roots of the polynomial v_z inversion method; and (c) estimation based on the approximately linear relationship between ATI phase and v_z .

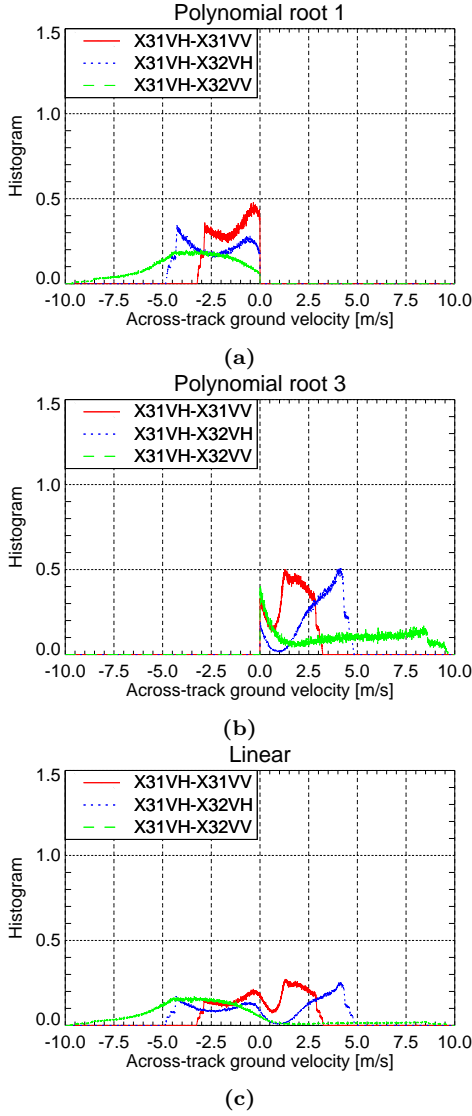


Figure 5.31: Vessels' estimated across-track ground velocity distributions over sea patch AOI_{FSAR} , DB on phase and magnitude has been applied (using CAL_{FSAR} as reference) for the different baseline configurations: (a) first and (b) third roots of the polynomial v_z inversion method; and (c) estimation based on the approximately linear relationship between ATI phase and v_z relationship.

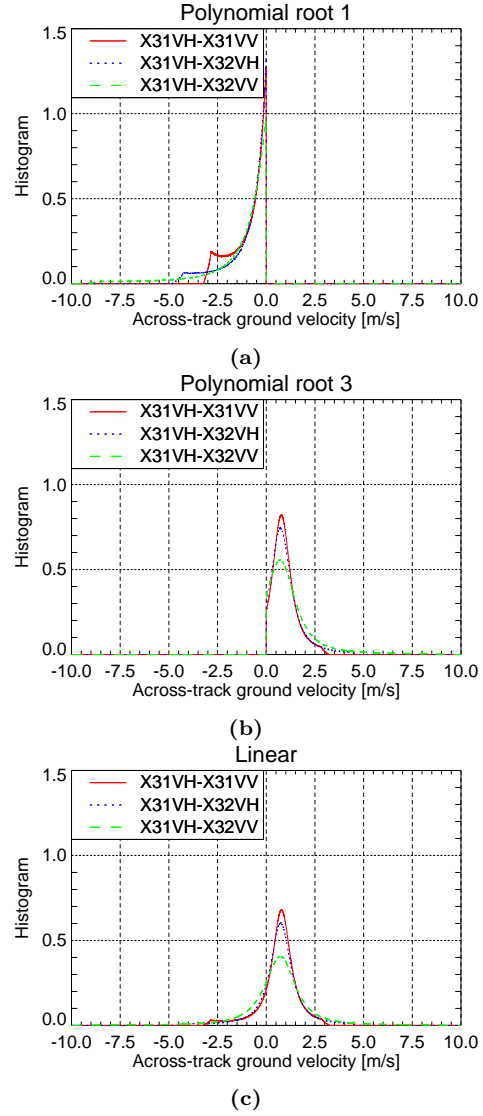


Figure 5.32: Sea clutter's estimated across-track ground velocity distributions over sea patch AOI_{FSAR} , DB on phase and magnitude has been applied (using CAL_{FSAR} as reference) for the different baseline configurations: (a) first and (b) third roots of the polynomial v_z inversion method; and (c) estimation based on the approximately linear relationship between ATI phase and v_z relationship.

are represented in Fig. 5.31. In the polynomial case [Figs. 5.31a-b], the first root provides the negative valued velocities, while the third root gives the positive velocities. A good match between these two methods is obtained. For the shortest baseline configuration (X31VH-X32VV), where the directional ambiguity is between 8.5 m/s and 10 m/s (depending on the incidence angle), the velocity distribution over the detected pixels of the different vessels is between -2.5 m/s and -5 m/s, which is coherent with the results of the EDPCA and ISTAP processing, where the maximization of the output SCNR is obtained close to -4.5 m/s and -5 m/s for vessel V1 and V4, respectively (see Table 5.4). For the X31VH-X32VH, having an absolute directional ambiguity 4-5 m/s, the effect of phase/velocity wrapping can be recognized ($-4.5\text{m/s} \leq \hat{v}_z \leq 4.5\text{m/s}$). In a similar way, the estimated v_z for the longest baseline formation (with the lowest directional ambiguity 3 m/s) lies between -2.5 m/s and 2.5 m/s.

Analogously, sea current velocity maps can be obtained for the non-detected pixels at the output of the 2D CFAR detector, as shown in Fig. 5.30. As in the vessel's case, the two approaches for across-track velocity estimation have been applied showing similar results. These can be better interpreted from the velocity distribution obtained over the sea clutter pixels as depicted in Fig. 5.32. A (ground) current velocity close to 0.7 m/s is obtained for both estimation techniques (linear and polynomial approximations) and the different configurations. Such figures are consistent with the measured current velocities over the same area exploiting ATI TSX (in AS mode) as done in [92]. In this case values of ground current velocities between -3.3 m/s and 2.47 m/s (-1.74 m/s and 1.30 m/s line-of-sight for incidence angle around 32 degrees) have been obtained from TSX, matching quite good the available numerical models.

5.3.2.3 EDPCA processing

The impact of channel balancing on the EDPCA processing over the region of interest AOI_{FSAR} is presented in Fig. 5.33, where a portion of the image (delimited by the solid white box in Fig. 5.24b) free of moving vessels, has been used for covariance matrix estimation. If DB (on phase and magnitude) is applied considering the (range-compressed) calibration weights extracted from the reference land region CAL_{FSAR} [see Fig. 5.33b], there is an improvement in terms of SCNR all over the vessel's structure for V1 (down-right corner) and V4 (upper-left corner), compared to the case of no calibration in Fig. 5.33a. When DB is applied considering the region itself for calibration (including the different vessels) there is a degradation on the SCNR comparable to or even below the non-calibrated case in Fig. 5.33c.

The related detection maps are presented in Figs. 5.34a-b. The increased SCNR conditions when applying EDPCA over the calibrated channels using the reference land patch CAL_{FSAR} provides a much higher number of detected pixels around the vessels, which are precisely related to the higher contribution of the sidelobes. A good fitting is obtained with the Rayleigh distribution on the (normalized) amplitude of the residual interference, as shown in Fig. 5.34d. The estimation region delimited by the solid white box in Fig. 5.24b has been used to extract statistical parameters required by the parametric CFAR detector. The corresponding threshold level has also been included as a vertical dotted blue line in Fig. 5.34d.

The effect of target self-whitening can be clearly appreciated in Fig. 5.35, where all

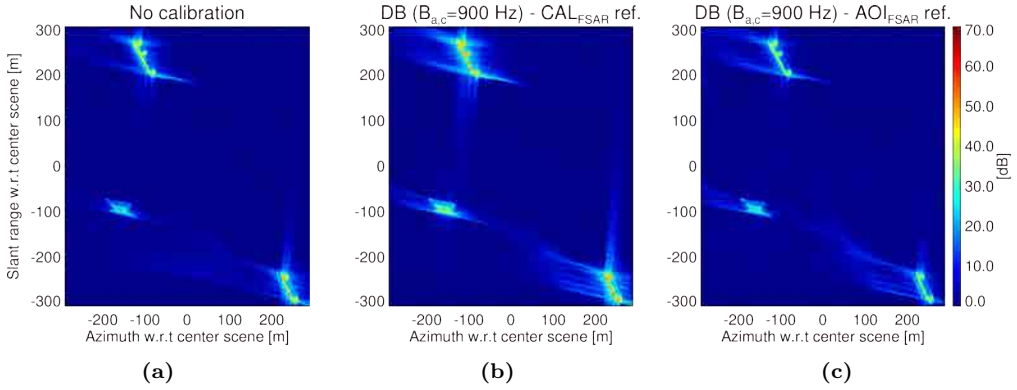


Figure 5.33: SCNR images for EDPKA over sea patch AOI_{FSA} with adaptation (SAR processing and steering vector) to motion parameters $v_z = -5$ m/s and $v_x = 1.8$ m/s, using the portion of image indicated in Fig. 5.24b for estimation of the covariance matrix: (a) no calibration has been applied; (b) DB considering the reference patch CAL_{FSA} ; and (c) DB using the region AOI_{FSA} itself (including the vessels).

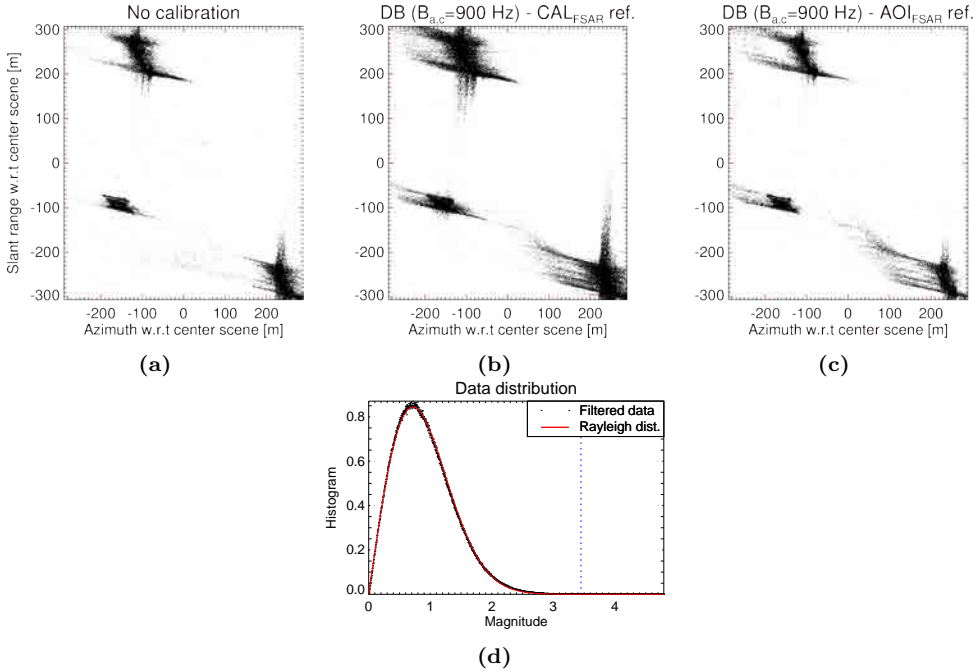


Figure 5.34: EDPKA detection maps over sea patch AOI_{FSA} with adaptation (SAR processing and steering vector) to motion parameters $v_z = -5$ m/s and $v_x = 1.8$ m/s, using the portion of image indicated in Fig. 5.24b for estimation of the covariance matrix: (a) no calibration; (b) DB considering the reference patch CAL_{FSA} (c) DB using the region AOI_{FSA} itself (including the vessels); and (d) depicts the distribution of the residual interference after EDPKA processing for the processing considered in (b).

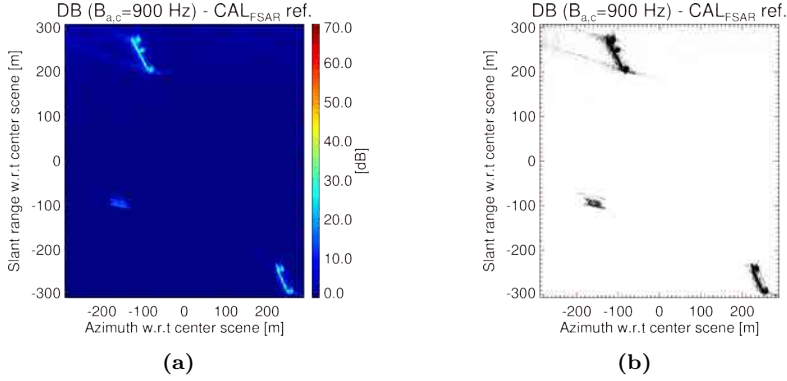


Figure 5.35: SCNR images for EDPKA over sea patch AOI_{FSA} with adaptation (SAR processing and steering vector) to motion parameters $v_z = -5$ m/s and $v_x = 1.8$ m/s, using the whole image itself for estimation of the interference covariance matrix: (a) SCNR image and (b) detection map (DB using reference land patch CAL_{FSA} has been applied).

image pixels have been considered for the estimation of the interference covariance matrix. In this case the degradation in terms of SCNR is notorious and below the single-channel SCNR image in Fig. 5.24b, leading to a reduction in the number of detected pixels associated to the different vessels. This case study is an extreme situation, but it points out how crucial is the proper estimation of the covariance matrix in the EDPKA operation. In the results here presented the estimation of this matrix has been based on using an isolated portion of the image free of moving targets to reduce the computational load of a sliding window approach. Nevertheless, in other scenarios, where this region is not so easily defined and/or with high heterogeneous background, the boxcar-based approach could provide better performance. In this sense, and to avoid target self-whitening, proper definition of the guard zones around the pixel under test are required taking into account the expected vessels' size.

For the best case situation, with adapted focusing and DB using a land reference calibration, the EDPKA technique provides the best SCNR when compared to DPCA; which, even for such large and bright vessels, proves and validates the EDPKA processing concept. The EDPKA processor, based on a MFB SAR focusing and the adaptation of the steering or beamformer vector, provides an estimation of the vessels motion parameters as summarized in Table 5.4. A velocity of -5 m/s and -4.5 m/s on the adaptive EDPKA processor maximizes the response of the output SCNR for vessel V1 and V4, respectively. These values are coherent with the across-track velocity estimation obtained exploiting the ATI phase as described in the previous section.

5.3.2.4 ISTAP processing

ISTAP technique integrates a suboptimal post-Doppler STAP in the SAR formation process to provide high-resolution SAR images of the moving targets. Fig. 5.36 depicts the range-Doppler amplitude images before and after post-Doppler STAP operation over the region of interest AOI_{FSA} for different calibration conditions. The images have been accordingly normalized to the noise floor. The post-Doppler beamformer is tuned to v_z

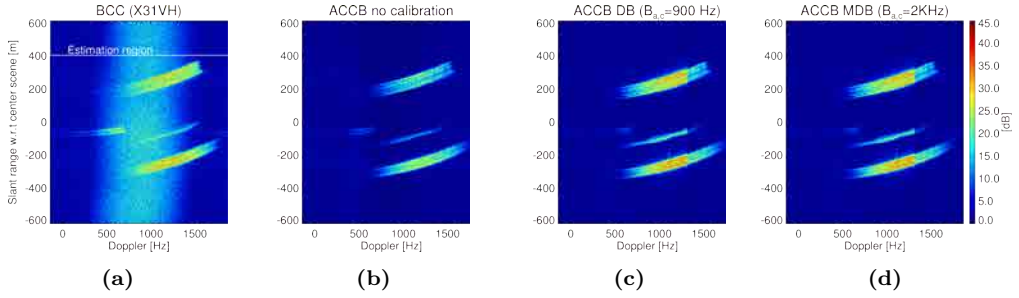


Figure 5.36: F-SAR range-Doppler images (normalized to the average noise floor) before and after post-Doppler operation over region AOI_{FSAR} : (a) X31VH image before clutter cancellation (BCC); (b) after clutter cancellation and beamforming (ACCB) with no channel balancing; (c) ACCB with DB; and (d) ACCB with modified DB (post-Doppler beamformer for $v_z = -5$ m/s and $v_x = 1.8$ m/s, CAL_{FSAR} patch used for calibration).

$= -5$ m/s and $v_x = 1.8$ m/s.

Before clutter cancellation (BCC) the clutter contribution weighted by the antenna pattern can be clearly recognized within the spectral Doppler range of 300 Hz to 1300 Hz. The different range-compressed vessels' signatures can be also identified close to the right edge of the clutter bandwidth. After clutter cancellation and beamforming (ACCB) operations, clutter contribution has been reduced down to the noise level for the different calibration situations [see Figs. 5.36b-d]. In this case, the upper region of the image (within the white box in Fig. 5.36a) has been used for interference covariance matrix estimation. A degradation in the SNR over the vessels' signature can be appreciated when no channel balancing has been applied compared to the DB and MDB cases and, even before the post-Doppler STAP operation. Therefore, a loss in SCNR is expected in the final ISTAP images as indicated by the different processing results, comparing the SCNR images with no channel balancing [Fig. 5.37a] and once the original DB has been applied [Fig. 5.37b].

Analogous to the study made for EDPCA processing, the fact of using the region of interest itself (including moving vessels) for calibration purposes, produces a degradation in the ISTAP performance, as shown in Fig. 5.37c. In the different ISTAP images there is an odd pattern along-azimuth and at both sides of the vessels, which is not present in the EDPCA images. It is not related to secondary lobes responses, but rather it seems to be a kind of constant level replicas or ghosts of the vessel. Additional processing of the data, considering only the post-Doppler STAP combination of the different channels (beamforming) with no application of the interference covariance matrix inverse to the data (no clutter cancellation), doesn't show up these ghost patterns. Therefore, filtering the multichannel data with the Doppler-dependent interference covariance matrix inverse modifies the spectrum of the vessel producing this odd effect.

Comparing the different calibration situations considered in Fig. 5.37, for non-proper channel balancing strategies or not equalization at all, the level of these ghosts w.r.t the real vessels is smaller compared to the case of an adequate calibration. This ratio is around 40-50 dB when applying DB with the land patch CAL_{FSAR} as reference calibration. The different detection maps obtained once the magnitude of the ISTAP output

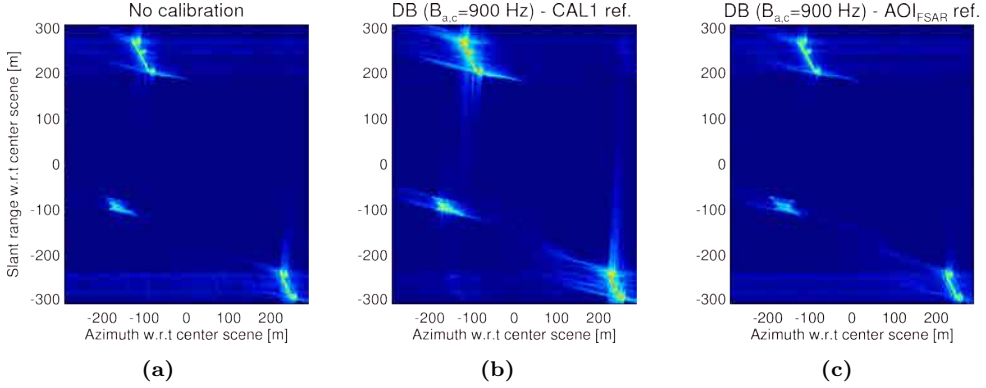


Figure 5.37: SCNR images for ISTAP over sea patch AOI_{FSAR} with adaptation (SAR processing and steering vector) to motion parameters $v_z = -5$ m/s and $v_x = 1.8$ m/s, using the portion of range-compressed image indicated in Fig. 5.36a for estimation of the interference covariance matrix in the range-Doppler domain: (a) no calibration; (b) DB considering the reference patch CAL_{FSAR} ; and (c) DB using the region AOI_{FSAR} itself (including the vessels).

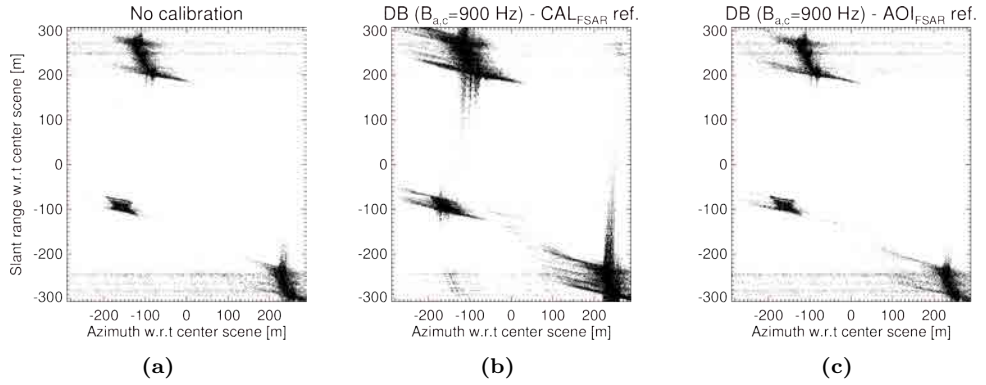


Figure 5.38: ISTAP detection maps over sea patch AOI_{FSAR} with adaptation (SAR processing and steering vector) to motion parameters $v_z = -5$ m/s and $v_x = 1.8$ m/s, using the portion of range-compressed image indicated in Fig. 5.36a for estimation of the interference covariance matrix in the range-Doppler domain: (a) no calibration; (b) DB considering the reference patch CAL_{FSAR} ; and (c) DB using the region AOI_{FSAR} itself for calibration (including the vessels).

is passed through a CFAR detector [Fig. 5.38], clearly demonstrate the effect of these ghost patterns, which are especially appreciable in the case of inappropriate calibration methodologies. In scenarios with lower reflectivity vessels and smaller SNR conditions, these secondary replicas will be probably masked by the noise. In this sense, further studies are required to fully understand how the post-Doppler technique introduces this non-desirable behavior on the data.

In Table 5.3 the estimated SCNRs of the brightest scatterer of vessels V1 and V4 are indicated for DPCA, EDPCA and ISTAP, under different calibration conditions. EDPCA and ISTAP provide improved SCNR performance compared to DPCA (around 6

dB better) and to the single channel case (approximately 16 dB better). The EDPCA operation gives an average additional gain around 1.2 dB in terms of SCNR when compared to ISTAP. Comparing the different calibration strategies, no big differences are appreciated, but the original DB and the modified DB show slightly better performance compared to the phase-only equalization (around 0.1 dB of SCNR improvement). Analogous to EDPCA, the ISTAP can roughly estimate the target kinematic parameter, through the combined adaptive beamformer and SAR processor operations. Table 5.4 shows the across-track ground velocity providing the maximum response in terms of SCNR for the brightest scatterer of the different vessels and for both EDPCA and ISTAP algorithms. ISTAP is coherent with the estimated values provided by EDPCA, -5 m/s and -4.5 m/s for vessels V1 and V4, respectively.

At this point it must be noted that a range of across-track velocities between 0 m/s and -10 m/s in steps of 0.5 m/s has been considered as a prove of concept of both EDPCA and ISTAP techniques. The target detection for both EDPCA and ISTAP is performed for each image pixel by searching the maximum of the corresponding test statistics over the range of possible target velocities, leading to computationally very expensive operations.

Alternative suboptimal approaches consider a given set of filters in a MFB approach, taking into account some admissible SCNR degradation. Then, a coarse estimate of the target parameters can be obtained at a reduced computational load. In this case, once a target is detected in a given pixel, the corresponding range-line can be isolated and the test statistics can be iteratively performed trying to maximize the SCNR response, such that an accurate estimation of the target parameters is obtained, [28, 29].

Table 5.3: Estimated SCNR for brightest scatterer of vessels V1 and V4 in region AOI_{FSAR} , considering an adaptive SAR processing with $v_x = 1.8$ m/s (results for different calibration approaches are presented).

Vessel	SCNR [dB]												
	Input	DPCA (X31VH-X32VV)				EDPCA				ISTAP			
		No cal.	DB	ph. DB	MDB	No cal.	DB	ph. DB	MDB	No cal.	DB	ph. DB	MDB
V1	50.239	28.413	59.464	59.329	59.497	62.424	66.994	66.799	66.973	58.713	65.744	65.480	65.621
V4	46.576	20.970	55.230	55.163	55.256	57.854	63.252	63.157	63.227	53.977	61.531	61.368	61.430

Table 5.4: Estimated \hat{v}_z from the MFB integration in the EDPCA and ISTAP processing for the brightest scatterer of vessels V1 and V4 in region AOI_{FSAR} , considering an adaptive SAR processing with $v_x = 1.8$ m/s (results for different calibration approaches are presented).

Vessel	\hat{v}_z [m/s]							
	EDPCA				ISTAP			
	No cal.	DB	ph. DB	MDB	No cal.	DB	ph. DB	MDB
V1	-4.5	-5.0	-5.0	-5.0	-5.0	-5.0	-5.0	-5.0
V4	-4.5	-4.5	-4.5	-4.5	-4.5	-4.5	-4.5	-4.5

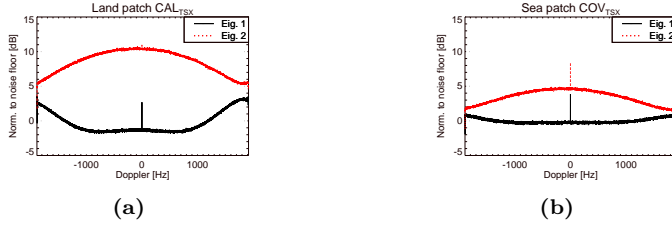


Figure 5.39: Average (along range) eigenvalue spectra versus Doppler of the range-compressed data over (a) land patch CAL_{TSX} and (b) sea patch COV_{TSX} .

5.4 TerraSAR-X data

5.4.1 Processing results

5.4.1.1 Data analysis

In Fig. 5.39 the average (along-range) eigenvalue distribution of the range-compressed data is represented as a function of Doppler frequency for a land CAL_{TSX} and a sea COV_{TSX} patches. The first eigenvalue shows the multichannel CNR, i.e., after a coherent combination of the two channels, as a function of Doppler, where the antenna pattern weighting can be appreciated. The second eigenvalue is an indicator of the noise level contained in the fore and aft channel signals, which has been used as reference level (normalization) of the plots in Fig. 5.39. The impact of azimuth ambiguities produces an increase on this second eigenvalue, which can be more clearly appreciated in the land patch case at the edges of the spectrum [Fig. 5.39a].

The higher impact of the ambiguities in the TSX-DRA mode is due to a reduced operational PRF, taking into account that the receive antenna has been halved into two sub-apertures. In case any channel balancing has to be applied to the data, the spectral equalization should be performed avoiding the regions with higher impact of azimuth ambiguities. Compared to the F-SAR case, with a high PRF sufficient to sample the “complete” antenna pattern weighting, the CNR is almost 15 dB below in the mainlobe clutter region for both land and sea patches. The reduced CNR limits channel correlation and prevents the use of a sea patch for calibration purposes.

Phase imbalances between fore and aft channels, before and after channel balancing (MDB) are shown in Fig. 5.40. Analogous to the F-SAR case a moving average filter of 3×3 has been applied to the image to reduce noise impact. The phase imbalances, with values up to 7 degrees within the mainlobe region, are range frequency and Doppler variant as noticed in Fig. 5.40a. After channel balancing, a reduction on the phase imbalances can be observed over the calibration bandwidth $B_{a,c}$ of 2 KHz; outside this spectral range, where the ambiguities play a major role, no calibration has been considered. As expected, similar results of phase imbalances for both the phase-only DB and modified DB are obtained.

Fig. 5.41 show the amplitude imbalances between the fore and aft channels, before and after channel balancing, considering different calibration strategies. Before channel balancing [Fig. 5.41a], the average of amplitude imbalances is around -0.88 dB with both range frequency and Doppler dependent fluctuations. After application of channel bal-

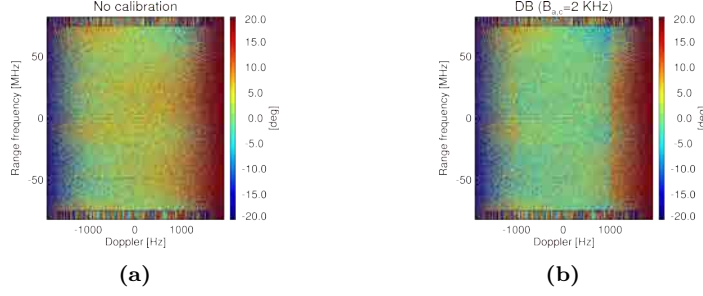


Figure 5.40: TSX-DRA channel imbalances' phase for region CAL_{TSX} as a function of range frequency and Doppler: (a) no calibration; and (b) digital balancing (DB).

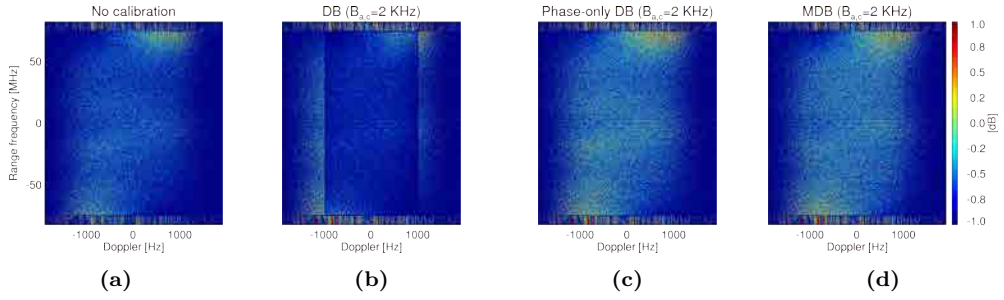


Figure 5.41: TSX-DRA amplitude imbalances for region CAL_{TSX} as a function of range frequency and Doppler: (a) no calibration; (b) DB; (c) phase-only DB; and (d) modified digital balancing (MDB).

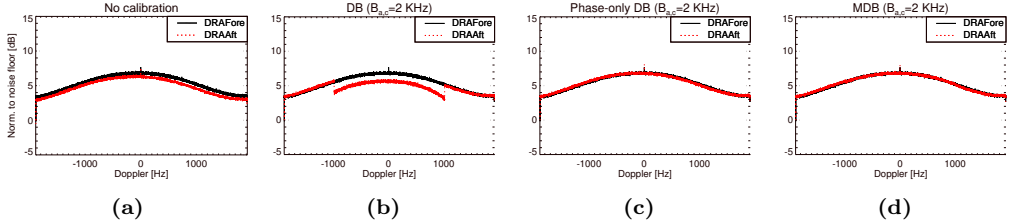


Figure 5.42: TSX-DRA average Doppler spectra (normalized to the average noise floor) for region CAL_{TSX}: (a) no channel balancing, (b) DB, (c) phase-only DB and (d) MDB.

ancing for the phase-only DB and the modified digital balancing (MDB) [Figs. 5.41c-d], a reduction (around 0.25 dB) of the imbalances can be recognized with a more uniform distribution over the two-dimensional spectral extent. Nonetheless, when the original DB algorithm, proposed by Gierull in [74], is applied to balance the DRAAft channel an important degradation is observed compared to the other calibration strategies and even to the non-calibrated case (average imbalance of -1.19 dB). From the mathematical formulation of the DB operation in (5.10), the calibration weights can be interpreted as a correlation coefficient. In this sense, and for the region CAL_{TSX}, the average value of $H_{1,2}^{(n,r)}(f_r)$, understood as an “equivalent” coherence, was 0.878 in the first iteration,

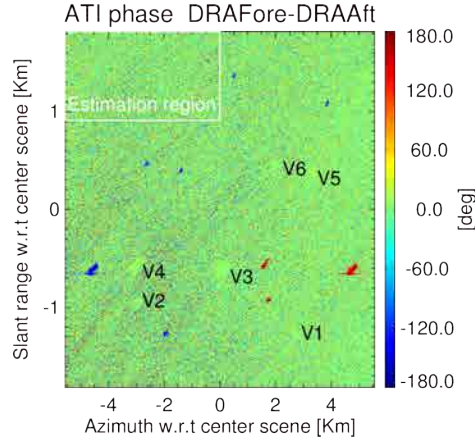


Figure 5.43: TSX-ATI phase image over sea patch AOI_{TSX} considering an adaptive processing with $v_x = 5$ m/s and no channel balancing.

which mainly produces this clear average increase observed in the amplitude imbalances [see Fig. 5.41b].

This behavior of the DB algorithm can be clearly recognized when comparing the average (along-range) channel response as a function of Doppler before and after channel balancing, as represented in Fig. 5.42. These transfer functions have been averaged over the different range bins in the range-Doppler image domain and normalized to the average noise floor. From Fig. 5.42b, a common gain reduction of the DRAAft channel is observed within the calibration bandwidth. The phase-only DB and the MDB provide similar results with a slightly better matching of the aft channel to the fore as a function of Doppler for the MDB case. It must be noted that prior to any of the iterative two-dimensional spectral equalizations a range dependent power balancing in the image domain (range-azimuth) has been carried out.

5.4.1.2 ATI processing

Azimuth ambiguities are among the major issues for proper operation of SAR-GMTI when using the TSX DRA mode, as it can be noticed from Fig. 5.4. For the specific region AOI_{TSX} , the azimuth ambiguities of some of the big sized vessels are clearly visible in the image and could be falsely interpreted as moving targets.

Fig. 5.43 corresponds to the ATI image phase over patch **AOI** with no channel balancing. An adaptive SAR focusing to v_x of 5 m/s has been applied, providing generally a better vessels' image sharpening, specifically on V3 as previously analyzed in Fig. 5.12. A multilook processing of 3x3 has been applied to the image in order to enhance the detection capabilities and reduce the noise impact on the across-track velocity estimation. From Fig. 5.43, the left and right ambiguities of the different vessels can be easily recognized with negative and positive ATI phases around 150 degrees, respectively; meanwhile the vessels of interest have reduced ATI phases. To build up the CFAR detectors for any of the considered GMTI techniques, a portion of the resulting SAR-GMTI image, free of moving targets (as indicated by the rectangular white box in Fig. 5.43), is used to

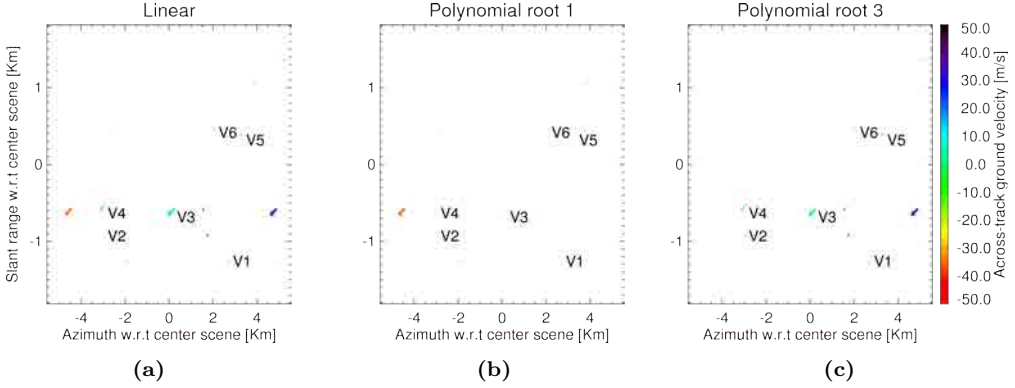


Figure 5.44: Estimated \hat{v}_z for TSX-DRA mode on top of the ATI detected pixels over region AOI_{TSX} considering an adaptive SAR processing to $v_x = 5$ m/s: (a) linear method; and (b) first and (c) third roots of the polynomial v_z inversion method (DB calibration has been applied considering CAL_{TSX} region as reference).

Table 5.5: Estimated \hat{v}_z in m/s for brightest scatterer at each of the six vessels in region AOI_{TSX}, using the ATI phase linear relationship with the motion parameters (results for different calibration approaches are presented).

Vessel	\hat{v}_z [m/s]			
	No cal.	DB	ph. DB	MDB
V1	2.560	1.817	1.777	1.776
V2	2.638	2.127	1.979	1.955
V3	1.980	1.034	1.039	1.032
V4	3.077	2.317	2.321	2.316
V5	3.457	2.553	2.583	2.582
V6	2.466	1.667	1.612	1.591

estimate the required statistical parameters. This patch is also used for the estimation of the interference covariance matrix when operating the EDPCA technique.

The estimated across-track velocity map over the ATI detected pixels is shown in Fig. 5.44 for the linear as well as polynomial ATI phase- v_z relationships, considering a channel balancing based on the original DB technique. Both approaches, linear and polynomial, provide similar results, with values of \hat{v}_z between 1 m/s and 2.5 m/s for the different vessels moving away from the satellite's track. The polynomial first root solution provides an estimation of the negative valued across-track velocities, in a way that only the left-sided ambiguities are present in the corresponding velocity map as noticed in Fig. 5.44b; whereas, the third root solution gives positive valued v_z estimations, as shown in Fig. 5.44c.

The influence of channel balancing on the ATI estimated v_z is summarized in Table 5.5 for each of the calibration strategies. This table provides \hat{v}_z for the brightest scattering point of each vessel using the classical linear ATI phase- v_z relationship, considering an

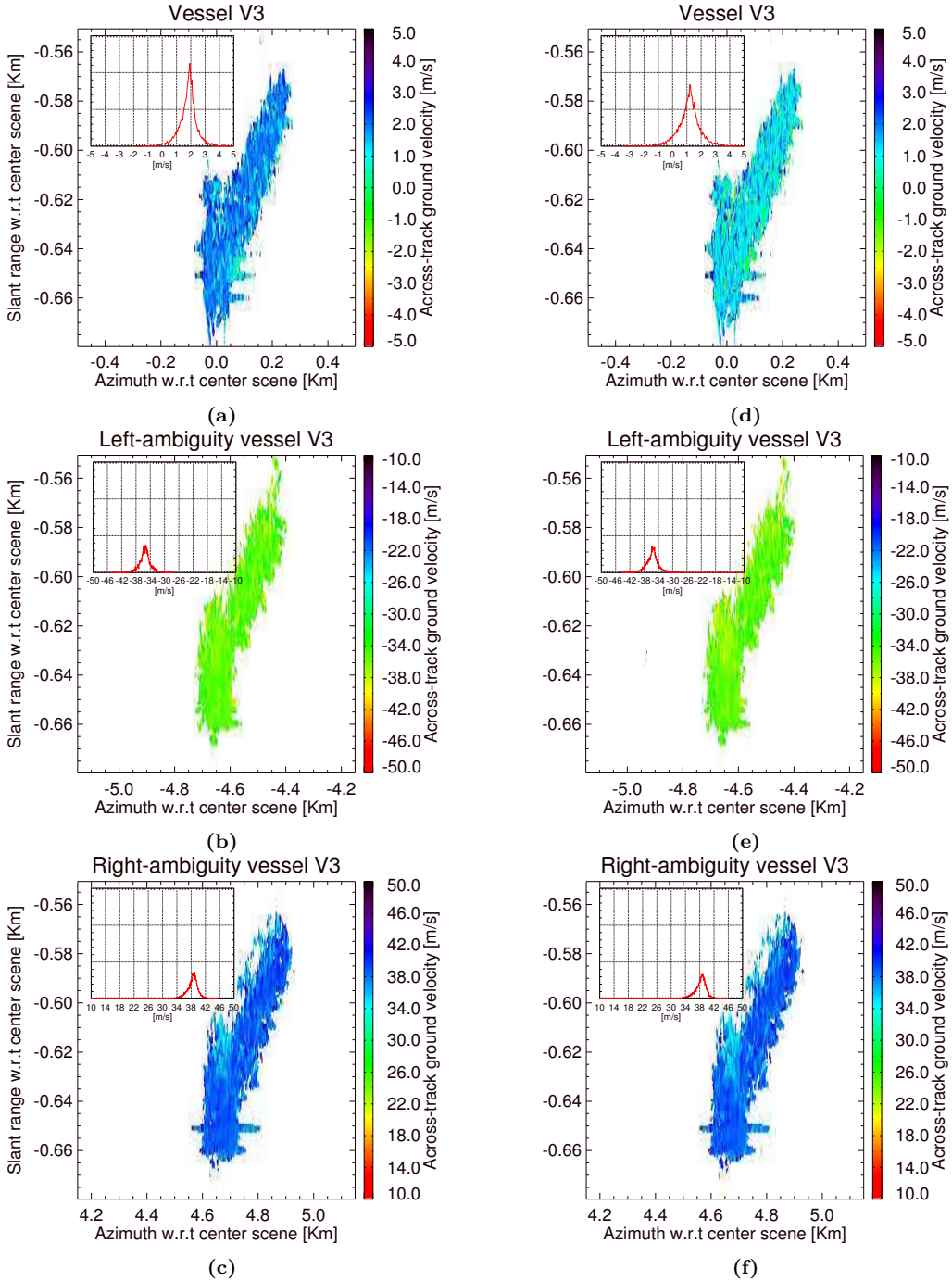


Figure 5.45: Estimated \hat{v}_z for TSX-DRA mode, using the linear relationship with ATI phase over the ATI detected pixels of vessel V3 (first row) and its related left (second row) and right (third row) ambiguities; no channel balancing results are shown in the left column and for the DB approach, with CAL_{TSX} as reference, in the right column (histograms of the estimated velocities are also included on top of the images).

adaptive SAR processing to v_x of 5 m/s. It can be recognized that after channel balancing the estimated velocity is reduced compared to the non-calibrated scenario. Little variations are observed among the different calibration strategies, even for the original DB approach. Similar values are obtained for the polynomial-based approach.

In Fig. 5.45 a zoom of the estimated v_z maps over vessel V3 as well as its left/right ambiguities is sketched before and after channel balancing. A histogram of the velocity distribution over the vessel and its ambiguities is also included on top of each image. An over-estimation of the corresponding V3 velocity for the non-calibrated case when compared to the channel balanced one (original DB) can be noticed, i.e., from 2 m/s to 1 m/s. This behavior is not so clear in the case of ambiguities, where the ambiguous component phase is dominant, giving unrealistic velocities on maritime scenarios $34 \text{ m/s} \leq |\hat{v}_z| \leq 38 \text{ m/s}$. It must be also noted that channel balancing has been restricted to a 2 KHz bandwidth around the Doppler centroid and so the phase impact on the ambiguities is almost unaffected.

Unfortunately, there is no access to ground truth data for that region at the acquisition time, which could help support the validity of the presented results. Nevertheless, from the estimated across-track ground velocity and considering in a first approximation $v_x = 5 \text{ m/s}$, the related velocity of the vessels is between 9-10 knots. These values are congruent with the available AIS information for vessels cruising in this geographical area (typically 7-13 Knots), obtained from on-line sources such as *Maritime Traffic* [155] or *Vessel Finder* [156].

5.4.1.3 DPCA processing

DPCA detection maps over region AOI_{TSX} are represented in Fig. 5.46 for different channel balancing conditions. Compared to the two-dimensional CFAR ATI detector, the number of detected pixels over the different vessels has been reduced. This behavior is expected from the complex subtraction of the two channels, which degrades the effective SCNR for the slowly moving vessels as observed from the theoretical analysis in Fig. 4.9 (comparing the operation of X-DPCA and single channel SCNR). This tendency is also ratified from the SCNR analysis over the brightest scattering point of each vessel summarized in Table 5.6 (at the end of the TSX results section).

Regarding the ambiguous vessels, and specifically for the V3 case, the detection is somehow reinforced due to the phase induced error on the ambiguities, as observed from the analysis of the ATI technique. This is related to the fact that the DPCA condition for this TSX-DRA acquisition configuration is not fulfilled, which otherwise would reduce the impact of the ambiguous vessels in the same manner as the non-ambiguous.

Comparing DPCA detection maps for the different channel balancing methodologies, no clear differentiation is observed, except for the vessel V3, for which the number of detected pixels is slightly lower in the MDB compared to the original DB. When analyzing the DPCA response in detail and comparing the effective SCNR at the output of the DPCA's processor some discrepancy between the different methodologies can be found. From Table 5.6, similar results are obtained for the phase-only DB and the MDB, with SCNR values around 2 to 4 dB below the case of original DB, which has an SCNR close to the non-calibrated case.

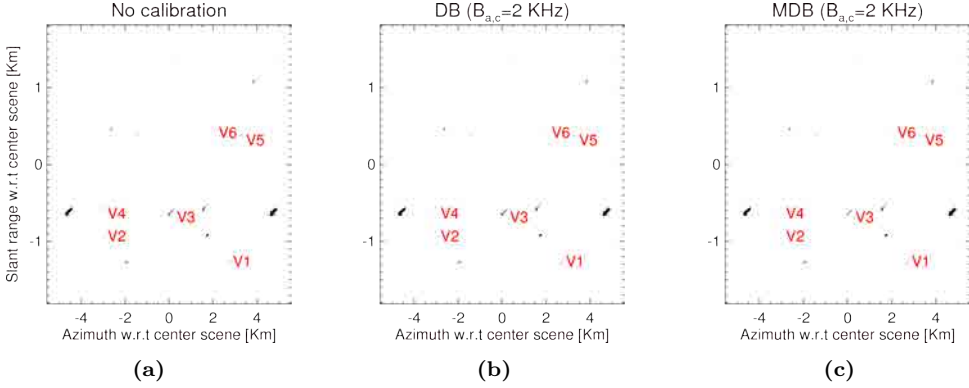


Figure 5.46: DPCA detection maps over region AOI_{TSX} , considering an adaptive SAR processing to $v_x = 5$ m/s: (a) no channel balancing; (b) original DB and (c) modified DB (MDB).

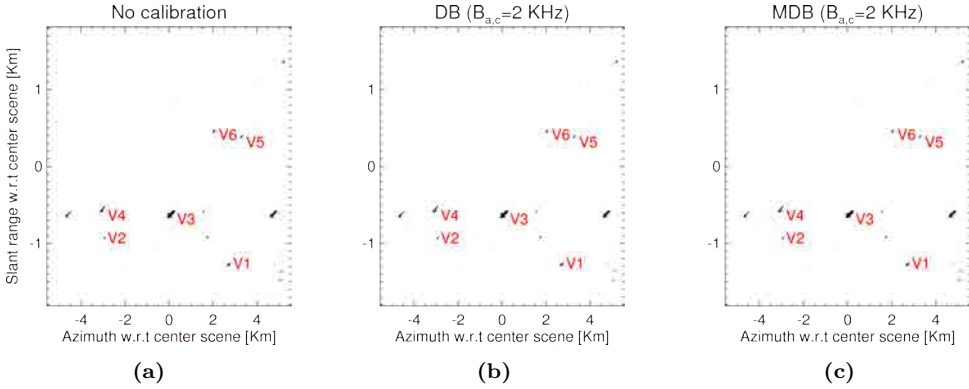


Figure 5.47: EDPCA merged detection maps over region AOI_{TSX} , considering an adaptive SAR processing to $v_x = 5$ m/s and a variation of -1 m/s $\leq v_z \leq 10$ m/s in steps of 0.5 m/s: (a) no channel balancing; (b) DB and (c) MDB.

5.4.1.4 EDPCA processing

In case of EDPCA processing, and compared to DPCA, an improvement in the detection capabilities can be clearly appreciated over the different vessels in region AOI_{TSX} , as demonstrated by the corresponding detection maps in Fig. 5.47. These images correspond to the merged detections, where the different detection maps for each iteration of the EDPCA beamformer v_z (from -1 m/s to 10 m/s in steps of 0.5 m/s) and $v_x = 5$ m/s adaptation have been combined through the logical *OR* operator.

When comparing the results for the different channel balancing approaches, quite similar results are obtained. In terms of SCNR, there is an improvement of approximately 1.4 dB w.r.t the single channel case, even for the non-calibrated conditions. The reduced number of channels and the corresponding short baseline configuration in combination with the low CNR conditions over the ocean for TSX (around 3 dB for this acquisition) limits the EDPCA improvement compared to the single channel for the small velocity

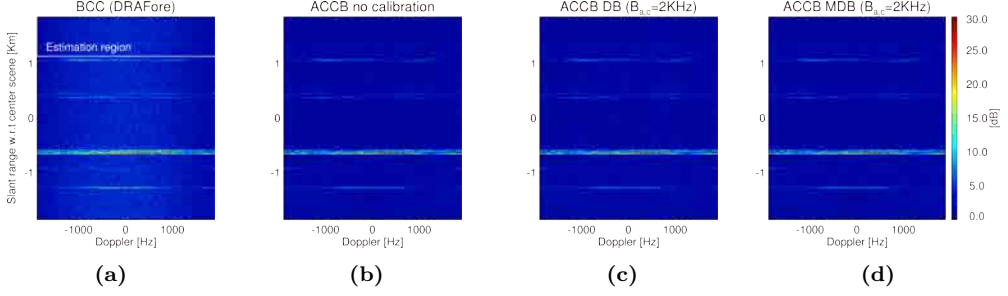


Figure 5.48: TSX range-Doppler images before and after post-Doppler operation over region AOI_{TSX}: DRAFore image (a) before clutter cancellation (BCC); (b) after clutter cancellation and beamforming (ACCB) with no channel balancing; (c) ACCB with DB; and (d) ACCB with MDB (post-Doppler beamformer tuned to $v_z = 1$ m/s and $v_x = 5$ m/s).

region (-10 m/s to 10 m/s). These metrics are consistent with the results predicted by the SAR-GMTI theoretical evaluation of TSX carried out in section 4.2.2.

The values of v_z , providing the corresponding maximum SCNR response, are different for each calibration strategy, as indicated in Table 5.7. In the non-calibrated case there is an over-estimation of the across-track velocity compared to the case of operating with balanced channels. Taking into account that a coarse step of 0.5 m/s has been considered in the MFB, the corresponding estimated \hat{v}_z is, using the EDPCA-SCNR maximization, coherent with the results obtained for the ATI approach in Table 5.5.

5.4.1.5 ISTAP processing

DRAFore and DRAAft SSC products are already co-registered, the systematic phase ramp (in Doppler domain) due to the baseline time delay should be re-introduced (after any channel balancing) since it bears crucial information for array processing-based techniques such as ISTAP.

In Fig. 5.48 the range-Doppler amplitude images normalized to the noise floor are shown, before and after operation of the post-Doppler STAP integrated in the ISTAP algorithm. Fig. 5.48a refers to DRAFore channel before clutter cancellation (BCC), where the clutter contribution can be recognized in the spectral Doppler range between -1 KHz and 1 KHz. After clutter cancellation and beamforming in the range-Doppler domain for different calibration conditions [Figs. 5.48b-5.48d], it can be observed that the clutter contribution has been reduced to the noise level. This effect is not as obvious as in the case of F-SAR acquisitions due to the comparatively reduced CNR conditions. No big differences can be appreciated after the post-Doppler STAP operation among the different calibration strategies.

For ISTAP, similar detection performance to EDPCA is achieved, as indicated by the combined or merged detection maps presented in Fig. 5.49. Nevertheless, there is a different behavior on the ambiguous response for both techniques. The so called left-sided vessel ambiguities are reinforced when compared to EDPCA operation under the same calibration conditions and for the same beamformer variation (-1 m/s $\leq v_z \leq 10$ m/s in steps of 0.5 m/s); while, the impact of the right-sided is reduced. The interference

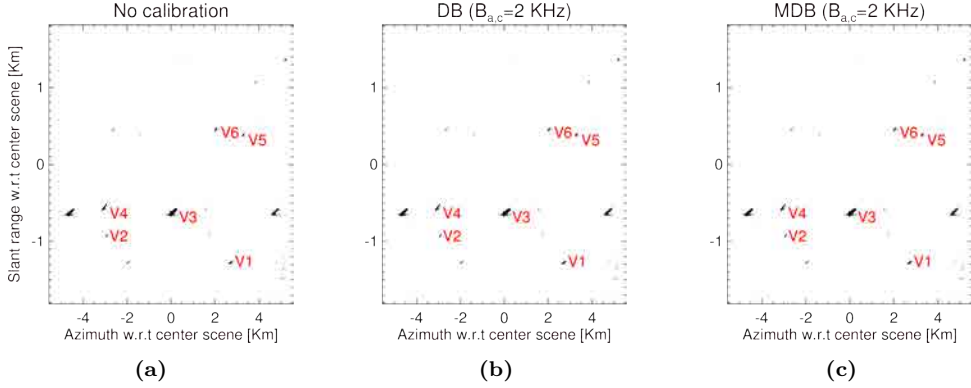


Figure 5.49: ISTAP merged detection maps over region AOI_{TSX} acquired with TSX-DRA, considering an adaptive SAR processing to $v_x = 5$ m/s and a variation of -1 m/s $\leq v_z \leq 10$ m/s in steps of 0.5 m/s: (a) no channel balancing; (b) DB and (c) MDB.

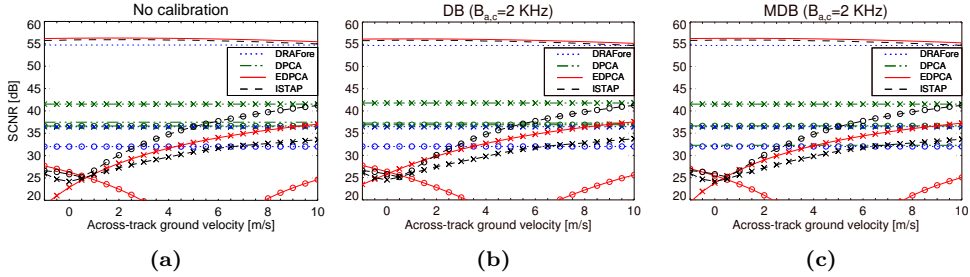


Figure 5.50: SCNR as a function of v_z for brightest scatterer on vessel V3 over region AOI_{TSX} , considering an adaptive SAR processing to $v_x = 5$ m/s and a variation of -1 m/s $\leq v_z \leq 10$ m/s in steps of 0.5 m/s (left and right ambiguities identified by the different line styles with circle and cross symbols, respectively): (a) no channel balancing; (b) DB and (c) MDB.

covariance matrix is estimated for each Doppler bin using only the upper part portion of the range-compressed data (as denoted by the white rectangular region in Fig. 5.48a).

The SCNR as a function of the across-track velocity for the brightest scatterer over vessel V3, as shown in Fig. 5.50, is a good and illustrative metric to understand the operation of the different clutter cancellation based techniques (DPCA, EDPCA and ISTAP) for different channel balancing conditions. The SCNR input conditions for the DRAFore channel are also included for comparative purposes as well as the SCNR related to the left and right ambiguities, identified by the circle and cross symbols, respectively.

As expected DRAFore and DPCA response are independent on the v_z variation; while EDPCA and ISTAP SCNR vary slightly as function of the adapted beamformer velocity. This small sensitivity of EDPCA and ISTAP w.r.t the across-track ground velocity is due to the compact baseline configuration and to the reduced CNR when operating with TSX; which is consistent with the theoretical SAR-GMTI performance analysis of TSX done in section 4.2.2.

The SCNR for DPCA is well below the single channel SCNR, around 17 dB for the

non-calibrated and the original DB cases; whereas the MDB SCNR is approximately 22 dB smaller than DRAFore response. Comparatively, for the ambiguities case, DPCA provides values of SCNR only 13 dB and 18 dB (right and left ambiguities) below the single channel case, being almost insensitive to channel calibration. This is because the balancing techniques are restricted to 2 KHz Doppler bandwidth around the Doppler centroid, excluding the regions where the azimuth ambiguities have higher impact.

For the EDPCA case an improvement on the SCNR (≈ 1.4 dB) compared to the single channel case is obtained, with a quite flat response as a function of the across-track velocity. Such a behavior is in accordance with the theoretical analysis of the TerraSAR-X mission considered in section 4.2.2. Comparing the different calibration conditions (from left to right), the maximum of the EDPCA SCNR response moves towards smaller across-track velocities as already observed from the ATI v_z estimation. Contrary to the DPCA case the SCNR for the ambiguous vessels varies significantly with v_z when processing with EDPCA. In any case, and for the set of considered across-track velocities, EDPCA provides lower response on the ambiguities compared to DPCA.

In case of ISTAP similar performance to EDPCA is obtained. As already pointed out from the detection maps, the impact of the left-sided vessel ambiguity for ISTAP is comparatively higher, while the right-sided keeps below the EDPCA case for beamformer velocities above 0 m/s. Very small differences in terms of SCNR response for the different calibration strategies are obtained when using ISTAP as indicated in Table 5.6, phase-only calibration giving the “best” performance. It can be also noticed that EDPCA provides slightly better SCNR in general. Since ISTAP is operating directly on the range-compressed Doppler domain, the Doppler-dependent covariance matrix estimation and inversion (for clutter cancellation) applied across the PRF band is affected by the azimuth ambiguities. Hence, this could justify the slight reduction in terms of SCNR when compared to the EDPCA technique. Differences between ISTAP and EDPCA can be also appreciated in the across-track velocity of the MFB that produces the maximum SCNR response of the brightest scatterer for the different vessels in region AOI_{TSX}, as summarized in Table 5.7. For the channel balanced scenarios, ISTAP provides smaller values of \hat{v}_z with an average variation of 0.5 m/s for vessels V3 to V6. Nonetheless, for the small vessels V1 and V2 the velocity is much lower and deviates from the expected velocity using the ATI technique. Further analysis on the operation of the ISTAP algorithm is required to properly understand the different issues here raised up.

Table 5.6: Estimated SCNR for the brightest scatterer at each of the six vessels in region AOI_{TSX}, considering an adaptive SAR processing with $v_x = 5.0$ m/s (results for different calibration approaches are presented).

Vessel	SCNR [dB]												
	Input	DPCA				EDPCA				ISTAP			
		No cal.	DB	ph. DB	MDB	No cal.	DB	ph. DB	MDB	No cal.	DB	ph. DB	MDB
V1	46.108	30.851	30.977	26.992	27.019	47.601	47.447	47.578	47.598	47.051	47.064	47.079	47.099
V2	35.490	20.885	20.111	18.648	18.469	37.031	37.110	37.019	37.038	37.435	37.452	37.470	37.479
V3	54.724	37.472	37.273	32.506	32.280	56.292	56.203	56.332	56.336	55.936	55.906	55.971	55.961
V4	44.590	30.705	30.008	27.693	27.761	46.082	46.011	46.134	46.133	46.011	46.010	46.075	46.074
V5	40.088	27.088	26.347	24.150	24.199	41.598	41.392	41.609	41.590	40.796	40.731	40.820	40.813
V6	38.586	22.983	23.901	19.050	18.977	40.090	39.806	40.058	40.049	39.701	39.649	39.712	39.700

Table 5.7: Estimated \hat{v}_z from the MFB integration in the EDPCA and ISTAP processing for the brightest scatterer at each of the six vessels in region AOI_{TSX}, considering an adaptive SAR processing with $v_x = 5.0$ m/s (results for different calibration approaches are presented).

Vessel	\hat{v}_z [m/s]							
	EDPCA				ISTAP			
	No cal.	DB	ph. DB	MDB	No cal.	DB	ph. DB	MDB
V1	2.5	2.0	1.5	1.5	1.5	-1.0	-1.0	-1.0
V2	2.5	2.0	2.0	2.0	0.0	0.0	0.0	0.0
V3	2.0	1.0	1.0	1.0	2.5	0.5	0.5	0.5
V4	3.0	2.0	2.0	2.0	1.5	1.5	1.5	1.5
V5	3.5	2.5	2.5	2.5	3.0	2.0	2.0	2.0
V6	2.5	1.5	1.0	1.0	1.5	1.5	1.5	1.5

5.5 Concluding remarks

This chapter has explored the SAR-GMTI capabilities of current state-of-the-art airborne (F-SAR) and spaceborne (TSX) sensors, when operating over maritime scenarios. The performance of both classical dual-channel GMTI techniques (DPCA and ATI) as well as promising adaptive techniques recently proposed (EDPCA and ISTAP) has been analyzed. The objective of the chapter was to raise up possible limitations and issues to be considered when processing multichannel real data from pioneering airborne and spaceborne SAR sensors. In this sense, one of the main focus of the chapter is the study of different calibration or channel balancing strategies and how they can impair the GMTI performance.

Two complete SAR-GMTI processing chains have been implemented, providing flexibility in the different stages. Specific reference patches, different from the ones of interest, can be accordingly selected for calibration and estimation purposes (interference covariance matrix and antenna pattern). The first processor integrates jointly the SAR-GMTI image based techniques (ATI, DPCA and EDPCA); while, in the second one the adaptive ISTAP technique has been implemented. In both chains, an adaptive SAR processor has been build up on the basis of a range-Doppler (RD) algorithm, being able to process both airborne and spaceborne multichannel data. This processor has been integrated in the processing chain using a MFB approach, and it can be used to refocus and estimate target parameters. Its ability to compensate for motion related defocusing has been demonstrated for airborne and spaceborne acquisitions. The image quality improvement as well as the SCNR recovery are much more clear for the airborne case, where the longer aperture times produce an important image degradation compared to the spaceborne case. In the same manner, the MFB sensitivity with across-track accelerations or/and along-track velocities is, as expected, much higher for the aerial platforms. This refocusing capability could be crucial for the SAR-GMTI detection performance, when imaging small fast boats as analyzed in section 4.3.2, and it is of great interest for post-processing target classification, delivering high-resolution images of the moving vessels.

As pointed out in the literature, accurate channel balancing is crucial for the GMTI operation and the corresponding moving target parameter extraction. Under this view, different calibration strategies have been applied, being the so called digital balancing (DB), a two-dimensional spectral iterative equalization technique, the basis of these methodologies. It has been observed that reduced CNR conditions and so channel coherence could produce an important channel degradation when using such balancing techniques. This has suggested first, to limit its applicability to a given spectral extent, i.e., to define calibration bandwidths; and second, to propose alternative strategies based on a phase-only DB and a modified version of the original DB. When the TSX operates in the DRA mode, the impact of azimuth ambiguities is important, particularly at the edges of the Doppler spectrum. Thus, the calibration strategy should avoid these spectral regions when computing the balancing weights.

The reduced CNR conditions over maritime scenarios, especially important for spaceborne acquisitions, has suggested the use of land patches as a reference for extraction of the iterative calibration/balancing weights. For F-SAR data, it has been observed that an important residual phase between the different channels exists even after application of MOCO, which also performs channel coregistration. Channel equalization, consider-

ing the different strategies, allows an improvement of 30 to 34 dB in terms of SCNR for DPCA technique over the shortest baseline configuration for two of the vessels in the region of interest; in case of EDPCA and ISTAP this figure is around 4-6 dB. For the spaceborne acquisitions using TSX data, no big differences are observed when considering or not channel balancing, taking into account that some type of phase calibration has been already applied on the TSX products [148].

Despite the fact that the available data sets contain only big vessels with high reflectivity, such that the potential subclutter detection capabilities of the sensors combined with the adaptive processing techniques has not been evidenced, a proof of the processing concept for the different GMTI algorithms has been achieved. For the four channel F-SAR configuration, the EDPCA and ISTAP techniques provide a considerable improvement in terms of SCNR around 16 dB compared to the single channel case and close to 6 dB w.r.t DPCA technique. For the TSX data set, with slow moving targets (1-2 m/s of across-track velocity), both EDPCA and ISTAP provide similar detection capabilities with an SCNR slightly above the single channel case. In the same line, the DPCA technique provides a lower number of detected pixels over the different vessels compared to ATI, which shows similar detection capabilities to the new adaptive techniques EDPCA and ISTAP. A major concern in the evaluation of the SAR-GMTI operation of the TSX-DRA mode is the role of the vessel ambiguities, which could be falsely detected as moving targets. From the different processed results, it seems that EDPCA and ISTAP provide a much better signal-to-ambiguity-ratio. For these scenarios, with bright vessels and the related ghost or ambiguous artifacts, several proposals have been considered to discriminate the real vessels from their related ambiguities exploiting polarimetry: in [157,158] the use of cross-polarized channels HV and VH filters vessel ambiguities; and in [159] time-frequency (TF) analysis of polarimetric data allows discriminating the real ships from the ghosts.

From the analysis carried out in this chapter some points remain open and need to be further analyzed: the fringe-like pattern along azimuth in the F-SAR ISTAP images; and the different behavior of EDPCA and ISTAP over the moving target ambiguities. Apart from these considerations, a much more interesting study to investigate the potential capabilities of both X-band sensors is required based on ad-hoc experimental campaigns, which consider worse-case scenario of moving vessels, i.e., small slow moving boats sailing on a rough sea. These experiments should be well-defined in order to make available ground-truth data of both vessels and sea conditions at the acquisition instants for validation purposes. Additionally, an accurate characterization of the instrument would be desirable, specifically regarding the measured antenna patterns.

In summary, the different results presented in this chapter show the capability to exploit several SAR-GMTI algorithms for maritime surveillance using both airborne and spaceborne SAR sensors, providing (re-focused) high-resolution images of the moving vessels. The study performed points out also the key role of the channel balancing (calibration) strategies in the SAR-GMTI operation.

6

Chapter 6

SAR sea clutter characterization

*C*HARACTERIZATION and modeling of the sea clutter returns observed by SAR sensors are of great interest for the accurate evaluation of future SAR missions imaging the sea, and intended to cover a wide variety of applications, among others, GMTI and sea/ocean parameter inversion. This chapter is devoted to a detailed characterization of sea/ocean clutter returns at X-band imaged by TSX mission in a three-level basis: average radar backscattering coefficient; statistical; and polarimetric descriptions. A set of 17 TSX polarimetric data takes covering the typical spaceborne incidence angle range (20-40 degrees) is analyzed. The applicability of different theoretical models for the three level characterization has been as well assessed. An extension of the well-known X-Bragg model, named as X2-Bragg (extended-extended Bragg), is also proposed and evaluated. X2-Bragg properly accounts for the impact of additive thermal noise as well as sea clutter temporal decorrelation, due to the DRA acquisition mode. The suitability of such model on the available data sets provides better matching than the original X-Bragg model¹.

¹This chapter contain portions, sometimes verbatim, of the author's publication [JA3].

6.1 Introduction

The imaging capability of a SAR, independent from daylight and weather conditions, represents a potential tool for globally monitoring the ocean. SAR is a very important forecast instrument in Oceanography, allowing, among others, the retrieval of ocean wave spectrums [160] and the measurement of ocean or river current velocities using along-track interferometry (ATI) configurations [88].

Different approaches have been proposed to properly characterize the radar response of sea clutter, following a physical (electromagnetic) description [119,120] or, as in [122,127], trying to model the electromagnetic interaction between radar signal and sea in terms of a stochastic process. Low resolution sea clutter can be accurately modeled as an uncorrelated Gaussian process (Rayleigh in magnitude). However, as the radar resolution increases, the echo returns are spikier with heavy-tailed distributions. Log-normal and Weibull distributions have been commonly used to describe such non-Gaussian clutter [161,162]. K-distribution, which provides a good description of the sea clutter magnitude for high-resolution radars [82,133], has been theoretically justified on the basis of the compound model introduced by Ward [82].

Most of the experimental measurements that prove the validity of such statistical distributions rely on ground-based real aperture radars [82], or airborne systems [81,161], operating at low and medium grazing angles (typically above 40 degrees of incidence angle). Despite the large amount of data available from spaceborne SAR missions, there is a lack of an exhaustive analysis and characterization of the sea clutter statistics. This chapter evaluates the consistency of some sea clutter statistics, with special interest on K-distribution, for the X-band region using a data set of 17 TSX polarimetric SSC images.

Exploiting polarimetry jointly with SAR confers the polarimetric SAR (PolSAR) instruments a unique and powerful capability to extract quantitative geophysical and biophysical information. For proper interpretation of the data from PolSAR sensors, physical models have to be precisely defined, such that adequate parametric inversion of the physical scattering mechanism can be obtained. In this way, and to complement the stochastic characterization of the sea, a quantitative polarimetric analysis is performed using entropy (H) and mean alpha angle ($\bar{\alpha}$), parameters introduced by Cloude and Pottier in [163]. It is generally accepted that the backscattering of the sea surface in the microwaves spectral region is dominated by Bragg scattering, [164]–[170]. In this regard, a basic model for the sea surface is the small perturbation model (SPM) or Bragg scattering, which predicts zero cross-polar components. However, as some studies stated [166,168–170], depolarisation in the measured data is observed. In [170] a simple model is proposed, based on the so called extended or X-Bragg model [171], to predict the entropy of breaking waves events in littoral areas.

This chapter evaluates also the applicability and fitness of the X-Bragg surface scattering model to X-band sea clutter using fully polarimetric TSX data sets. In TSX quad-pol acquisition, using DRA mode [172], the receive antenna is split into two halves (receiving two different polarizations simultaneously) and the polarization of the transmit antenna is toggled in a pulse basis. On one hand, there is an increase of 3 dB in the NESZ due to a reduced antenna effective area per channel. On the other hand, a temporal lag exists between the different polarimetric channels, during which sea clutter decorrelates. From these considerations, an extension of the X-Bragg model (X2-Bragg) to account for

thermal noise and temporal decorrelation is proposed and evaluated.

One of the main difficulties encountered in modeling the sea clutter is to find an appropriate model of its average mean power, described by the radar backscattering coefficient σ^0 . A lot of effort has been devoted to develop semi-empirical models that could relate this coefficient to radar parameters, acquisition geometry and sea conditions, among which the Georgia Institute of Technology (GIT) [125], the Hybrid (HYB) [126], the Technology Service Corporation (TSC) [127] and the Naval Research Laboratory (NRL) [128]. Recently, in [173] a geophysical model function (GMF), known as XMOD2, has been proposed to model the reflectivity of dual-pol TSX and TDX data. The work here presented also addresses the validity of the two latter empirical models for an X-band sea clutter using the same set of TSX polarimetric data.

This chapter presents a characterization of the sea clutter returns imaged by X-band SAR missions, such as TSX, in terms of its radar backscattering coefficient, statistical description and polarimetric behavior. A set of 17 SSC TSX images, collected at different geographical locations and with different polarizations (dual-pol and quad-pol), has been analyzed, trying to cover the range of typical spaceborne SAR incidence angles (20-40 degrees). Especial emphasis is devoted to study the impact of system-driven and scenario-dependent constraints (noise and temporal decorrelation), when using polarimetry to model the backscattering mechanism from the seas and oceans.

The remainder of this chapter is organized as follows. The first section reviews the basic principles of radar sea clutter theory. The foundations of the polarimetric decomposition and the related X-Bragg model are also reported. In the second section an extension of the X-Bragg model (X2-Bragg) accounting for the thermal noise and temporal decorrelation impacts is proposed and theoretically evaluated. The methodology followed to perform the sea clutter characterization is introduced in the third section. Then, the TSX data base used to perform the sea clutter analysis is described. The last part of the chapter reports the different results of the study.

6.2 Radar sea clutter theory

Many different theoretical and experimental studies have been dedicated to the analysis and modeling of the sea/ocean clutter, but its behavior is not yet completely understood. In some cases, as remote sensing of the ocean with SAR sensors, the sea clutter is the signal of interest; while in others, as maritime surveillance using GMTI radars, it is the unwanted signal, against whom the target of interest should compete. Therefore, it is important to understand the radar response of the sea clutter to validate the application under analysis, e.g., performance evaluation of SAR-GMTI over maritime scenarios. The following lines present the extendedly used reflectivity models and statistical descriptions as well as the basics on polarimetry necessary to interpret the different results. For the interested reader: references [82] and [174] are textbooks devoted to sea/ocean radar imaging theory and applications; and [175] covers polarimetric radar from basics to applications.

6.2.1 Radar backscattering coefficient models

In order to properly assess the performance of any radar when detecting targets over maritime scenarios, it is required to quantitatively predict the sea radar backscattering

coefficient² σ^0 as a function of system and scenario parameters. In this way, it is possible to define metrics as the SCNR and the CNR of key importance in determining the detection capability in the presence of interference signal (clutter plus noise).

Due to the complexity of the sea clutter itself and the lack of complete mathematical descriptions, semi-empirical models appear as the best option to provide some insight into the response of the sea clutter reflectivity as a function of radar parameters, geometry and sea conditions. At this point it must be noted that these models are limited by the fact that they rely on site and condition specific experimental measurements. Therefore, care must be taken when considering a direct extrapolation to model any desired scenario/system condition to be evaluated. This is also evidenced by the dispersion in σ^0 when comparing the different semi-empirical models.

A lot of research has been devoted to determine the sea backscattering coefficient σ^0 as a function of radar parameters, geometry and sea conditions. Table 6.1 summarizes the main characteristics of some of those sea clutter σ^0 models. Three semi-empirical models have been widely referenced in the literature: GIT [125], HYB [126] and TSC [127]. Recently, a new model, referred as NRL, has been proposed in [128], giving the lowest absolute deviation w.r.t the reference tables of Nathanson [176] when compared to the other models. To date, the tables of Nathanson are the standard reference for the sea clutter reflectivity as a function of frequency, grazing angle (or complementary incidence angle), sea state and polarization. In [176], Nathanson compiled a large body of σ^0 measurements, from approximately 60 experiments, covering frequencies from 500 MHz to 35 GHz, grazing angles between 0.1 to 60 degrees (30-89 degrees incidence angle), horizontal and vertical polarizations, and for sea states 0 to 6. It must be noted that some of these tabulated values were result of extrapolation and interpolation between different measurements, and were averaged for the different wind directions (up-, down- and cross-wind).

The GIT model combines empirical factors with mathematical models of the different mechanisms involved in the radar backscattering of the sea clutter. Three main components contribute to the computed mean clutter reflectivity: an interference (multipath) term, a wind speed factor and a wind directional factor. This model allows a more complete description of the sea conditions since both wind speed and wave height can be provided as input parameters [125]. The main drawback of this model is the limited range of grazing angles 0.1-10 degrees (89-90 degrees incidence angle), which makes it unsuitable for application to spaceborne SAR (20-40 degrees incidence angle).

The HYB model is an empirical model derived from fitting curves to Nathanson's tables. It has also been discarded as its validity is limited to small grazing angles, 0.1-30 degrees. TSC model has been derived based on Nathanson database. It provides the largest span of grazing angles (0.1-90 degrees), covering most radar bands of interest (0.5-35 GHz). However, this model has also been rejected: differences in the mathematical formulation presented in some published works [127, 177] and the unclarity on the units' definition of some input parameters, difficult its validation against published results.

Recently a new GMF, denoted by XMOD2, has been proposed and optimized for TSX co-polarized (VV and HH) acquisitions, [173]. This model is applicable to X-band

²In the literature the radar backscattering coefficient σ^0 is also referred as normalized radar cross section (NRCS).

Table 6.1: Models of sea radar backscattering coefficient (or NRCS) σ^0 .

Parameter	Models				
	GIT	HYB	TSC	NRL	XMOD2
Spectral domain [GHz]	1-100	0.5-35	0.5-35	0.5-35	9.65
Incidence angle [deg]	80-89.9	60-89.9	0-89.9	30-89.9	20-45
Polarization	HH, VV	HH, VV	HH, VV	HH, VV	HH, VV
Average wave height [m]	0-4	×	×	×	×
Wind speed [m/s]	1.5-15.5	Douglas SS (0-5)	Douglas SS (0-5)	Douglas SS (0-5)	<20
Wind aspect angle	✓	✓	✓	×	✓

TSX/TDX data for incidence angles between 20 and 45 degrees to extract sea surface wind velocity in the range of 2-20 m/s. To retrieve σ^0 at horizontal polarization (HH), polarization ratio (PR) models should be used. In [173], three PR models (T-PR, E-PR and X-PR) have been proposed and optimized for co-polarized TSX data. Unlike the NRL model, XMOD2 takes into account the wind aspect component to model the NRCS.

The XMOD2 and NRL models will be taken as reference for the σ^0 characterization done in 6.6.1, and their predicted values will be compared with the estimated radar backscattering coefficient from the available data set. At this point it must be noted that non of these models provide a prediction of σ^0 for the cross-polar channels. HV and VH are expected to have similar behavior due to the reciprocity theorem with lower backscattering returns compared to the co-polar channels.

6.2.2 Statistical models

Accurate modeling of the radar sea clutter is one of the most demanding and complex topics, due to its high variability and the involved complex interdependencies between sea conditions, radar parameters and acquisition geometry. The high heterogeneity of variables affecting the backscattering response of the sea poses many difficulties to find a comprehensive standard characterization, which translates into a dissimilarity between the different proposed models.

For low resolution radars and grazing angles typically above 10 degrees (incidence angles below 80), the amplitude (or magnitude) statistics of the sea returns have a “speckle”-like pattern [82, 133], due to the interference of many scattering centers in the resolution cell. Thus, under these conditions and according to the central limit theorem, the sea can be modeled as a complex Gaussian random process, i.e., Rayleigh distributed in amplitude.

For higher resolution systems and high incidence angles the statistical description of the echo returns deviates from the Gaussian hypothesis, having a target-like response with more heavy tailed distributions [82, 127, 133, 134]. In this regard, good fitting of the data distribution’s tail is of key importance for the construction of CFAR detectors [50], since the shape of the tail determines the threshold used in the detection.

One way to quantitatively evaluate the non-Gaussian behavior of the involved data is

by computing the normalized intensity moments (NIM) of the n -th order [82, 120]

$$\text{NIM}_n = \frac{E\{z^n\}}{E^n\{z\}} \quad (6.1)$$

where z refers to data intensity (or power), i.e., $z = y^2$ being y the magnitude; and $E\{\cdot\}$ is the expectation operator:

$$E\{z^n\} = \int_{-\infty}^{+\infty} z^n p_z(z) dz \quad (6.2)$$

where $p_z(z)$ is the PDF of z . Values of the n -th order NIM above $n!$ (Gaussian limit) are indicators of spiky data.

Among these non-Gaussian descriptors log-normal and Weibull distributions have been found to provide a good fit to some radar sea clutter measurements [161, 162, 178]. The PDF of a log-normally distributed random variable y is expressed by

$$p_y(y) = \frac{1}{y\sqrt{2\pi\sigma^2}} \exp\left(-\frac{(\ln y - \mu)^2}{2\sigma^2}\right); \quad y \geq 0 \quad (6.3)$$

where μ and σ are the location and scale parameters, respectively.

From (6.1) and (6.3) and after some mathematical manipulation, the n -th order NIM of a log-normally distributed random variable can be obtained as

$$\text{NIM}_n = \frac{\exp(2\mu n + 2n^2\sigma^2)}{(\exp(2\mu + 2\sigma^2))^n} \quad (6.4)$$

The ML estimates of the mean and variance can be obtained from the sample estimates [161]

$$\begin{aligned} \hat{\mu} &= \frac{1}{K} \sum_{k=1}^K \ln y_k, \\ \hat{\sigma}^2 &= \frac{1}{K} \sum_{k=1}^K (\ln y_k - \hat{\mu})^2 \end{aligned} \quad (6.5)$$

where K is the number of available magnitude samples y_k .

The fitting of Weibull distribution to sea clutter amplitude statistics, as shown in [162, 179], can be parametrized by means of two terms, the shape β and scale a parameters, where the related PDF is expressed as

$$p_y(y) = \beta \frac{y^{\beta-1}}{a^\beta} \exp\left(-\left(\frac{y}{a}\right)^\beta\right); \quad y \geq 0 \quad (6.6)$$

The n -th order NIM of a Weibull distributed magnitude y can be expressed by [82]

$$\text{NIM}_n = \frac{a^{2n} \Gamma\left(\frac{2n}{\beta} + 1\right)}{\left(a^2 \Gamma\left(\frac{2}{\beta} + 1\right)\right)^n} \quad (6.7)$$

where $\Gamma(\cdot)$ is the gamma function.

The ML estimates of the Weibull parameters involve iteratively solving a system of equations using the sample data. This approach could be time consuming, especially taking into account the proposed statistical characterization's procedure presented in section 6.4, and based on a sliding window (boxcar) method. In [81, 180], efficient algorithms to estimate the Weibull parameters are presented. An attractive procedure considered in [180] and originally proposed by Menon in [181] has been selected:

$$\begin{aligned}\hat{\beta} &= \left\{ \frac{6}{\pi^2} \frac{N}{N-1} \left[\frac{1}{N} \sum_{n=1}^N (\ln y_i)^2 - \left(\frac{1}{N} \sum_{n=1}^N \ln y_i \right)^2 \right] \right\}^{-1/2}, \\ \hat{a} &= \exp \left(\frac{1}{N} \sum_{n=1}^N \ln y_i + \frac{\gamma}{\beta} \right)\end{aligned}\quad (6.8)$$

where γ is Euler's constant.

Different from the other models, K-distribution, which provides a good statistical fit to the sea clutter returns of high resolution radars [82, 133, 134, 161], has a theoretical support and a physical interpretation based on the compound theory [82, 134]. The sea surface structure is a complex assemblage of many types of waves with different characteristics. The rapidly (temporally) decorrelating small structures, such as ripples and foams, result in a speckle-like process, i.e., many different scatterers will be present in a resolution cell. These small structures are modulated by the slowly varying larger-structures, as long-waves and swell³, in a way that the power of the speckle process (Rayleigh in amplitude) is governed by these longer structures.

It is precisely this two-scale behavior that gives rise to the compound model theory justifying the physical link of the K-distribution. Such a stochastic descriptor can be obtained as the product of two independent random variables, i.e., a complex Gaussian (speckle-like term) by a Chi distribution (modulating process). This latter is a result of square rooting a Gamma distribution, which models the local power. In this case the PDF of the magnitude y is given by the K-distribution [82]

$$p_y(y) = \frac{4b^{\frac{(v+1)}{2}} y^v}{\Gamma(v)} K_{v-1}(2y\sqrt{b}); \quad y \geq 0 \quad (6.9)$$

where b and v refer to the scale and shape parameters, respectively; $K_n(\cdot)$ is the modified Bessel function of second kind and order n . The related n -th order NIM can be calculated as

$$\text{NIM}_n = n! \frac{\Gamma(n+v)}{\Gamma(v) v^n} \quad (6.10)$$

The estimation of the K-distribution's parameters using a ML approach requires from a time-consuming iterative approach. The fact that no closed expression for the Bessel

³According to the National Oceanic and Atmospheric Administration (NOAA) definition, swell refers to wind-generated waves that have traveled out of their generating area. Swell characteristically exhibits smoother, more regular and uniform crests and a longer period than wind waves.

function's derivative is available, poses even more difficulties to obtain the ML estimates [81]. Different tractable, but sub-optimal approaches have been proposed and analyzed in [81, 182, 183]. Among them, the *fractional moments* [182] and *Blacknell* [183] methods have been selected for the analysis here considered. The latter is based on the estimates of the mean of data's intensity and the mean of its logarithm as follows

$$\begin{aligned}\hat{v} &= \frac{1}{\langle z \ln z \rangle / \langle z \rangle - \langle \ln z \rangle}, \\ \hat{b} &= \frac{\hat{v}}{\langle z \rangle}\end{aligned}\quad (6.11)$$

where $\langle x^n \rangle$ refers to the sample moment of order n -th

$$\langle x^n \rangle = \frac{1}{K} \sum_{k=1}^K x_k^n \quad (6.12)$$

The method proposed in [182] is a computationally efficient approach based on fractional moments of order p (any positive number)

$$\begin{aligned}\hat{v} &= \frac{\left(\frac{p+2}{2}\right)^2 - \beta_p}{\beta_p - \left(\frac{p+2}{2}\right)} + 1, \\ \hat{b} &= \left[4 \left(\frac{\Gamma(\hat{v}) \langle y \rangle}{\sqrt{\pi} \Gamma(\hat{v} + 0.5)} \right)^2 \right]^{-1}\end{aligned}\quad (6.13)$$

where the ratio β_p is obtained as

$$\beta_p = \frac{\langle y^{(p+2)} \rangle}{\langle y^p \rangle \langle y^2 \rangle} \quad (6.14)$$

6.2.3 Polarimetric description

Several applications use PolSAR data to image the ocean surface, exploiting the additional information provided by fully polarimetric SAR sensors: directional wave spectra, wave slopes and current-driven surface extraction [163]. Polarimetry can be also used for GMTI vessel detection, as proposed in [157] and later in [158].

In the work here presented, and taking into account the availability of PolSAR data (quad and dual-pol), the Cloude-Pottier polarimetric analysis based on $(H/A/\bar{\alpha})$ decomposition has been studied for fully polarimetric data⁴. In [163] Cloude and Pottier propose a method for extracting average parameters, based on the computation of the polarimetric scattering entropy H , anisotropy A and the mean alpha angle $\bar{\alpha}$, providing a useful apparatus for unsupervised classification.

A fully polarimetric SAR system measures the scattering matrix, which, for the monostatic case and in the Pauli base, can be expressed in vectorial notation as

$$\mathbf{k} = \frac{1}{\sqrt{2}} \begin{bmatrix} S_{HH} + S_{VV} & S_{HH} - S_{VV} & 2S_{HV} \end{bmatrix}^T, \quad (6.15)$$

⁴In case of dual-pol, analogous $H/\bar{\alpha}$ decomposition can be obtained as presented by Cloude in [184].

where $(\cdot)^T$ refers to the transpose operator and S_i is the complex data of the i -th polarimetric channel (polarization states in transmission and reception are indicated by the first and second subindices, respectively). The distribution of \mathbf{k} is completely described by the Hermitian positive definite coherency matrix $\mathbf{T} = E\{\mathbf{k}\mathbf{k}^H\}$ under the Gaussian assumption [185]. The main advantage of expressing the scattering vector in the Pauli basis (6.15) is that its components can be directly related with elementary scattering mechanisms. The first element of the vector is assigned to odd bounce scatterer such as the sphere, the plane surface or reflectors of trihedral type. The second term is related to dihedral scatters or double isotropic bounce. The third element is associated to diffuse or volume scattering.

A measure of the randomness of the different scattering mechanisms present in the ensemble (average) coherency matrix is given by the polarimetric entropy defined as

$$H = - \sum_{k=1}^M P_k \log_M (P_k) \quad (6.16)$$

where \log_M is the logarithm with basis M (polarimetric dimension, $M = 3$ for monostatic case); P_k refers to the pseudo-probability obtained from the eigenvalues λ_k of \mathbf{T} as

$$P_k = \frac{\lambda_k}{\sum_{k=1}^M \lambda_k} \quad (6.17)$$

The polarimetric anisotropy provides a measure of the relative significance level between the two lowest (second and third) eigenvalues

$$A = \frac{\lambda_2 - \lambda_3}{\lambda_2 + \lambda_3} \quad (6.18)$$

typically used to discern between scattering classes when entropy H is high.

The alpha angle $\bar{\alpha}$ is a useful metric to identify the dominant scattering mechanism in the averaged information contained in the coherency matrix, providing a physical interpretation of the scattering process. In fact $\bar{\alpha}$ is an average value obtained from

$$\bar{\alpha} = \sum_{k=1}^M P_k \alpha_k \quad (6.19)$$

with α_k as the arc cosine of the absolute value of the first element of the k th eigenvector (rank-1 k -th mechanism).

In the literature [164–169], it is generally assumed that sea clutter responses exhibit typical characteristics of Bragg scattering. In the field of remote sensing, the small perturbation model (SPM) is the most common approximate method used to describe the scattering problem from randomly rough surfaces [171]. The SPM assumes the variation in surface height s to be electrical small (compared to the wavelength). In the limit of a smooth surface $ks < 0.3$, where k is the wavenumber and s the surface rms height (or roughness), the SPM or Bragg scattering applies. Therefore, the scattering is mainly due to the spectral component of the surface in resonance with the incident wavelength and

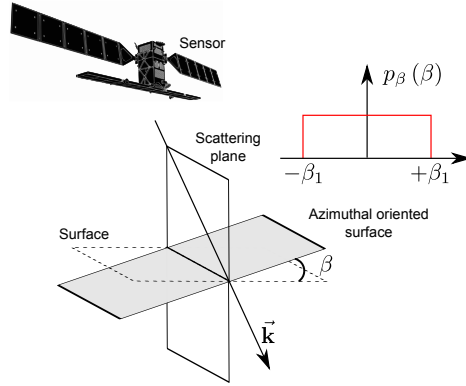


Figure 6.1: Schematic representation of the rotating (an angle β in the plane perpendicular to the scattering plane) symmetric depolarizer to model roughness disturbance according to X-Bragg model; the PDF of a uniform distribution of β angle is also shown (figure adapted from [171]).

the angle of incidence [186]. Apart from its limited applicability to small surface roughness conditions, its sensitivity to soil moisture content m_v gets saturated above 20 [vol.%]. For this model, the surface roughness is a common to all polarimetric channels [187], such that all polarization ratios remain independent of roughness and depend only on dielectric constant ϵ and incidence angle γ_0 . Therefore, this surface has no depolarization. However, natural surfaces are observed to depolarize the incident waves [171, 186, 187]. As noted by Cloude in [187], rough surface scattering provides an important example of reflection symmetric depolarization, where the mean surface normal represents the axis of symmetry. The inability of the SPM to describe depolarization effects restricts its application to the interpretation and inversion of experimental data from natural surfaces, and hence this simplistic model should be modified.

The extended or X-Bragg model is an upgrade of the simplistic SPM, where depolarization as well as cross-polarized backscattering effects are included, broadening the applicability of the Bragg scattering to a wider range of roughness conditions. The X-Bragg is a two-component model including a Bragg scattering term and a roughness induced rotation symmetric disturbance. As proposed in [170, 171, 187], this can be obtained modeling the surface as a reflection symmetric depolarizer, rotating the Bragg coherency matrix about an angle β w.r.t the local surface normal and averaging it over a statistical distribution $p_\beta(\beta)$, as schematically sketched in Fig. 6.1.

For a uniform distribution $p_\beta(\beta)$ with zero mean and width β_1 , as assumed in [171], the coherency matrix of the extended Bragg surface can be expressed by

$$\mathbf{T} = m_s^2 \begin{bmatrix} C_1 & C_2 \operatorname{sinc}(2\beta_1) & 0 \\ C_2^* \operatorname{sinc}(2\beta_1) & C_3 (1 + \operatorname{sinc}(4\beta_1)) & 0 \\ 0 & 0 & C_3 (1 - \operatorname{sinc}(4\beta_1)) \end{bmatrix} \quad (6.20)$$

where m_s is the backscatter amplitude related to the surface roughness; sinc function refers to $\operatorname{sinc}(x) = \sin(x)/x$. Distribution's width β_1 models the roughness disturbance

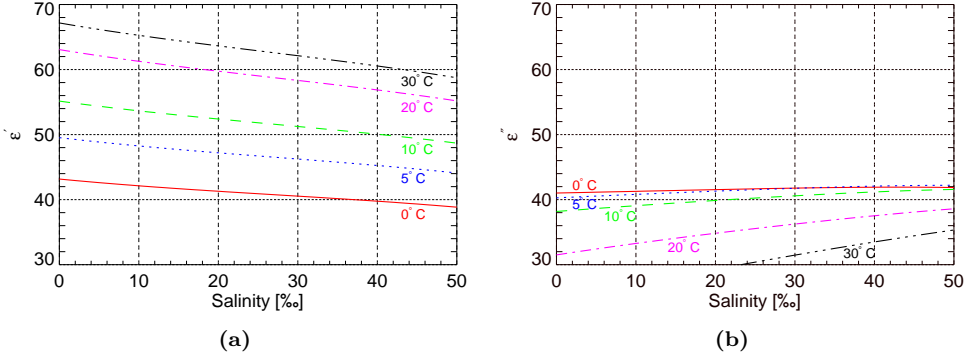


Figure 6.2: Sea water dielectric constant (at 9.65 GHz) as a function of salinity (in ‰) for different temperatures: (a) real and (b) imaginary parts (computed according to Klein's model [189]).

of the surface⁵ and controls the polarimetric $(S_{HH} + S_{VV})(S_{HH} - S_{VV})$ coherence and the level of cross-polarized power [171]. For β_1 of 0° , i.e., in the limit of a smooth surface, the polarimetric $(S_{HH} + S_{VV})(S_{HH} - S_{VV})$ coherence is one, and the HV backscattered power is zero. In this case the coherency matrix has the form of a “pure” Bragg and the SPM applies. Higher contribution of the cross-polarized returns is obtained when increasing the roughness (increasing β_1); while $(S_{HH} + S_{VV})(S_{HH} - S_{VV})$ coherence decreases. For values of β_1 up to 90° (i.e., $ks = 1$), the coherence converges to zero.

Coefficients C_1 , C_2 and C_3 in (6.20) can be expressed in terms of the perpendicular and parallel Bragg scattering coefficients, B_\perp and B_\parallel as

$$\begin{aligned} C_1 &= |B_\perp + B_\parallel|^2 \quad C_2 = (B_\perp + B_\parallel)(B_\perp - B_\parallel)^*, \\ C_3 &= \frac{1}{2}|B_\perp - B_\parallel|^2 \end{aligned} \quad (6.21)$$

The Bragg scattering coefficients, perpendicular and parallel to the incidence plane, are functions of the complex permittivity ϵ and the local incidence angle γ_0 :

$$\begin{aligned} B_\perp &= \frac{\cos \gamma_0 - \sqrt{\epsilon - \sin^2 \gamma_0}}{\cos \gamma_0 + \sqrt{\epsilon - \sin^2 \gamma_0}}, \\ B_\parallel &= \frac{(\epsilon - 1)(\sin^2 \gamma_0 - \epsilon(1 + \sin^2 \gamma_0))}{(\epsilon \cos \gamma_0 + \sqrt{\epsilon - \sin^2 \gamma_0})^2} \end{aligned} \quad (6.22)$$

The dielectric constant $\epsilon = \epsilon' - j\epsilon''$ is extracted from the model developed by Klein and Swift in [189], which parametrizes the sea water permittivity in terms of the salinity content and the temperature for a given frequency of operation. Fig. 6.2 shows the real (ϵ') and imaginary (ϵ'') parts of the complex dielectric constant (at 9.65 GHz) as function of the salinity (in parts-per-thousand ‰) and for different temperatures (in degrees Celsius $^\circ\text{C}$).

⁵ β_1 can be understood as the amount of deformation of the scattering surface as pointed out in [188].

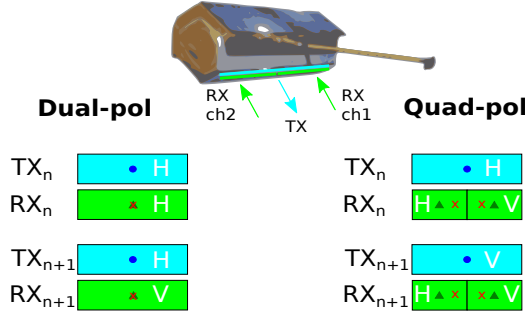


Figure 6.3: Schematic representation of the TSX dual- and quad-pol acquisition modes (DRA operation is used to obtain fully polarimetric data); transmit (TX) phase center denoted by the solid circle, receive (RX) by the triangle symbol and effective two-way (2-W) by the cross symbol; TX_n-RX_n and TX_{n+1}-RX_{n+1} refer to the transmit-receive instance for the n -th and $n + 1$ -th pulses, respectively.

6.3 Extended X-Bragg (X2-Bragg) model

6.3.1 Modeling

The schematic representation of the TSX dual- and quad-pol acquisitions is shown in Fig. 6.3. The DRA mode [172], employed to obtain fully polarimetric images with an along-track interferometric configuration, has a two-fold impact on measured data. On one hand, as the receive antenna is halved, a direct consequence is a reduction on the received gain, which translates into higher values of the NESZ. On the other hand, the alternate transmission of horizontal and vertical polarizations in a pulse-by-pulse basis jointly with the along-track configuration (to receive simultaneously H and V polarizations), produces a temporal lag between different pairs of channels.

The different polarimetric channels should be spatially aligned (coregistrated), such that they observe the scene from the same positions but at different times. During this time-lag, around $\tau_{coreg.} = 1$ ms for TSX S_{HH} and S_{VV} channels (or S_{HV} and S_{VH}), the sea backscattered field decorrelates due to ICM. Typical decorrelation times of the sea are between 8 ms and 10 ms for wind speeds of 15 m/s down to 5 m/s [84]. For an X-band system at VV the temporal coherence ρ_{temp} could be between 0.9 and 1.0 for a time-lag around 1 ms [84]. From the results presented in section 6.6 for TSX quad-pol, it has been observed that both the noise level and the sea clutter temporal decorrelation should be accounted for in the X-Bragg model to properly characterize the sea clutter in polarimetric terms. In the following lines an extension of the X-Bragg model, referred as X2-Bragg (extended-extended Bragg), is presented to introduce the impact of both noise and additional temporal decorrelation, in a two-step procedure.

First of all, let's define an equivalent coherency matrix which accounts for the noise perturbation (analogous to the study in [190])

$$\mathbf{T}' = \mathbf{T} + \mathbf{N} \quad (6.23)$$

where \mathbf{T} refers to the expected coherency matrix related to the sea clutter and $\mathbf{N} = \sigma_n^2 \mathbf{I}_{3 \times 3}$ the noise coherency matrix, with $\mathbf{I}_{3 \times 3}$ as the 3x3 identity matrix. For simplicity, it has

been assumed that the different polarimetric channels have uncorrelated additive circular complex Gaussian noise with the same power σ_n^2 .

From the previous considerations, and using a general formulation, (6.23) can be expressed as

$$\mathbf{T}' = (\sigma_1^2 + \sigma_n^2) \overline{\mathbf{T}}' \quad (6.24)$$

where the normalized (to \mathbf{T}'_{11}) coherency matrix is

$$\overline{\mathbf{T}}' = \begin{bmatrix} 1 & \sqrt{\frac{\sigma_2^2}{\sigma_1^2}} \overbrace{\rho_{\text{SNR}_1} \rho_{12}}^{\rho_T} & 0 \\ \sqrt{\frac{\sigma_2^2}{\sigma_1^2}} \rho_{\text{SNR}_1} \rho_{12}^* & \frac{\sigma_2^2}{\sigma_1^2} \frac{1+1/\text{SNR}_2}{1+1/\text{SNR}_1} & 0 \\ 0 & 0 & \frac{\sigma_3^2}{\sigma_1^2} \frac{1+1/\text{SNR}_3}{1+1/\text{SNR}_1} \end{bmatrix} \quad (6.25)$$

with σ_1^2 , σ_2^2 and σ_3^2 referring to the signal power of the three polarimetric channels (in the Pauli base); SNR_1 , SNR_2 and SNR_3 the corresponding signal-to-noise ratios, i.e., $\text{SNR}_i = \sigma_i^2 / \sigma_n^2$; ρ_{12} represents the polarimetric correlation (coherence) coefficient between $(S_{HH} + S_{VV})$ and $(S_{HH} - S_{VV})$ channels; and ρ_{SNR_1} models the decorrelation effect induced by the presence of thermal noise:

$$\rho_{\text{SNR}_1} = \frac{1}{1 + 1/\text{SNR}_1} \quad (6.26)$$

such that the total coherence, based on a multiplicative model, is defined by ρ_T .

From the original X-Bragg model formulation in (6.20), the different parameters in (6.25) can be expressed as

$$\begin{aligned} \sigma_1^2 &= m_s^2 C_1, \\ \sigma_2^2 &= m_s^2 C_3 (1 + \text{sinc}(4\beta_1)), \\ \sigma_3^2 &= m_s^2 C_3 (1 - \text{sinc}(4\beta_1)), \\ \rho_{12} &= \frac{C_2 \text{sinc}(2\beta_1)}{\sqrt{C_1 C_3 (1 + \text{sinc}(4\beta_1))}} \end{aligned} \quad (6.27)$$

From the previous relationships, the three polarimetric SNR can be defined in terms of an equivalent SNR_{Eq}

$$\begin{aligned} \text{SNR}_1 &= C_1 \text{SNR}_{Eq}, \\ \text{SNR}_2 &= C_3 (1 + \text{sinc}(4\beta_1)) \text{SNR}_{Eq}, \\ \text{SNR}_3 &= C_3 (1 - \text{sinc}(4\beta_1)) \text{SNR}_{Eq} \end{aligned} \quad (6.28)$$

in a way that if the SNR_1 is estimated from the data, the equivalent $\text{SNR}_{Eq} = m_s^2 / \sigma_n^2$ can be inverted from the model and used to properly account for the thermal noise impact in the X-Bragg model fitting.

In multichannel adaptive array and GMTI theory, the impact of temporal decorrelation is known to cause an increase in the number of eigenvalues (of the clutter-plus-noise

covariance matrix) different from the noise floor, [13]. In this sense, the X-Bragg model has been further extended to account for temporal decorrelation, in terms of an additional coherence coefficient ρ_{temp} . It must be noted that this term cannot be directly introduced in matrix (6.25) since the temporal decorrelation is between the individual polarimetric channels with some spatial or temporal baseline. This additional term should be considered in the covariance matrix \mathbf{C} formulation. For the X-Bragg model, where the cross-correlations between co-polar and cross-polar channels are zero, the additional temporal decorrelation ρ_{temp} is included only in the off-diagonal terms of \mathbf{C} corresponding to the correlation between S_{HH} and S_{VV} . First, a transformation of the normalized coherency matrix $\bar{\mathbf{T}}'$ (6.25) into the covariance matrix is performed

$$\bar{\mathbf{C}}' = \{\mathbf{U}_{3(L \rightarrow P)}\}^{-1} \bar{\mathbf{T}}' \{\mathbf{U}_{3(L \rightarrow P)}^H\}^{-1} \quad (6.29)$$

where $\{\cdot\}^{-1}$ refers to matrix inversion and the unitary transformation (L \rightarrow P) from the Lexicographic target vector to the Pauli vector is [175]

$$\mathbf{U}_{3(L \rightarrow P)} = \frac{1}{\sqrt{2}} \begin{bmatrix} 1 & 0 & 1 \\ 1 & 0 & -1 \\ 0 & \sqrt{2} & 0 \end{bmatrix} \quad (6.30)$$

Then, the additional coherence coefficient ρ_{temp} is included as multiplicative term into the off-diagonal terms of $\bar{\mathbf{C}}'$ to obtain $\bar{\mathbf{C}}''$:

$$\bar{\mathbf{C}}''_{13} = \bar{\mathbf{C}}'_{13} \rho_{temp}, \quad \bar{\mathbf{C}}''_{31} = \bar{\mathbf{C}}'_{31} \rho_{temp} \quad (6.31)$$

The normalized coherency matrix for the X2-Bragg model $\bar{\mathbf{T}}''$ can be obtained using a matrix transformation of $\bar{\mathbf{C}}''$ by means of $\mathbf{U}_{3(L \rightarrow P)}$, inversely analogous to the case in (6.29), i.e., $\bar{\mathbf{T}}'' = \mathbf{U}_{3(L \rightarrow P)} \bar{\mathbf{C}}'' \mathbf{U}_{3(L \rightarrow P)}^H$.

From now on, the polarimetric analysis and decomposition are applied over the normalized coherency matrix $\bar{\mathbf{T}}''$. After some mathematical manipulation the (non-sorted) eigenvalues resulting from the eigendecomposition of $\bar{\mathbf{T}}''$ are:

$$\begin{aligned} \lambda_1 &= \frac{1}{2} \left\{ 1 + \bar{\mathbf{T}}''_{22} - \sqrt{1 + \bar{\mathbf{T}}''_{22} (-2 + \bar{\mathbf{T}}''_{22}) + 4|\bar{\mathbf{T}}''_{12}|^2} \right\}, \\ \lambda_2 &= \frac{1}{2} \left\{ 1 + \bar{\mathbf{T}}''_{22} + \sqrt{1 + \bar{\mathbf{T}}''_{22} (-2 + \bar{\mathbf{T}}''_{22}) + 4|\bar{\mathbf{T}}''_{12}|^2} \right\}, \\ \lambda_3 &= \bar{\mathbf{T}}'_{33} \end{aligned} \quad (6.32)$$

and the related eigenvectors

$$\begin{aligned} \mathbf{u}_1 &= \begin{bmatrix} -\frac{-1 + \bar{\mathbf{T}}''_{22} + \sqrt{1 + \bar{\mathbf{T}}''_{22} (-2 + \bar{\mathbf{T}}''_{22}) + 4|\bar{\mathbf{T}}''_{12}|^2}}{2\bar{\mathbf{T}}''_{21}} & 1 & 0 \end{bmatrix}, \\ \mathbf{u}_2 &= \begin{bmatrix} -\frac{-1 + \bar{\mathbf{T}}''_{22} - \sqrt{1 + \bar{\mathbf{T}}''_{22} (-2 + \bar{\mathbf{T}}''_{22}) + 4|\bar{\mathbf{T}}''_{12}|^2}}{2\bar{\mathbf{T}}''_{21}} & 1 & 0 \end{bmatrix}, \\ \mathbf{u}_3 &= [0 \ 0 \ 1] \end{aligned} \quad (6.33)$$

which should be properly normalized to obtain the unitary eigenvectors, i.e., $\bar{\mathbf{u}}_i = \frac{\mathbf{u}_i}{\|\mathbf{u}_i\|}$.

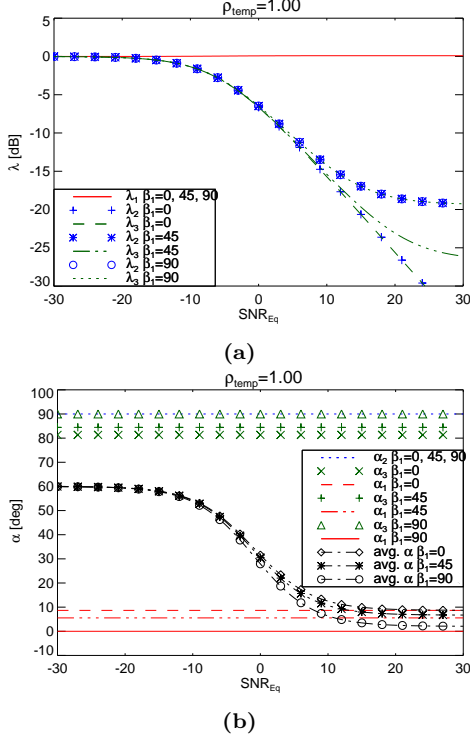


Figure 6.4: Sensitivity w.r.t. SNR_{Eq} for the X2-Bragg model, considering the noise impact and a temporal decorrelation $\rho_{temp} = 1.0$ for three values of the uniform's distribution width β_1 ; an X-band system (9.65 GHz), an incidence angle $\gamma_0 = 24.6$ degrees, a sea temperature of 10°C and a salinity of 35 ‰ are assumed: (a) eigenvalues; (b) alphas.

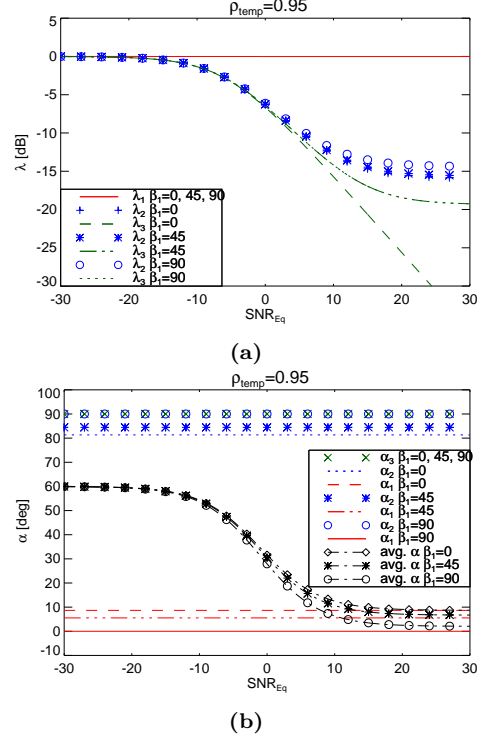


Figure 6.5: Sensitivity w.r.t. SNR_{Eq} for the X2-Bragg model, considering the noise impact and a temporal decorrelation $\rho_{temp} = 0.95$ for three values of the uniform's distribution width β_1 ; an X-band system (9.65 GHz), an incidence angle $\gamma_0 = 24.6$ degrees, a sea temperature of 10°C and a salinity of 35 ‰ are assumed: (a) eigenvalues; (b) alphas.

6.3.2 Evaluation

The sensitivity of the eigenvalues and α parameters as a function of SNR_{Eq} for $\rho_{temp} = 1.0$ and $\rho_{temp} = 0.95$ is shown, respectively, in Figs. 6.4 and 6.5, exploiting the theoretical coherency matrix formulation $\bar{\mathbf{T}}''$ of the X2-Bragg model. An X-band system (9.65 GHz), an incidence angle γ_0 of 24.6 degrees (corresponding to the center of TSX-4 acquisition, see Table 6.2), and sea conditions of 10°C and 35 ‰ salinity content have been assumed. In Figs. 6.4a and 6.5a the eigenvalue distribution is represented as a function of SNR_{Eq} for ρ_{temp} of 1 and 0.95, respectively. The three eigenvalues collapse, regardless of β_1 and ρ_{temp} , when the SNR_{Eq} is below -10 dB, being the noise the dominant mechanism.

In case of $\beta_1 = 0^\circ$ (smooth surface) and with increasing SNR_{Eq} , the two smallest eigenvalues λ_2 and λ_3 have the same decreasing trend when no temporal decorrelation is included, see Fig. 6.4a. Their contribution is 30 dB below λ_1 for $SNR_{Eq} > 20$ dB, in

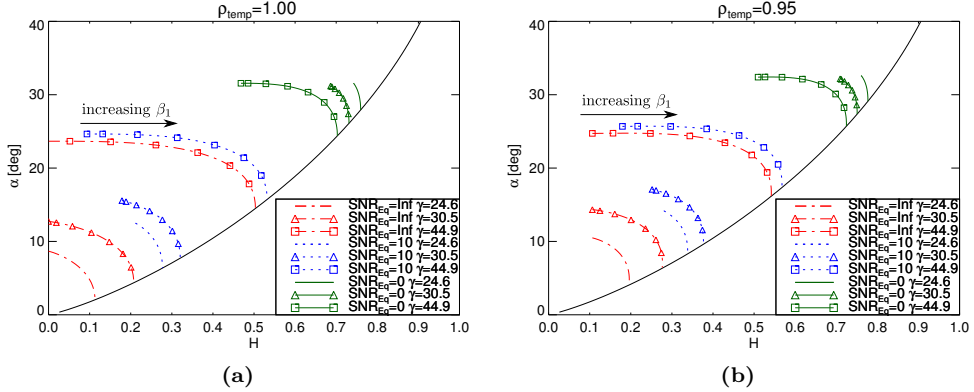


Figure 6.6: $H/\bar{\alpha}$ plane for the X2-Bragg model at three incidence angles (24.6, 33.8 and 44.9 degrees) and for three SNR_{Eq} conditions (∞ , 10 and 0 dB): (a) $\rho_{temp} = 1.0$ and (b) $\rho_{temp} = 0.95$ (sea water with salinity content of 35 ‰ and temperature of 10°C).

which case SPM applies with a single dominant mechanism. This can be observed also from the averaged value ($\bar{\alpha}$), which tends to α_1 for increasing values of SNR_{Eq} [Fig. 6.4b].

As β_1 (roughness) gets larger, the cross-polar component grows, and hence more than a single dominant mechanism exists. For $\beta_1 = 45^\circ$ and $SNR_{Eq} > 10$ dB the two smallest eigenvalues start to diverge. In the limit $\beta_1 = 90^\circ$ and with no additional temporal decorrelation, λ_2 and λ_3 have the same trend as a function of the effective SNR, since polarimetric coherence ρ_{12} decreases to 0. Considering a temporal decorrelation of $\rho_{temp} = 0.95$, a general increase of the second eigenvalue can be recognized (for $SNR_{Eq} > 10$ dB), comparing Figs. 6.4a and 6.5a, especially for $\beta_1 = 0^\circ$. In case of λ_3 this behavior is also observed but for $\beta_1 \geq 45^\circ$.

Different from the eigenvalues' trend, the individual α parameters are almost unaffected by the presence of noise as shown in Figs. 6.4b and 6.5b. Polarimetric decomposition considers the mean $\bar{\alpha}$ for its classification, based on proper weighting of the individual α terms through the eigenvalues' probabilities (6.19). As shown in Figs. 6.4b and 6.5b, $\bar{\alpha}$ presents a large variation as a function of SNR_{Eq} for different values of β_1 . In the limit (noise being the dominant mechanism), $\bar{\alpha}$ tends to 60 degrees, such that the scattering mechanism lies in the extreme edge of region 2 of the Cloude-Pottier $H/\bar{\alpha}$ plane, i.e., no polarization dependence. Temporal decorrelation exchanges the behavior of the individual α_2 and α_3 parameters, comparing Figs. 6.4b and 6.5b but does not affect the averaged values. When no temporal decorrelation is considered ($\rho_{temp} = 1$) α_2 collapses to 90 degrees regardless of β_1 and α_3 sweeps the values from 80 to 90 degrees; whereas for $\rho_{temp} = 0.95$ α_3 is 90 degrees regardless of the roughness parameter. Therefore, temporal decorrelation is not impairing the values of α parameters but it is modulating the contribution of the different mechanisms. For $\rho_{temp} = 0.95$ the cross-polar component (related to $\alpha = 90$ regardless of β_1) is no longer the second dominant scattering mechanism, as in the case of no temporal decorrelation ($\rho_{temp} = 1$).

The impact of both thermal noise and temporal decorrelation in the X2-Bragg model is also analyzed in the $H/\bar{\alpha}$ plane, as represented in Figs. 6.6a and 6.6b for $\rho_{temp} = 1$ and $\rho_{temp} = 0.95$, respectively. Different incidence angles have been considered, corresponding

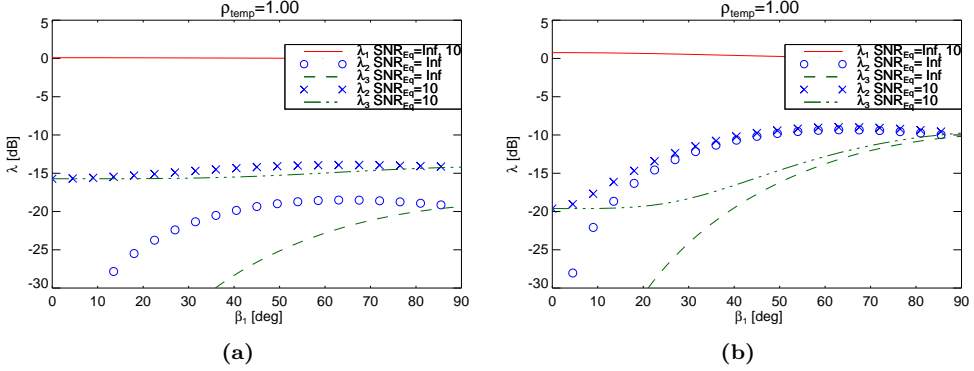


Figure 6.7: Sensitivity w.r.t. β_1 for the X2-Bragg model considering the noise impact and $\rho_{temp} = 1.0$: incidence angle of (a) $\gamma_0 = 24.6$ degrees and (b) $\gamma_0 = 44.9$ degrees (sea water with salinity content of 35 ‰ and temperature of 10°C).

to the center of data takes TSX-4 (24.6 degrees), TSX-7 (30.5 degrees) and TSX-17 (44.9 degrees), defined in Table 6.2. The noise impact is translated into a progressive increase of both $\bar{\alpha}$ and H as SNR_{Eq} decreases. Moreover, the variation of the $H/\bar{\alpha}$ pairs as a function of β_1 is reduced when the noise contribution increases. Temporal decorrelation produces similar effects but its impact gets reduced as long as the entropy increases, clearly visible for the region with $H > 0.6$ when comparing Figs. 6.6a and 6.6b.

A particular case in the $H/\bar{\alpha}$ plane is recognized for $\text{SNR}_{Eq} = 0$ dB, where the variation as a function of incidence angle is reversed, i.e., the near range presents higher entropy values than the far range. As long as the noise contribution increases the divergence between the two smallest eigenvalues (λ_2 and λ_3) gets reduced (increasing the entropy) and this effect is more severe in the near range. This relative separation is also a function of the roughness (β_1), which for noisy near range scenarios is quite flat, as demonstrated in Fig. 6.7. This figure shows the eigenvalue's sensitivity w.r.t β_1 for two different incidence angles ($\gamma_0 = 24.6$ and 44.9 degrees) and for two SNR_{Eq} conditions (∞ and 10 dB). Such a response justifies the reduction on H as a function of β_1 for increasing noise, especially at near range.

In summary, the additional source of decorrelation, i.e., noise and/or temporal decorrelation of the scene, tends to increase the entropy of the scattering matrix, affecting mainly the distribution of the related eigenvalues, while keeping unchanged the individual alpha parameters. This means that the corresponding eigenvectors are not influenced by these disturbances. Therefore, such system/scenario-dependent terms can limit the correct interpretation of the scattering mechanisms.

6.4 Sea Clutter Characterization Methodology

A software module has been implemented to automatically perform a complete and exhaustive characterization of the data based on the three-level approach (σ^0 , statistics and polarimetry), as depicted in the block diagram in Fig. 6.8. It can accept as input a set of different data takes from different sensors, where each one is processed sequentially. Each

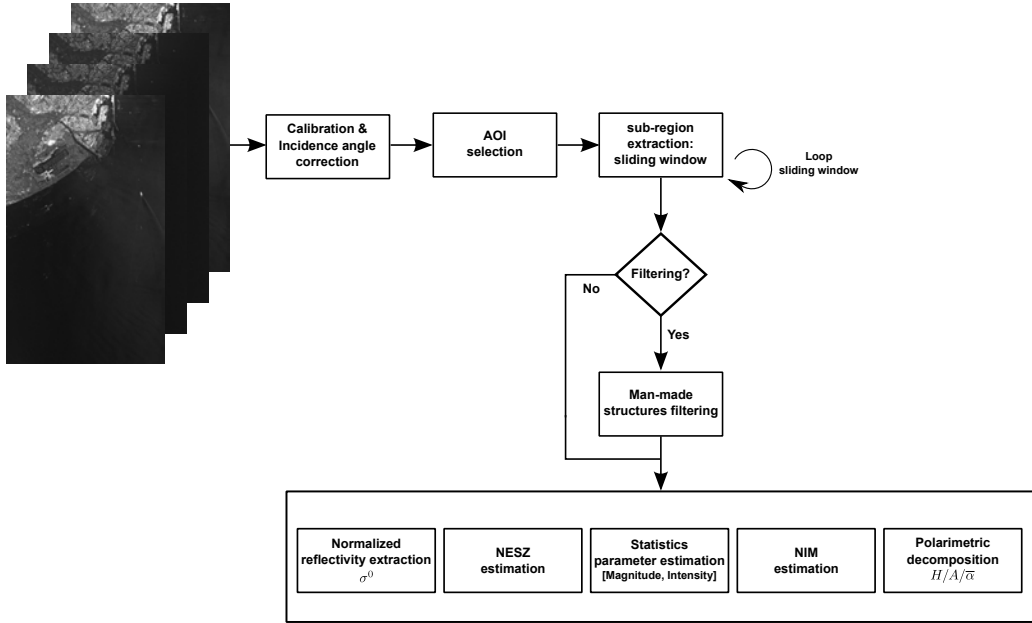


Figure 6.8: Block diagram of the sea clutter characterization module.

data take can be conformed either by single channel or multichannel (either polarimetric or GMTI) products. The first sub-module performs a radiometric calibration and incidence angle correction, based on the input product information, such that the intensity of the pixels at its output is related to σ^0 values⁶. The next block performs a selection of the sea clutter AOI, which is, to date, carried out simply by a visual inspection of the image product considering a rectangular AOI. A fully automatic selection could integrate a pre-processing operation to generate a land mask over the image. In this line, the alternative proposed by Alonso-González *et al.* in [191], exploits the polarimetric information jointly with binary partition tree (BPT) for image segmentation, which can be applied to coastline detection, among others.

Once the AOI has been determined, a sub-region characterization based on a sliding window (or boxcar) over this very AOI is performed. The use of a boxcar enables the possible spatial variabilities of the three-level descriptors (σ^0 , statistics and polarimetry) to be accounted for in the analysis. The size of such a sliding window as well as the overlapping in both range and azimuth dimensions can be defined. The selection of the window size is a compromise between accuracy on the estimation of the underlying three-level parameters and resolution of their spatial variation. For the statistical characterization and σ^0 estimation a window considering the whole azimuth strip for each range bin (range line basis) has been selected, such that the dependence of different descriptors (such as σ^0 and K-distribution shape parameter) with the incidence angle can be studied.

For the polarimetric decomposition, the coherency matrix \mathbf{T} is estimated from the

⁶It must be noted that pixels with negative intensities once the calibration is performed are excluded from subsequent characterizations.

data, such that the speckle noise is filtered. The ML estimator of \mathbf{T} can be obtained as the spatial averaging (boxcar or multilook filter)

$$\hat{\mathbf{T}} = \frac{1}{L} \sum_{l=1}^L \mathbf{k}_l \mathbf{k}_l^H \quad (6.34)$$

where L refers to the number of looks or samples employed in the estimation of \mathbf{T} and \mathbf{k}_l the vector in the Pauli base for the l -th sample. To avoid mixing different scattering mechanisms and to obtain adequate speckle filtering, a sliding window of 11x11 without overlapping has been used [192].

As proposed in [171], an additive noise filtering (for quad-pol data) can be performed in order to reduce the noise impact. It is generally assumed that the scattering matrix is symmetric, i.e., $S_{HV} = S_{VH}$, hence the 4x4 scattering coherency matrix \mathbf{T}_4 , formed using the outer product ($\mathbf{k}_4 \mathbf{k}_4^H$) of the 4-dimensional scattering vector \mathbf{k}_4 in (6.35), is a Hermitian positive semidefinite matrix of rank three.

$$\mathbf{k}_4 = \frac{1}{\sqrt{2}} \begin{bmatrix} S_{HH} + S_{VV} & S_{HH} - S_{VV} & S_{HV} + S_{VH} & j(S_{HV} - S_{VH}) \end{bmatrix}^T \quad (6.35)$$

The eigendecomposition of \mathbf{T}_4 provides three real non-negative eigenvalues, while the fourth one (λ_4) is zero. Under noise-free conditions the HV and VH polarization channels are completely correlated [175]. Nevertheless, the receivers have the unavoidable thermal noise, which reduces the correlation between the cross-polar channels and hence \mathbf{T}_4 becomes a rank-4 matrix with $\lambda_4 > 0$. This means that an estimation of λ_4 allows the assessment of the noise level (power) in the data. Assuming that the four polarimetric channels have the same noise power, subtracting the estimated $\hat{\lambda}_4$ from the diagonal of the 3x3 coherency matrix $\hat{\mathbf{T}}$ removes the noise level in the data

$$\hat{\mathbf{T}}_{NF} = \hat{\mathbf{T}} - \hat{\lambda}_4 \mathbf{I}_{3 \times 3} \quad (6.36)$$

where $\mathbf{I}_{3 \times 3}$ is the 3x3 identity matrix; and $\hat{\mathbf{T}}_{NF}$ corresponds to the averaged coherency matrix after noise filtering (NF). Therefore, the polarimetric description can be performed before and after NF.

Prior to sub-AOI dependent characterization, specific filtering on the data can be completed, such that the impact of man-made structures present in the open sea (vessels, oil platforms, wind farms and alike) is minimized in subsequent steps, avoiding corruption of the data analysis. Taking into account that most of the selected data takes have none or only few vessels within the imaged area, a simple filter approach has been implemented: those pixels, whose magnitude y_i

$$y_i \geq \mu_{subAOI} + \beta \sigma_{subAOI} \quad (6.37)$$

exceeds the mean statistical value μ_{subAOI} in a given number of times β the standard deviation σ_{subAOI} , are discarded. Both statistical moments are estimated from the available samples within the sub-AOI, while the β term is experimentally adjusted, with typical values between 2 to 6. At this point it must be noted that a more sophisticated filtering approach, as the one proposed in [157], could be integrated when an area of really dense maritime traffic is imaged.

Table 6.2: TSX data takes used in the sea clutter characterization (B_r and B_a range and azimuth processed bandwidths, respectively; v_{win} and θ_{win} wind speed and direction from where the wind is blowing).

ID	Date	Time	Region	Mode	γ [deg]	B_r [MHz]	B_a [Hz]	v_{win} [m/s]	θ_{win} [deg]
TSX-1	05.03.2013	19:09:26	Senegal	Dual-Pol	19.85-21.74	150	1380	-	-
TSX-2	09.03.2013	06:04:15	Gulf of Guinea	Dual-Pol	22.43-24.26	150	1380	-	-
TSX-3	25.04.2010	14:55:05	Vancouver Island	Quad-Pol	23.75-25.49	150	1380	12.1	143
TSX-4	06.05.2010	14:55:05	Vancouver Island	Quad-Pol	23.75-25.49	150	1380	6.3	331
TSX-5	16.03.2013	07:09:03	Mauritania	HH	24.80-27.99	150	2765	-	-
TSX-6	30.04.2010	22:31:50	Bermuda	Quad-Pol	29.70-31.30	150	1380	6.5	258
TSX-7	11.05.2010	22:31:50	Bermuda	Quad-Pol	29.70-31.30	150	1380	6.9	62
TSX-8	05.03.2013	07:09:15	Mauritania	Dual-Pol	30.81-32.33	150	1380	-	-
TSX-9	05.03.2013	07:10:32	Senegal	Dual-Pol	31.91-33.42	150	1380	-	-
TSX-10	12.04.2010	06:02:48	Barcelona	Quad-Pol	33.04-34.50	150	1380	-	-
TSX-11	28.04.2010	15:35:59	Southeast Yakutat	Quad-Pol	36.18-37.54	150	1380	7.2	164
TSX-12	09.05.2010	15:36:00	Southeast Yakutat	Quad-Pol	36.18-37.54	150	1380	5.7	350
TSX-13	23.04.2010	10:16:02	Pratas Island	Quad-Pol	39.03-40.29	150	1380	-	-
TSX-14	25.04.2010	14:54:27	South Hecate Strait	Quad-Pol	40.02-41.25	150	1380	13.1	140
TSX-15	06.05.2010	14:54:27	South Hecate Strait	Quad-Pol	40.02-41.25	150	1380	6.7	318
TSX-16	17.03.2013	18:48:09	Gulf of Guinea	Dual-Pol	43.45-44.58	150	1380	-	-
TSX-17	21.04.2010	17:18:53	North Sea	Quad-Pol	44.37-45.48	150	1380	-	-

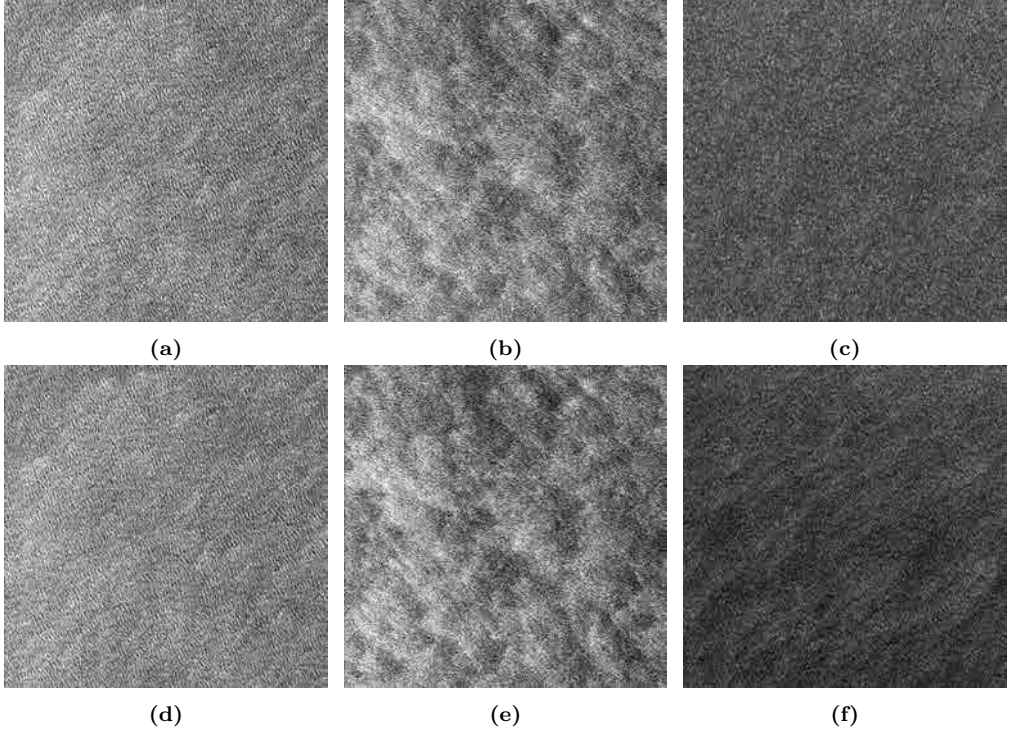


Figure 6.9: Multilook (11x11) sea patches (512x512 pixels size): (a), (d) S_{HH} and S_{VV} for TSX-4; (b), (e) S_{HH} and S_{VV} for TSX-7; (c), (f) S_{HH} and S_{VV} for TSX-17.

6.5 Data Set Description

The main parameters of the TSX products used in the analysis are summarized in Table 6.2. Different aspects were considered for the selection of the data under analysis: (i) covering the spaceborne SAR operational range of incidence angles from 20 to 40 degrees; (ii) avoiding heterogeneity in the reflectivity over the imaged area; (iii) avoiding regions with high density of maritime traffic and/or marine littorals (because of the high ambiguities' impact in the DRA acquisition); (iv) when possible, polarimetric acquisitions are preferred over single-polarized ones.

The available fully polarimetric TSX data was acquired during the experimental DRA mode campaign, April and May 2010. It is well-known that sea or ocean conditions and hence its radar response could be quite different depending on the geographical location of the marine scenario under analysis; this is why, the acquisitions have been chosen trying to sample different oceans (Atlantic and Pacific) and seas (North, Mediterranean and China). Portions of the images of three representative data takes (near/TSX-4, middle/TSX-7 and far incidence/TSX-17) are represented in Fig. 6.9 showing the variability of the sea clutter returns.

Some of the major difficulties encountered were to find ground-truth data for the whole set of acquisitions, and for the ones available, to obtain accurate measurements of the sea

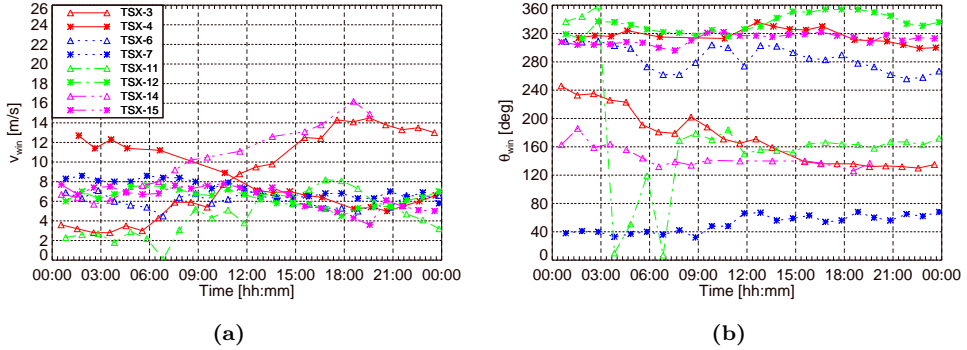


Figure 6.10: Evolution of the sea conditions during the day of acquisition for the data takes with available meteorological information: (a) wind speed and (b) direction from where the wind is blowing.

conditions (for the acquisition's time and spatial location). In this regard, only for some acquisitions, whose imaging regions were Vancouver Island, Bermuda, Southeast Yakutat and South Hecate Strait, ground-truth data is available from the historical data base of the National Data Buoy Center of the NOAA and Canadian Moored Bouy of the DFO. The geographical location of the employed buoys matches the center of the acquired images, but the temporal sampling rate is not sufficient to determine the exact meteorological conditions of the sea for the acquisition time. Fig. 6.10 shows the evolution of the sea conditions in terms of wind speed and wind direction (from where the wind is blowing) during the day of acquisition for the different data sets with available meteorological information.

6.6 Results

6.6.1 Radar backscattering coefficient

The estimated σ^0 for the different data takes is depicted as a function of the incidence angle for the co-polar channels in Figs. 6.11a-b, and the cross-polar one S_{HV} in Fig. 6.11c⁷. NESZ is also reported for the different data takes as dotted black lines. From Fig. 6.11, some expected general trends can be stated: the sea radar return decreases as a function of incidence angle, where S_{VV} channel has generally higher backscattering (for $\gamma_0 > 30$ degrees) than HH polarization. The cross-polar channels have low σ^0 values, close to noise level. Comparing the NESZ of quad-pol data with dual-pol acquisitions (e.g., TSX-6 vs TSX-8), a degradation around 3 dB is obtained due to the DRA mode operation (antenna in reception is halved into two parts). Therefore, the increase in NESZ for quad-pol data (reduced SNR) will impair the proper characterization of the sea clutter using TSX data, as exhaustively analyzed in section 6.6.3 for polarimetric description.

In Figs. 6.11a-b the co-polar values predicted by the NRL and XMOD2 models are indicated by the shaded regions, delimited by dash-dot-dot gray and dashed gray lines,

⁷Symmetric behavior is obtained for the VH channel.

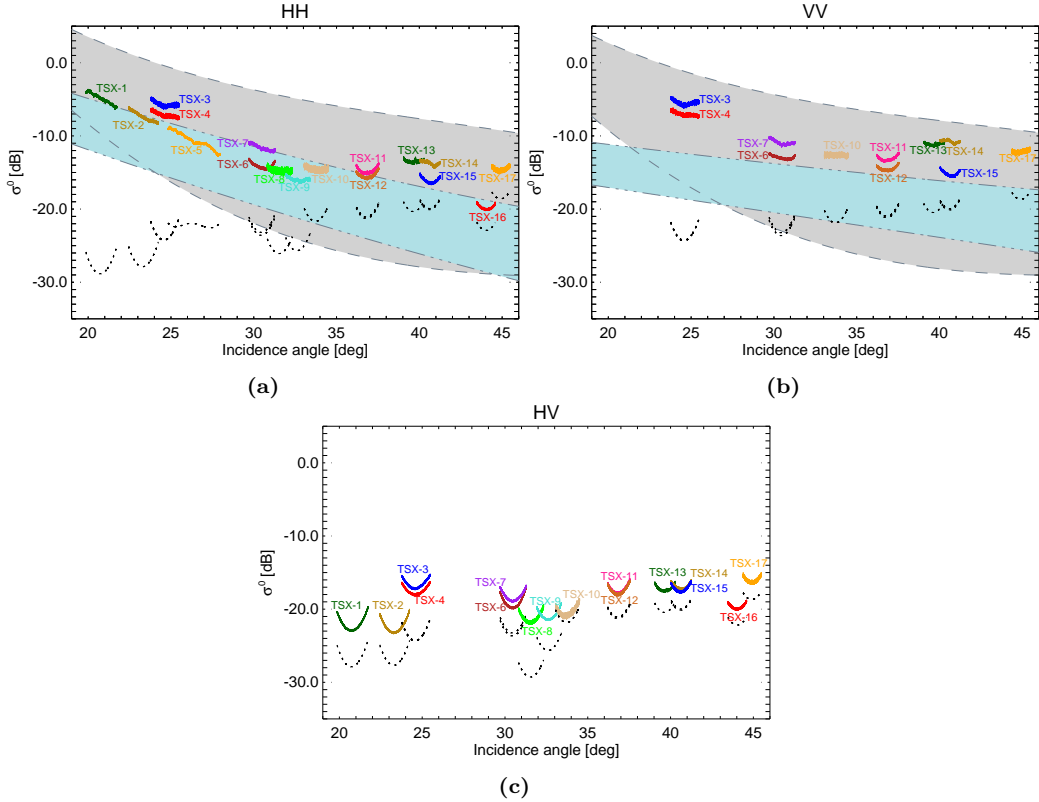


Figure 6.11: Estimated σ^0 as a function of the incidence angle, using a sliding window in a range line basis with no overlap: (a) HH, (b) VV and (c) HV; the different data takes are color coded; the estimated NESZ (dotted black line) is also plotted; and the shaded regions represent the predicted values from the NRL (powder blue) and XMOD2 (light gray) models, for a wind speed variation of 0.1-20.0 m/s (average value between upwind, crosswind and downwind is performed for the XMOD2 as well as an average over the different PR models for HH extraction).

respectively, for a sea surface wind speed range of 0.1-20 m/s. In the XMOD2 case, an average of the upwind, crosswind and downwind conditions has been considered. Moreover, the expected values for HH have been also averaged for the different PR models (T-PR, E-PR and X-PR). It must be noted that the NRL model is a general purpose σ^0 model that covers the microwave spectral band for a wide range of incidence angles; whereas XMOD2 is an ad-hoc descriptor for TSX/TDX data.

The mean values of the estimated σ^0 for the different data takes are reported in Table 6.3, where the NRL and XMOD2 predicted values for co-polar channels and data takes with ground truth (gray shaded rows) are included. This is an illustrative table to show the level of applicability of the two theoretical models, since average values of the estimated σ^0 are taken and sea conditions are available only for a specific location on the image.

Table 6.3: Estimated σ^0 (in dB) compared to the expected value from NRL and XMOD2 models for the data takes with ground truth.

HH							VV			HV	VH	
ID	Est.	XMOD2					NRL	Est.	XMOD2	NRL	Est.	Est.
		T-PR	E-PR	X-PR	$x_0 = 0.6$	X-PR						
TSX-1	-4.86										-21.90	
TSX-2	-7.32										-22.22	
TSX-3	-5.66	-5.01	-4.31	-2.44	-5.00	-10.17	-5.47	-4.55	-14.18	-16.52	-16.29	
TSX-4	-7.09	-8.85	-8.15	-6.28	-8.84	-12.64	-7.02	-8.39	-16.27	-17.43	-17.20	
TSX-5	-10.50											
TSX-6	-14.08	-12.27	-11.68	-9.52	-12.09	-16.59	-12.95	-11.62	-17.99	-18.97	-18.71	
TSX-7	-11.60	-11.41	-10.83	-8.67	-11.23	-16.36	-10.89	-10.77	-17.79	-18.19	-18.00	
TSX-8	-14.73										-21.12	
TSX-9	-15.95										-20.75	
TSX-10	-14.54						-12.63				-20.28	-19.75
TSX-11	-14.74	-16.26	-16.15	-13.32	-15.89	-20.20	-13.09	-15.42	-19.53	-17.28	-17.27	
TSX-12	-15.41	-17.37	-17.25	-14.43	-16.99	-21.17	-14.46	-16.52	-20.35	-17.44	-17.34	
TSX-13	-13.47						-11.13				-17.15	-16.51
TSX-14	-13.72	-12.65	-13.02	-9.615	-12.17	-19.46	-10.76	-11.70	-18.15	-16.90	-16.00	
TSX-15	-16.09	-16.03	-16.40	-12.99	-15.56	-22.73	-15.13	-15.08	-20.90	-17.19	-17.17	
TSX-16	-19.77										-19.65	
TSX-17	-14.55						-12.13				-16.00	-15.86

The NRL model has an average deviation w.r.t. the estimated values of 6.92 dB and 5.11 dB for S_{VV} and S_{HH} channels, respectively. While XMOD2 presents a mean error of 0.98 dB for S_{VV} ; and for S_{HH} channel, the average deviation is 1.12 dB, 1.23 dB and 2.63 dB for T-PR, E-PR and X-PR. Since the available information of the sea conditions does not correspond precisely to the time of acquisition some error could be introduced in the inversion of the σ^0 for the theoretical models.

The higher discrepancy obtained for NRL model is due to the optimization of its coefficients on the basis of minimizing the absolute deviation w.r.t. Nathanson's tables [176]. The NRL parametrization uses only two tables, at 30 and 60 degrees of incidence angle, while five tables are used to model reflectivity at incidence angles greater than 80 degrees. Therefore, a degradation in modeling properly σ^0 is expected when considering typical spaceborne geometries with 20-40 degrees of incidence angle. In case of XMOD2, which agrees much better with the estimated values, the source of discrepancy should also be related to the fact that this model has been optimized for a given set of TSX/TDX co-polarized data sets, and not for quad-pol data. In order to reduce the higher deviation observed when retrieving σ^0 for HH using the X-PR model, an experimental tuning of the parameter x_0 used in [173] to a value of 1.1, allows reducing the average deviation to 1.19 dB, similar to the results obtained with T-PR and E-PR models.

6.6.2 Statistical characterization

Fig. 6.12 shows the fitting of the considered distributions (K, Rayleigh, log-normal and Weibull) to the magnitude (or amplitude) for data takes TSX-4, -7 and -17 (from left to right) and for HH, VV and HV polarizations (from top to bottom). Only the results for a specific single sub-AOI are shown. The distributions are plotted on a logarithmic scale, i.e., the clutter is expressed in dB, which for calibrated data refers to σ^0 . For TSX-4, in the small incidence angle region, K-distribution fits best the data distribution, especially in the distribution's tail (higher values of σ^0), see Fig. 6.12a. This is crucial in GMTI operation, since the tail's shape determines the detection threshold for a given false alarm rate. Weibull distribution shows good agreement with the data only for smaller σ^0 values, while the log-normal does not fit the data distribution. Similar results are obtained for the S_{VV} channel, Fig. 6.12d. In the cross-polar channel S_{HV} , Fig. 6.12g, the three distributions (K, Rayleigh and Weibull) collapse to a complex Gaussian distribution mainly due to the noise impact. Similar trends are observed also for TSX-7 case Figs. 6.12b, 6.12e and 6.12h.

As far as data take TSX-17 is concerned, the reduction in SNR comparatively with TSX-4, leads to a major contribution of the thermal noise, which is translated into a more Gaussian-like distribution (Rayleigh in amplitude). This behavior can be recognized from the statistical fitting in Fig. 6.12c, where the K- and Weibull distributions tend to a Rayleigh one, i.e., shape parameters $v > 30$ and $\beta \approx 2$, accordingly. For the S_{VV} channel, there is an increase of around 3-4 dB in SNR compared to HH polarization, and K-distribution slightly departs from Gaussianity fitting best the data, particularly in the tail's region.

K-distribution's shape parameter (v) is a good indicator that allows deciding whether the data under analysis is spikier (small values) or tends to a Gaussian distribution (high values). In Fig. 6.13 the estimated shape parameter of a K-distribution fitting on the

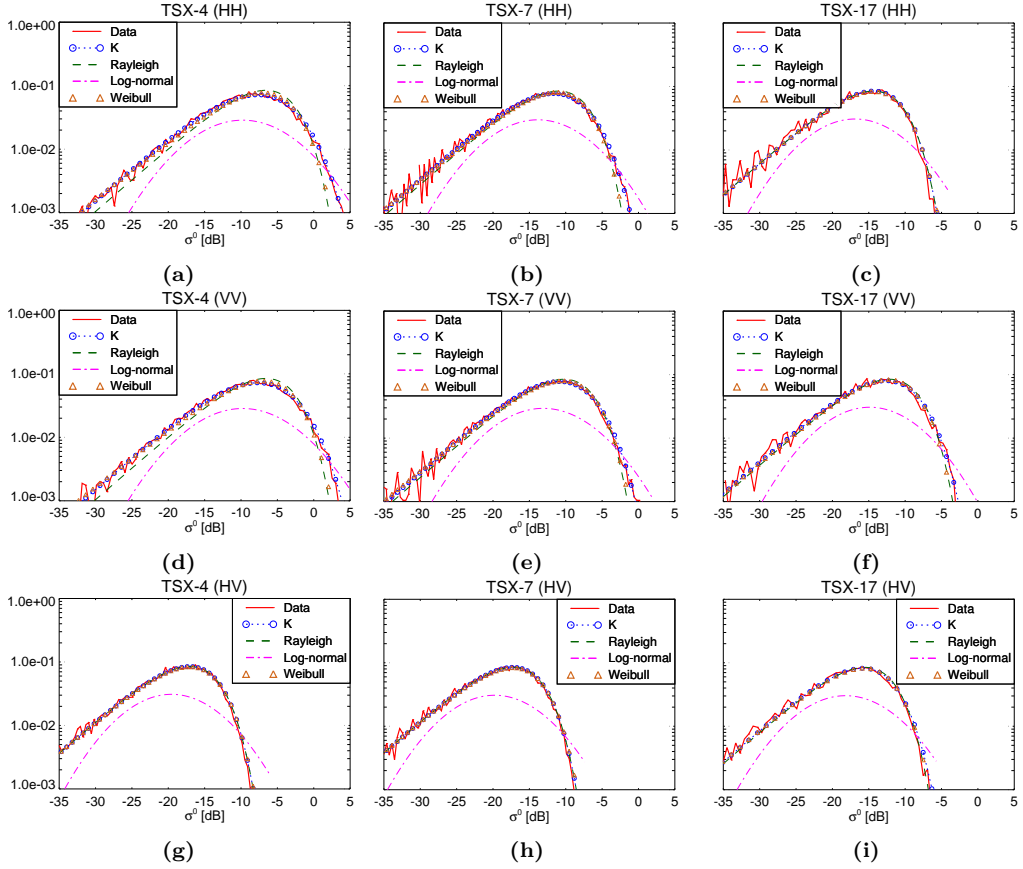
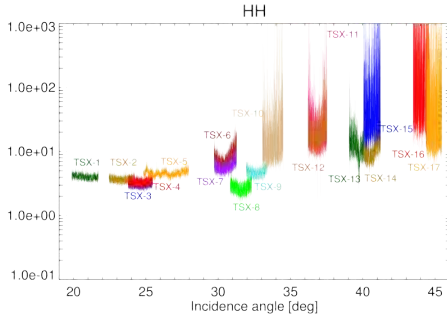


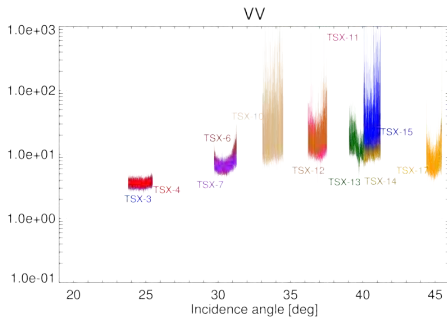
Figure 6.12: Fitting of theoretical distributions (K, Rayleigh, log-normal and Weibull) to different data takes (TSX-4, -7 and -17 from left to right) and for the different polarimetric channels (HH, VV and HV from top to bottom) using a sliding window in a range line basis with no overlap (plots refer to a single sub-AOI window within each data take): (a), (d) and (g) TSX-4 HH, VV and HV; (b), (e) and (h) TSX-7 HH, VV and HV; (c), (f) and (i) TSX-17 HH, VV and HV.

data's amplitude is shown as a function of incidence angle for the different data takes and for the three polarimetric channels S_{HH} , S_{VV} and S_{HV} . Blacknell's method [183] has been used to estimate the shape and scale parameters of a K-distribution fitting on data's amplitude. Similar results have been obtained using the *fractional moments* method [182].

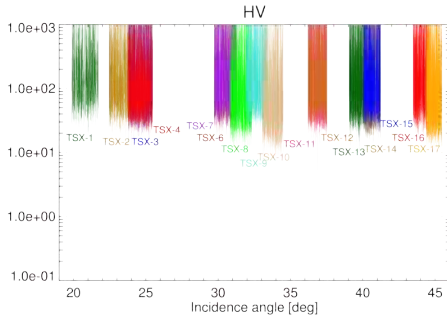
In S_{HH} channel, Fig. 6.13a, and for incidence angles between 20 and 33 degrees, the shape parameter has a range of 3-10, with contained variation for each data take. For incidence angles greater than 35 degrees the values of the shape parameter are above 10 with much higher dispersion, which is related to the reduction in SNR as incidence angle increases, see Fig. 6.11a. This can be clearly observed at data takes TSX-16 and TSX-17 (with the highest incidence angle), where noise impact produces a variation on the shape parameter from 10 to 1000. For VV polarization, Fig. 6.13b, similar trends



(a)

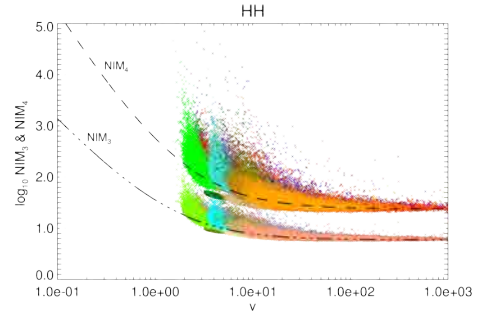


(b)

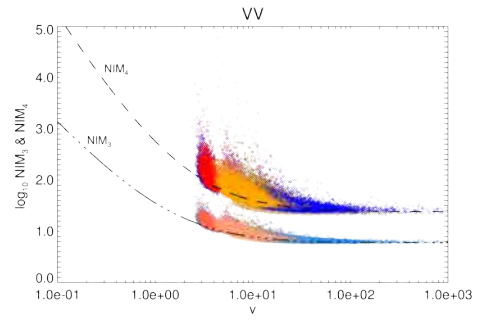


(c)

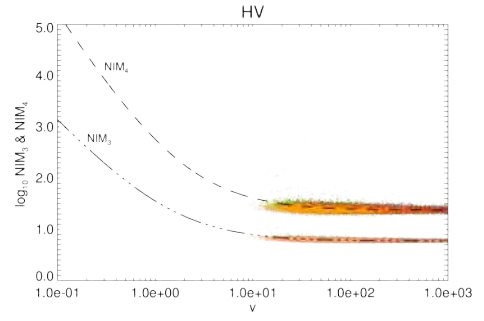
Figure 6.13: Estimated shape parameter for a K-distributed amplitude fitting of the data as a function of incidence angle, using a sliding window in a range line basis with no overlap: (a) HH, (b) VV and (c) HV; the different data takes are color coded as in Fig. 6.11 (shape parameter estimated using Blacknell's approach (6.11)).



(a)



(b)



(c)

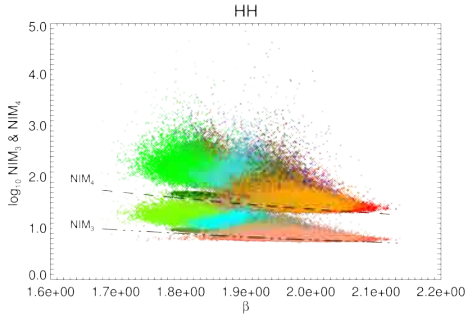
Figure 6.14: Estimated third and fourth order NIM as a function of the estimated K-distribution shape parameter v for the different data takes, using a sliding window in a range line basis with no overlap: (a) HH, (b) VV and (c) HV; the different data takes are color coded as in Fig. 6.11; theoretical third (dash-dot-dot line) and fourth (dashed line) order NIM for the fitted K-distribution are included.

are observed; but in this case the higher sea clutter returns in the high incidence region reduce the shape parameter dispersion on data take TSX-17, with values between 5 to 20. As expected from the reflectivity analysis, the low sea backscattering at cross-polar channels, with levels comparable to the system sensitivity (NESZ), justifies the shape parameter's high values (above 20) and its high dispersion, see Fig. 6.13c.

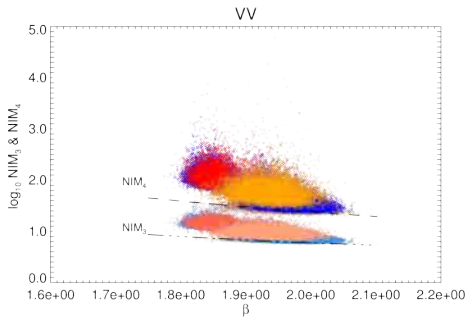
Comparing the shape parameters of the polarimetric channels (e.g., TSX-4 and TSX-6), different values are obtained showing that the scalar product model (on which K-distribution is based) can be extended to a multivariate product model, associating an individual texture variable per polarimetric channel, [193, 194]. This multivariate modeling can be used jointly with the Mellin kind statistics (MKS) in the log-cumulant domain as a valuable analysis tool to characterize statistics based on the product model approach [194].

NIM is a useful metric to evaluate the non-Gaussian behavior of the data under analysis. Fig. 6.14 shows the estimated third (pale color) and fourth (bright color) NIM as a function of the estimated K-distribution shape parameter for the different data takes. On top of the scattering plots, the expected theoretical third (dash-dot-dot line) and fourth (dashed line) order NIM for the fitted K-distribution in magnitude are depicted. In general, for the co-polar channels, see Figs. 6.14a and 6.14b, estimated values are in good agreement with the theoretical ones, indicating that the sea clutter magnitude could be modeled as a K-distribution. Higher dispersion is observed in the estimated fourth order NIM, since the same number of samples has been used to estimate both moments; however, it is well-known that the higher the statistical order to be estimated the larger the number of samples to be used. When comparing both co-polar channels, it can also be noted that the S_{VV} channel has lower dispersion on the estimated NIM. For the cross-polar channels, Fig. 6.14c, the 3rd and 4th order NIM collapse on the tail of the theoretical ones, proving the Gaussian statistics of these channels.

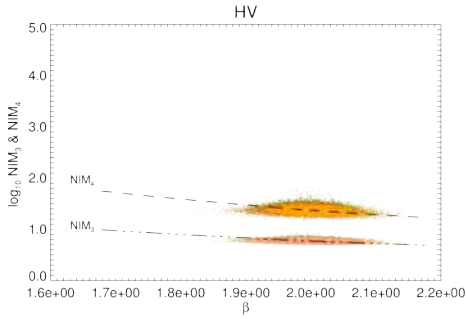
Analogously, the estimated 3rd and 4th order NIM are represented as a function of the estimated shape parameter β for a Weibull distribution fitting on the amplitude's data, as presented in Fig. 6.15. When compared to K-distribution fitting, the Weibull presents generally a worse matching with the theoretical trends for the co-polar channels. For some acquisitions (e.g., TSX-15 in S_{HH} and S_{VV} or TSX-17 in S_{HH}), which are more Gaussian-like, there is a good fitting of the estimated NIM with the theoretical Weibull ones, i.e., in the β region around 2.0, where the Weibull tends to a Rayleigh distribution. When considering a log-normal distribution fitting to the magnitude of the available data sets, a poor matching between the estimated NIM and the theoretical ones, (6.4), is obtained, as observed in Fig. 6.16. The 3rd and 4th order NIM are represented as a function of the estimated standard deviation σ , which in essence can be thought as a shape parameter, but it is not totally equivalent to v and β shape parameters.



(a)

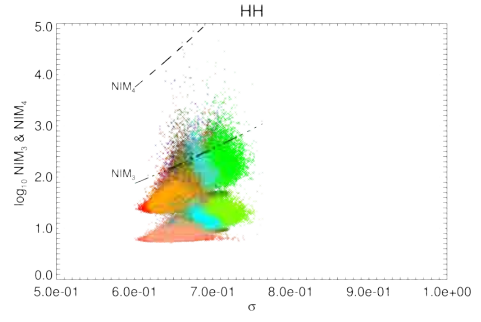


(b)

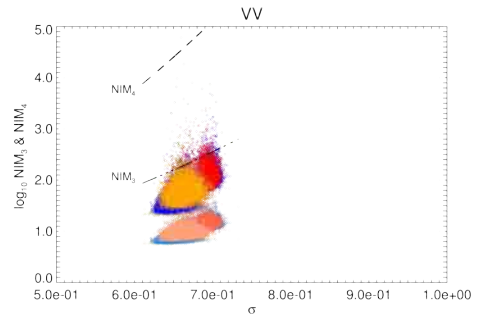


(c)

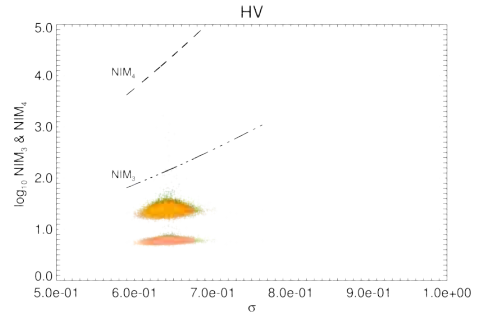
Figure 6.15: Estimated third and fourth order NIM as a function of the estimated Weibull shape parameter β for the different data takes, using a sliding window in a range line basis with no overlap: (a) HH, (b) VV and (c) HV; the different data takes are color coded as in Fig. 6.11; theoretical third (dash-dot-dot line) and fourth (dashed line) order NIM for the fitted Weibull distribution are included.



(a)



(b)



(c)

Figure 6.16: Estimated third and fourth order NIM as a function of the estimated log-normal standard deviation σ for the different data takes, using a sliding window in a range line basis with no overlap: (a) HH, (b) VV and (c) HV; the different data takes are color coded as in Fig. 6.11; theoretical third (dash-dot-dot line) and fourth (dashed line) order NIM for the fitted log-normal distribution are included.

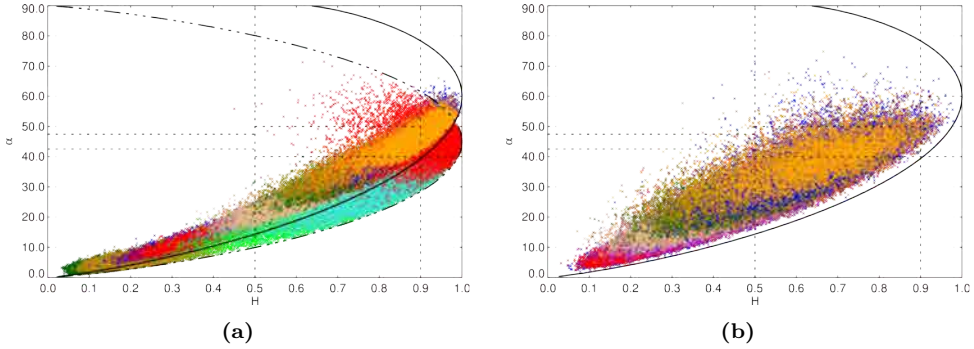


Figure 6.17: $H/\bar{\alpha}$ for the different TSX data sets (colored coded as in Fig. 6.11): (a) before and (b) after noise filtering; solid and dash-dot-dot lines refer to boundaries of feasible $H/\bar{\alpha}$ combinations for quad- and dual-pol data, respectively; dotted lines bound the different scattering zones (a 11x11 boxcar for spatial averaging is used).

6.6.3 Polarimetric characterization

In this section the polarimetric $H/\bar{\alpha}$ decomposition is used to determine the average scattering mechanism expected from the sea clutter. It is widely accepted that backscattering from sea or ocean can be regarded as a Bragg scattering (surface mechanism). The analysis presented in the following lines tries to foresee the applicability of this Bragg modeling to X-Band TSX data using dual and fully polarimetric acquisitions. The well known X-Bragg (or extended Bragg) model is used to fit the data, considering its extension (X2-Bragg) to include the impact of noise as well as sea temporal decorrelation effects, as proposed in section 6.3.

Scattering plots in the $H/\bar{\alpha}$ plane for the different data takes are shown in Figs. 6.17a and 6.17b, before and after additive noise filtering, respectively. Most data takes lie in the Bragg and random surface zones. The data takes, corresponding to incidence angles above 38 degrees, have high entropy values ($H > 0.85$) and are located in zone 1 and 5 according to Cloude-Pottier classification [163], i.e., medium and high entropy vegetation scattering. However, such mechanisms are not representative of the processes involved in the sea, since Bragg surface is expected [164]–[169]. The higher impact of thermal noise in this high incidence angle region, as observed from σ^0 and statistical analyses, could produce such large entropy values. Systematic increase of H and $\bar{\alpha}$ can be noticed as a function of incidence angle (from left to right in Figs. 6.17a-b). This trend is expected from the X-Bragg model [171], but with values of H and $\bar{\alpha}$ below 0.5 and 30.0 degrees, respectively. After additive noise filtering (NF), for quad-pol data, a reduction both on H and $\bar{\alpha}$ can be recognized, as seen in Fig. 6.17b.

Distributions of the eigenvalues, in Fig. 6.18 for three data takes (near to far incidence, from left to right), are a good visual indicator of the polarimetric mechanisms' evolution as a function of incidence angle. For TSX-4 [Fig. 6.18a] there is a clear dominant mechanism (λ_1), surface Bragg scattering, as observed from α_1 distribution in Fig. 6.19a, centered around 5 degrees. As incidence angle increases, the first eigenvalue decreases, since lower Bragg surface mechanism is being imaged. At the furthest available incidence angle (TSX-17), Fig. 6.18c, no clear dominant mechanism is present, being the distributions

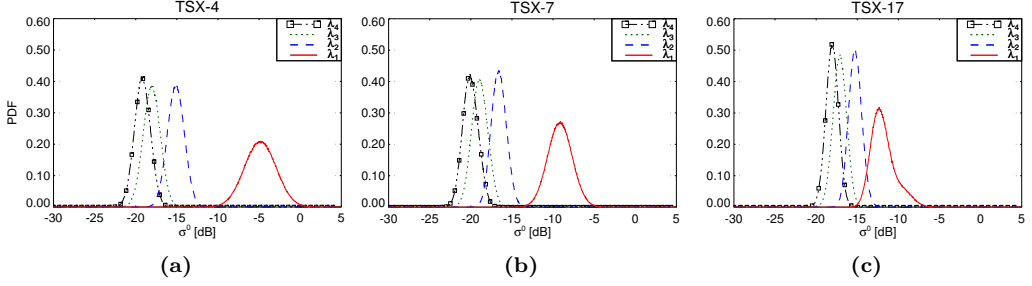


Figure 6.18: Distribution of the eigenvalues, before noise filtering, for different data takes (TSX-4, -7 and -17, from left to right).

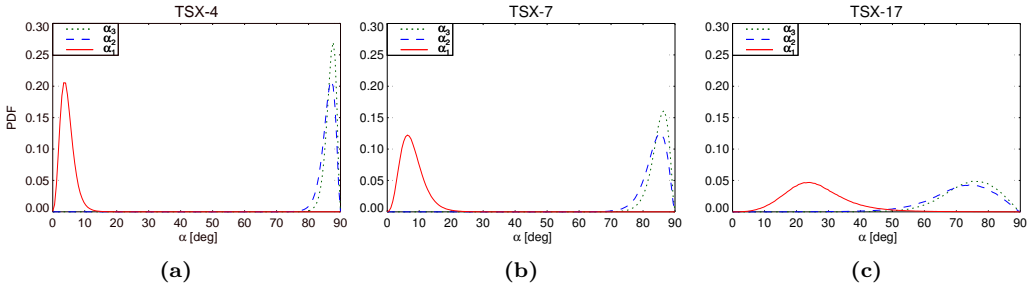


Figure 6.19: Distribution of the individual alpha parameters, before noise filtering, for different data takes (TSX-4, -7 and -17, from left to right).

of the eigenvalues closer to each other, such that a noise-like mechanism is expected in accordance with σ^0 and statistical characterizations.

In general, the second mechanism almost keeps its relative strength w.r.t. noise floor regardless of incidence angle. From Fig. 6.19, where the distributions of the individual α parameters are shown, the related α_2 with a similar trend as α_3 lies between 70 and 90 degrees. These values are representative of double bounce scattering, less probable in the sea backscattering. In this sense, and considering the X-Bragg model extension to account only for thermal noise impact, parameters associated to the second mechanism do not agree with the observations from experimental data. On one hand, α_2 should correspond to 90 degrees independently of β_1 and SNR_{Eq} ; on the other hand, the expected level of λ_2 should be much closer to λ_3 than what observed from real data. These considerations reinforce the necessity to include also the impact of sea clutter temporal decorrelation between the polarimetric channels. From the theoretical analysis in section 6.3.2, temporal decorrelation induces a higher value of λ_2 , as seen from TSX data, and at the same time the related α_2 is not fixed to 90 degrees but lies, e.g., between 80 and 90 degrees for TSX-4 (as shown in Fig. 6.5b), which agrees with α_2 distribution in Fig. 6.19a.

To properly evaluate the validity of the X2-Bragg model with the available experimental data, the equivalent SNR_{Eq} should be computed by means of SNR_1 estimation, using the relationship in (6.28). In order to extract SNR_1 the corresponding noise level σ_n^2 is inferred as the lowest eigenvalue (λ_4) resulting from the 4x4 scattering coherency matrix \mathbf{T}_4 , [171].

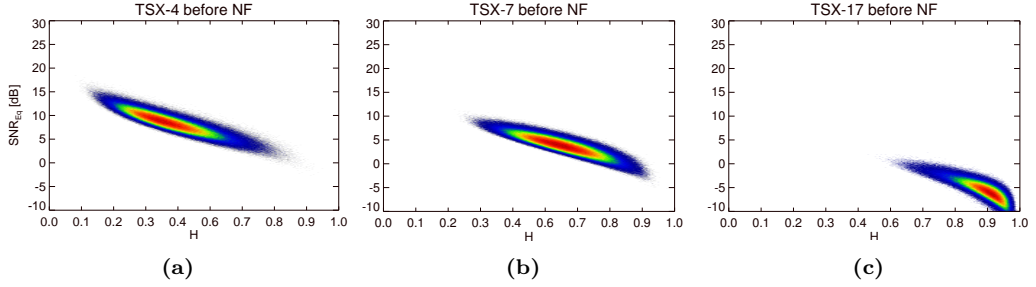


Figure 6.20: 2-dimensional distributions of the estimated SNR_{Eq} versus H before noise filtering: (a) TSX-4; (b) TSX-7; and (c) TSX-17.

Fig. 6.20 shows the 2-dimensional distributions of the estimated SNR_{Eq} /entropy plane for different quad-pol data takes at different incidence angles (from small to high incidence angles Figs. 6.20a-c). From the estimated SNR_{Eq} and using the relationships (6.26)-(6.27), the normalized noisy coherency matrix $\bar{\mathbf{T}}'$ is computed. Then, temporal decorrelation (ρ_{temp}) is included in $\bar{\mathbf{C}}'$ leading to the normalized coherency matrix $\bar{\mathbf{T}}''$ as described in 6.3. From the experimental data, \mathbf{T}_{11}'' is estimated and applied over $\bar{\mathbf{T}}''$ to obtain the non-normalized \mathbf{T}'' matrix. Then, the different polarimetric descriptors as H or $\bar{\alpha}$ can be derived for specific model parameters β_1 and ϵ , and for the incidence angles of interest.

Fig. 6.21 represents 2-dimensional distributions in the $H/\bar{\alpha}$ plane for the same three data takes considered in Figs. 6.18 and 6.19. Figs. 6.21a-c correspond to the polarimetric decomposition before noise filtering (NF), while Figs. 6.21d-f refer to the analysis after additive noise reduction as proposed in [171]. On top of the different distributions, the classical X-Bragg model (black triangles) and the extended model X2-Bragg (magenta diamond symbols) are depicted for different values of β_1 , from 0 to 90 degrees in steps of 15 degrees. Standard deviations in the $H/\bar{\alpha}$ plane are also included as error bars for the X2-Bragg model, related to the error in estimating SNR_{Eq} from the data set. After NF, Figs. 6.21d-f, the residual noise level to include the impact of SNR_{Eq} has been estimated from the new λ_3 value. Standard sea conditions have been assumed, 10°C and 35 ‰ salinity, to compute the dielectric constant ϵ according to the model in [189]. From Fig. 6.2, the real part of the permittivity ϵ' is above 40 for a wide variety of sea surface temperatures and salinities, such that its impact on the variability of the X-Bragg related parameters is quite limited.

The dominant mechanism moves from Bragg surface (near incidence) passing by random surface region (middle incidence), ending up to high entropy region characterized by random anisotropic scatters (for TSX-17), mainly caused by the higher noise contribution, see Figs. 6.21a-c. Comparatively, noise filtering tends to reduce entropy [Figs. 6.21d-f], leading to a dominant scattering primarily located in the Bragg surface zone, except for the region of high incidence angles (above 36 degrees), where the different contributions lie in the random surface region with a wider dispersion of the scattering plot due to the reduced SNR conditions.

From Fig. 6.21, an important bias between the original X-Bragg model and the data is recognized, especially before noise filtering [Figs. 6.21a-c]. For the X2-Bragg, a much

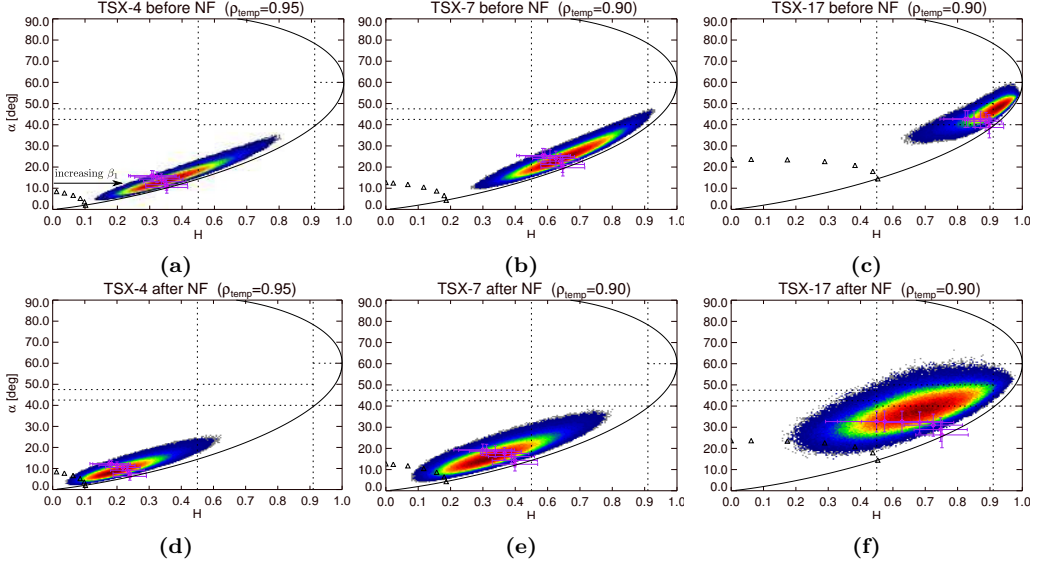


Figure 6.21: 2-dimensional distributions on $H/\bar{\alpha}$ plane for different data takes (TSX-4, -7 and -17, from left to right) including the theoretical X/X2-Bragg models (β_1 variation from 0 to 90 degrees and single dielectric constant for standard sea conditions of 10°C and 35 ‰ salinity); black triangles refer to the original X-Bragg model and magenta diamonds correspond to the X2-Bragg model (error bars/standard deviations in $H/\bar{\alpha}$ are included): (a)-(c) before and (d)-(f) after noise filtering (NF); (a) and (d) TSX-4 with $\rho_{temp} = 0.95$, (b) and (e) TSX-7 with $\rho_{temp} = 0.90$ and (c) and (f) TSX-17 with $\rho_{temp} = 0.90$.

better matching between the theoretical model and the experimental data is obtained. For TSX-4 [Fig. 6.21a] a ρ_{temp} of 0.95 provides a good matching between the theoretical extended model and the data before noise filtering; while for TSX-7 [Fig. 6.21b] this value reduces to 0.90. In case of TSX-17 [Fig. 6.21c] a higher bias is recognized and reducing ρ_{temp} below 0.9 does not provide any additional improvement: from the theoretical analysis of X2-Bragg model, higher clutter decorrelation does not increase entropy for regions with $H > 0.6$. Additive noise subtraction reduces entropy from 0.92 to 0.7 [Fig. 6.21f], but the proposed extended model predicts an average alpha value below the one observed in the data. Therefore, there might be an additional mechanism contributing to this discrepancy, which is not considered in the proposed X-Bragg model. Additional measurements with higher SNR conditions should be analyzed to support this hypothesis.

After noise filtering, the X2-Bragg model, keeping ρ_{temp} , is biased towards higher combined values of $H/\bar{\alpha}$ for TSX-4 and TSX-7, Figs. 6.21d and 6.21e. This effect is due to the fact that the second mechanism (represented by λ_2 in Fig. 6.18) is modeled partially by the temporal decorrelation, but the thermal noise is also affecting: comparing the distribution of λ_2 before and after noise filtering its level has decreased around 2 dB for the different data takes. Therefore, the noise contribution is somehow biasing the “fitting” of the corresponding temporal correlation coefficient. It has been observed that after noise filtering a ρ_{temp} of 0.98 provides a good matching between the model and the data for TSX-4 and TSX-7 as well as for other data takes.

The X2-Bragg model can be applied also over land surfaces, where the main driven parameter will be the noise floor, especially for small roughness conditions, since *a priori* temporal decorrelation impact is expected to be low when compared to the sea clutter case.

6.7 Concluding remarks

In this chapter, a detailed characterization of the sea/ocean clutter returns imaged by an X-band SAR sensor such as TSX has been performed in a three-level basis: radar backscattering coefficient σ^0 , statistical and polarimetric descriptions.

As generally hypothesized, the reflectivity for the co-polarized channels (S_{HH} and S_{VV}) decreases with increasing incidence angles, where S_{VV} returns are higher than S_{HH} , especially for incidence angles above 30 degrees. The validity of two semi-empirical σ^0 models, as NRL and XMOD2 has been evaluated. On one hand, the NRL model underestimates the radar backscattering coefficient for the spaceborne TSX data with a deviation between 5 dB and 7 dB for the co-polarized channels. As the NRL model optimizes its coefficients on the basis of Nathanson's tables, where the collected data corresponds mostly to ground-based radars with flat incidence angles, higher discrepancies are obtained when trying to extrapolate the model to spaceborne SAR geometries. On the other hand, the XMOD2 model provides better fitting to the estimated values (average errors between 1 dB and 3 dB). Such deviations can be related to the fact that XMOD2 coefficients have been adjusted from TSX/TDX dual-pol data. Therefore, it would be interesting to consider a refinement of the model parameters for quad-pol data in further studies.

The magnitude of the SAR sea clutter returns are fitted to three typical distributions when working with high resolution radars (Weibull, log-normal and K-distribution). The normalized intensity moments (NIM) have been computed and compared to the theoretical ones for those distributions. The K-distribution proves to have better fitting for a higher number of acquisitions; while the log-normal provides the worst or even no fitting to the experimental data. Typical values of the K-distribution shape parameter (an indicator of clutter spikiness) are between 3-10 for the co-polar channels at near incidence angles (20-30 degrees). Nonetheless, as the incidence angle increases the shape parameter is well above 10, since the sea clutter returns reduce getting closer to the noise level. This effect is particularly important for the TSX quad-pol acquisitions, where the NESZ degrades 3 dB w.r.t. single or dual-pol data. The cross-polarized channels, which have reduced levels, 2 to 10 dB below the co-polarized ones, are highly affected by thermal noise.

To complement the statistical characterization, a polarimetric description using the $H/\bar{\alpha}$ plane, as proposed by Cloude and Pottier in [163], has also been performed over the set of dual- and quad-pol acquisitions. This analysis shows that most acquisitions lie in regions 9 and 6 of the Cloude-Pottier $H/\bar{\alpha}$ plane, i.e., low to medium entropy surface scattering. Actually, it has been observed that as incidence angle increases the mechanism moves from low to high entropy zones, which is consistent with the higher noise contribution for the far range regions. As proposed in [171], an additive noise filtering has been applied to quad-pol data, in a way that the distributions on the $H/\bar{\alpha}$ plane

move towards smaller values. Since the main scattering contribution to the sea clutter returns is assumed to be Bragg surface, the suitability of the well known X-Bragg model has been evaluated, showing poor fitting with the experimental data. An extension of the X-Bragg model (X2-Bragg) to account for thermal noise and temporal decorrelation impacts has been proposed and its applicability with experimental TSX data assessed, showing a better fitting with the real data compared to the original X-Bragg model.

The characterization of the sea clutter at X-band from spaceborne TerraSAR-X polarimetric data proves the validity of some generally assumed hypothesis in the field of sea radar imaging: K-distribution provides a good fitting to the magnitude, and Bragg surface represents the single scattering mechanism. The study carried out shows that in case of TSX quad-pol data thermal noise is an important limiting factor, especially for the high incidence angle region.

The along-track interferometric configuration combined with alternate polarization transmission, for quad-pol acquisitions, produces additional decorrelation on the sea clutter data. For proper interpretation of the sea/ocean fully polarimetric data, additional sources of polarimetric decorrelation (thermal noise and sea temporal decorrelation) have to be considered. Therefore, the work described in this chapter tried to fill the gap between the physical modeling approaches and the signal-based approximations, stressing the requirement to account for the technological limitations of current SAR missions when imaging challenging scenarios, such as the seas or oceans.

SAR has entered the golden age with the increased number of recent and forthcoming missions (TSX, TDX, CSK, RS2, Sentinel-1 and PAZ). Consequently, an important amount of data is available for an exhaustive sea clutter characterization. This represents an excellent opportunity to broaden the comprehension on sea/ocean radar imaging. This chapter provides preliminary insight that should be complemented and even extended if dedicated campaigns with available ground truth were planned.

7

Chapter 7

SAR internal calibration strategies

*C*ALIBRATION is of key relevance for image interpretation (e.g., sea parameter inversion) and for proper operation in SAR-GMTI with multichannel systems. This chapter presents a novel approach in the instrumental error analysis of SAR based on active phased array antennas (APAAs). A residual post-calibration error exists due to differences between the calibration and operational excitations of the transmit receive modules (TRMs) for source errors monitored by the internal calibration subsystem. Analytical expressions are derived for the residual post-calibration errors and validated through intensive simulations of some instrumental errors for a specific sensor architecture. Alternative internal global calibration strategies are proposed to reduce the impact of the post-calibration error. The simulations show that the proposed elevation dependent calibration can provide a substantial reduction of the post-calibration errors even in the case of relaxed tolerance of the TRM setting errors¹.

¹The following sections contain portions, sometimes verbatim, of the author's publication [JA5].

7.1 Introduction

Current state-of-the-art spaceborne SAR missions, such as TSX, TDX, CSK and RS2, are equipped with active phased array antennas (APAAs), which provide flexibility in the sensor operation. In order to retrieve information meaningful and interpretable for the final user, the different SAR products provided by these modes have to be properly calibrated. The basic idea behind the calibration is to characterize the transfer function of the SAR sensor, trying to compensate for possible deviations from the ideal operation. In fact, calibration is the one that guaranties instrument's performance and the quality of SAR products. In this way, it is possible to retrieve/invert reliable information from calibrated SAR images, e.g., sea radar backscattering coefficient extraction for wind speed velocity estimation as in [173].

SAR evolution towards multichannel systems represents a change of paradigm: in the specific case of multichannel SAR-GMTI operation, additional efforts in the calibration strategies are required as different receive channels are involved in the operation of the instrument. A good isolation and balancing of the different receive chains should be kept in order to maintain an adequate performance of the different GMTI processing techniques, as it has been pointed out in Chapter 5 when processing real data.

In case of DPCA operation as well as EDPCA, clutter cancellation performance is driven by channel correlation, and so suitable calibration techniques have to be used, [74]. Decorrelation of clutter returns can be caused by antenna deformations, such that the two receiving beams illuminate the scene in a slightly different way. In current SAR missions the receive beams are synthesized using different excitations of the transmit receive modules (TRMs) of an APAA, such that there may be uncompensated errors that differ randomly between the modules.

ATI works properly when the imperfections and unbalances are removed between the two channels. As in the case of DPCA, unbalances in the channel transfer functions and/or antenna patterns produce systematic phase errors in the interferogram. These channel mismatches affect also the performance of STAP, see [13]. Contrary to ATI, DPCA and STAP-based techniques (e.g., EDPCA and ISTAP) require both phase and magnitude balancing/calibration, [74].

Taking these considerations into account, the need to perform adequate calibration processes motivates the study of calibration strategies used in current spaceborne missions, equipped with APAAAs. In this sense and within the framework of the support to the Spanish PAZ SAR mission, a detailed and exhaustive study of the radiometric budget for Stripmap [195] and ScanSAR [196] operational modes has been carried out. A new analytical error formulation has been derived, taking into account that residual post-calibration errors exists since calibration weights on the TRMs are not proportional to the ones used during the internal calibration. This analysis allows to better understand which can be the limitations of current SAR sensors and set the basis to study and derive new calibration strategies. An interesting point would be also to analyze the possible impact of the different instrumental errors in the GMTI performance when operating multichannel systems.

The objective of this chapter is to present the novel analysis of instrumental errors for SAR sensors equipped with APAAAs and to show the limitations of the actual internal

calibration strategies. In the first part, the basics associated to SAR calibration are presented. Then, the new theoretical error formulation as well as the concept of post-calibration errors are described. In the third section, the novel proposed calibration strategies are presented. Last, the validity of the analysis is proved through numerical simulations for specific instrumental errors.

7.2 SAR calibration

A SAR sensor is able to form high resolution images of the Earth surface by processing the corresponding backscattered echoes. In order to interpret this data and extract meaningful information calibration and characterization of the complete SAR system is required [197,198]. The process of calibration consists in the determination of the transfer function that relates the SAR system under analysis to a reference predefined system. Specifically, this process tries to translate the digital stream of data into physical information related to the observed NRCS or radar backscattering coefficient σ^0 . The quality of the radar backscattering maps is essentially defined by the capability to determine the radiometric characteristics of the radar system.

Current state-of-the-art SAR missions are equipped with APAAs consisting of a large number of subarray radiation elements, which are controlled by dedicated TRMs programmable in amplitude and phase. This type of antenna configuration provides a high degree of flexibility and reconfigurability. It allows the formation of multiple beams, which can be electronically steered, and the operation of different modes like the classical Strimap [23], ScanSAR [199], Spotlight [200], and also more advanced, such as the high-resolution wide-swath (HRWS) mode [58]. However, the calibration of such systems with a large number of programmable active elements is a complex procedure due to the huge amount of different beams that can be operated. In this sense TSX, TDX and PAZ carry out similar strategies in order to achieve an efficient and affordable calibration procedure [201,202]. The calibration is mainly based on the use of on-ground pre-launch characterization data, an accurate antenna model, an in-flight internal characterization as well as external calibration data with additional in-flight measurements.

First, the SAR system is characterized on ground before launch. Since the radar subsystems' parameters are affected by temperature, aging and other factors, an internal calibration protocol is established in order to characterize the system response during operational data acquisitions. As the internal calibration is typically based on series of pulses routed through the instrument signal path [203,204], it does not completely characterize the radar since, for example, the detailed radiation characteristics of the antenna are not sensed by the internal calibration loops. Therefore, mutual coupling effects between the radiative elements, thermo-elastic deformations and/or thermal variations of the radiating antennas are not monitored by the internal calibration facility. For this reason external calibration methods based on radar calibrators or specific random surfaces are used to complement the internal calibration data [201,205]. The internal calibration network can be employed to determine the individual TRM response and failures based on element switching or orthogonal Pseudo Noise sequences [203,206]. Such information can be used to optimize the array excitations and the resulting antenna beams. However, this type of calibration involves a high number of measurements and it is usually performed with lower periodicity compared to the conventional internal calibration, which is

typically carried out at the beginning and end of each data take.

The internal calibration consists in the measurement of the instrument complex transfer function (phase and amplitude) of the transmission and reception sections. This chapter focuses on the error analysis of the internal calibration proposed in spaceborne SAR missions equipped with APAAs. The study concentrates on the impact of error sources that can be sensed by the internal calibration network, excluding additional errors, such as the ones induced by the radiating elements (thermal variations of the antennas, thermo-elastic deformations, mutual coupling, ...) or thermal variations of the calibration network. The objective is to analyze and propose internal calibration strategies able to correct those errors that affect directly the excitations of the TRMs, producing variations on the antenna pattern.

Differences in the TRM coefficients used in calibration and SAR operation result in residual post-calibration errors that arise in a multilevel hierarchic architecture of a SAR instrument. For a better interpretation of the internal calibration limitations, the error has been expressed in terms of parallel and orthogonal components of the array excitation vector for each required beam with respect to the internal calibration array weights. Theoretical analysis and simulation results show that the residual post-calibration error is proportional to the orthogonal component (w.r.t calibration weights) of the effective operational excitations. From these considerations alternative internal calibration strategies have been proposed: (i) calibrating with the same operational excitations (expect the linear phase term to steer the beams) and (ii) an elevation dependent calibration valid for different look angles² that are coupled with different range positions over the imaged scene.

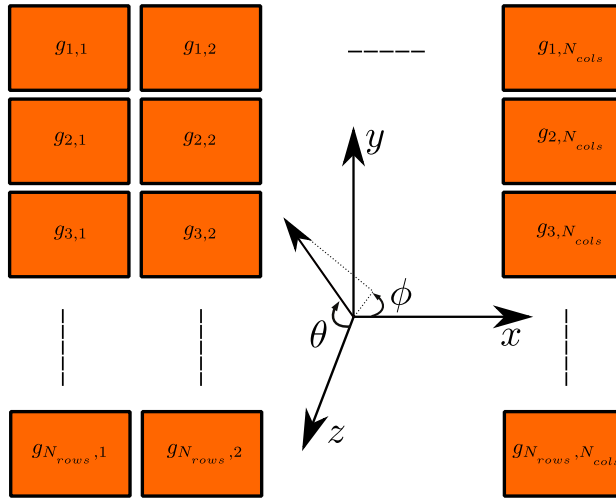


Figure 7.1: Planar active phased array antenna (APAA) with N_{rows} by N_{cols} TRMs (located in the $x - y$ plane and the system of coordinates' origin at the antenna's center).

²Look angle denotes the angle between the sensor-to-scatterer line and the platform's nadir.

7.3 Theoretical formulation

7.3.1 Preliminary concepts

7.3.1.1 Phased Array Antennas

A key point in the analysis of the SAR instrument radiometric budget is the translation of the different errors introduced along the hierarchic architecture of the instrument to complex errors in the different set of N_{rows} by N_{cols} TRM complex excitations, $\{\{g_{m,n}\}_{m=1}^{N_{rows}}\}_{n=1}^{N_{cols}}$. N_{rows} represents the number of TRMs in the vertical dimension of the antenna (number of rows); while N_{cols} refers to the number of TRMs collocated in the horizontal dimension of the antenna, i.e., the number of columns (also known as panels), see Fig. 7.1.

From [207], the ideal array factor AF^{θ_t, ϕ_t} for a planar configuration (Fig. 7.1) can be expressed as

$$AF^{\theta_t, \phi_t} = \sum_{m=1}^{N_{rows}} \sum_{n=1}^{N_{cols}} SA_{m,n}^{\theta_t, \phi_t} \cdot g_{m,n} \cdot \exp \left\{ j \frac{2\pi}{\lambda} \overbrace{(d_{m,n}^x \cdot \sin \theta_t \cos \phi_t + d_{m,n}^y \cdot \sin \theta_t \sin \phi_t)}^{\alpha_{m,n}^{\theta_t, \phi_t}} \right\} \quad (7.1)$$

$SA_{m,n}^{\theta_t, \phi_t}$ models the single element pattern, which in practice corresponds to a subarray of basic radiators [208]; and $g_{m,n}$ is the ideal complex excitation for the m th TRM of the n th column. From now on, the superscript θ_t, ϕ_t denotes dependence on the inclination angle θ_t (measured from z axis) and azimuth angle ϕ_t (measured in x-y plane). The subscript t denotes the different instants of echo acquisition within the formation of the synthetic aperture.

Equation (7.1) assumes that the reference phase center corresponds to the array's center. The longitudinal and vertical separations of the m, n th subarray w.r.t the array reference position are represented by $d_{m,n}^x$ and $d_{m,n}^y$, respectively.

For notational convenience and easiness in the mathematical derivation, the AF^{θ_t, ϕ_t} in (7.1) is compacted to

$$AF^{\theta_t, \phi_t} = \sum_{i=1}^N SA_i^{\theta_t, \phi_t} \cdot g_i^{\theta_t, \phi_t} \quad (7.2)$$

where N represents the total number of TRMs, i.e., N_{rows} by N_{cols} . The additional phase term, $\alpha_{m,n}^{\theta_t, \phi_t}$ in (7.1), related to the direction of arrival (DOA) of the impinging signal and the position of the subarray in the antenna, has been included in the excitations of the TRMs. This leads to an effective excitation $g_i^{\theta_t, \phi_t}$.

7.3.1.2 Amplitude vs power error coefficients

Variations in gain of any given component can be expressed in a number of ways, related to how the gain itself is formulated. In most SAR literature, gain variations are expressed with respect to power gain [23]. For example, the gain, G , of an amplifier can be expressed as

$$G = G_0 \cdot (1 + \epsilon_G) = G_0 + \Delta G \quad (7.3)$$

where G_0 is the nominal gain and ϵ_G corresponds to the gain error.

In the context of a multilevel architecture, as it is the case of most of the state-of-the-art SAR systems equipped with phased arrays, the signal is divided and the gain is achieved in a parallel number of branches, and so it would be convenient to work with amplitude (and phase) instead of power. The gain in amplitude can be defined as

$$g = g_0 \cdot (1 + \epsilon_g) = g_0 + \Delta g \quad (7.4)$$

The amplitude gain in (7.4) can be converted to power taking

$$\begin{aligned} G &= g^2 = g_0^2 \cdot (1 + 2\epsilon_g + \epsilon_g^2) \\ &= G_0 \cdot (1 + \epsilon_G) \approx g_0^2 \cdot (1 + 2\epsilon_g) \end{aligned} \quad (7.5)$$

where the approximation is valid for small error coefficients, assumption considered throughout the chapter. Note that these error terms can be expressed in decibels (dB), by taking

$$\begin{aligned} 10 \log_{10} (1 + \epsilon_G) &= 20 \log_{10} (1 + \epsilon_g) \\ &\approx 10 \log_{10} (1 + 2\epsilon_g) \approx 8.69 \epsilon_g \end{aligned} \quad (7.6)$$

7.3.2 Accumulated errors of components in parallel

Let's consider that a number of N branches (parallel elements) are aggregated, as it is the case of signal combination of N TRMs, located in a two-dimensional planar array. The aggregated gain can be expressed as

$$\begin{aligned} g_T &= \sum_{m=1}^N g_m (1 + \epsilon_m) e^{j\xi_m} \\ &\approx \sum_{m=1}^N g_m (1 + \epsilon_m + j\xi_m) \\ &= g_{T,0} \left(1 + \frac{\sum_{m=1}^N g_m (\epsilon_m + j\xi_m)}{g_{T,0}} \right) \end{aligned} \quad (7.7)$$

where $g_{T,0}$ refers to the total gain with no errors; g_m is the weight of the m th branch; ϵ_m and ξ_m denote the amplitude and phase errors for the m th branch, respectively. The multiplicative term $(1 + \epsilon_m) e^{j\xi_m}$ has been approximated by $(1 + \epsilon_m + j\xi_m)$ for the first order Taylor expansion under the assumption of small amplitude and phase errors.

The resulting aggregated amplitude error is

$$\epsilon_T = \frac{\sum_{m=1}^N g_m \epsilon_m}{\sum_{m=1}^N g_m} \quad (7.8)$$

a weighted average of the error introduced by each branch. Similarly, the phase error is approximately

$$\xi_T = \frac{\sum_{m=1}^N g_m \xi_m}{\sum_{m=1}^N g_m} \quad (7.9)$$

This approach of modeling the amplitude and phase error coefficients as done in (7.8) and (7.9), is based on the assumption of small error signal for the set of N branches such that the real part is associated to an amplitude error and the imaginary part to a phase error.

SAR instruments are multilevel hierarchic architectures, where the signals are divided (or combined) and subdivided (or combined). In this sense, errors produced at intermediate or inner layers of the architectures can be translated to excitation errors on the TRMs, which are located at the outer level. This extrapolation of the errors should be carefully considered taking into account that the different layers and branches introduce delay τ . Using a time-harmonic variation of signals according to a phasor $e^{+j2\pi f_c t}$ and under the assumption of a narrow-band model, this delay can be treated as a phase-shift:

$$\Delta\psi = -2\pi f_c \tau \quad (7.10)$$

where f_c corresponds to the carrier frequency. The narrow-band hypothesis is correct when the delay introduced by the N branches is nominally the same and possible delay dispersion is much smaller than the time resolution of the radar (inverse of the radar bandwidth).

7.3.3 Error formulation

7.3.3.1 Internal calibration procedure

Internal calibration performs a complete characterization (in phase and gain) of the signal's path within the SAR sensor since thermal drifts, aging and internal hardware characteristics produce gain and phase fluctuations along data acquisitions. For monitoring the instrument stability a dedicated internal calibration facility is embedded in the SAR sensors, providing internal calibration measurements, which are used to perform the corresponding corrections on the ground processor.

The analysis here presented considers the internal calibration strategy adopted in TSX [203], which will be also used in the Spanish PAZ mission. Three calibration pulses, at the beginning and end of each data take, are routed through three different paths within the SAR instrument as illustrated in Fig. 7.2: **P1** (dashed red) characterizes the transmit path; **P2** (solid blue) the receive path and **P3** (dotted green) the central electronics³ (CE) as well as the influence of the auxiliary transmit/receive ports. **P3** does not include the part of the calibration network on the front end of the antenna and is used to correct possible variations in pulses **P1** and **P2**.

7.3.4 Residual post-calibration errors

In the following section the impact of excitation errors that can be monitored by the internal calibration is analytically derived through a mathematical model. The so called residual post-calibration errors are formulated at image level. The echo signal backscattered from an arbitrary point target on ground is measured by the radar with a complex gain G_t and can be expressed, after range compression, as

$$G_t = K \sum_{i=1}^N SA_i^{\theta_t, \phi_t} g_{\text{TX}_i}^{\theta_t, \phi_t} c_{\text{TX}_i} \sum_{i=1}^N SA_i^{\theta_t, \phi_t} g_{\text{RX}_i}^{\theta_t, \phi_t} c_{\text{RX}_i} \quad (7.11)$$

where K depends on common mode radar parameters and will be characterized through external calibration; $SA_i^{\theta_t, \phi_t}$ models the impact of the subarray pattern; $g_{\text{TX}_i}^{\theta_t, \phi_t}$ and $g_{\text{RX}_i}^{\theta_t, \phi_t}$

³CE corresponds to the instrumental control unit, providing the timing signal generator, embedding the analog-to-digital converters (ADCs) and the block adaptive quantizers (BAQs), [208].

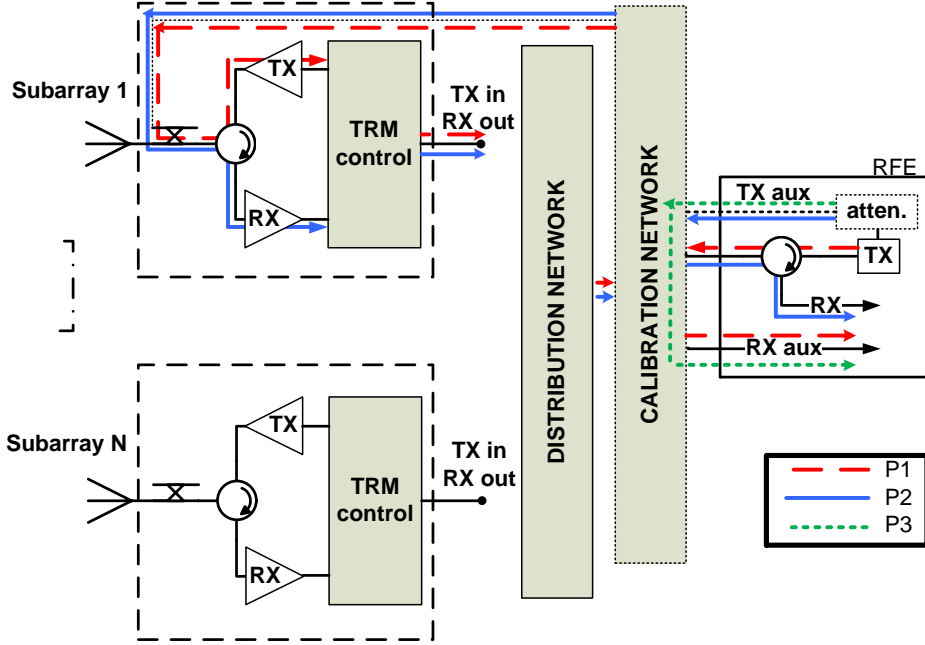


Figure 7.2: Internal calibration scheme: signal path for the calibration pulses P1 (TX-transmission) in dashed red, P2 (RX-reception) in solid blue and P3 (central electronics) in dotted green.

correspond to the effective complex excitations of the i th TRM in transmission (TX) and reception (RX), respectively; c_{TX_i} and c_{RX_i} represent multiplicative terms that contain the complex excitation errors associated to the i th TRM in transmission and reception:

$$c_{\text{TX/RX}_i} = (1 + \epsilon_{\text{TX/RX}_i}) e^{j\xi_{\text{TX/RX}_i}} \quad (7.12)$$

It must be noted that $\epsilon_{\text{TX/RX}_i}$ and $\xi_{\text{TX/RX}_i}$ do not consider errors due to the radiative subarrays (e.g., thermo-elastic deformation or mutual coupling between elements), such that an ideal antenna model is considered, as expressed in (7.1). Those additional errors can not be monitored by the internal calibration. Their impact should be accounted in a separated budget analysis, uncorrelated with the residual post-calibration errors here considered.

The combined calibration signals, associated to pulses **P1** (TX) and **P2** (RX), can be analogously expressed by a calibration constant as

$$G_{\text{cal}} = \left(\sum_{i=1}^N g_{\text{cal}_{\text{TX}_i}} c_{\text{TX}_i} + n_{\text{TX}} \right) \left(\sum_{i=1}^N g_{\text{cal}_{\text{RX}_i}} c_{\text{RX}_i} + n_{\text{RX}} \right) \quad (7.13)$$

where $g_{\text{cal}_{\text{TX}_i}}$ and $g_{\text{cal}_{\text{RX}_i}}$ correspond to the calibration excitations applied to the TRMs in TX and RX, respectively; noise influence on the calibration pulses measurement is denoted by n_{TX} and n_{RX} for TX and RX, respectively. This thermal noise, modeled as zero-mean circular complex Gaussian distribution, is characterized by a variance related to the SNR after range compression.

The impact of the radiative subarray in calibration measurements is not considered since the calibration loop does not monitor these elements. It must be pointed out that possible variations between **P1** and **P2** (monitored through the measure of **P3**), as well as instabilities in the calibration network due to thermal variations, have been neglected.

From (7.11) and (7.13), the received signal after internal calibration can be expressed as

$$G_{t_{\text{cal}}} = \frac{\sum_{i=1}^N SA_i^{\theta_t, \phi_t} g_{\text{TX}_i}^{\theta_t, \phi_t} c_{\text{TX}_i} \sum_{i=1}^N SA_i^{\theta_t, \phi_t} g_{\text{RX}_i}^{\theta_t, \phi_t} c_{\text{RX}_i}}{\left(\sum_{i=1}^N g_{\text{calTX}_i} c_{\text{TX}_i} + n_{\text{TX}} \right) \left(\sum_{i=1}^N g_{\text{calRX}_i} c_{\text{RX}_i} + n_{\text{RX}} \right)} \quad (7.14)$$

where K has been omitted as the external calibration takes it into account.

Modeling internal signal routing errors as an alteration of the nominal complex gain coefficient introducing a gain and phase error can be carried out under a narrow band assumption. This hypothesis is correct when the delay of the N branches of the array distribution/combination network is nominally the same and the possible delay dispersion is well below the inverse of the radar bandwidth. This condition can be usually accomplished by appropriate cabling design.

The assumption of narrow-band for the slow time domain is also fulfilled since the antenna beamwidth (around 0.37 degrees for TSX) is very narrow and the differential time of arrival along the array is small respect to radar time resolution (inverse of the radar bandwidth).

The calibrated signal in (7.14) can be expressed as

$$G_{t_{\text{cal}}} = \frac{\sum_{i=1}^N SA_i^{\theta_t, \phi_t} g_{\text{TX}_i}^{\theta_t, \phi_t} \sum_{i=1}^N SA_i^{\theta_t, \phi_t} g_{\text{RX}_i}^{\theta_t, \phi_t}}{\sum_{i=1}^N g_{\text{calTX}_i} \sum_{i=1}^N g_{\text{calRX}_i}} \left(1 + e_{2-w}^{\theta_t, \phi_t} \right) \quad (7.15)$$

where two relevant terms can be identified: the first refers to a normalization constant that can be determined by the antenna model; and the second includes the residual two-way complex error $e_{2-w}^{\theta_t, \phi_t}$ that cannot be compensated either by the antenna model or by the internal calibration procedure.

From (7.14) and (7.15) the post-calibration complex error is expressed as

$$e_{2-w}^{\theta_t, \phi_t} = \frac{\sum_{i=1}^N g_{\text{calTX}_i} \sum_{i=1}^N g_{\text{calRX}_i}}{\sum_{i=1}^N SA_i^{\theta_t, \phi_t} g_{\text{TX}_i}^{\theta_t, \phi_t} \sum_{i=1}^N SA_i^{\theta_t, \phi_t} g_{\text{RX}_i}^{\theta_t, \phi_t}} \cdot \frac{\sum_{i=1}^N SA_i^{\theta_t, \phi_t} g_{\text{TX}_i}^{\theta_t, \phi_t} c_{\text{TX}_i} \sum_{i=1}^N SA_i^{\theta_t, \phi_t} g_{\text{RX}_i}^{\theta_t, \phi_t} c_{\text{RX}_i}}{\left(\sum_{i=1}^N g_{\text{calTX}_i} c_{\text{TX}_i} + n_{\text{TX}} \right) \left(\sum_{i=1}^N g_{\text{calRX}_i} c_{\text{RX}_i} + n_{\text{RX}} \right)} - 1 \quad (7.16)$$

From (7.16), it is clear that if no noise is present ($n_{\text{TX}/\text{RX}} = 0$) and assuming equal subarray patterns, this error becomes zero only when the effective operational excitations

are coincident with the calibration weights. Assuming this noise free condition, no error after internal calibration (with broadside excitations) will exist for the center of the beams operating with the calibration weights. If a linear phase is introduced for steering the beam (with no tapering) the error will be zero at the beam-center, because this additional phase is compensated with the phase induced by the DOA of the signal and the position of the subarrays in the APAA.

The different effective operational weights both in TX and RX can be decomposed into a component parallel to the calibration weights and an orthogonal one as

$$\vec{g}_{\text{TX/RX}}^{\theta_t, \phi_t} = \vec{g}_{\text{TX/RX}}^{\parallel \theta_t, \phi_t} + \vec{g}_{\text{TX/RX}}^{\perp \theta_t, \phi_t} \quad (7.17)$$

where these terms can be obtained based on the projection and orthogonal projection over the normalized calibration weights as

$$\begin{aligned} \vec{g}_{\text{TX/RX}}^{\parallel \theta_t, \phi_t} &= \left(\vec{g}_{\text{TX/RX}}^{\theta_t, \phi_t} \cdot \hat{g}_{\text{cal}} \right) \hat{g}_{\text{cal}}, \\ \vec{g}_{\text{TX/RX}}^{\perp \theta_t, \phi_t} &= \vec{g}_{\text{TX/RX}}^{\theta_t, \phi_t} - \vec{g}_{\text{TX/RX}}^{\parallel \theta_t, \phi_t} \end{aligned} \quad (7.18)$$

with \hat{g}_{cal} the normalized vector of calibration weights.

For the case of broadside excitations on calibration and the assumption of small error signal, the two-way error in (7.16), under noise free conditions ($n_{\text{TX/RX}} = 0$) and after some mathematical manipulation, can be expressed as the combination of the residual orthogonal errors in TX and RX plus a negligible cross-term error:

$$e_{2-w}^{\theta_t, \phi_t} \approx \frac{\sum_{i=1}^N g_{\text{TX}_i}^{\perp \theta_t, \phi_t} \cdot e_{\text{TX}_i}}{\sum_{i=1}^N g_{\text{TX}_i}^{\theta_t, \phi_t}} + \frac{\sum_{i=1}^N g_{\text{RX}_i}^{\perp \theta_t, \phi_t} \cdot e_{\text{RX}_i}}{\sum_{i=1}^N g_{\text{RX}_i}^{\theta_t, \phi_t}} \quad (7.19)$$

$$+ \frac{\sum_{i=1}^N g_{\text{TX}_i}^{\perp \theta_t, \phi_t} \cdot e_{\text{TX}_i} \cdot \sum_{i=1}^N g_{\text{RX}_i}^{\perp \theta_t, \phi_t} \cdot e_{\text{RX}_i}}{\sum_{i=1}^N g_{\text{TX}_i}^{\theta_t, \phi_t} \cdot \sum_{i=1}^N g_{\text{RX}_i}^{\theta_t, \phi_t}} \quad (7.20)$$

where $e_{\text{TX/RX}_i} \approx \epsilon_{\text{TX/RX}_i} + j\xi_{\text{TX/RX}_i}$ correspond to excitation errors in transmission and reception. From (7.20), it can be stated that after internal calibration there is still a residual component, due to the projection of the excitation errors to the orthogonal component of the effective operational excitations w.r.t calibration vector. The formulation considered in (7.20) is strictly valid for the case of uniform excitation with no tapering (broadside calibration beam) under the assumption that all subarrays have the same response. This error formulation allows understanding the impact of the residual error depending on the operational beam, in the sense that the higher the orthogonal component of the excitations the higher the residual error contribution.

The decomposition presented in (7.18) is also valid for operational modes with steering both in elevation and azimuth, such as Spotlight or TOPSAR [209], since the effective excitations, which correspond to the operational weights on the TRMs including the phase induced by the DOA (in elevation and azimuth) of the impinging signal on the array, are projected over the calibration ones. Even if the calibration is adapted to the elevation component of the effective excitations, the latter will change when targets pass through the antenna beam as the synthetic aperture is formed. In this case the calibration weights will not be perfectly matched for each acquisition instant. In other words, the orthogonal component of the effective excitations will vary along the acquisition. These

considerations apply for any operation mode, and the synthetic aperture formation should be considered in the error analysis.

7.3.4.1 Integration of the error

To assess the impact of the internal calibration errors on the SAR image, the coherent integration of the echoes along the synthetic aperture must be accounted for. This integration can be seen as a multilevel stage of M elements in parallel, where each element corresponds to the echo within the synthetic aperture characterized by the two-way error, $e_{2-w}^{\theta_t, \phi_t}$. Therefore, the integrated (complex) error for a specific imaged target in the scene can be obtained as an additive weighted combination of the errors of M elements in parallel:

$$e_{2-w}^{int} = \frac{\sum_{t=1}^M g_{T2-w}^{\theta_t, \phi_t} \cdot e_{2-w}^{\theta_t, \phi_t}}{\sum_{t=1}^M g_{T2-w}^{\theta_t, \phi_t}} \quad (7.21)$$

where

$$g_{T2-w}^{\theta_t, \phi_t} = \sum_{i=1}^N S A_i^{\theta_t, \phi_t} g_{TX_i}^{\theta_t, \phi_t} \cdot \sum_{i=1}^N S A_i^{\theta_t, \phi_t} g_{RX_i}^{\theta_t, \phi_t} \quad (7.22)$$

represents the total two-way gain at the t th acquisition instant.

This integration of the error during the synthetic aperture formation accounts for the impact of azimuth variation on the residual post-calibration errors. In the case of Stripmap mode, targets with different azimuth locations are always observed by the same part of the main beam, while for Spotlight or TOPSAR, these targets maybe illuminated by different parts of the antenna beam. This latter consideration is intrinsically accounted for in the integration of the error.

7.4 Calibration strategies

From the analytical study performed in section 7.3.3, two alternative internal calibration strategies are proposed, whose principle of operation is the same as the conventional internal approach, based on calibration pulses routed through the instrument's signal path.

7.4.1 Calibration with operational excitations

Since the residual post-calibration error arises from the fact that differences between the operational and calibration excitations exist, the first alternative approach is to set the operational weights on the different TRMs during the internal calibration procedure, both in transmission and reception. In this case excitations are the operational except for the linear phase term that steers the beam (in elevation) from broadside. At the beginning and end of each data take a series of calibration pulses are transmitted to characterize the instrument response:

1. Transmission of pulse **P1** with calibration excitations corresponding to the TX operational ones, including the linear phase term to compensate for the beam steering.
2. Transmission of pulse **P2** loading the TRM excitations with the RX operational

weights and an adequate linear phase to account for the beam steering.

3. Digitized pulses **P1** and **P2** are downlinked to the ground station. Combining the information of these pulses, the complex calibration constant in (7.13) is extracted and used as normalization in the pulse replica considered for range compression.

Taking into account that different data takes can be acquired with different operational beams, this calibration strategy should consider for each beam a pair of calibration excitations (or calibration beams) in order to characterize TX and RX. As expected, simulations show that this calibration is accurate at beam-center for the different operational beams. Thus, this strategy provides the expected improvement only for a specific part of the imaged scene in terms of post-calibration error reduction.

7.4.2 Elevation dependent calibration

A second alternative calibration is proposed, such that the impact of the residual post-calibration error is minimized according to the portion of the observed scene in the range dimension (related to the elevation direction). Based on the same principle of operation used in the conventional approach, this strategy performs a set of L range/elevation dependent measurements at the beginning and end of each data take:

1. Transmission of **P1** with calibration excitations corresponding to the TX operational ones including the linear phase compensation for a specific range/elevation.
2. Transmission of **P2** loading the TRM excitations with the RX operational weights and the corresponding linear phase compensation for a specific range/elevation.
3. The previous steps are repeated to cover L range/elevation dependent measurements.
4. Digitized pulses **P1** and **P2** for the L different measurements are downlinked. For each measurement (out of L) a complex calibration constant is extracted. Then, a range dependent calibration function can be obtained, considering an interpolation of the different calibration constants. This calibration function is used as a range dependent normalization on the SAR image.

For each operational beam a set of $2L$ different calibration excitations should be stored on-board the SAR instrument. Simulation results show that 3 elevation dependent calibration measurements provide still good performance compared to the conventional strategy. This calibration reproduces the effective excitations of the array in both TX and RX, by introducing appropriate linear phase terms. This means the system is being calibrated with coefficients close to the actual signal complete path weights. Signal reduction on the calibration pulses is expected compared to the case of calibrating with broadside weights. However, cancellation of the calibration pulse will never occur since the calibration excitations reproduce closely the actual antenna gain in the elevation range of interest.

7.5 Numerical results

To prove the performance of the proposed internal calibration strategies comparatively with the conventional approach a series of numerical simulations has been carried out. In

Table 7.1: System and numerical simulation parameters.

Parameter	Value	Unit
Carrier frequency (f_c)	9.65	GHz
Antenna length	4.8	m
Antenna height	0.7	m
Pulse bandwidth (B_r)	150	MHz
Pulse duration (T_p)	50	μ s
Number of TRM rows (N_{rows})	32	-
Number of TRM columns (N_{cols})	12	-
Number of trials	1000	-
Number of range lines	101	-
Number of integration points	50	-
TRM amplitude error (1σ)	0.5	dB
TRM phase error (1σ)	5.0	deg

this case the TRM setting errors have been simulated for a specific instrument configuration in the framework of the Spanish mission PAZ.

The influence of the TRM setting error on the radiometric budget, considering noise limited calibration measurements, has been analyzed in terms of two differentiated concepts: relative radiometric accuracy, understood as the standard deviation of the measured radar cross section (RCS) of a point target within the scene (spatial radiometric variation); and radiometric stability, defined as the standard deviation of the measured RCS for a fixed point in the scene for different data takes (temporal radiometric variability). The numerical simulations have been carried out considering the formulation of the integrated post-calibration error, see (7.16) and (7.21).

The different parameters of the Monte Carlo simulations are summarized in Table 7.1. Assuming saturated operation of the TRM power amplifiers in transmission, the TRM setting error has been modeled as a zero-mean Gaussian process in amplitude and phase, uncorrelated and with a standard deviation of 0.5 dB (RX) and 5.0 degrees (TX, RX), which are typical specifications of present state-of-the-art SAR missions. The error process has been assumed to be uncorrelated for the set of 384 TRMS ($N_{row} = 32$ and $N_{col} = 12$) and between TX and RX. TRMs' excitations are programmed with 6 bits both in phase and gain, over a range of 360 degrees and 20 dB, respectively.

The different calibration measurements are corrupted by thermal noise, which is characterized by a SNR ranging from 23 dB to 30 dB (before range compression). Some reduction on SNR is present for the alternative strategies compared to the conventional internal calibration, due to tapering in the excitations of some beams. Moreover, some calibration measurements, for the elevation dependent approach, are taken away from the beam-center, inducing also signal attenuation. It must be noted that in any case the noise impact should be considered with the additional range compression gain for nominal pulse parameters in the order of 39 dB.

A set of 26 different beams covering incidence angles between 16 and 60 degrees have been evaluated for the Stripmap mode, considering 101 range lines. Attention must be

paid to the fact that the simulations take into account only points along the swath (range direction) since different azimuth locations at the same range line are affected in the same way when no azimuth steering of the beam is considered⁴. At each range line the integrated error is computed for a set of 50 positions within the synthetic aperture extension, delimited by the -3 dB (one-way) or -6 dB (two-way) contour with respect to the specific elevation/range position. This value is much below the number of pulses integrated during the synthetic aperture according to the corresponding PRF in order to reduce the computational effort in the simulations. Additional simulations have been carried out with a higher number of integrated points and the results are completely correlated with the results here presented. For the stability, different results are presented: worst case and mean value over the different set of 101 range lines, and the results at edges (far and near) as well as center of the beam.

The impact of the residual two-way error on the relative accuracy and the radiometric stability for the three (conventional, operation and elevation dependent calibration) strategies is represented in Fig. 7.3 in terms of 1σ values. The beam labeled as 0 corresponds to broadside excitations (broadside calibration beam). From Figs. 7.3a and 7.3b the standard deviation of the error after conventional internal calibration, for beams 1 to 6, is in the order of 0.033 dB and 0.043 dB for the relative and (mean) stability terms, respectively. In order to maintain the swath width at these lower incidence angles, the beams are widened in transmission introducing appropriate phase alterations (phase spoiling) in the column excitations of the array [172]. The higher error impact on these specific beams is related to the phase spoiling used in transmission, which in turn translates to a higher level of orthogonality, as represented by the dashed (TX) and dotted (RX) green lines in Fig. 7.3a, and in agreement with the theoretical derivation obtained in (7.20). From the stability term in Fig. 7.3b, the error impact is higher at the edges of the beams than at beam center. However, phase error is more sensitive at the swath center in the case of beams with phase spoiling.

In Section 7.4.1, it has been suggested to use as calibration excitations the corresponding operational ones for each beam once the linear phase term to steer the beam has been removed. The impact of the error on the relative accuracy and radiometric stability is shown in Figs. 7.3c and 7.3d, respectively. No improvement is obtained in relative accuracy since the calibration is more effective at beam-center but still degrades at the edges of the beams, as depicted in Fig. 7.3d. Clear improvement can be observed in radiometric stability for the center of the swath and a small improvement in terms of mean value over the different ranges. The worst case impact on stability, particularly at the edges of the beam, follows a similar trend as the conventional calibration.

From these considerations, an elevation dependent calibration strategy is proposed. The performance of this approach is represented in Figs. 7.3e and 7.3f, where three calibration points, at edges (near/far) and center of the beam, have been considered. The complex calibration constants provided by these elevation dependent measurements have been interpolated to create a range/elevation dependent calibration function along the swath of the image to be calibrated. From Figs. 7.3e and 7.3f an improvement can be

⁴In the case of Stripmap mode the different targets over the same range line but at different azimuth positions have the same angular sweep within the mainlobe beam and so a TRM setting error (deformation of the antenna pattern) has the same impact over those targets. Thermal drifts of the setting error during the acquisition should be analyzed separately.

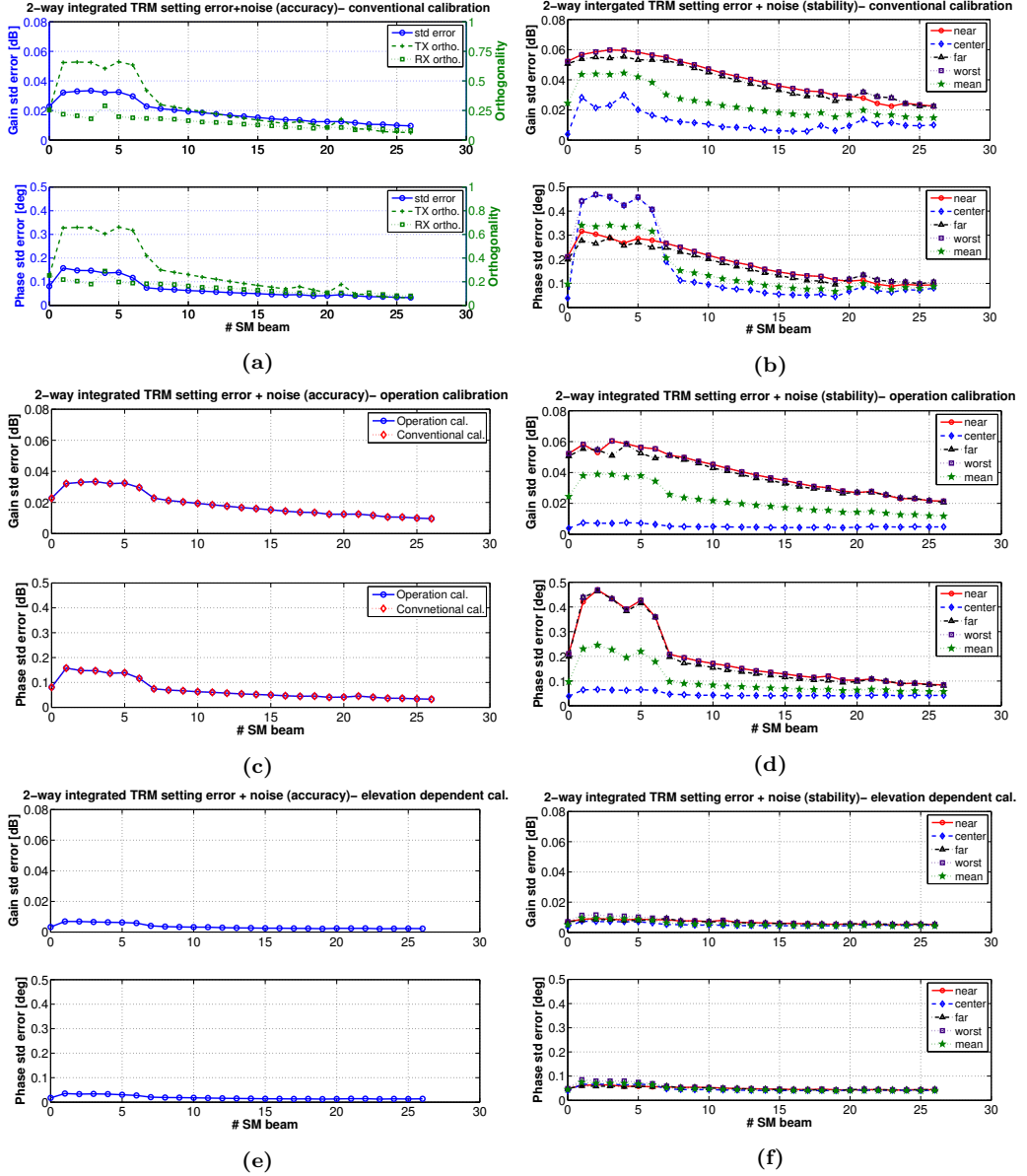


Figure 7.3: Impact of the residual TRM setting error in terms of relative accuracy and radiometric stability for Stripmap beams 1 (incidence angle of 16°) to 26 (incidence angle of 60°): (a)-(b) calibrating with (conventional) broadside beam, where TX/RX orthogonality is also shown; (c)-(d) with operational excitations (except for a linear phase to steer the beam), where broadside calibration is superimposed; and (e)-(f) with an elevation dependent calibration (noisy calibration measurements and error integration during the synthetic aperture formation have been considered).

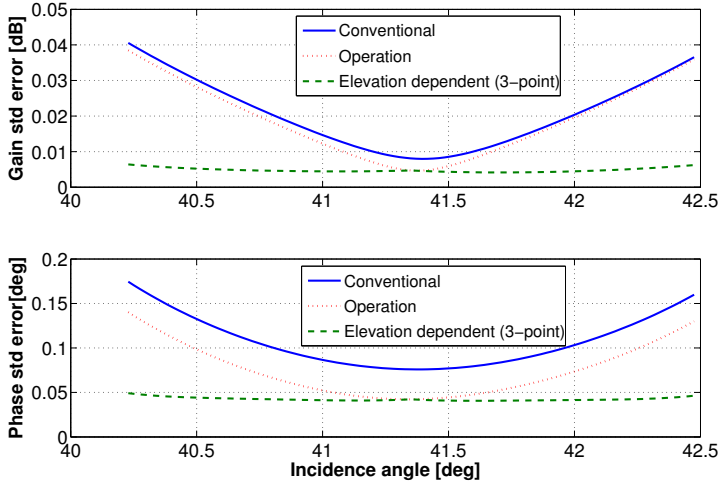


Figure 7.4: Standard deviation of the error (gain and phase) over the different Monte Carlo trials as a function of the incidence angle for operation beam 13.

appreciated for both the relative accuracy (≈ 0.0069 dB and 0.035 degrees - 1σ) and the (mean) radiometric stability (≈ 0.011 dB and 0.085 degrees - 1σ), for beams 1 to 6. When considering noise free calibration measurements, the 1σ error for the elevation dependent calibration reaches 0.0052 dB and 0.026 degrees for the accuracy, while for the (mean) stability the values approach 0.008 dB and 0.066 degrees, slightly better figures for both radiometric terms compared to the noise limited case.

Fig. 7.4 shows clearly the improvement achieved by the elevation dependent calibration compared to the conventional and operation one. In this figure the standard deviation of the error over the different trials is represented as a function of the incidence angle for beam 13. Similar curves are obtained for other beams. This metric corresponds to the stability term extended for the 101 range lines considered along the swath. The error is bigger at the edges of the beam for the conventional and operation one, as concluded from the analysis of the stability term. In the case of elevation dependent calibration a much flatter response of the error along the swath is obtained.

Additional simulations have been carried out considering more range dependent measurements with higher sampling along the main beam: 5-point elevation measurements, at the edges (near/far) and center of the beam as well as two measurements halfway the beam-center and the edges. Close results are obtained for the case of 5-point calibration compared to the 3-point approach; with differences below 0.0015 dB and 0.0022 dB for the accuracy and (mean) stability, respectively. Therefore, it is possible to achieve good performance with a reduced set of elevation dependent calibration measurements properly selected, providing a simple and powerful calibration strategy.

The presented internal calibration methodology would eventually allow to relax the resolution of the TRM attenuators and phase shifters, while still preserving good internal calibration performance. In Fig. 7.5 a setting error of 1.25 dB (RX) and 22.5 degrees (TX,RX), and a quantization of 4 bits for both gain and phase has been simulated,

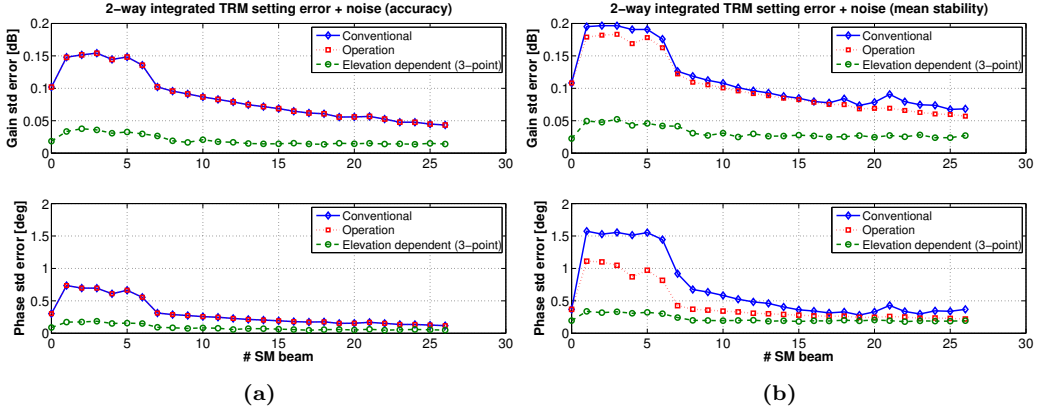


Figure 7.5: Impact of the residual TRM setting error in terms of (a) relative accuracy and (b) mean radiometric stability for the different calibration strategies; relaxed TRM specifications for a setting error with standard deviation of 1.25 dB (TX) and 22.5 degrees (TX, RX) and quantization of 4 bits (noisy calibration measurements and error integration during the synthetic aperture formation have been considered).

considering the same noise conditions as in Fig. 7.3. Compared to the conventional calibration, the elevation dependent approach allows reduction of the error on accuracy from 0.15 dB to 0.037 dB, while the (mean) stability decreases from 0.19 dB to 0.052 dB. Similar trends are also obtained for the phase. Therefore, the elevation dependent calibration represents an appropriate strategy for cost-effective instruments, while still able to provide good radiometric performance.

7.6 Concluding remarks

A novel approach to describe the internal calibration errors in a SAR system equipped with active phased array antennas (APAAs) has been presented, based on the formulation of post-calibration errors. Theoretical and numerical analysis show that the conventional calibration strategy (with broadside excitations) partially compensates the errors associated to the parts of the instrument monitored by the global internal calibration procedure. A residual post-calibration error related to the projection of the errors over the orthogonal TRMs' excitation component (w.r.t calibration weights) exists after internal calibration, even under noise-free conditions. Therefore, internal calibration is strictly correct when both effective TRM operational and calibration excitations are proportional or related by a linear phase term associated to the beam steering.

Two alternative internal calibration strategies based on pulse routing through the instrument path have been proposed: one considering operational excitations on the TRMs during calibration (except for the linear phase term to steer the beam) and a second approach providing range/elevation dependent calibration. Numerical simulations have been carried out considering specific TRM setting errors for the PAZ architecture (similar to the one of TSX) operating in the Stripmap mode, for preliminary non-optimized

beam excitations. These simulations have demonstrated that the elevation dependent calibration provides improved performance in terms of relative accuracy and radiometric stability compared to the conventional approach. For systems with relaxed TRM setting specifications such a calibration methodology is an attractive solution in order to obtain adequate radiometric budget performance.

The proposed calibration strategies have been analyzed and simulated for the Stripmap operation, where different targets with different azimuthal locations (but same range) pass through the main beam of the antenna as the platform moves. Whereas, in the case of Spotlight or TOPSAR, these targets may be illuminated by different parts of the mainlobe. In this sense, the analytical study here presented is valid and the radiometric performance results (relative accuracy and stability) should consider not only targets at different range lines (as here analyzed) but also at different azimuth lines to account for the possible non-uniform azimuthal illumination. Future work should consider the extension of the elevation dependent calibration for the case of Spotlight or the TOPSAR mode to account for an azimuth dependent component, adapting the calibration both in elevation and azimuth, such that the error can be further reduced.

The study of new SAR missions, such as the one proposed in the frame of this thesis for SAR-GMTI purposes, requires likewise the development of adequate calibration strategies: mission optimization goes hand in hand with proper calibration procedures to fully exploit the potentialities of the proposed SAR systems. The evolution towards multichannel SAR architectures to operate new imaging modes, such as SAR-GMTI or HRWS, opens a new and challenging path in the framework of calibration. The study presented in this chapter is mainly focused on the evaluation of alternative internal calibration strategies for APAAs considering a single channel configuration, but it has a direct application to systems with more receiving channels. The complexity comes in rethinking adequate approaches for inter-channel calibration, which ideally could be performed using on-board strategies, increasing system complexity for dedicated calibration loops per channel.

Current channel balancing techniques infer the calibration from the (on-ground) received signal itself to match channel responses as the *Digital Channel Balancing* proposed by Gierull in [74]. This iterative approach, based on 2D-spectral balancing of channels' transfer functions, can be time-consuming and it is applicable mainly over regions with sufficient CNR. An attractive data driven strategy is the clutter-based calibration proposed in [210], which exploits the spatial correlation between any pair of channels: differences between the correlation coefficients, estimated for pairs of adjacent channels with equal baseline configurations, are due to calibration errors. This technique requires redundant baselines in the configuration under analysis, selecting, insofar as possible, the shortest baseline combinations to ensure high correlation values.

The new generation of spaceborne SAR with multiple digital channels exploiting digital beamforming (DBF), such as HRWS [58], proves their potential capabilities, with special interest for wide area SAR-GMTI surveillance operation. Nevertheless, there is still work to be done concerning the adequate calibration methodologies to be applied. The study in [211] represents a first step on possible digital calibration strategies for the new SAR missions. In the same line, a calibration error model is presented in [212] to support the evaluation of multichannel systems operating with DBF in presence of inter-channel errors. Recently, Farquharson *et al* have proposed in [213] a phase calibration

strategy based on the maximization of the image contrast for multichannel systems with DBF. The basic idea behind this contrast-based calibration is that inter-channel phase errors produce defocusing and blurring in the final beamformed image. Therefore, maximizing the contrast should be, in principle, equivalent to estimate the phase calibration vector.

A new complete research line should be devoted to the study of alternative calibration methodologies for upcoming multichannel SAR missions. The error formulation and analysis presented in this chapter as well as the proposed internal calibration strategies can be considered as a possible reference framework for the multiple receive configurations, taking into account that most of these SAR systems will be based on TRM technologies, except for Ka-band and higher frequencies due to power generation efficiency [211].

8

Chapter 8

Conclusions

As a conclusion of the present doctoral thesis, this chapter summarizes the main ideas that have been developed through the 5-year research study, with the intent of wrapping them up into solid concepts for future research and applications.

8.1 Main contributions

During the last decades there has been a tremendous expansion of the shipping market, with an increased number of sea transportation corridors. This has resulted in a continuously growing demand for maritime surveillance, with special emphasis in vessel detection/identification and geo-information recovery. In this framework, spaceborne synthetic aperture radar (SAR) has proved to be a suitable tool for global marine surveillance, being able to provide high-resolution images regardless of daylight and weather conditions.

The combination of a ground moving target indication (GMTI) mode with spaceborne SAR operation is a very attracting system for vessel detection and imaging, with the possibility of information (speed and heading) retrieval. Recently, the operation of GMTI with spaceborne SAR has become a hot topic of research with special emphasis on the road traffic monitoring, with few studies in the maritime scenario case.

With the work described in this thesis, the feasibility to detect small and slowly moving boats in challenging scenarios has been demonstrated with the proposal of a new optimized spaceborne SAR-GMTI mission. Hence, the contents of this thesis intend to contribute to the development of multichannel SAR-GMTI missions as testified by the multilevel study and research carried out. This analysis converge the system-mission design and performance, with proper processing strategies, scenario characterization/modeling, and calibration methodologies proposals. The author aims to provide the scientific community with a complete and detailed analysis of SAR-GMTI operation over maritime scenarios and the tools to simulate, model and evaluate it. The main and original contributions to this thesis together with the reference to the corresponding publications are outlined below:

- *SAR-GMTI state-of-the-art review.* To help understanding the current SAR-GMTI context and the ongoing trends, a detailed compilation and study of the GMTI literature has been carried out based on a historical perspective.
- *Multichannel SAR-GMTI image-based data modeling.* A comprehensive mathematical data formulation has been developed at image level for multichannel SAR-GMTI systems [JA1]; which is of key importance to properly interpret and analyze the different performance results as well as to understand the related operation of the different GMTI techniques. This formulation was critical for the theoretical-based performance evaluation of the different SAR-GMTI missions.
- *SAR-GMTI simulation environments.* In the frame of this doctoral activity, the purpose was to conceive simulation software with sufficient realistic emulation capabilities, being flexibility, modularity and integrability the main characteristics to ease the optimization and evaluation of different SAR conceptual missions. In this sense, a lot of effort has been devoted to the design and implementation of SAR simulation software, which is pivotal to understand and evaluate the capabilities of different SAR-GMTI missions [CA4, CA6, CA7, CA8]. The emulation of realistic SAR systems' operation has been and still is a hot topic of research, merging multidisciplinary knowledge.
- *Development and evaluation of SAR-GMTI missions for maritime surveillance.* The software-based simulation tools have been exploited to test and propose differ-

ent SAR-GMTI missions in order to foresee and demonstrate the capabilities of current state-of-the-art SAR missions as well as the potential future mission concepts [JA1, CA6, CA8]. The GMTI performance of TSX and TDX like missions has been compared with a new optimized multichannel mission using both classical (ATI, DPCA) and optimum (EDPCA) GMTI techniques. The proposed configuration, referred as Boom, is based on non-uniformly displaced receive phase centers, taking advantage of baseline diversity to ensure high sensitivity to slow moving targets and simultaneously alleviating the Doppler ambiguities. The proposed mission has been optimized, trying to minimize the impact of noise contribution (in terms of NESZ) and ambiguities' level (CRAASR metric) in the region of interest (20-40 degrees of incidence angle).

- *Adaptive SAR focusing algorithm.* It is well-studied that in case target kinematic is not properly envisaged in the SAR imaging formation process, severe degradation at image level is present and this in turn can prevent the detection of moving object, especially small and fast boats, which from an operative point of view are also of great interest in maritime surveillance. To compensate for such effects a matched filter bank (MFB) approach incorporating an adaptive SAR processor has been implemented and integrated in the different processing chains [JA1, JA2].
- *SAR-GMTI processing of experimental airborne and spaceborne data over marine scenarios.* Flexible processing chains integrating classical (ATI and DPCA) as well as the new optimum adaptive SAR-GMTI techniques (EDPCA and ISTAP) have been developed to process both airborne (F-SAR) and spaceborne (TSX) data [JA2]. These processors considered a MFB approach to recover SAR image degradation and so SCNR, induced by the motion of the targets. The flexibility of the SAR-GMTI processing chains allowed the selection of different calibration approaches, with the possibility to choose specific regions of interest as reference for calibration weights extraction.
- *Sea clutter characterization.* Some effort has been devoted to perform a characterization of the sea clutter returns imaged by an X-band spaceborne SAR mission as TerraSAR-X [CA3]. The study covered a transversal and compact analysis using three-level descriptors: average radar backscattering coefficient (radiometry), statistics and polarimetry. In the literature, these aspects are investigated mainly as separated topics; but the work here considered has proposed a different approach, filling the gap between the physical approaches of modeling the sea clutter and the signal-based approximations; showing the necessity to account for the technological limitations of current missions [JA3, CA2, CA1].
- *Internal calibration methodologies for SAR equipped with active phased array antennas (APAAs).* When conceiving and optimizing a SAR mission, the development of adequate calibration strategies is pivotal to properly interpret the data and to maximize the potential outcome of the instrument. In this framework, an analysis of the internal calibration strategies for SAR equipped with APAAs has been carried out, proposing and evaluating new calibration methodologies [JA5, CA11].

Part of these contributions have been collected in technical reports related to the projects that have supported this thesis. References to these projects can be found in the list of publications at the end of this book.

8.2 Main conclusions

The main conclusions of this doctoral research are summarized as follows:

- *Spaceborne SAR-GMTI framework.* The exhaustive bibliographic research confirmed the low level of maturity and readiness of spaceborne SAR-GMTI missions, especially in the case of maritime reconnaissance.
- *Theoretical data modeling.* Internal clutter motion (ICM) modeled as decorrelating process and the adequate inclusion of clutter ambiguous returns through the new combined-range-azimuth-ambiguity-to-signal ratio (CRAASR) metric resulted in an accurate modeling of the SAR-GMTI performance, providing useful tools to theoretically evaluate the capabilities of any SAR-GMTI mission.
- *Software-based simulation tools.* Three different flexible simulation tools (multichannel raw data SAR simulator, MSAR-GMTI mission performance tool and Monte Carlo based MSAR-GMTI simulator) have been implemented based on different levels of complexity, related computational cost and potential outcomes. These three emulation entities provide jointly a powerful simulation environment and complement each other perfectly. The final product can provide high-resolution detection images of the moving vessels with any given configuration to be tested, with the corresponding velocity maps and possibly an additional layer of probabilities of detection obtained from the MC data-base in a very cost-effective way. This is of great interest for any potential investor to prove the capabilities of a conceptual mission definition.
- *SAR-GMTI mission conceptual definition and performance evaluation.* The different simulation results indicate that the proposed Boom architecture (3-channel) provides much better detection performance for slowly small boats when using optimum processing strategies such as EDPCA. This configuration is much less affected by the decorrelation impact compared to the TanDEM-X like architecture (4-channel). In case of considering more realistic sea clutter scenarios with a non-Gaussian like modeling, based on a K-distributed clutter's amplitude, the proposed Boom configuration demonstrates that it is more robust compared to the other system-technique combinations.
- *SAR imaging high-speed boats.* A preliminary analysis of high-speed boats, experiencing relatively high longitudinal and horizontal accelerations, has been carried out, showing that in case of integrating a matched filter bank (MFB) approach in the SAR-GMTI processing chain an important improvement factor can be obtained compared to the stationary world matched filter (SWMF). This study has revealed that vertical accelerations modify the line-of-sight acceleration and so produce similar effects as an across-track velocity, i.e., second order phase error in the slant range history (Doppler rate modification).
- *Experimental SAR-GMTI validation over maritime scenarios.* Although the scenario conditions (smooth sea with high reflectivity big vessels) are not the optimal to show the potential capability of state-of-the-art airborne (F-SAR) and spaceborne (TSX) systems in combination with novel GMTI techniques, a proof of concept has been carried out: the adaptive EDPCA and ISTAP techniques give the best performance in terms of SCNR compared to the DPCA algorithm and the single channel

case for both airborne and spaceborne acquisitions. In the airborne case, channel balancing provides improved performance (in terms of SCNR) compared to the non-calibrated case; while for TSX no big differences are observed between the different calibration strategies.

The integrated adaptive SAR focusing algorithm is able to retrieve refocused images of some vessels, where the improvement in the final image quality is especially important for the case of airborne acquisitions (with longer integration times).

- *Sea clutter characterization.* The different results indicated that when observing the sea with TSX, the reduced SNR conditions, especially for the fully polarimetric acquisition mode (based on splitting the receiving antenna into two parts), were a limiting factor in order to extract meaningful information. This effect was more important at high incidence angles, where the reflectivity (average power) of the sea/ocean returns drops off getting closer to the noise level. The statistical analysis showed that the sea clutter response can be modeled as K-distributed in amplitude especially in the small incidence angle region.

The polarimetric description in terms of $H/\bar{\alpha}$ indicated that most of the TSX acquisitions were characterized by low to medium entropy surface scattering, moving to higher entropy values as the incidence angle increased and so consistent with the higher thermal noise contribution. The well-known X-Bragg model demonstrated poor fitting with the data. The extension of this model to account for system-dependent limitations, thermal noise and temporal decorrelation, proved a much better fitting to the real data.

- *SAR with APAA and internal calibration strategies.* The mathematical formulation of the propagated instrumental errors in a SAR instrument using active phased array antennas (APAAs), indicated that the residual post-calibration error is related to the projection of the instrument error over the orthogonal TRM's excitation component. Conventional internal calibration (with broadside excitations) partially compensates those internally monitored errors. Two alternative strategies have been proposed. The elevation-dependent calibration resulted in a much better performance in terms of relative accuracy and radiometric stability; while the internal calibration (with operational excitations) proved a better response compared to the conventional approach only at beamcenter. The range/elevation strategy is a cost-effective solution when considering relaxed TRM setting specifications, as adequate radiometric budget performance can be obtained.

8.3 Future research lines

During this doctoral research several open points have been identified as well as opportunities for further investigations, and are highlighted as follows:

- *SAR high-resolution wide-swath (HRWS) mode with GMTI capabilities.* This combined operation offers a potential tool for wide-swath and high-resolution imaging over maritime scenarios, that translates into a reduction of the revisit time hence the required number of satellites to provide “real-time” maritime surveillance systems:
 - The performance simulation tools developed in the present doctoral research

can be exploited and further extended to incorporate this operational mode and foresee the related SAR-GMTI performance¹.

- Development of proper SAR processing strategies to fully exploit the capabilities of the HRWS mode and how this can be integrated with current GMTI algorithms, especially with the new adaptive techniques such as EDPKA and ISTAP.
- The suitability of the available channel balancing methods when operating with HRWS needs also to be tested, foreseeing the best suitable strategies, taking into account that additional degrees of freedom in the vertical dimension exist and they probably could introduce an elevation/range dependent source of mismatch.
- *Realistic raw data-based simulators.* The development of accurate and realistic SAR raw data-based simulation environments to account for complex maritime scenarios is a topic to be further investigated. Another open point to be tackled is related to realistic modeling of vessels, being able to reproduce any random movement and the corresponding interaction with the ocean waves.
- *Second order sea/ocean backscattering mechanisms.* It is widespread that second order mechanisms such as breaking waves could also be present when imaging the ocean, but the reduced SNR conditions didn't allow extracting solid conclusions regarding this additional mechanism. Further studies are required to understand the impact of breaking-waves on the radar echoes backscattered from the ocean when imaged by a spaceborne SAR.
- *Extension of system-dependent limitations to other physical-based backscattering models.* The polarimetric study of the sea clutter allowed to the identification of system-dependent limitations, which if not properly considered in the related physical model cannot be used to extract reliable parametric information. The extension of the X-Bragg model (X2-Bragg) to include the thermal noise and temporal decorrelation (due to the DRA acquisition) sets the basis to further investigate the same phenomena under other well-known backscattering physical models and hence in the related parametric inversion problem.
- *Multichannel extension of the internal calibration methodologies and analysis.* A lot of effort has been devoted to investigate adequate calibration methodologies for the upcoming multichannel SAR missions. Taking into account that most of these new SAR missions are based on APAAs, the proposed theoretical formulation of the instrument-dependent errors and so of the residual post-calibration errors should be extrapolated to the multichannel configuration case, and specifically trying to derive their impact on the theoretical SAR-GMTI performance.
- *Evaluation and proposal of SAR-GMTI missions for higher operating frequencies.* Operating SAR-GMTI systems at higher carrier frequencies (Ku- and Ka-bands) with higher available bandwidths, is a unique opportunity to provide very high resolution images using smaller instruments with reduced costs, that can be mounted

¹A preliminary study for the SIMTISYS project [31] showed that a constellation of 32 satellites on 8 orbital planes separated 22.5 degrees and with TerraSAR-X like orbit operation provide a revisit time of approximately 1.4 hours (using the conventional Stripmap mode) compared to the 20 hours single satellite case, assuming right and left looking capabilities.

in small cost-effective satellites or even in drones. This will change the paradigm of the radar remote sensing, such that the reconnaissance capabilities move from the governmental authorities to the end-user. However, a lot of research is still required to develop the technology and the corresponding processing strategies. Modeling and characterization of the radar echoes backscattered from the sea at these higher frequencies is also missing.

In summary, the work developed in the present thesis has demonstrate the capability of multichannel SAR sensors for maritime surveillance based on the development of an optimized SAR-GMTI mission, providing the adequate models and tools for its evaluation. This doctoral activity compiles multidisciplinary studies covering system mission definition, data processing and calibration, as well as signal modeling/characterization, showing the intrinsic complexity of the multichannel SAR (specifically SAR-GMTI) problematic. Such a diversification allowed the identification of different issues to be tackled in future research when defining and evaluating new missions with the aim of monitoring the oceans and seas; but also for any multichannel SAR devoted to other geoscience applications that are essential for understanding our planet.

